



National Library  
of Canada

Bibliothèque nationale  
du Canada

Canadian Theses Service

Service des thèses canadiennes

Ottawa, Canada  
K1A 0N4

## NOTICE

The quality of this microform is heavily dependent upon the quality of the original thesis submitted for microfilming. Every effort has been made to ensure the highest quality of reproduction possible.

If pages are missing, contact the university which granted the degree.

Some pages may have indistinct print especially if the original pages were typed with a poor typewriter ribbon or if the university sent us an inferior photocopy.

Reproduction in full or in part of this microform is governed by the Canadian Copyright Act, R.S.C. 1970, c. C-30, and subsequent amendments.

## AVIS

La qualité de cette microforme dépend grandement de la qualité de la thèse soumise au microfilmage. Nous avons tout fait pour assurer une qualité supérieure de reproduction.

S'il manque des pages, veuillez communiquer avec l'université qui a conféré le grade.

La qualité d'impression de certaines pages peut laisser à désirer, surtout si les pages originales ont été dactylographiées à l'aide d'un ruban usé ou si l'université nous a fait parvenir une photocopie de qualité inférieure.

La reproduction, même partielle, de cette microforme est soumise à la Loi canadienne sur le droit d'auteur, SRC 1970, c. C-30, et ses amendements subséquents.

Theory and observations of internal wave  
reflection off sloping topography.

by

Denis Gilbert

Submitted in partial fulfillment of the requirements  
for the degree of Doctor of Philosophy

at

Dalhousie University  
Halifax, Nova Scotia  
December 10, 1990

© Copyright by Denis Gilbert, 1990



National Library  
of Canada

Bibliothèque nationale  
du Canada

Canadian Theses Service    Service des thèses canadiennes

Ottawa, Canada  
K1A 0N4

The author has granted an irrevocable non-exclusive licence allowing the National Library of Canada to reproduce, loan, distribute or sell copies of his/her thesis by any means and in any form or format, making this thesis available to interested persons.

The author retains ownership of the copyright in his/her thesis. Neither the thesis nor substantial extracts from it may be printed or otherwise reproduced without his/her permission.

L'auteur a accordé une licence irrévocable et non exclusive permettant à la Bibliothèque nationale du Canada de reproduire, prêter, distribuer ou vendre des copies de sa thèse de quelque manière et sous quelque forme que ce soit pour mettre des exemplaires de cette thèse à la disposition des personnes intéressées.

L'auteur conserve la propriété du droit d'auteur qui protège sa thèse. Ni la thèse ni des extraits substantiels de celle-ci ne doivent être imprimés ou autrement reproduits sans son autorisation.

ISBN 0-315-64583-0

Canada

Je dédie cette thèse à Émile Péan, professeur de Physique en Secondaire V à la Polyvalente Kénogami, pour m'avoir inculqué le goût de comprendre le monde qui nous entoure.

# Contents

<b>List of figures</b>	<b>ix</b>
<b>List of tables</b>	<b>xiii</b>
<b>Abstract</b>	<b>xiv</b>
<b>List of abbreviations</b>	<b>xv</b>
<b>List of symbols</b>	<b>xvi</b>
<b>Acknowledgements</b>	<b>xix</b>
<b>1 Introduction</b>	<b>1</b>
1.1 The issue of boundary mixing . . . . .	1
1.2 Basic physics of internal wave reflection and historical background . .	5
1.3 Outline of the thesis . . . . .	8
<b>2 Theoretical background</b>	<b>10</b>
2.1 Elements of linear internal wave theory . . . . .	10
2.1.1 The dispersion relation . . . . .	10
2.1.2 Consistency relations . . . . .	14
2.2 Laws of specular internal wave reflection . . . . .	15
2.2.1 Incident energy propagation normal to isobaths. . . . .	15
2.2.2 Generalisation to arbitrary angle of incidence with respect to the isobaths. . . . .	19

2.3	Other processes that could lead to near-bottom energy enhancement within the internal waveband above sloping topography . . . . .	26
2.3.1	Internal tide generation by the surface tide . . . . .	26
2.3.2	Bottom-trapped buoyancy oscillations . . . . .	30
<b>3</b>	<b>Estimates of the dissipated energy flux</b>	<b>35</b>
3.1	Introduction . . . . .	35
3.2	Theoretical estimates of the energy flux available for mixing. . . . .	36
3.2.1	Eriksen's redistributed energy flux . . . . .	36
3.2.2	A more explicit model for estimating the dissipated energy flux due to shear instability of the reflected waves. . . . .	38
3.3	Evaluation of the total residual energy . . . . .	44
3.3.1	Evaluation of $I_1$ and $I_3$ . . . . .	47
3.3.2	Evaluation of $I_2$ . . . . .	49
3.3.3	Total residual energy . . . . .	51
3.4	Distribution of energy within the residual spectrum . . . . .	53
3.5	Dissipated energy flux due to bottom drag associated with the residual currents . . . . .	59
3.6	Discussion . . . . .	60
<b>4</b>	<b>The effects of a non-uniform slope</b>	<b>63</b>
4.1	Introduction . . . . .	63
4.2	Sinusoidal topography . . . . .	64
4.3	Local topographic effects . . . . .	66
4.3.1	Locally convex topography . . . . .	67
4.3.2	Locally concave topography . . . . .	72
4.4	Generalisation of the concavity criterion to the case where $N = N(z)$	77
4.4.1	A simple criterion: $\partial\omega_c/\partial z > 0$ . . . . .	77
4.4.2	WKB-stretching: $\partial^2 h'/\partial x^2 > 0$ . . . . .	79
4.4.3	Application to a model ocean. . . . .	80
4.4.4	Application to the case of the Bermuda slope. . . . .	81
4.4.5	Other observational support . . . . .	82

4.5	Energy back-scatter off rounded and sharp corners . . . . .	83
4.6	Kinematic effects of finite topography . . . . .	85
4.7	Summary . . . . .	90
<b>5</b>	<b>The Scotian Rise and Slope Internal Wavefield</b>	<b>92</b>
5.1	Introduction . . . . .	92
5.2	Description of the data base . . . . .	93
5.2.1	Current meter data . . . . .	93
5.2.2	Hydrographic data . . . . .	97
5.2.3	Bathymetric data . . . . .	97
5.3	Testing the critical reflection hypothesis . . . . .	100
5.3.1	Estimation of $\omega_c$ . . . . .	100
5.3.2	A list of criteria . . . . .	103
5.4	Results . . . . .	105
5.4.1	The Risex Experiment . . . . .	105
5.4.2	The Shelf Break Experiment . . . . .	106
5.5	Discussion . . . . .	117
5.5.1	Energy enhancement (or lack thereof) at mooring sites where $\omega_c \sim f$ . . . . .	117
5.5.2	Internal wave reflection versus internal tide generation at mooring sites where $\omega_c \approx M_2$ . . . . .	119
5.5.3	Energy density at the first overtide ( $M_4$ ). . . . .	120
5.5.4	Evidence for bottom-trapped buoyancy oscillations with $\omega > f$ ? . . . . .	124
<b>6</b>	<b>A closer look at the 3–4 day motions from the Western Boundary Sill Experiment.</b>	<b>130</b>
6.1	The low-frequency currents . . . . .	130
6.2	Power spectral analysis at mooring 636 . . . . .	135
6.2.1	Kinetic energy spectra . . . . .	135
6.2.2	Temperature spectra . . . . .	137
6.2.3	Rotary spectra and the ratio $P_{++}/P_{--}$ . . . . .	137
6.3	Ellipse orientation and stability at mooring 636 . . . . .	140

6.4	Power spectral analysis at mooring 637 . . . . .	146
6.5	Cross-spectral analysis . . . . .	150
6.5.1	In the horizontal: mooring 636 versus mooring 637 . . . . .	150
6.5.2	In the vertical: mooring 636 . . . . .	150
6.6	Complex demodulation at $\omega = 0.0117cph$ . . . . .	152
6.7	Discussion . . . . .	155
6.7.1	Horizontal and vertical cross-spectra . . . . .	156
6.7.2	Harmonic generation of the peak at $\omega \approx 2f$ ? . . . . .	157
6.7.3	Alternative explanation for $P_{++}/P_{--} \approx 1$ near the bottom at mooring 636. . . . .	157
<b>7</b>	<b>Conclusions and Discussion</b>	<b>159</b>
7.1	Summary of the thesis . . . . .	159
7.2	Discussion and suggestions for future work . . . . .	163
<b>A</b>	<b>Data analysis techniques</b>	<b>169</b>
A.1	Estimation of the auto and cross-spectra, and number of equivalent degrees of freedom. . . . .	169
A.2	Estimation of the 95% confidence intervals and significance levels. . .	170
A.3	Clockwise and anticlockwise velocity spectra . . . . .	171
A.4	Current ellipse orientation and stability . . . . .	172
<b>B</b>	<b>Permission to use published work</b>	<b>174</b>
	<b>References</b>	<b>175</b>

# List of Figures

1.1	Schematic of an ocean basin in which boundary mixing leads to an effective vertical diffusivity in the interior. . . . .	3
2.1	Diagram showing the orthogonality of energy and phase propagation for internal waves. . . . .	13
2.2	Schematics of the reflection process for onshore incident energy propagation. . . . .	16
2.3	Definition sketch for the azimuthal angle of incidence $\phi_i$ . . . . .	21
2.4	Wavenumber amplification $ m_r/m_i $ as a function of $a = \tan \alpha \tan \theta$ , and $\phi_i$ . . . . .	23
2.5	Diagram showing the tendency for current ellipses to orient themselves perpendicular to the isobaths upon reflection off a sloping bottom. . .	25
2.6	Diagram explaining the generation of the internal tide over a continental slope. . . . .	28
2.7	Cartesian coordinate system chosen by Rhines (1970) above a uniformly sloping bottom. . . . .	32
3.1	Cutoff modenumbers $j_p$ for which $Ri(j_p) = 1$ . . . . .	40
3.2	Dissipated energy flux $F_{ds}$ due to shear instability of the reflected waves. 41	
3.3	Ratio $R$ of the sum of the incident and residual energy to the total GM79 energy. . . . .	43
3.4	Diagram showing the maximum reflected modenumbers $j_r$ as a function of frequency for the incident modenumbers $j = 1$ and $j = 5$ . . . . .	46
3.5	Domain of integration for $I_2$ . . . . .	50

3.6	Distribution of residual energy density as a function of the frequency $\omega$ .	55
3.7	Distribution of residual energy density as a function of the reflected modenumber $j_r$ .	56
3.8	Inverse Richardson function $Ri^{-1} = \langle (\partial u / \partial z)^2 / N^2 \rangle$ as a function of the reflected modenumber $j_r$ .	57
3.9	Distribution of residual energy density as a function of the reflected azimuth $\phi_r$ .	58
3.10	Energy dissipation rate $F_{dr}$ due to bottom drag associated with the residual currents.	61
4.1	Schematic diagram of locally convex topography.	68
4.2	Schematic diagram of locally concave topography.	73
4.3	Two examples of locally concave topography.	78
4.4	Topographic shape where two plane surfaces intersect via a rounded corner.	84
4.5	Mooring above convex topography with local radius of curvature $R$ .	86
4.6	Variation of the reflected energy spectrum with height above a rounded, convex corner, with $\tan \alpha = 0.125$ .	87
5.1	Map of the Scotian Rise and Slope showing the location of moorings used in chapter 5.	94
5.2	Yearly-averaged profiles of in situ temperature, salinity, and buoyancy frequency on the Scotian Slope.	98
5.3	Bathymetric profiles at $63^\circ 30' W$ and $64^\circ W$ on the Scotian Slope.	99
5.4	Critical frequency $\omega_c$ at $63^\circ 30' W$ , allowing for a $\pm 33\%$ uncertainty in both $N$ and $\tan \alpha$ .	101
5.5	Kinetic energy spectra for mooring R1J.	107
5.6	Kinetic energy spectra from 200m, 1000m and 2900m at mooring R4J, and from 2900m depth at mooring R1J.	108
5.7	Kinetic energy spectra for mooring R5H.	109
5.8	Kinetic energy spectra from 150m and 1530m depth at mooring S5F, and from 1500m depth at mooring S8F.	110

5.9	Kinetic energy spectra for mooring S4E. . . . .	112
5.10	Kinetic energy spectra for mooring S3E. . . . .	113
5.11	Current ellipse orientation and stability 20m above the bottom at mooring S3E. . . . .	114
5.12	Current ellipse orientation and stability 480m above the bottom at mooring S3E. . . . .	115
5.13	Kinetic energy spectra 20m above the bottom at moorings S1D and S2D.	116
5.14	Contours of equal amplitude of the body force responsible for the generation of the internal tide at 63°30'W. . . . .	121
5.15	Kinetic energy spectra from Petrie's (1975) mooring 1A. . . . .	122
5.16	Frequency cutoff $\bar{N} \sin \alpha$ for internal edge waves versus $\bar{\omega}_c = (\bar{N}^2 \sin^2 \alpha + f^2 \cos^2 \alpha)^{1/2}$ at 63°30'W. . . . .	125
5.17	East and North velocity spectra 20m above the bottom at mooring S3F.	126
5.18	Ratio $P_{++}/P_{--}$ of anticlockwise to clockwise kinetic energy 20m above the bottom at mooring S2G. . . . .	127
5.19	Current ellipse orientation and stability 20m above the bottom at mooring S2G. . . . .	128
6.1	Topography in the vicinity of moorings 636 and 637 of the Western Boundary Sill Experiment. . . . .	131
6.2	Low-passed East and North velocity components 10m, 50m, 100m and 200m above the bottom at mooring 636. . . . .	133
6.3	Progressive vector diagrams 10m, 50m, 100m and 200m above the bottom at mooring 636. . . . .	134
6.4	Kinetic energy spectra 10m, 50m, 100m and 200m above the bottom at mooring 636. . . . .	136
6.5	Temperature spectra 10m, 50m, 100m and 200m above the bottom at mooring 636. . . . .	138
6.6	Ratio $P_{++}/P_{--}$ at 10m, 50m, 100m and 200m above the bottom at mooring 636. . . . .	139

6.7	Current ellipse orientation and stability 10m above the bottom at mooring 636. . . . .	142
6.8	Current ellipse orientation and stability 50m above the bottom at mooring 636. . . . .	143
6.9	Current ellipse orientation and stability 100m above the bottom at mooring 636. . . . .	144
6.10	Current ellipse orientation and stability 200m above the bottom at mooring 636. . . . .	145
6.11	Kinetic energy spectra 50m, 100m and 200m above the bottom at mooring 637. . . . .	147
6.12	Temperature spectra 50m, 100m and 200m above the bottom at mooring 637. . . . .	148
6.13	Ratio $P_{++}/P_{--}$ at 50m, 100m and 200m above the bottom at mooring 637. . . . .	149
6.14	Cross-spectra between the current meter 200m above the bottom at mooring 636, and the current meter 50m above the bottom at mooring 637. . . . .	151
6.15	Temperature cross-spectra, for the 50m-10m pair of current meters, and the 100m-10m pair of current meters, at mooring 636. . . . .	153
6.16	East and North components of the velocity complex demodulated at $\omega = 0.0117cph$ 10m, 50m, 100m and 200m above the bottom at mooring 636. . . . .	154

# List of Tables

2.1	Consistency relations for internal waves and Rhines' bottom-trapped buoyancy oscillations. . . . .	33
5.1	Mooring locations on the Scotian Rise and Slope. . . . .	95
5.2	Mooring deployment periods on the Scotian Rise and Slope. . . . .	96
5.3	Cutoff frequency $\overline{N} \sin \alpha$ for internal edge waves, and critical frequency $\overline{\omega}_c$ at various moorings sites on the Scotian Rise and Slope. . . . .	102
5.4	Summary of results from the Scotian Rise and Slope. . . . .	118
6.1	Average potential temperature $\overline{\theta}$ and salinity $\overline{S}$ at mooring 636 of the Western Boundary Sill Experiment. . . . .	132
6.2	Average temperature gradient, salinity gradient, and buoyancy frequency at mooring 636. . . . .	132

## Abstract

When internal waves reflect off a sloping bottom, the angle which the incident and reflected wave rays make with respect to the horizontal is preserved. Close to the critical frequency  $\omega_c$ , for which the wave ray slope equals the bottom slope, the wavenumber, energy density, and shear of the incident waves are greatly amplified upon reflection. Theoretical estimates of the rate of energy dissipation that could result from the enhanced shear of the reflected waves are presented. They are compared with the average energy dissipation rate that would be required if boundary mixing accounted for the inferred vertical eddy diffusivity of the ocean interior, and are found to be within the right order of magnitude, although somewhat too low.

For internal waves incident on a bottom of non-uniform slope, it is argued that one is less likely to observe energy enhancement at the critical frequency above concave than above convex topography. Historical current meter data from the Scotian Rise and Slope, which is mostly concave, are used to test this as well as the critical reflection hypothesis. Some evidence of near-bottom energy enhancement at  $\omega_c \approx f$  was found at a few moorings, and evidence for a cross-isobath alignment of motions and near-bottom energy enhancement over a broad range of frequencies was found at other moorings where  $\omega_c \approx M_2$ .

Finally, current meter data from  $4^\circ\text{N}$ , at a location where Antarctic Bottom Water enters the Northwest Atlantic Basin, are examined in order to determine whether the energetic 3–4 day motions that are observed there can be attributed to critical internal wave reflection. An alternative explanation of these motions in terms of bottom-trapped waves is also examined.

## List of abbreviations

AABW: AntArctic Bottom Water

GM79: Internal wave model proposed by Munk (1981)

IWEX: Internal Wave Experiment

K.E.: Kinetic Energy

NODC: National Oceanographic Data Center

OGCM: Ocean General Circulation Model

P.E.: Potential Energy

RISEX: Scotian Rise Experiment

WBSE: Western Boundary Sill Experiment

## List of symbols

### Roman symbols:

$a$ : frequency parameter such that  $a = \tan \alpha \tan \theta$ .

$A$ :  $A = (1 - f^2/\omega_c^2)$

$b$ : scale height equal to 1300m in the GM79 internal wave model.

$c_1$ :  $c_1 = (1 + a^2)^{3/2}/8s^2 R$

$\mathbf{c}_g$ : group velocity vector

$C_d$ : drag coefficient

$E$ :  $E = 3.3 \times 10^{-5}$  in the GM79 internal wave model.

$\langle |\mathcal{E}(\omega)|^2 \rangle$ : estimated current ellipse stability

$f$ : inertial frequency;  $f = 0.833 \sin(\text{latitude})$  in cycles per hour.

$\mathbf{F}$ : body force responsible for the generation of the internal tide.

$F_{dr}$ : dissipated energy flux due to bottom drag associated with the residual currents.

$F_{ds}$ : dissipated energy flux due to shear instability of the reflected waves

$g$ : gravitational constant;  $g = 9.8ms^{-2}$

$h$ : bottom depth

$i$ : subscript used for the incident wave

$j$ : vertical modenumber

$j_p$ : cutoff vertical modenumber such that  $\sum_{j=1}^{j=j_p} Ri^{-1}(j) = 1$

$\mathbf{k}$ : wavenumber vector;  $\mathbf{k} = (k, \ell, m)$ , and  $|\mathbf{k}| = 2\pi/\lambda$

$k$ : component of the wavenumber vector  $\mathbf{k}$  in the onslope direction.

$K_1$ : diurnal tidal frequency;  $K_1 = 0.0418cph$

$K_v$ : coefficient of vertical eddy diffusivity

$\ell$ : component of the wavenumber  $\mathbf{k}$  in the alongslope direction.

$m$ : vertical component of the wavenumber vector  $\mathbf{k}$

$M_2$ : semi-diurnal tidal frequency;  $M_2 = 0.0805cph$

$M_4$ : first harmonic of  $M_2$ ;  $M_4 = 0.151cph$

$N$ : buoyancy frequency; also known as the Brunt-Väisälä frequency.

$r$ : subscript used for the reflected wave.

$R$ : radius of curvature of the topography

$Re$ : Reynolds number;  $Re = \mathbf{u} \cdot \nabla \mathbf{u} / \nu \nabla^2 \mathbf{u}$

$Ri$ : Richardson number;  $Ri = N^2 / (\partial u / \partial z)^2$

$s$ : characteristic slope;  $s = \tan \mu$ .

$t$ : time

$\mathbf{u}$ : velocity vector;  $\mathbf{u} = (u, v, w)$

$u_*$ : friction velocity

$u$ : velocity component in the  $x$  direction.

$v$ : velocity component in the  $y$  direction.

$w$ : velocity component in the  $z$  direction.

$x$ : horizontal coordinate; in some cases, it is chosen positive in the East direction, and in other cases, it is chosen positive in the onslope direction.

$y$ : horizontal coordinate; in some cases, it is chosen positive in the North direction, and in other cases, it is chosen positive in the alongslope direction.

$z$ : vertical (upwards) coordinate

### Greek symbols:

$\alpha$ : angle which the bottom makes with respect to the horizontal.

$\beta$ :  $\tan \beta =$  bottom slope in chapter 4; also used for  $\beta = df/dy$

$\epsilon$ :  $\epsilon = (\omega - \omega_c) / \omega_c$  in chapter 3; also used for incident wave amplitude in chapter 4.

$\epsilon_f$ :  $\epsilon_f = -(f - \omega_c) / \omega_c$

$\epsilon_j$ :  $\epsilon_j = 2Aj/j_p$

$\epsilon_N$ :  $\epsilon_N = (N - \omega_c) / \omega_c$

$\eta$ : characteristic coordinate;  $\eta = z - sx$

$\gamma$ : ratio of the inertial to the buoyancy frequency;  $\gamma = f/N$

$\Gamma$ : mixing efficiency; fraction of the rate of kinetic energy dissipation that is converted to potential energy

$\kappa$ : horizontal component of the wavenumber vector  $\mathbf{k}$ ;  $\kappa = (k^2 + \ell^2)^{1/2}$

$\lambda$ : wavelength;  $\lambda = 2\pi/|\mathbf{k}|$

$\mu$ : angle which the group velocity vector  $\mathbf{c}_g$  makes with respect to the horizontal.

$\nu$ : kinematic viscosity of water

$\omega$ : frequency

$\omega_c$ : critical frequency such that  $\tan \alpha = \tan \mu$ .

$\omega_T$ : tidal frequency

$\phi$ : angle which the major axis of a current ellipse makes with respect to the onslope direction.

$\langle \phi(\omega) \rangle$ : estimated current ellipse orientation

$\Psi$ : stream function such that  $u = -\partial\Psi/\partial z$ , and  $w = \partial\Psi/\partial x$ .

$\rho$ : water density

$\tau$ : bottom stress;  $\tau \equiv \rho u_*^2 \mathbf{u}$

$\theta$ : angle which the wavenumber vector  $\mathbf{k}$  makes with the horizontal; also used for potential temperature.

$\xi$ : characteristic coordinate;  $\xi = z + sx$

## Acknowledgements

I would like to thank my thesis adviser Chris Garrett for the innumerable suggestions offered during the course of this work. His enthusiasm and willingness to help at various stages of the work were greatly appreciated. Informal discussions with Barry Ruddick improved my understanding of the basic physics of internal waves. I also benefited from many discussions with Hal Sandstrom on the problem of internal wave scattering off irregular topography, and on the problem of internal tide generation by the barotropic tide. Peter Smith made several remarks which helped improve the quality of the thesis, and kindly offered current meter data from the Scotian Rise and Slope to test the critical reflection hypothesis. Doug Gregory copied those data onto magnetic tape for me. The financial support of the Natural Sciences and Engineering Research Council of Canada, the Killam Foundation, and the U.S. Office of Naval Research, is gratefully acknowledged. The moral support and friendship of Dwight Syms, Charlie Martin, Frank Schwing and Renzo Perissinotto is also acknowledged, for without them thoughts of quitting along the way would have conquered my mind.

# Chapter 1

## Introduction

### 1.1 The issue of boundary mixing

Ocean General Circulation Models (OGCM's) are sensitive to the parameterization of sub-grid scale processes. For example, Bryan (1987) showed that the poleward oceanic heat flux increases by an order of magnitude when the vertical heat diffusivity is changed from 0.1 to  $2.5 \times 10^{-4} m^2 s^{-1}$ . Thus it is important that we try to determine  $K_v$  as accurately as possible for present-day conditions. It is also important that we understand what are the dominant mixing mechanisms if we wish to develop any predictive capability as to what the climatic role of the oceans may be in the future.

In a now classic paper, Munk (1966) fitted the vertical profiles of temperature, salinity and Carbon-14 in the Pacific to a simple one-dimensional model in which vertical diffusion is matched by upwelling, and obtained a value of  $1.3 \times 10^{-4} m^2 s^{-1}$  for the "vertical" (or diapycnal) eddy diffusivity  $K_v$ . Somewhat larger values of  $K_v$  have been obtained from abyssal basin heat budgets. Hogg et al (1982) measured the flux of Antarctic Bottom Water (AABW) through the Vema Channel into the Brazil Basin, where water with a temperature less than  $1^\circ C$  vanishes, and assumed a steady state heat balance from which they inferred  $K_v \approx 3$  to  $4 \times 10^{-4} m^2 s^{-1}$ . Saunders (1987) applied the same technique to the Madeira Basin in the northeast Atlantic, and found  $K_v \approx 1.5$  to  $4 \times 10^{-4} m^2 s^{-1}$ .

Whitehead (1989) argues that the values of  $K_v$  obtained from abyssal basin heat

budgets may have to be revised (possibly downwards) due to uncertainties in the inflow rates and areas of isothermal surfaces, but his own calculations based on geostrophic estimates of the flow of AABW entering the Northwest Atlantic at  $4^\circ N$  (Whitehead and Worthington, 1982) still yield  $K_v \approx 1.0 \times 10^{-4} m^2 s^{-1}$ .

Basin-averaged values of  $K_v$  of this magnitude are at odds with most direct measurements of the rates of dissipation of kinetic energy and temperature variance made in the upper part of the main thermocline. Such measurements typically yield  $K_v \approx 10^{-5} m^2 s^{-1}$  or less (Gregg, 1987). They also suggest (Gregg, 1989) that  $K_v$  is independent of the buoyancy frequency  $N$  down to about 1000m, and thus should not increase with depth, but this awaits confirmation from microstructure measurements at greater depths, where the shear and temperature variance are lower, and hence harder to measure reliably.

If conclusions drawn from the microstructure measurements of Gregg and others are correct, and if inferred values of  $K_v$  are also correct, we are left asking where most of the diapycnal mixing takes place in the ocean. Munk (1966) raised the possibility that an effective diapycnal mixing for the ocean may actually arise from vigorous mixing at ocean boundaries, followed by advection and stirring along isopycnals into the more quiescent ocean interior.

The energetic requirements of this were discussed by Garrett and Gilbert (1988) with reference to the schematic ocean shown here in figure 1.1, where  $A_{\text{boundary}}(z, \delta z)$  denotes the area of the bottom exposed to water between two isopycnals which are assumed to be flat and lie at depths  $z$  and  $z + \delta z$ . Note that  $A_{\text{boundary}}$  on figure 1.1 includes the sides of topographic features such as seamounts as well as the sloping sides of ocean basins. If  $F_d$  denotes the average energy dissipation rate per unit area at this boundary, then the total rate of energy dissipation is given by  $F_d A_{\text{boundary}}(z, \delta z)$ .

Meanwhile, if  $K_v$  represents the effective diapycnal mixing rate in the ocean interior, with buoyancy frequency  $N$ , the rate of gain of potential energy there is  $\rho K_v N^2$  per unit volume, or  $\rho K_v N^2 A(z) \delta z$  for the volume of thickness  $\delta z$  and surface area  $A(z)$ . Thus if  $\Gamma$  is the mixing efficiency, i.e. the fraction of energy dissipated at the boundaries which is converted to interior potential energy, we obtain

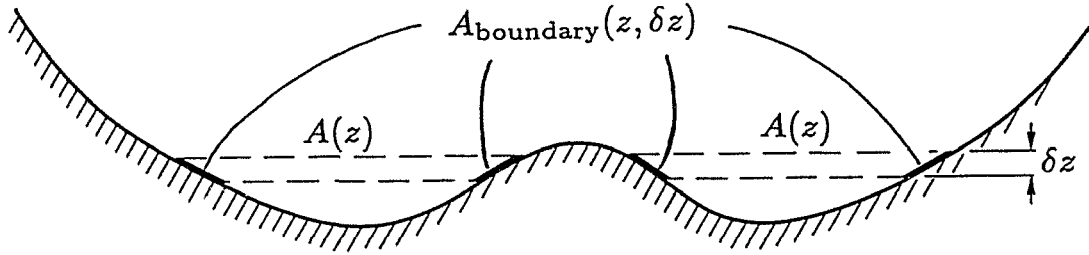


Figure 1.1: Schematic of an ocean basin in which boundary mixing leads to an effective vertical diffusivity in the interior, after Garrett and Gilbert (1988).

$$K_v = \frac{A_{\text{boundary}}(z, \delta z) \Gamma F_d}{A(z) \delta z \rho N^2}. \quad (1.1)$$

Armi (1979) quotes values for the ratio  $A_{\text{boundary}}(z, \delta z)[A(z)\delta z]^{-1}$  for various depth ranges and different oceans. It averages to  $2.2 \times 10^{-4} m^{-1}$  for the 3 to 4 km depth range and  $3.5 \times 10^{-4} m^{-1}$  for the 4 to 5 km depth range. Taking  $N^2 \simeq 10^{-6} s^{-2}$  as typical of the deep ocean, Garrett and Gilbert (1988) then point out that  $K_v \approx 10^{-4} m^2 s^{-1}$  in the ocean interior requires

$$\Gamma F_d \approx 0.3 m W \cdot m^{-2}. \quad (1.2)$$

Munk's (1966) boundary mixing hypothesis was more recently advocated by Armi (1978), who was able to track homogeneous layers of fluid originating at ocean boundaries several hundreds of kilometers into the ocean's interior, and did a rough calculation suggesting that mixing associated with the bottom friction of low-frequency currents ( $\omega \ll f$ ) could be sufficient to account for a basin-averaged value of  $K_v \approx 10^{-4} m^2 s^{-1}$ . However, Garrett (1979) argued that Armi's calculation exaggerated the importance of boundary mixing, because near-bottom turbulence generated by low

frequency currents would likely mix fluid that is more weakly stratified than the ocean interior, and hence may be largely ineffective.

In an important new contribution to research on boundary mixing, Phillips et al. (1986) performed a laboratory experiment which shed some light on possible exchange processes between the ocean interior, and fluid within the boundary layer above sloping topography. Using a tank in which  $N = 0$  near the top and bottom, but is a maximum at mid-depth, they studied the flow patterns that result due to the oscillation of a rigid grid on a bottom of constant slope.

They found that buoyancy flux divergences within the boundary layer cause the establishment of a secondary circulation, such that fluid enters the turbulent boundary layer near the top and bottom of the tank, where  $N$  is small, and leaves it at intermediate depths, intruding the interior fluid in the range of depths where it is more strongly stratified. As time goes by, the isopycnals in the interior fluid separate and the density gradients are reduced, so that boundary mixing acts as an effective interior diffusivity. They suggested that similar exchange processes should be possible in the ocean.

Our observational knowledge of the processes that occur near the sloping boundaries of the ocean is rather limited however. Some of the current measurements suggest a counter-clockwise change in mean current direction as the bottom is approached (in the Northern hemisphere), as in Ekman layers above flat topography. At one of their moorings on the continental slope off New England, Wunsch and Hendry (1972) found the veering angle was  $10^\circ$  from 97m to 10m above the bottom, and  $11^\circ$  from 10m to 2m above the bottom. Bird et al. (1982) found a smaller counter-clockwise veering angle,  $6^\circ$  between 62m and 6.9m off the sea bed, at a mooring 4630m deep on the Bermuda Rise, where the mean current was much larger with an average speed of  $22\text{ cm s}^{-1}$ .

Detailed temperature measurements in the first 100m above the bottom were more recently performed by Thorpe (1987a) and Thorpe et al. (1990) on the Porcupine Bank and the Hebrides Slope. They found that most of the variability in the structure of the boundary layer was associated with the semi-diurnal tide at those locations. They also found that conditions favorable to static instability and overturning tended

to occur during the upslope phase of the tide. The bottom mixed layer sometimes extended up to a few tens of meters above the bottom, but only for a few hours, after which its thickness was generally reduced to less than 10m. This is in sharp contrast with the results of Armi and D'Avanzo (1980), who found that bottom mixed layers several tens of meters thick could persist for several consecutive days above flat topography. Armi and Millard (1976) found that, in general, the thickness of the bottom mixed layer tends to be less above sloping topography than above flat topography. This may be due to secondary circulations of the type studied by Phillips et al. (1986), induced by gradients of the buoyancy flux in the boundary layer, which tend to restratify the fluid within the boundary layer.

In a theoretical paper based upon the work of Phillips et al. (1986), Garrett (1990) looked at the role of the secondary circulation within the boundary layer, and showed that it reduces the mixing efficiency; the overall effectiveness of boundary mixing should involve the square of the reduction factor that would occur for the diffusive flux alone in a region of reduced stratification. Garrett (1990,1991) argues that steady boundary mixing probably cannot produce a significant vertical buoyancy flux unless the mixing extends well into the region that can be restratified by buoyancy forces. He also points out that the reflection of internal waves (Eriksen, 1985) and the reflection and/or generation of internal tides off sloping bottoms (Thorpe, 1987a) may meet this criterion, i.e. those processes raise the possibility not only of increased dissipation within the benthic boundary layer, but also of shear instability and mixing in the stratified region above the bottom mixed layer.

## 1.2 Basic physics of internal wave reflection and historical background

The reflection of internal waves off a plane rigid surface differs markedly from the reflection of electromagnetic or acoustic waves. In Optics or Acoustics, the incident and reflected wave rays make the same angle with respect to the normal to the reflecting surface, whereas for internal waves, the incident and reflected wave rays

make the same angle with respect to the vertical. The unusual nature of the law of reflection for internal waves is a direct consequence of their dispersion relation which states that, for waves of a given frequency, energy must propagate at a given angle with respect to the vertical. As linear theory requires frequency to be conserved upon reflection, the angles which the incident and reflected wave rays make with respect to the vertical must be the same.

Close to the critical frequency  $\omega_c$  for which the wave ray slope equals the bottom slope, simple arguments (Phillips 1977, p.227) show that, upon reflection, the wavenumber, energy density, and shear associated with the incident waves are greatly amplified, so that shear instability and energy dissipation are more likely. This amplification of motions upon reflection results from simple geometric effects together with the law of conservation of energy: as the reflected internal wave beam is narrower than the incident beam, the amplitude (and hence energy density) of the reflected waves must be greater than that of the incident waves in order for energy flux normal to the bottom to be conserved.

Phillips (1963) first pointed this out for inertial waves incident on a bottom of constant slope in a rotating, homogeneous, inviscid fluid, and generalised the theory to internal gravity waves in Phillips (1966). In both cases he assumed that the direction of energy propagation of the incident waves was perpendicular to isobaths.

For an arbitrary angle of incidence with respect to the isobaths, Sandstrom (1966) pointed out that the component of the wavenumber vector parallel to the isobaths is conserved upon reflection. Consequently, the waves should orient themselves closer to the normal to the isobaths upon reflection. Sandstrom was the first to report (p.78) observational evidence for energy enhancement at  $\omega_c$ , using thermistor data from the Bermuda slope (Haurwitz, Stommel and Munk, 1959). He also performed laboratory experiments which clearly demonstrated the amplification of parcel motions that results from internal wave reflection off a sloping bottom (figure 21, p.71), and published that work in Sandstrom (1969).

Carl Wunsch and co-workers at the Massachusetts Institute of Technology also contributed to early research on the problem of internal wave reflection off sloping topography. Wunsch (1968) found progressive internal wave solutions for wedge-like

topography, and pointed out that for waves with ray slope steeper than the bottom slope ( $\omega > \omega_c$ ), one should expect an accumulation of energy, and hence enhanced energy dissipation near the apex of the wedge.

Wunsch (1972a,b) drew attention to the enhanced temperature finestructure found near Bermuda, and suggested that internal wave reflection off the slope of Bermuda could be partly responsible for it. He recomputed the power spectrum of the thermistor data of Haurwitz, Stommel and Munk (1959), and argued that unusually high energy levels at 1-2 hour periods are likely due to internal wave reflection, as Sandstrom (1966) suggested.

Wunsch and Hendry (1972) used data from a complex array of current meters on the New England continental slope, and found rather little support for the theory of Wunsch (1968), i.e. they found no systematic increase in the energy density of waves with  $\omega > \omega_c$  as one progresses toward shallower water. However, their data did show evidence of energy enhancement at the critical frequency at a few mooring sites.

Cacchione and Wunsch (1974) performed laboratory simulations of the process of critical internal wave reflection. They demonstrated the occurrence of an instability manifest as a series of regular vortices, along the sloping boundary, with horizontal axes parallel to the slope. Those regular vortices were not observed in the laboratory experiments of Thorpe and Haines (1987) and Ivey and Nokes (1989), conducted at much higher, and oceanographically more relevant Reynolds numbers ( $Re \approx 2, 20$  and 170 in the experiments of Cacchione and Wunsch, Thorpe and Haines, and Ivey and Nokes respectively).

Other people worked on the problem of internal wave interaction with sloping topography in the late 1960's and early 1970's (e.g. Longuet-Higgins 1969, Hurley 1970, Baines 1971a,b, etc.); their work will be discussed elsewhere in this thesis.

The most recent surge of interest in the problem of internal wave reflection off sloping bottoms is largely due to the work of Eriksen (1982, 1985). Eriksen (1982) presented convincing observational evidence for energy and shear enhancement near the critical frequency at a few mooring sites. He also provided observational evidence for cross-isobath alignment of motions near  $\omega_c$  at a few mooring sites. However, he pointed out this prediction of linear internal wave theory failed at mooring 636

of the Western Boundary Sill Experiment, where the most convincing evidence of near-bottom energy enhancement at  $\omega_c$  was found.

In a later paper, Eriksen (1985) explored the implications for ocean mixing of internal wave reflection off sloping bottoms. Using the observational requirement that the internal wave spectrum a few hundred meters above a sloping bottom has seemingly readjusted to the canonical GM79 form (Munk, 1981), he computed a quantity which he called the “redistributed energy flux” normal to the bottom. He defined it as the integral over all azimuths, frequencies, and wavenumbers of the modulus of the difference between the reflected energy flux and what this flux would be for a reflected spectrum of canonical form.

The values Eriksen obtained for the redistributed energy flux are so large ( $10\text{--}30\text{mW m}^{-2}$ ) that only a small fraction of it could account for a basin-averaged value of the coefficient of vertical eddy diffusivity  $K_v$ , consistent with inferred values (1.2). However, a major shortcoming with Eriksen’s calculation of the “redistributed energy flux” was that he offered no explicit criterion for how much of it should be lost to dissipation, the remainder being presumably redistributed in the four-dimensional internal wave spectrum by nonlinear processes. Nevertheless, his suggestion that internal wave breaking at sloping boundaries may cause diapycnal mixing of global oceanic significance is important and deserves closer attention.

### 1.3 Outline of the thesis

In chapter 2, I summarize the essentials of linear internal wave theory, following Gill (1982). I derive the specular laws of reflection for incident energy propagation normal to isobaths first, and then for arbitrary angle of incidence. The process of internal tide generation over a continental slope is briefly discussed, and I give the main results of Rhines (1970) on internal edge waves.

In chapter 3, I describe the mechanistic hypothesis of Garrett and Gilbert (1988) for estimating the dissipated energy flux that might result from internal wave breaking above sloping topography. The algebraic steps leading to the evaluation of the total residual energy are given, and the rate of energy dissipation that could result from

bottom drag associated with the residual currents is evaluated.

In chapter 4, I deal with a few aspects of internal wave scattering off irregular topography, following Gilbert and Garrett (1989). For the most part, this chapter consists of a review of work published on that topic in the early 1970's. A great deal of attention is paid to the convex and concave topographic shapes of Baines (1971b,1974), and a physical interpretation of his most important findings is given. His conclusions are generalised for the case where the buoyancy frequency  $N$  varies with depth.

In chapter 5, current meter data from the continental rise and slope off Nova Scotia are used to look for evidence of energy enhancement and/or cross-isobath alignment of motions near  $\omega_c$ . I also pay attention to other processes taking place on the Scotian Rise and Slope, such as the generation of internal tides, and the possible existence of bottom-trapped waves within the internal waveband.

In chapter 6, current meter data from the Western Boundary Sill Experiment are analysed in detail. In particular, I try to verify whether the near-bottom enhancement of motions with 3-4 day periods at mooring 636 can be attributed to internal wave reflection off sloping topography, as Eriksen (1982) suggested. An alternative interpretation of those energetic motions in terms of bottom-trapped buoyancy oscillations is examined.

In chapter 7, I summarise the results of earlier chapters. Questions left unanswered in this thesis are raised, and possible ways of tackling them in the future are proposed in some cases.

# Chapter 2

## Theoretical background

### 2.1 Elements of linear internal wave theory

In this section, I summarise the main results of linear internal wave theory, following Gill (1982) for the most part. Lighthill (1978) and LeBlond and Mysak (1978) also give detailed accounts of linear internal wave theory. The reader is referred to any of these books for algebraic steps omitted here for the sake of brevity.

#### 2.1.1 The dispersion relation

The linearised equations of motion for a stratified, rotating, incompressible, inviscid, Boussinesq fluid are given by

$$\frac{\partial u}{\partial t} - fv = \frac{-1}{\rho_o} \frac{\partial p}{\partial x} \quad (2.1)$$

$$\frac{\partial v}{\partial t} + fu = \frac{-1}{\rho_o} \frac{\partial p}{\partial y} \quad (2.2)$$

$$\frac{\partial w}{\partial t} = \frac{-1}{\rho_o} \frac{\partial p}{\partial z} - \frac{\rho' g}{\rho_o} \quad (2.3)$$

together with the continuity equation

$$\frac{\partial u}{\partial x} + \frac{\partial v}{\partial y} + \frac{\partial w}{\partial z} = 0 \quad (2.4)$$

where  $(u, v, w)$  are the velocity components in the  $(x, y, z) = (\text{Eastward, Northward, Upward})$  directions respectively,  $f = 2\Omega \sin \phi$  is the Coriolis parameter given in terms of the Earth's angular speed  $\Omega$  and latitude  $\phi$ ,  $p$  is the departure from hydrostatic pressure,  $\rho_o = \rho_o(z)$  is the background mean density,  $\rho' = \rho - \rho_o$  is the perturbation density, and  $g = 9.8 \text{ms}^{-2}$  is the Earth's gravitational constant. Finally, the linearised form of the equation expressing the conservation of density for a material particle ( $D\rho/Dt = 0$ ) is given by

$$\frac{\partial \rho'}{\partial t} + w \frac{\partial \rho_o}{\partial z} = 0. \quad (2.5)$$

We thus have a system of five differential equations in the five unknowns  $u, v, w, p$  and  $\rho'$ . It is possible to eliminate  $u, v, p$  and  $\rho'$  from this set of equations, and reduce it to a single differential equation in terms of the vertical velocity  $w$ :

$$\frac{\partial^2}{\partial t^2} \left( \frac{\partial^2 w}{\partial x^2} + \frac{\partial^2 w}{\partial y^2} + \frac{\partial^2 w}{\partial z^2} \right) + f^2 \frac{\partial^2 w}{\partial z^2} + N^2 \left( \frac{\partial^2 w}{\partial x^2} + \frac{\partial^2 w}{\partial y^2} \right) = 0, \quad (2.6)$$

$$\text{where} \quad N^2 = \frac{-g}{\rho_o} \frac{\partial \rho_o}{\partial z} \quad (2.7)$$

is the square of the Brunt-Vaisala frequency, the frequency at which a water parcel oscillates when displaced vertically from its equilibrium position. Gill (1982, p.129) suggests we should simply call  $N$  the buoyancy frequency, as Rayleigh drew attention to it before Brunt and Vaisala, and it is a physically more relevant name as the restoring force responsible for its existence is the buoyancy term  $g\rho'/\rho_o$  in (2.3).

To obtain the dispersion relation for internal gravity waves in a rotating fluid (also referred to as inertio-gravity waves), wave solutions of the form

$$w = w_o \exp [i(kx + ly + mz - \omega t)] \quad (2.8)$$

are substituted into (2.6), yielding

$$\omega^2 = \frac{N^2(k^2 + \ell^2) + f^2 m^2}{k^2 + \ell^2 + m^2} \quad (2.9)$$

where  $(k, \ell, m)$  are the  $(x, y, z)$  components of the wavenumber vector  $\mathbf{k}$ , and  $\omega$  is the frequency of the waves. Letting  $\kappa = (k^2 + \ell^2)^{1/2}$  denote the horizontal component of the wavenumber vector  $\mathbf{k}$ , the dispersion relation (2.9) can also be written as

$$\omega^2 = \frac{N^2 \kappa^2 + f^2 m^2}{\kappa^2 + m^2}, \quad (2.10)$$

$$\text{or} \quad \omega^2 = N^2 \cos^2 \theta + f^2 \sin^2 \theta \quad (2.11)$$

where  $\theta$  is the angle which the wavenumber vector makes with respect to the horizontal. Since  $0 \leq |\theta| \leq \pi/2$ , it follows that  $f \leq \omega \leq N$ . One can also write (2.11) in the commonly used form

$$\tan^2 \theta = \left( \frac{N^2 - \omega^2}{\omega^2 - f^2} \right). \quad (2.12)$$

The group velocity of internal waves can be obtained by differentiating the dispersion relation (2.10) with respect to the horizontal and vertical components of the wavenumber vector, giving

$$\mathbf{c}_g = \left( \frac{\partial \omega}{\partial \kappa}, \frac{\partial \omega}{\partial m} \right) = \frac{\kappa m (N^2 - f^2)}{\omega (\kappa^2 + m^2)^2} (m, -\kappa), \quad (2.13)$$

which implies that  $\mathbf{c}_g \cdot \mathbf{k} = 0$ , i.e.  $\mathbf{c}_g \perp \mathbf{k}$ . This is one of the most important results of linear internal wave theory. It expresses the remarkable fact that the direction of energy propagation is perpendicular to the direction of phase propagation for internal waves, so that a packet of waves would appear to slide sideways along the crests. It also means that when phase propagation is upwards, energy propagation is downwards, and vice versa (see figure 2.1). From (2.13), the modulus of the group velocity vector is given by

$$|\mathbf{c}_g| = \frac{\kappa m (N^2 - f^2)}{\omega (\kappa^2 + m^2)^{3/2}} = \frac{N^2 - f^2}{\omega |\mathbf{k}|} \cos \theta \sin \theta. \quad (2.14)$$

The group velocity thus vanishes at  $N$  and  $f$ , where  $\theta = 0$  and  $\pi/2$  respectively (2.12), and is inversely proportional to  $\omega$  and  $|\mathbf{k}|$ . If we let  $\mu$  denote the angle which  $\mathbf{c}_g$  makes with respect to the horizontal (figure 2.1), we have that  $|\theta| = \pi/2 - |\mu|$ , so that

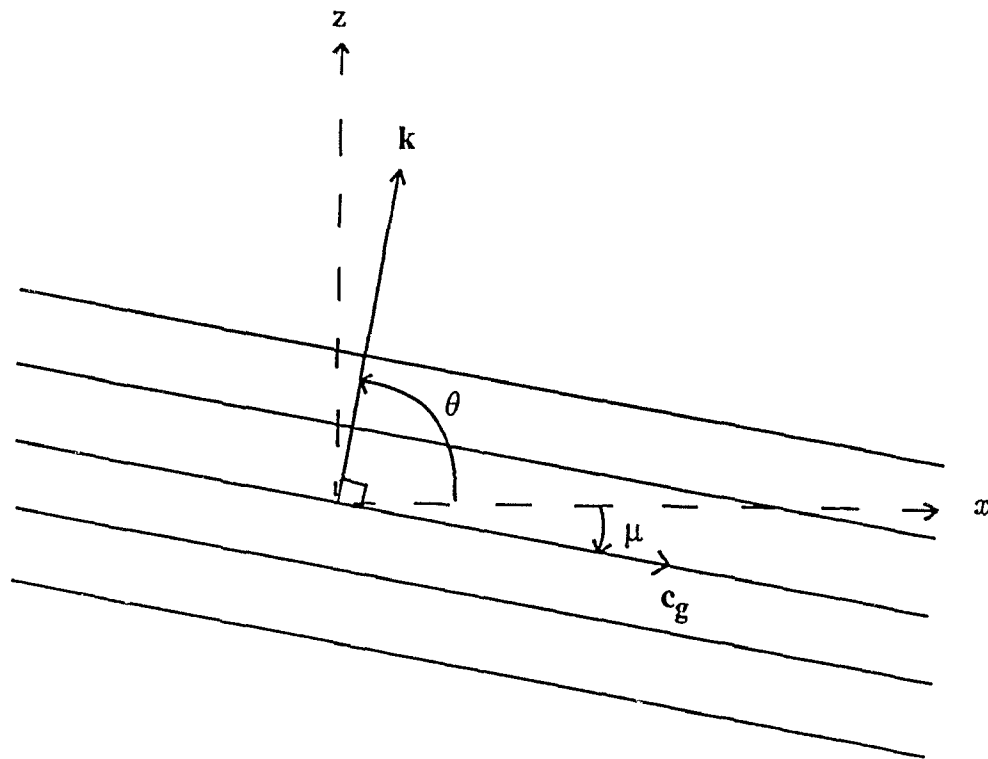


Figure 2.1: Diagram showing the orthogonality of energy and phase propagation for internal waves. The oblique lines represent planes of constant phase. They propagate in the direction of the wavenumber vector  $k$  as time progresses. Meanwhile the energy of a wave packet propagates at right angles to that, with group velocity  $c_g$ , i.e. in a direction parallel to individual wave crests. The angles which  $k$  and  $c_g$  make with respect to the horizontal are denoted by the symbols  $\theta$  and  $\mu$  respectively.

$$\tan^2 \mu = \frac{1}{\tan^2(\pi/2 - |\mu|)} = \frac{1}{\tan^2 \theta}, \quad (2.15)$$

and from (2.12), we get

$$\tan^2 \mu = \left( \frac{\omega^2 - f^2}{N^2 - \omega^2} \right). \quad (2.16)$$

Internal wave energy thus propagates at small angles with respect to the horizontal at near-inertial frequencies, and this angle increases with frequency, becoming vertical at the buoyancy frequency.

## 2.1.2 Consistency relations

Fofonoff (1969) has shown that it is possible to determine whether fluctuations in moored measurements are consistent with linear internal wave theory. For given values of  $f$  and  $N$ , he showed that the ratio of potential energy to horizontal kinetic energy should be a function of frequency only, and is given by

$$\frac{N^2 P_{\zeta\zeta}}{P_{uu} + P_{vv}} = \left( \frac{N^2}{N^2 - \omega^2} \right) \left( \frac{\omega^2 - f^2}{\omega^2 + f^2} \right), \quad (2.17)$$

where  $P_{\zeta\zeta}$ ,  $P_{uu}$  and  $P_{vv}$  are the autospectra of vertical isopycnal displacement, East velocity, and North velocity.

Decomposing the elliptical motion of a water parcel into cyclonically and anticyclonically rotating parts, it can also be shown that the energy in the cyclonically rotating part ( $P_{++}$ ) should be smaller than that in the anticyclonically rotating part ( $P_{--}$ ) by the factor (Gill 1982, p. 306):

$$\frac{P_{++}}{P_{--}} = \left( \frac{\omega - |f|}{\omega + |f|} \right)^2 \quad (2.18)$$

independently of the directional properties of the spectrum. In the Northern hemisphere,  $P_{++}$  represents the anticlockwise energy density, and  $P_{--}$  represents the clockwise energy density (Appendix A). Note that while (2.18) can be derived from the spectral functions of Fofonoff (1969), it is not explicitly written down in that form there.

## 2.2 Laws of specular internal wave reflection

### 2.2.1 Incident energy propagation normal to isobaths.

Let us consider an ocean of infinite depth in which the buoyancy frequency  $N$  is constant, and the bottom slope is  $\tan \alpha$  (figure 2.2). It is possible to derive the linear laws of specular reflection for internal waves incident on such a boundary simply by invoking

1. the conservation of wave crests upon reflection,
2. the conservation of frequency upon reflection,
3. the conservation of energy flux upon reflection.

Conservation of frequency upon reflection implies that the angle  $\mu$  which the incident and reflected wave rays make with the horizontal must be the same (2.16), as illustrated on figure 2.2, and conservation of wavecrests upon reflection implies that each incident wavecrest gives rise to a reflected wavecrest, so that incident and reflected wavecrests must match on the boundary.

Mathematically, those two conservation laws translate into

$$\mathbf{k}_i \cdot \hat{\mathbf{s}} = \mathbf{k}_r \cdot \hat{\mathbf{s}}, \quad \hat{\mathbf{s}} = (\cos \alpha, 0, \sin \alpha) \quad (2.19)$$

where  $\hat{\mathbf{s}}$  is a unit vector in the plane of the slope, pointing in the upslope direction, and

$$\mathbf{k}_i = |\mathbf{k}_i|(\sin \mu, 0, \cos \mu), \quad (2.20)$$

$$\mathbf{k}_r = |\mathbf{k}_r|(\sin \mu, 0, -\cos \mu) \quad \text{for } \mu > \alpha. \quad (2.21)$$

We can thus rewrite (2.19) as

$$|\mathbf{k}_i|(\sin \mu, 0, \cos \mu) \cdot (\cos \alpha, 0, \sin \alpha) = |\mathbf{k}_r|(\sin \mu, 0, -\cos \mu) \cdot (\cos \alpha, 0, \sin \alpha) \quad (2.22)$$

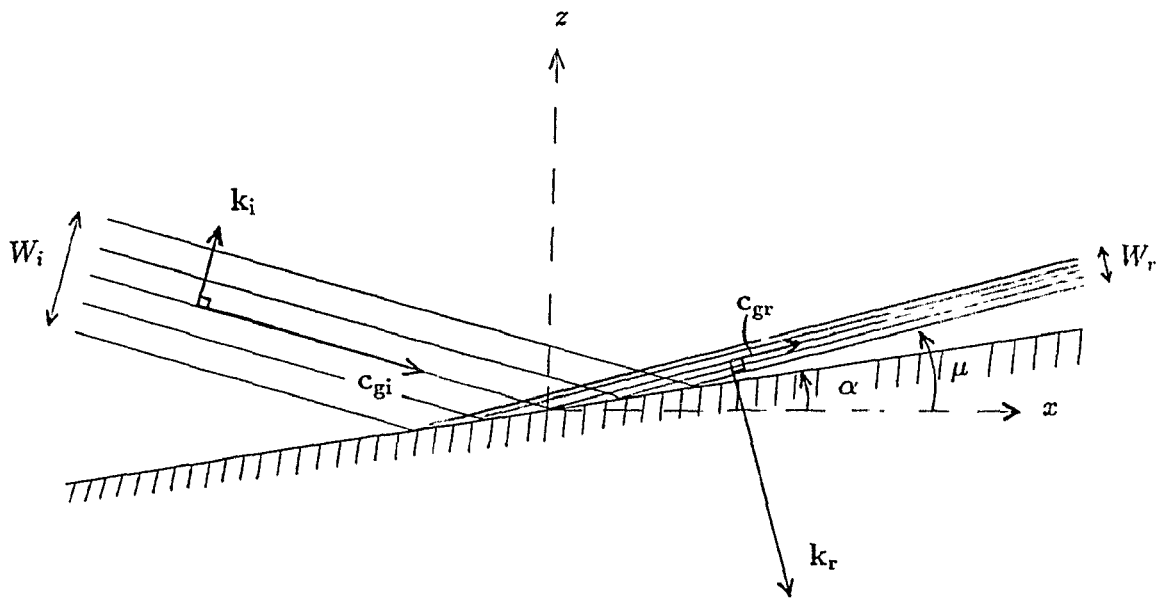


Figure 2.2: Schematics of the reflection process for incident energy propagation normal to isobaths. The  $i$  and  $r$  subscripts refer to the incident and reflected waves respectively,  $c_g$  and  $k$  are the group velocity and wavenumber vectors,  $W$  is the width of the internal wavebeam, and  $\alpha$  and  $\mu$  are the angles which the bottom slope and the wave rays make with the horizontal.

$$|\mathbf{k}_i|(\sin \mu \cos \alpha + \cos \mu \sin \alpha) = |\mathbf{k}_r|(\sin \mu \cos \alpha - \cos \mu \sin \alpha) \quad (2.23)$$

$$\frac{|\mathbf{k}_r|}{|\mathbf{k}_i|} = \frac{\sin(\mu + \alpha)}{\sin(\mu - \alpha)} \quad (2.24)$$

Similarly, we have

$$\mathbf{k}_r = |\mathbf{k}_r|(-\sin \mu, 0, \cos \mu) \quad \text{for } \mu < \alpha, \quad (2.25)$$

and we can show that (2.19) leads to

$$\frac{|\mathbf{k}_r|}{|\mathbf{k}_i|} = \frac{\sin(\alpha + \mu)}{\sin(\alpha - \mu)}. \quad (2.26)$$

Thus according to (2.24) and (2.26), specular internal wave reflection off a sloping bottom leads to the wavenumber amplification

$$\frac{|\mathbf{k}_r|}{|\mathbf{k}_i|} = \pm \frac{\sin(\alpha + \mu)}{\sin(\alpha - \mu)} \quad \text{for } \mu \begin{matrix} < \\ > \end{matrix} \alpha, \quad (2.27)$$

and from (2.21) and (2.25), the amplifications of the vertical and horizontal components of the wavenumber vector are given by

$$\frac{m_r}{m_i} = \frac{\sin(\alpha + \mu)}{\sin(\alpha - \mu)}, \quad \frac{k_r}{k_i} = -\frac{\sin(\alpha + \mu)}{\sin(\alpha - \mu)}. \quad (2.28)$$

Hence  $m$  changes sign upon reflection when  $\mu > \alpha$ , and  $k$  changes sign when  $\mu < \alpha$ . Note that there is a singularity in the wavenumber amplification when  $\mu = \alpha$ . The frequency at which this occurs is called the critical frequency, and is such that  $\theta = \pi/2 - \alpha$ . Substituting this value of  $\theta$  into (2.11), we obtain

$$\omega_c^2 = N^2 \sin^2 \alpha + f^2 \cos^2 \alpha. \quad (2.29)$$

Now Gill (1982, p.267) points out that for internal waves, the energy flux density vector  $\mathbf{F}'$ , given by

$$\mathbf{F}' = \overline{p' \mathbf{u}}, \quad (2.30)$$

where  $p'$  and  $\mathbf{u}$  are the perturbation pressure and velocity, can also be written in the form

$$\mathbf{F}' = E \mathbf{c}_g, \quad (2.31)$$

where  $\mathbf{c}_g$  is the group velocity vector whose magnitude is given by (2.14), and  $E$  is the mean perturbation energy per unit volume associated with the internal waves

$$E = \frac{1}{2} \rho_o (\overline{u^2 + v^2 + w^2}) + \frac{1}{2} \frac{g^2 \overline{\rho'^2}}{\rho_o N^2}, \quad (2.32)$$

where each overbar denotes the mean over one wavelength. If we now invoke the third conservation law mentioned above, namely that energy flux be conserved upon reflection, then the incident energy flux across the section of width  $W_i$  must equal the reflected energy flux across the section of width  $W_r$  (figure 2.2). Using (2.31), this implies that

$$E_i |\mathbf{c}_{gi}| W_i = E_r |\mathbf{c}_{gr}| W_r, \quad (2.33)$$

$$\text{where} \quad \frac{W_r}{W_i} = \frac{\lambda_r}{\lambda_i} = \frac{|\mathbf{k}_i|}{|\mathbf{k}_r|}, \quad (2.34)$$

and from (2.14),

$$\frac{|\mathbf{c}_{gr}|}{|\mathbf{c}_{gi}|} = \frac{|\mathbf{k}_i|}{|\mathbf{k}_r|}, \quad (2.35)$$

so that

$$E_i |\mathbf{c}_{gi}| W_i = E_r |\mathbf{c}_{gi}| \frac{|\mathbf{k}_i|}{|\mathbf{k}_r|} W_i \frac{|\mathbf{k}_i|}{|\mathbf{k}_r|}, \quad (2.36)$$

$$\therefore \frac{E_r}{E_i} = \left( \frac{|\mathbf{k}_r|}{|\mathbf{k}_i|} \right)^2 = \left( \frac{m_r}{m_i} \right)^2. \quad (2.37)$$

The ratio of the reflected and incident energy density is thus equal to the square of the wavenumber amplification. Using (2.8) and (2.37), it is now straightforward to show that upon reflection, the mean square vertical shear of horizontal currents is amplified by the factor

$$\frac{\left(\left(\frac{\partial u}{\partial z}\right)^2 + \left(\frac{\partial v}{\partial z}\right)^2\right)_r}{\left(\left(\frac{\partial u}{\partial z}\right)^2 + \left(\frac{\partial v}{\partial z}\right)^2\right)_i} = \frac{m_r^2 \overline{(u^2 + v^2)}_r}{m_i^2 \overline{(u^2 + v^2)}_i} \quad (2.38)$$

$$= \frac{m_r^2 E_r}{m_i^2 E_i} \quad (2.39)$$

$$\frac{\left(\left(\frac{\partial u}{\partial z}\right)^2 + \left(\frac{\partial v}{\partial z}\right)^2\right)_r}{\left(\left(\frac{\partial u}{\partial z}\right)^2 + \left(\frac{\partial v}{\partial z}\right)^2\right)_i} = \left(\frac{m_r}{m_i}\right)^4. \quad (2.40)$$

The amplification of the mean square shear is thus equal to the wavenumber amplification (2.28) to the fourth power. Therefore one expects that the Richardson number  $Ri = N^2/(\partial u/\partial z)^2$  could fall to low values due to internal wave reflection off sloping bottoms, possibly leading to shear instability whenever  $Ri$  falls below a critical value ( $Ri_c = 1/4$  say).

### 2.2.2 Generalisation to arbitrary angle of incidence with respect to the isobaths.

In all generality, for internal waves impinging on a sloping bottom with arbitrary angle of incidence with respect to the isobaths, the vertical velocity associated with the incident and reflected waves can be written in the form

$$w_i \propto \exp[i(k_i x + \ell_i y + m_i z - \omega_i t)] \quad (2.41)$$

$$w_r \propto \exp[i(k_r x + \ell_r y + m_r z - \omega_r t)], \quad (2.42)$$

where the  $i$  and  $r$  subscripts refer to the incident and reflected waves respectively. Analogous expressions could be written down for the  $u$  and  $v$  velocity components. Therefore, the boundary condition of no normal flow across the bottom ( $\mathbf{u} \cdot \hat{\mathbf{n}} = 0$ ) must necessarily be of the form

$$\{\dots\} \exp[i(k_i x + \ell_i y + m_i z - \omega_i t)] + \{\dots\} \exp[i(k_r x + \ell_r y + m_r z - \omega_r t)] = 0 \quad (2.43)$$

at  $z = x \tan \alpha$ , so that

$$\{\dots\} \exp[i(k_i x + \ell_i y + m_i x \tan \alpha - \omega_i t)] + \{\dots\} \exp[i(k_r x + \ell_r y + m_r x \tan \alpha - \omega_r t)] = 0. \quad (2.44)$$

Such a boundary condition can be satisfied for all values of time  $t$  only if

$$\omega_i = \omega_r = \omega, \quad (2.45)$$

for all values of the alongslope coordinate  $y$  only if

$$\ell_i = \ell_r = \ell, \quad (2.46)$$

and for all values of  $x$  only if

$$k_i + m_i \tan \alpha = k_r + m_r \tan \alpha \quad (2.47)$$

$$\text{or} \quad k_r = k_i + (m_i - m_r) \tan \alpha. \quad (2.48)$$

Equation (2.45) merely states that frequency is unchanged upon reflection. It then follows from (2.12) that the angle  $\theta$  which the wavenumber vector makes with the horizontal is also conserved upon reflection, so that

$$\tan^2 \theta_r = \tan^2 \theta_i, \quad (2.49)$$

$$\frac{m_r^2}{\ell^2 + k_r^2} = \frac{m_i^2}{\ell^2 + k_i^2}, \quad (2.50)$$

which, using (2.48), becomes

$$\left(\frac{m_r}{m_i}\right)^2 = \frac{\ell^2 + [k_i + (m_i - m_r) \tan \alpha]^2}{\ell^2 + k_i^2} \quad (2.51)$$

$$= \frac{\ell^2}{\ell^2 + k_i^2} + \left[ \frac{k_i + (1 - m_r/m_i)m_i \tan \alpha}{(\ell^2 + k_i^2)^{1/2}} \right]^2 \quad (2.52)$$

$$\left(\frac{m_r}{m_i}\right)^2 = \sin^2 \phi_i + \left[ \cos \phi_i + \left(1 - \frac{m_r}{m_i}\right) \tan \theta_i \tan \alpha \right]^2 \quad (2.53)$$

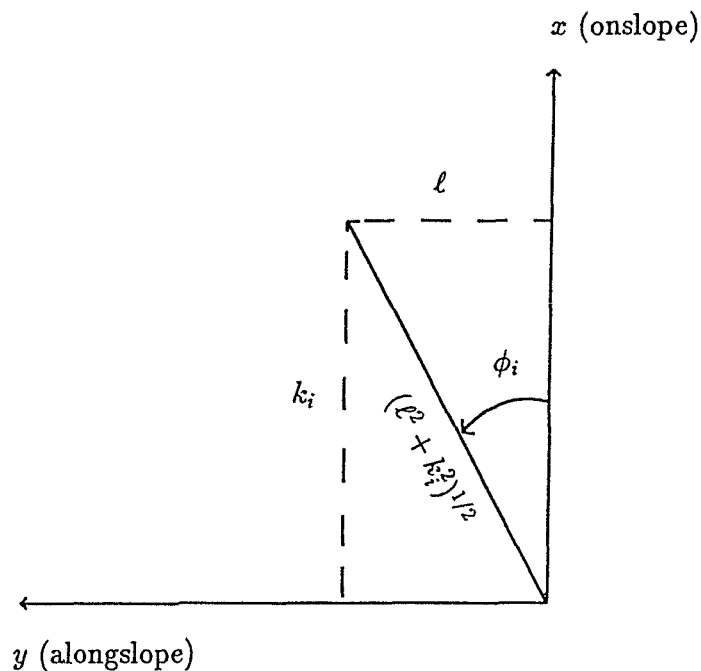


Figure 2.3: The projection of the wavenumber vector  $\mathbf{k}_i = (k_i, \ell, m_i)$  onto the horizontal plane makes the angle  $\phi_i$  with respect to the onslope direction.

where  $\phi_i$  is as defined on figure 2.3. If we now let

$$a = \tan \alpha \tan \theta_i, \quad \text{then} \quad (2.54)$$

$$\left(\frac{m_r}{m_i}\right)^2 = \sin^2 \phi_i + \cos^2 \phi_i + 2a \cos \phi_i \left(1 - \frac{m_r}{m_i}\right) + a^2 \left(1 - 2\frac{m_r}{m_i} + \frac{m_r^2}{m_i^2}\right) \quad (2.55)$$

Grouping like powers of  $m_r/m_i$ , we obtain the quadratic equation

$$\left(\frac{m_r}{m_i}\right)^2 (1 - a^2) + \left(\frac{m_r}{m_i}\right) 2a(\cos \phi_i + a) - (1 + 2a \cos \phi_i + a^2) = 0, \quad (2.56)$$

which can be solved in the usual way, yielding the two roots

$$\frac{m_r}{m_i} = 1, \quad \text{and} \quad (2.57)$$

$$\frac{m_r}{m_i} = \frac{a^2 + 2a \cos \phi_i + 1}{a^2 - 1}, \quad a = \tan \alpha \tan \theta_i. \quad (2.58)$$

We reject the first root on physical grounds, as it corresponds to the case where no reflection occurs, so that energy continues to propagate along its original path, through the bottom. When  $\phi_i = 0$ , (2.58) reduces to (2.28), as it should:

$$\frac{m_r}{m_i} = \frac{a + 1}{a - 1} = \frac{\tan \alpha \tan \theta_i + 1}{\tan \alpha \tan \theta_i - 1}, \quad (2.59)$$

$$= \frac{\tan \alpha + \tan \mu}{\tan \alpha - \tan \mu} \quad (2.60)$$

$$= \frac{\sin \alpha \cos \mu + \sin \mu \cos \alpha}{\sin \alpha \cos \mu - \sin \mu \cos \alpha} \quad (2.61)$$

$$\frac{m_r}{m_i} = \frac{\sin(\alpha + \mu)}{\sin(\alpha - \mu)}. \quad (2.62)$$

Figure 2.4 shows how the wavenumber amplification  $|m_r/m_i|$  varies as a function of the incident azimuth  $\phi_i$  and the frequency-dependent parameter  $a = \tan \alpha \tan \theta_i$ , using (2.58). We find that wavenumber amplifications larger than 1 are only possible for downward incident energy propagation ( $a > 0$ ). We also find that at all frequencies, maximum wavenumber amplification occurs for incident energy propagation in the onslope direction ( $\phi_i = 0$ ), and  $|m_r/m_i|_{max}$  decreases rapidly away from the critical frequency ( $a = 1$ ).

To show that (2.58) is equivalent to equation 5 of Eriksen (1982), we now rewrite it as

$$\frac{m_r}{m_i} = \frac{-2 \cos \phi_i \tan \theta_i \tan \alpha - (1 + \tan^2 \theta_i \tan^2 \alpha)}{1 - \tan^2 \theta_i \tan^2 \alpha} \cdot \frac{\cos^2 \theta_i \cos^2 \alpha}{\cos^2 \theta_i \cos^2 \alpha}, \quad (2.63)$$

$$\frac{m_r}{m_i} = \frac{-2 \cos \phi_i \sin \theta_i \sin \alpha \cos \theta_i \cos \alpha - (\cos^2 \theta_i \cos^2 \alpha + \sin^2 \theta_i \sin^2 \alpha)}{\cos^2 \theta_i \cos^2 \alpha - \sin^2 \theta_i \sin^2 \alpha} \quad (2.64)$$

$$\frac{m_r}{m_i} = \frac{-\frac{1}{2} \cos \phi_i \sin 2\theta_i \sin 2\alpha + \frac{1}{2} \sin 2\theta_i \sin 2\alpha - (\cos \theta_i \cos \alpha + \sin \theta_i \sin \alpha)^2}{(\cos \theta_i \cos \alpha + \sin \theta_i \sin \alpha)(\cos \theta_i \cos \alpha - \sin \theta_i \sin \alpha)} \quad (2.65)$$

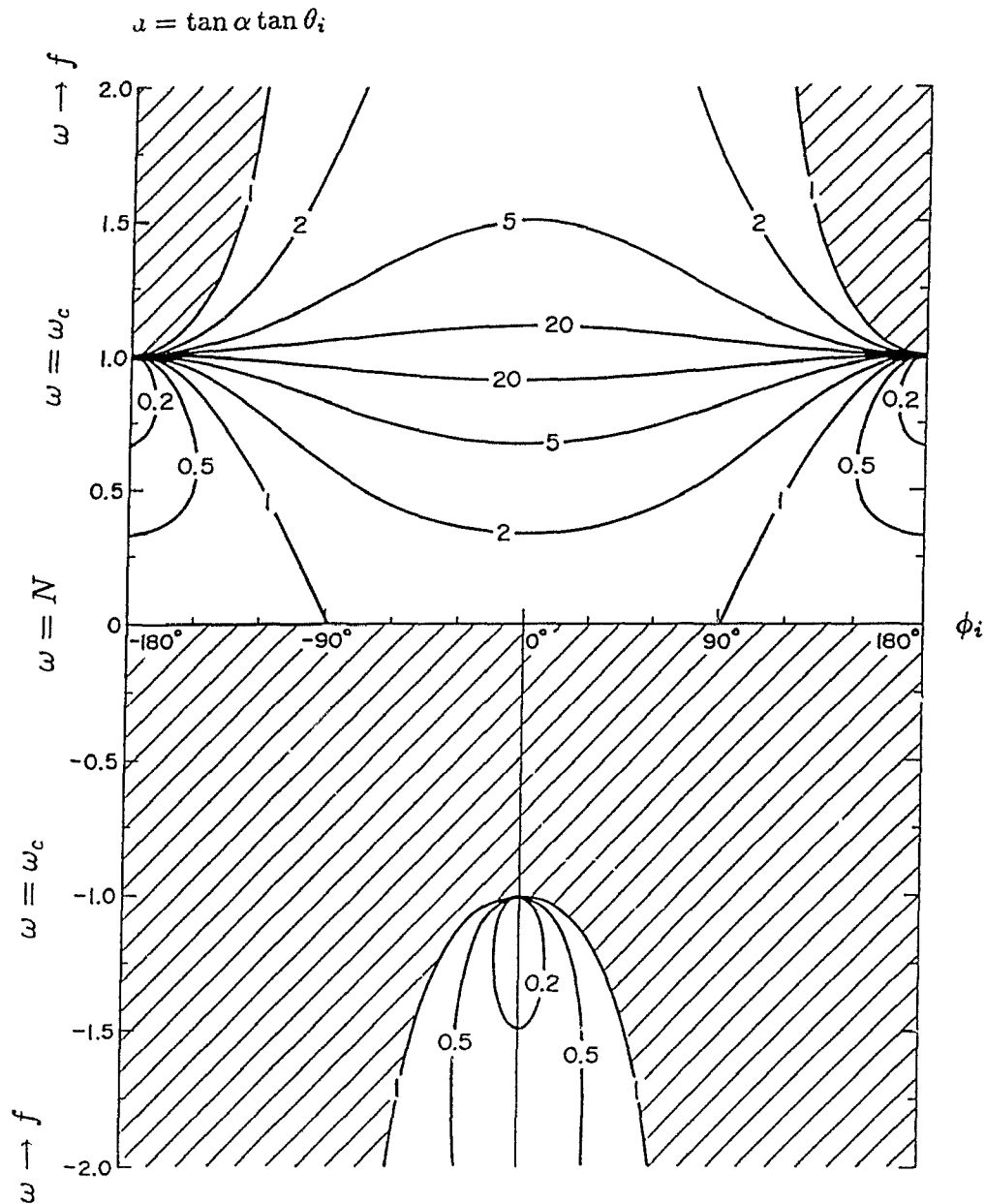


Figure 2.4: Wavenumber amplification  $|m_r/m_i|$  as a function of the incident azimuth  $\phi_i$  and the frequency-dependent parameter  $a = \tan \alpha \tan \theta_i$ , using (2.58). The regions of  $(a, \phi_i)$  space for which waves cannot be incident on the bottom are hatched. The direction of incident energy propagation is downward for  $a > 0$ , and upward for  $a < -1$  (after Garrett and Gilbert, 1988).

$$\frac{m_r}{m_i} = -\frac{\cos(\alpha - \theta_i)}{\cos(\alpha + \theta_i)} - \frac{\sin 2\theta_i \sin 2\alpha(\cos \phi_i - 1)}{2 \cos(\alpha + \theta_i) \cos(\alpha - \theta_i)}, \quad (2.66)$$

as in Eriksen (1982). However, in the remainder of the thesis, we shall always use (2.58) instead of (2.66), due to its greater compactness.

Now in order to obtain a formula for the reflected azimuth  $\phi_r$ , we note that conservation of frequency upon reflection requires that  $\tan |\theta_i| = \tan |\theta_r|$ , so that

$$\frac{|m_i|}{(\ell^2 + k_i^2)^{1/2}} = \frac{|m_r|}{(\ell^2 + k_r^2)^{1/2}}. \quad (2.67)$$

Defining  $\phi_r$  in a manner analogous to  $\phi_i$  on figure 2.3, we can write

$$\sin \phi_r = \frac{\ell}{(\ell^2 + k_r^2)^{1/2}}, \quad (2.68)$$

$$\sin \phi_r = \frac{\ell}{(\ell^2 + k_i^2)^{1/2}} \left| \frac{m_i}{m_r} \right|, \quad (2.69)$$

$$\sin \phi_r = \sin \phi_i \left| \frac{m_i}{m_r} \right|, \quad (2.70)$$

so that the incident and reflected azimuthal angles are related by

$$\phi_r = \sin^{-1} \left( \left| \frac{m_i}{m_r} \right| \sin \phi_i \right), \quad (2.71)$$

as in equation 8 of Eriksen (1982). It is important to note that near  $\omega_c$ ,  $|m_i/m_r| \rightarrow 0$  (figure 2.4), so that  $\phi_r \rightarrow 0$  or  $\pi$ , i.e. the reflected wave ray is oriented nearly perpendicular to the isobaths, as illustrated on figure 2.5. Using (2.71) and (2.58) together with simple geometry, it can be shown that for  $\omega < \omega_c$ , we always have

$$|\phi_r| \geq \pi/2, \quad (2.72)$$

whereas for  $\omega > \omega_c$ , we have

$$|\phi_r| \lesssim \pi/2 \quad \text{for} \quad |\phi_i| \lesssim \cos^{-1} \left( \frac{-2a}{a^2 + 1} \right), \quad (2.73)$$

as claimed by Eriksen (1985, equation 3).

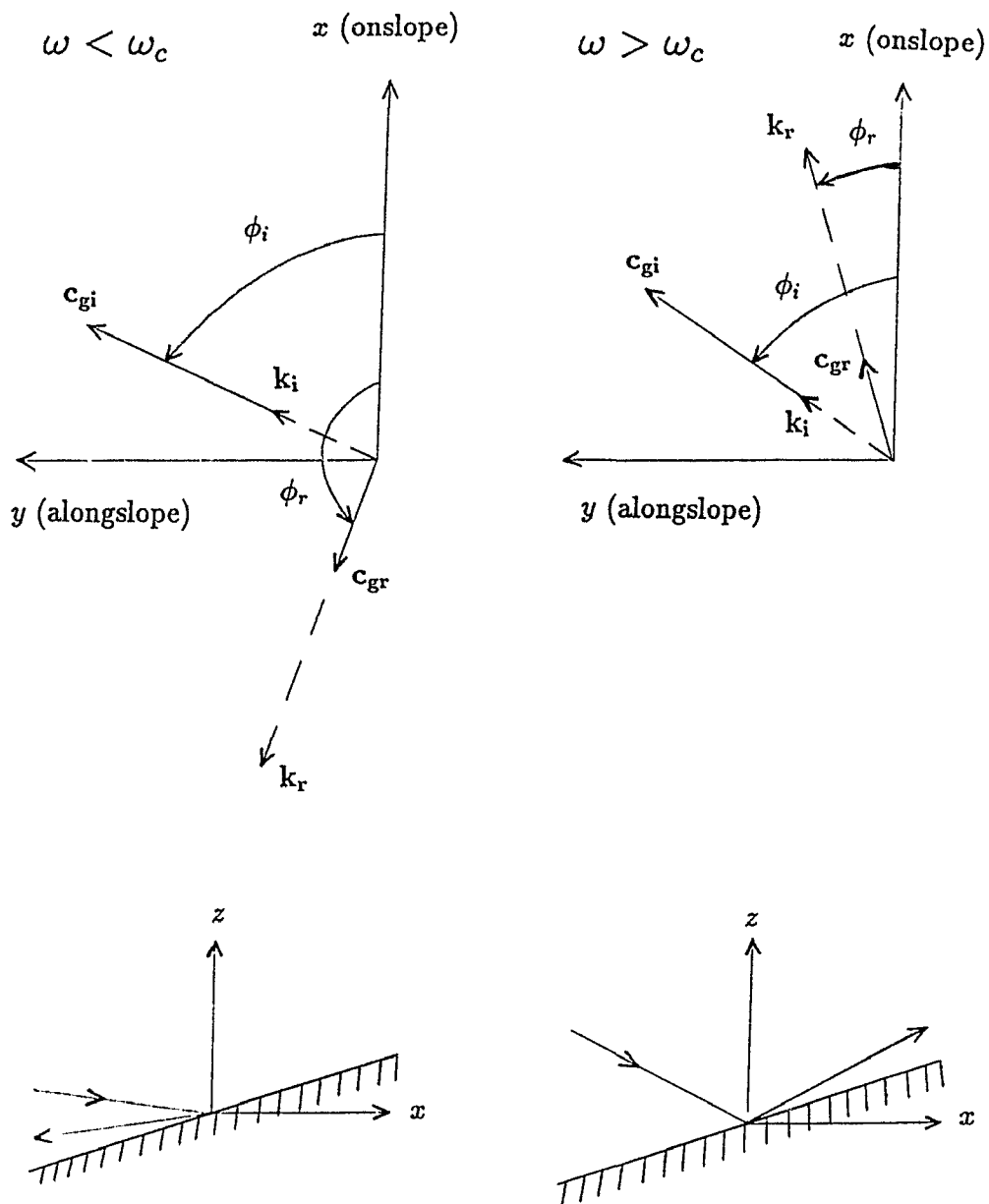


Figure 2.5: Diagram showing the tendency for current ellipses to orient themselves closer to the normal to the isobaths upon reflection off a sloping bottom. The  $i$  and  $r$  subscripts refer to the incident and reflected waves respectively,  $k$  and  $c_g$  are the wavenumber (---) and group velocity (—) vectors, and  $\phi$  is the azimuthal angle measured counterclockwise from the onslope direction. The subcritical case ( $\omega < \omega_c$ ) is depicted on the left, and the supercritical case ( $\omega > \omega_c$ ) is depicted on the right.

## 2.3 Other processes that could lead to near-bottom energy enhancement within the internal waveband above sloping topography

In the ocean, one rarely has the chance to study a single process in isolation, as can be done in the laboratory. Other processes besides internal wave reflection could lead to near-bottom energy enhancement within the internal waveband above sloping bottoms. In this section, I consider two of these, namely the generation of the internal tide by the surface tide, and bottom-trapped buoyancy oscillations.

### 2.3.1 Internal tide generation by the surface tide

The process of internal tide generation by the surface tide over large topographic features such as the continental slope can be envisaged as follows (Baines, 1982). Starting with the set of equations (2.1)–(2.5), which are more concisely written in vector form as

$$\rho_o \frac{\partial \mathbf{u}}{\partial t} + \rho_o \mathbf{f} \times \mathbf{u} + \nabla p + \rho' g \hat{\mathbf{z}} = 0, \quad (2.74)$$

$$\nabla \cdot \mathbf{u} = 0, \quad (2.75)$$

$$\frac{\partial \rho'}{\partial t} + w \frac{d\rho_o}{dz} = 0, \quad (2.76)$$

one can decompose the pressure and velocity fields associated with the tide into barotropic and baroclinic components:

$$\mathbf{u} = \mathbf{u}_1 + \mathbf{u}_i, \quad p = p_1 + p_i, \quad (2.77)$$

where the 1 and  $i$  subscripts refer to the surface and internal tides respectively. Subtracting the equations for  $\mathbf{u}_1$ ,  $p_1$  from (2.74)–(2.76), Baines obtains

$$\frac{\partial \mathbf{u}_i}{\partial t} + \mathbf{f} \times \mathbf{u}_i + \frac{\nabla p_i}{\rho_o} + \frac{\rho' g \hat{\mathbf{z}}}{\rho_o} = 0, \quad (2.78)$$

$$\nabla \cdot \mathbf{u}_i = 0, \quad (2.79)$$

$$\frac{\partial \rho'}{\partial t} + w_i \frac{d\rho_o}{dz} + w_1 \frac{d\rho_o}{dz} = 0, \quad (2.80)$$

where  $\bar{\rho}_o$  is the depth-averaged density. Baines (1973) shows that by letting  $\rho' = \rho_1 + \bar{\rho}$ , where  $\rho_1$  and  $\bar{\rho}$  are the density perturbations due to the surface and internal tides respectively, (2.78)–(2.80) can be rewritten so that the internal tide motion is driven by a virtual body force  $\mathbf{F}$ :

$$\frac{\partial \mathbf{u}_i}{\partial t} + \mathbf{f} \times \mathbf{u}_i + \frac{\nabla p_i}{\bar{\rho}_o} + \frac{\bar{\rho} g \hat{\mathbf{z}}}{\bar{\rho}_o} = \mathbf{F} = \frac{-g \rho_1 \hat{\mathbf{z}}}{\bar{\rho}_o}, \quad (2.81)$$

$$\text{where} \quad \frac{\partial \rho_1}{\partial t} = -w_1 \frac{d\rho_o}{dz}. \quad (2.82)$$

Baines also shows that the vertical velocity  $w_1$  due to the surface tide can be expressed in terms of the volume flux  $\mathbf{Q} \cos(\omega_T t)$  as follows:

$$w_1(x, y, z, t) = -z \mathbf{Q} \cdot \nabla \left( \frac{1}{h} \right) \cos(\omega_T t), \quad (2.83)$$

where  $\omega_T$  is the tidal frequency,  $h = h(x, y)$  is the bottom depth, and  $\mathbf{Q} = (Q_x, Q_y) = (h\bar{u}, h\bar{v})$  is assumed constant over the width of the continental slope. For the two-dimensional case where  $h$  is independent of  $y$ , this becomes

$$w_1(x, z, t) = Q_x \frac{z(dh/dx)}{h^2} \cos(\omega_T t), \quad (2.84)$$

yielding  $w_1 = 0$  at the free surface ( $z = 0$ ), and  $w_1 = -\bar{u} dh/dx$  at the bottom ( $z = -h(x)$ ). Substituting (2.84) into (2.82), one obtains

$$\rho_1 = -Q_x \frac{z(dh/dx)}{h^2} \frac{d\rho_o}{dz} \frac{\sin(\omega_T t)}{\omega_T}, \quad (2.85)$$

and substituting this into (2.81), we get the following expression for the body force:

$$\mathbf{F} = -\frac{Q_x N^2}{\omega_T} \frac{z(dh/dx)}{h^2} \sin(\omega_T t) \hat{\mathbf{z}}. \quad (2.86)$$

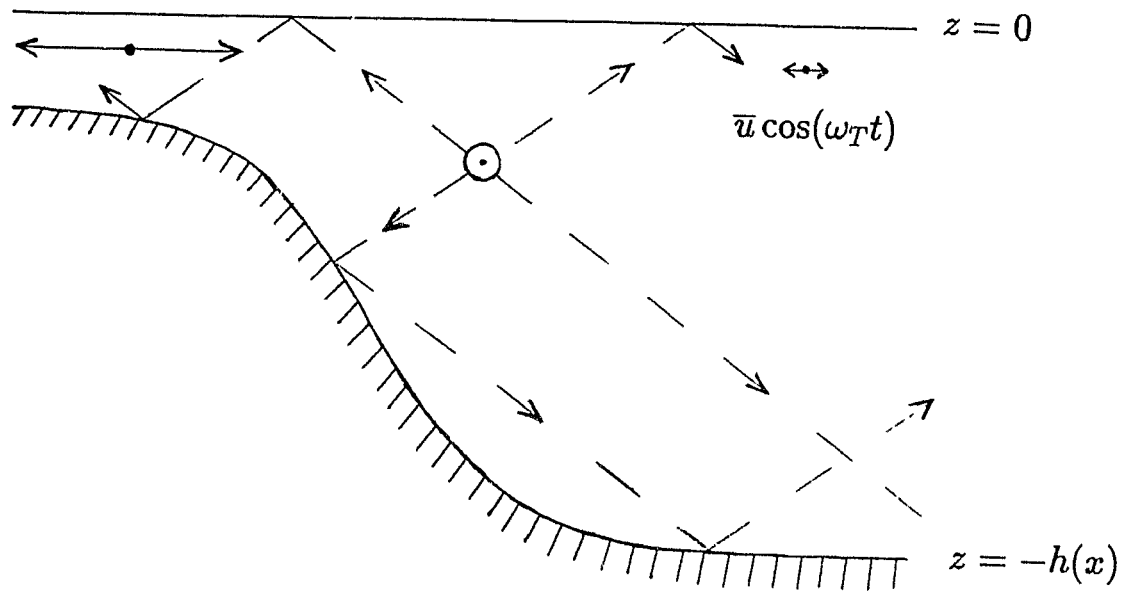


Figure 2.6: A cross-isobath volume flux  $Q_x = h\bar{u} \cos(\omega_T t)$  due to the barotropic tide sloshes to and fro over the continental slope. This causes a vertical motion  $w_1$  within the fluid whose amplitude is  $w_1 = -\bar{u}(d\bar{h}/dx)$  at the bottom, and decreases linearly to  $w_1 = 0$  at the free surface ( $z = 0$ ). The body force responsible for the generation of the internal tide is given by  $\mathbf{F} = -g\rho_1\hat{z}$ , where  $\rho_1$  is the buoyancy perturbation caused by the barotropic tide.

Having neglected any  $y$ -dependence in (2.8\*), Baines (1973) defined a stream function  $\Psi$  for the internal tide motion such that

$$u_i = -\frac{\partial \Psi}{\partial z} e^{-i\omega_T t}, \quad w_i = \frac{\partial \Psi}{\partial x} e^{-i\omega_T t}, \quad (2.87)$$

and showed that (2.81) can then be rewritten in the form

$$\frac{\partial^2 \Psi}{\partial x^2} - s^2 \frac{\partial^2 \Psi}{\partial z^2} = \left( \frac{Q_x z}{1 - \omega_T^2 / N^2} \right) \frac{d^2}{dx^2} \left( \frac{1}{h} \right), \quad s^2 = \frac{\omega_T^2 - f^2}{N^2 - \omega_T^2} \quad (2.88)$$

$$\text{subject to} \quad \Psi = 0 \quad \text{at } z = 0 \quad (2.89)$$

$$\text{and} \quad \Psi = 0 \quad \text{at } z = -h(x). \quad (2.90)$$

Note that in (2.88),  $s$  is the characteristic slope  $\tan \mu$  (2.16) evaluated at  $\omega = \omega_T$ , so that internal tide energy should travel along rays of slope  $s$ . To solve (2.88)–(2.90) across variable topography, Baines developed a theory which exploits this beamwise character of internal tide energy propagation, and cast the problem of surface–internal tide coupling in the form of integral equations.

He first dealt with the case where  $dh/dx < s$  everywhere on the slope ('flat-bump' topography) in Baines (1973), and extended that theory to the case where  $dh/dx > s$  over a portion of the topography in Baines (1974) ('steep-bump' topography). He found that, for steep-bump topography, the total energy flux from the barotropic tide to the baroclinic tide is 2 to 3 times greater than the maximum for flat-bump topography of comparable height. He also found that for steep-bump topography the largest internal tide velocities occur around characteristics emanating from regions of the topography where the  $M_2$  internal wave ray slope equals the bottom slope.

Baines (1982) extended the theory of Baines (1974) by allowing for the generation of interfacial waves at the base of the surface mixed layer, and estimated the total energy flux from the surface tide to the internal tide for several shelf areas around the world. He concluded that, although the internal tides of largest amplitude are likely to be observed near continental shelf breaks, the total energy flux from the surface

tide to the internal tide in the abyssal ocean, based on the estimates of Bell (1975a), is more important overall.

Sandstrom (1976) devised a theoretical framework quite different from that of Baines (1974) for studying the generation of the internal tide by the surface tide over a continental slope. Whereas in Baines' formalism the surface tide is treated as a body force in a non-homogeneous differential equation (2.88), in Sandstrom's formalism the differential equation to be solved is homogeneous, and tidal forcing enters the problem through non-homogeneous boundary conditions:

$$\frac{\partial^2 \Psi}{\partial x^2} - s^2 \frac{\partial^2 \Psi}{\partial z^2} = 0, \quad s^2 = \frac{\omega_T^2 - f^2}{N^2 - \omega_T^2} \quad (2.91)$$

$$\text{subject to} \quad \Psi = \Psi_0 \quad \text{at } z = 0 \quad (2.92)$$

$$\text{and} \quad \Psi = 0 \quad \text{at } z = -h(x). \quad (2.93)$$

In Sandstrom's method the problem of barotropic forcing over a bottom slope is reduced to solving a matrix equation by an iterative technique, and the form of the slope is contained in an inhomogeneous phase function  $S(x)$ . Much of his paper deals with the construction of that phase function.

He found, as Baines did, that the coupling between the surface and internal tide is relatively weak for 'flat'-bump topography, but is strong for 'steep'-bump topography. He also found that, for a step shelf, the baroclinic energy density on the deep water side should be about 2.5 times larger than the barotropic energy density (see his table IV). Since a step shelf is conceptually equivalent to steep-bump topography, this result appears to be consistent with Petrie's (1975) finding that the baroclinic component of the tide dominates on the Scotian Slope (which is steep).

### 2.3.2 Bottom-trapped buoyancy oscillations

Rhines (1970) has shown that, besides plane progressive waves with frequencies between  $f$  and  $N$ , a class of edge waves is possible in a uniformly stratified, uniformly rotating fluid bounded by a single plane wall with slope  $\tan \alpha$ .

He chose a set of coordinates  $(x_1, x_2, x_3)$  and corresponding velocities  $(u_1, u_2, u_3)$  such that the sloping wall lies at  $x_3 = 0$ , and  $Ox_1, Ox_2$  are rotated through an angle  $\phi$  from the onslope and alongslope directions respectively <sup>1</sup> (see figure 2.7). Besides choosing  $Ox_3$  as the coordinate axis normal to the slope, Rhines also chose  $Ox_1$  to lie along wavecrests, so that phase propagation is in the  $Ox_2$  direction. He then looked for wave solutions of the form

$$\exp [(-\kappa + ik_3)x_3 + i(k_2x_2 - \omega t)] \quad (2.94)$$

to the linearised, incompressible, non-diffusive, inviscid, Boussinesq equations, where  $\kappa$  and  $k_3$  are real. He pointed out that we must have  $u_3 = 0$  everywhere in the fluid in order to satisfy the condition of no normal flow at the boundary, and also pointed out that trapped waves which depend on the presence of the sloping boundary require  $u_2 = 0$  everywhere in the fluid.

Water parcel motions corresponding to the trapped wave solutions of Rhines (1970) are thus rectilinear (parallel to  $Ox_1$ ), implying the ratio of anticlockwise ( $P_{++}$ ) to clockwise ( $P_{--}$ ) kinetic energy

$$\frac{P_{++}}{P_{--}} = 1. \quad (2.95)$$

The frequency of these waves is a function of the Brunt-Väisälä frequency  $N$ , the slope angle  $\alpha$ , and the orientation  $\phi$  of the motions:

$$\omega = N \sin \alpha \cos \phi. \quad (2.96)$$

The maximum frequency ( $\omega = N \sin \alpha$ ) occurs for cross-isobath motions ( $\phi = 0$ ), and equals the Brunt-Väisälä frequency  $N$  for a vertical wall ( $\alpha = \pi/2$ ). The minimum frequency ( $\omega = 0$ ) occurs for alongslope motions ( $\phi = \pi/2$ ). LeBlond and Mysak (1978, p.188) gave the apt name of 'bottom-trapped buoyancy oscillations' to the motions described by Rhines (1970), who himself called them internal edge waves.

<sup>1</sup>The notation used here differs from that of Rhines (1970), where  $\Phi = \phi + \pi/2$ . My choice of notation ensures that the onslope direction is given by  $\phi = 0$  for internal waves (see figure 2.3) as well as for Rhines' bottom-trapped buoyancy oscillations.

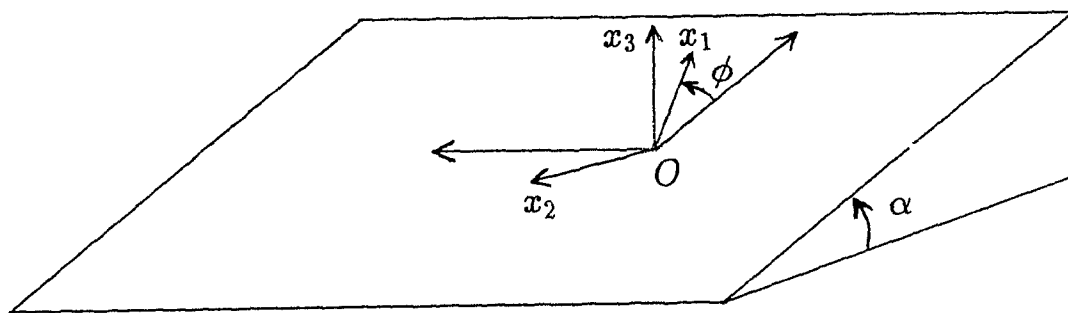


Figure 2.7: Cartesian coordinate system chosen by Rhines (1970) to describe the types of motion that are possible above a single wall with constant slope  $\tan \alpha$ , in a uniformly stratified, uniformly rotating fluid. The  $Ox_3$  axis is normal to the slope, and the  $Ox_2$  axis is in the direction of phase propagation. The trapped motions are rectilinear and parallel to the  $Ox_1$  axis.

	Frequency	Current Ellipse Orientation	Current Ellipse Stability	$P_{++}/P_{--}$	$\frac{N^2 P_{\zeta\zeta}}{P_{uu} + P_{vv}}$
Mid-water internal wavefield	$f < \omega < N$	Assumed isotropic	0	$\left(\frac{\omega - f}{\omega + f}\right)^2$	$\left(\frac{N^2}{N^2 - \omega^2}\right) \left(\frac{\omega^2 - f^2}{\omega^2 + f^2}\right)$
Near-bottom internal wavefield	Energy peak at $\omega_c =$ $(N^2 \sin^2 \alpha + f^2 \cos^2 \alpha)^{1/2}$	$\phi = 0$	1 at $\omega_c$ , but falling off to zero towards $f$ and $N$	$\left(\frac{\omega - f}{\omega + f}\right)^2$	$\left(\frac{N^2}{N^2 - \omega^2}\right) \left(\frac{\omega^2 - f^2}{\omega^2 + f^2}\right)$
Rhines' buoyancy oscillations	$\omega \leq N \sin \alpha$	$\phi = \cos^{-1} \left( \frac{\omega}{N \sin \alpha} \right)$	1	1	1

Table 2.1: Consistency relations for internal waves and Rhines' bottom-trapped buoyancy oscillations.

Rearranging terms in (2.96), it is useful to note that the orientation of bottom-trapped buoyancy oscillations should vary with frequency as follows:

$$\phi = \cos^{-1} \left( \frac{\omega}{N \sin \alpha} \right). \quad (2.97)$$

Some of the properties of Rhines' bottom-trapped oscillations are summarised and compared with those of internal waves in table 2.1.

# Chapter 3

## Estimates of the dissipated energy flux

### 3.1 Introduction

Garrett and Gilbert (1988) (hereafter GG88) have proposed a mechanistic model for estimating the energy dissipation rate that might result from internal wave breaking above sloping topography. In the first part of this chapter, I describe the physical assumptions on which their wave breaking model is based, and I summarize their most important results, contrasting them with those of Eriksen (1985).

The remainder of the chapter deals with what we shall refer to as the residual energy spectrum. This is the energy spectrum which GG88 are left with after removal of the waves which are assumed to break upon reflection. The derivation of an analytical formula for the total energy content of this spectrum parallels that given for the reflected shear spectrum in GG88, and thus provides us with an opportunity to reexamine the validity of some of the approximations made in that paper. The distribution of residual energy in frequency space, azimuthal space, and vertical modenumber space is shown for typical values of the bottom slope and the frequency ratio  $f/N$ . And finally, the additional energy dissipation rate that could result from bottom drag due to the residual currents is estimated.

## 3.2 Theoretical estimates of the energy flux available for mixing.

### 3.2.1 Eriksen's redistributed energy flux

Current meter data from mooring 349 of Wunsch and Hendry (1972, figure 11) on the New England continental slope have much less kinetic energy at the critical period (14–16 hours) 100m above the bottom than 10m above the bottom. Similarly, Eriksen (1982) pointed out that current meter data from mooring 636 of the Western Boundary Sill Experiment (discussed in chapter 6) show a rapid decay with height above the bottom of the spectral peak at  $\omega_c \approx 0.01cph$ , that peak having almost completely vanished 200m above the bottom. Using this observational requirement that the internal wave spectrum a few hundred meters above a sloping bottom has seemingly readjusted to the canonical GM79 form, Eriksen (1985) computed a quantity which he called the “redistributed energy flux” normal to the bottom. He defined it as

$$F_R = \sum_{j=1}^{j=32} \int_f^N \int_0^{2\pi} |F_i(\omega, j, \phi_i) - F_r(\omega, j_r, \phi_r)| d\phi_i d\omega, \quad (3.1)$$

$$\text{where} \quad F_i(\omega, j, \phi_i) = -\frac{\rho_o}{2} E_{GM}(\omega, j) \mathbf{c}_g(\omega, j, \phi_i) \cdot \hat{\mathbf{n}} \quad (3.2)$$

$$= \frac{\rho_o}{2} E_{refl}(\omega, j_r) \mathbf{c}_g(\omega, j_r, \phi_r) \cdot \hat{\mathbf{n}} \quad (3.3)$$

is the bottom-normal incident energy flux, and

$$F_r(\omega, j_r, \phi_r) = \frac{\rho_o}{2} E_{GM}(\omega, j_r) \mathbf{c}_g(\omega, j_r, \phi_r) \cdot \hat{\mathbf{n}}. \quad (3.4)$$

is the bottom-normal reflected energy flux. The signs on the right hand side of (3.2) and (3.4) have been chosen so as to ensure that both  $F_i$  and  $F_r$  are positive,  $\hat{\mathbf{n}}$  being a unit vector normal to the bottom which points toward the ocean's interior. In (3.4) the reflected modenummer  $j_r$  is the nearest integer to  $j|m_r/m_i|$ , where  $m_r/m_i$  is given by (2.58), and the reflected azimuth  $\phi_r$  is given by (2.71). Thus  $j_r$  and  $\phi_r$  are obtained using the specular reflection laws of chapter 2.

On the other hand, it is important to note that the energy density  $E_{GM}(\omega, j_r)$  in (3.4) is not obtained using the specular reflection law (2.37), i.e.  $E_{GM}(\omega, j_r) \neq (m_r/m_i)^2 E_{GM}(\omega, j)$ . If it were, the integrand in (3.1) would be trivially equal to zero, as the laws of reflection derived in chapter 2 conserve energy flux normal to the bottom.

In (3.2),  $E_{GM}(\omega, j)$  is the GM79 (Munk, 1981) energy density at frequency  $\omega$  and vertical modenumber  $j$ , and in (3.4),  $E_{GM}(\omega, j_r)$  is the GM79 energy density at frequency  $\omega$  and modenumber  $j_r$ . Since the reflected energy flux  $F_r(\omega, j_r, \phi_r)$  would be equal to the incident energy flux  $F_i(\omega, j, \phi_i)$  if (2.37) were used, Eriksen's redistributed energy flux (3.1) thus represents the integral over all azimuths, frequencies, and wavenumbers of the modulus of the difference between the reflected energy flux, and what that flux would be for a reflected spectrum of canonical GM79 form.

Quoting Eriksen (1985, p.1151), the reflected waves are "prescribed to take on amplitudes that are consistent with the canonical spectrum. The rationale for this calculation is that a reflected component must adjust to the canonical spectral level for its particular wavenumber and frequency in order for the observed total (incident plus reflected) spectrum not to imply a flux imbalance at that particular (reflected) wavenumber and frequency. The difference between incident flux and reflected flux accomplished within a prescribed distance from the bottom is then a measure of the power redistribution per unit volume of the internal wave field."

The values which Eriksen (1985) obtained for the redistributed energy flux are quite large. They range from a few  $mW \cdot m^{-2}$  to a maximum of nearly  $60mW \cdot m^{-2}$ , typical values being on the order of  $10-30 mW \cdot m^{-2}$ . If only a small fraction of that redistributed energy flux were dissipated, it could be sufficient to maintain a coefficient of vertical eddy diffusivity  $K_v$  of  $10^{-4}m^2s^{-1}$  in the deep ocean (1.2). However, a major shortcoming with Eriksen's calculation of the "redistributed energy flux" was that he did not say how much of it should be lost to dissipation, the remainder being presumably redistributed in the four-dimensional internal wave spectrum by nonlinear processes.

Now since shear instability and energy dissipation tend to occur at small spatial scales, it could be argued that the fraction of Eriksen's redistributed energy flux most

likely to cause mixing is that for which the transfer of energy takes place from small wavenumbers to high wavenumbers. However, it turns out that Eriksen's redistributed energy flux is dominated by the transfer of energy from high wavenumbers to low wavenumbers.

This is most clearly seen on Eriksen's figure 5c: for incident spectra including both upward and downward propagating energy, the total reflected energy flux  $F_r$  (summed from  $j_r = 1$  to 32) is always larger than the total incident energy flux  $F_i$ . This is so because incident waves which get reflected from high wavenumbers to low wavenumbers are prescribed the GM79 energy density appropriate to their reflected wavenumber. As  $|c_g|$  is inversely proportional to the magnitude of the wavenumber vector (2.14), and as the GM79 model spectrum has more energy at low modes than at high modes (3.11), the energy flux carried by Eriksen's reflected waves is larger than the incident energy flux whenever  $|m_r/m_i| < 1$ .

The overall tendency for  $F_r$  to be larger than  $F_i$  on Eriksen's figure 5c thus reveals the dominant role of reflection from high to low wavenumbers in his calculation of the redistributed energy flux. As  $|m_r/m_i| < 1$  leads to a reduction of the vertical shear rather than to its intensification (2.40), this implies that the major part of Eriksen's redistributed energy flux is very unlikely to cause vertical mixing.

In any event, it could also be argued that the energy flux lost from the internal wave spectrum cannot possibly be of the same order of magnitude as Eriksen's (1985) redistributed energy flux ( $10\text{--}30 \text{ mW} \cdot \text{m}^{-2}$ ), as this would drain the internal wavefield of its total energy of about  $4 \times 10^3 \text{ J} \cdot \text{m}^{-2}$  (Munk, 1981) in just a few days. A sink of internal wave energy of this magnitude would lead to far less universality of the internal wave spectrum in time and space than seems to be typical (Olbers, 1983).

### **3.2.2 A more explicit model for estimating the dissipated energy flux due to shear instability of the reflected waves.**

Garrett and Gilbert (1988) proposed a more specific model based on mechanistic ideas to estimate the energy flux that might be lost to dissipation. Their approach can be

outlined as follows:

- 1) using the GM79 model spectrum as their incident internal wavefield, they let each wave component in this spectrum give rise to a reflected wave according to (2.58), typically with higher wavenumber (figure 2.4) and greater energy (2.37) and shear (2.40)
- 2) the total shear spectrum of the incident and reflected wavefields is then summed from mode  $j = 1$  to  $j = j_p$ , such that the Richardson number based on the mean square shear from this part of the spectrum has some ‘critical’ value  $Ri_c(j_p) = O(1)$
- 3) finally, they suggest that waves with  $j > j_p$  are likely to undergo shear instability, and hence tend to break and get dissipated. The rate of energy dissipation due to internal wave breaking is assumed to be equal to the energy flux carried by those shear unstable waves.

The formulae they obtained for the cutoff modenummer  $j_p$  and the rate of energy dissipation  $F_{ds}$  due to shear instability depend only on  $\tan \alpha$  and  $\gamma$ , where  $\tan \alpha$  is the bottom slope and  $\gamma = f/N$  is the ratio of the inertial to the buoyancy frequency. They are given by

$$j_p = 111(\sin \alpha)^{-1/3}(\sin^2 \alpha + \gamma^2 \cos^2 \alpha)^{2/3}[\sin^2 \alpha + \gamma^2(1 + \cos^2 \alpha)]^{-1/3}, \quad (3.5)$$

$$F_{ds} = 85j_p^{-1}(\sin^2 \alpha + \gamma^2 \cos^2 \alpha)^{-3/2} \cos^3 \alpha \sin^3 \alpha \quad mW \cdot m^{-2}, \quad (3.6)$$

and are plotted on figures 3.1 and 3.2 respectively. We see on figure 3.1 that for typical values of the bottom slope  $\tan \alpha$  and the ratio  $f/N$ ,  $j_p$  is the range 30–100.

Figure 3.2 shows that the dissipated energy flux  $F_{ds}$  could be as large as  $1 \text{ mW} \cdot \text{m}^{-2}$ , but is generally much less than this for typical values of  $f/N$  and  $\tan \alpha$ . These estimates of  $F_{ds}$ , while much less than Eriksen’s “redistributed energy flux”, still appear to be significant for deep-ocean mixing rates (1.2), and may represent an important sink in the overall energy balance of the oceanic internal wavefield (Olbers,

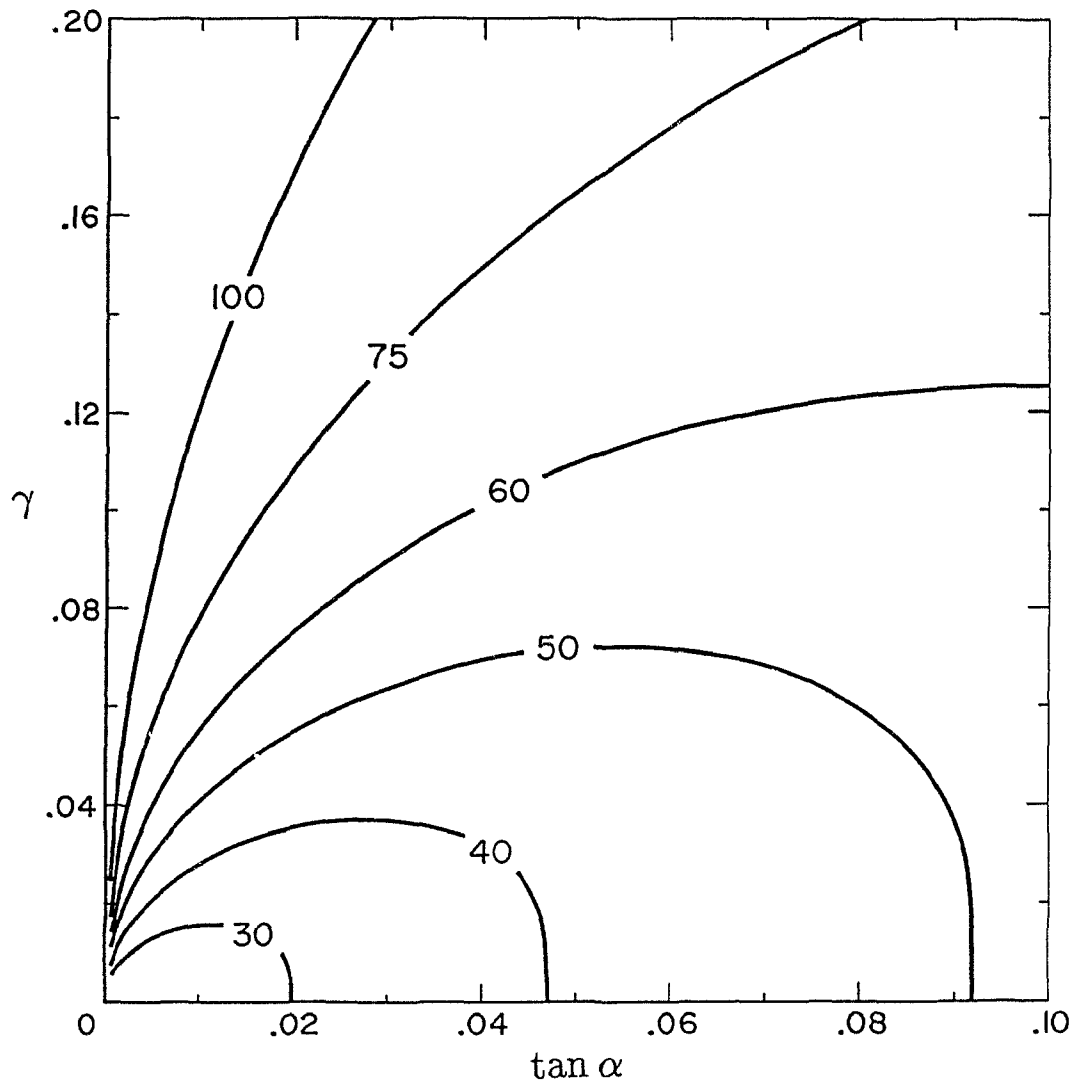


Figure 3.1: Cutoff modenumber  $j_p$  for which  $Ri(j_p) = 1$ , as a function of  $\gamma = f/N$  and the bottom slope  $\tan \alpha$  (after Garrett and Gilbert, 1988).

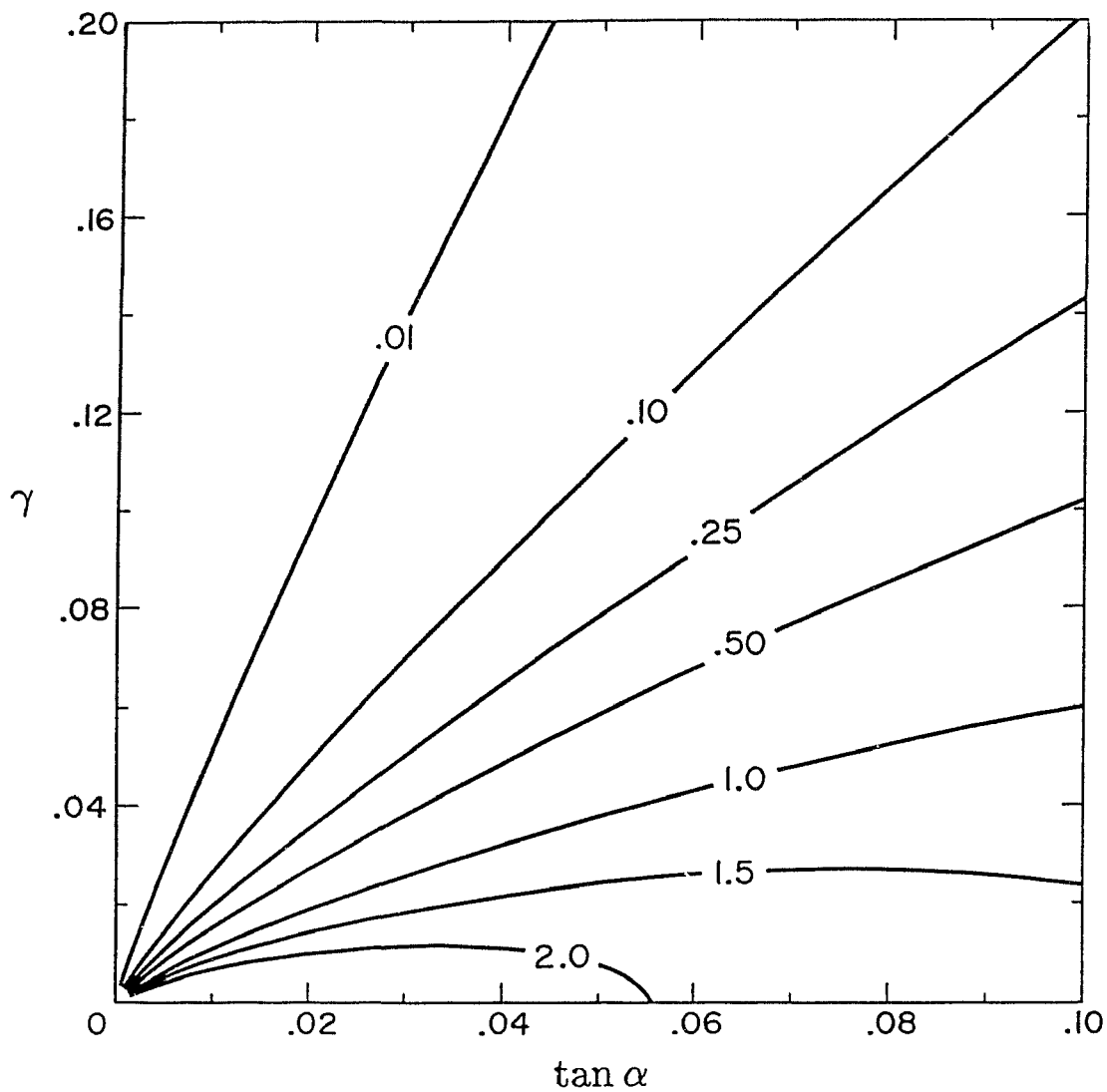


Figure 3.2: Dissipated energy flux  $F_{ds}$  due to shear instability of the reflected waves, as a function of  $\gamma = f/N$  and the bottom slope  $\tan \alpha$  (after Garrett and Gilbert, 1988).

1983). Figure 3.2 also suggests that (i), for a given value of  $f/N$ ,  $F_{ds}$  generally increases with bottom slope  $\tan \alpha$ , reaching a broad maximum when  $\tan \alpha \approx 3f/N$ , and (ii), for a given value of  $\tan \alpha$ ,  $F_{ds}$  increases as  $f/N$  gets smaller, so that boundary mixing via internal wave breaking might be more important at low latitudes than at mid-latitudes.

The latter remark should be taken with a 'grain of salt' however, as it results directly from Munk's (1981, footnote 14) suggestion that we should take  $Ef = \text{constant} = 4.6 \times 10^{-9} s^{-1}$ , instead of  $E = \text{constant} = 6.3 \times 10^{-5}$  in the GM79 model spectrum. This suggestion was made to give a more accurate energy density for  $\omega > M_2$  as we approach the equator; observational evidence (Wunsch and Webb 1979, and Eriksen 1980) suggests that the energy density is independent of latitude for  $\omega > 0.1 \text{ cph}$ . However, the problem with taking  $Ef = \text{constant}$  is that it tends to exaggerate the energy density for  $\omega < M_2$ , and we end up with a singularity in total energy content at the equator ( $E \rightarrow \infty$  as  $f \rightarrow 0$ ).

GG88 have listed some of the limitations of their calculations. One of them involves the assumption that the incident waves are reflected as if from a uniformly sloping bottom. Except for flat abyssal plains, realistic ocean topography does not usually fit that description. Even large scale topographic features such as the continental slope are rich in structure with many canyons and other indentations.

Another serious problem with GG88's calculation of the dissipated energy flux  $F_{ds}$  is that they cannot say anything about the ultimate fate of their residual energy spectrum. An analytical formula for the ratio  $R$  of the sum of the incident and residual energy to the total GM79 energy was given by GG88:

$$R = 1 + 0.26j_p \gamma \sin \alpha (\sin^2 \alpha + \gamma^2 \cos^2 \alpha)^{-1}, \quad (3.7)$$

and is plotted here on figure 3.3. The detailed algebraic derivation of this formula is given below. The main difference with the derivation of the reflected shear spectrum outlined in GG88 lies in the fact that  $E_r = (m_r/m_i)^2 E_i$  in (2.37), whereas  $S_r = (m_r/m_i)^4 S_i$  in (2.40).

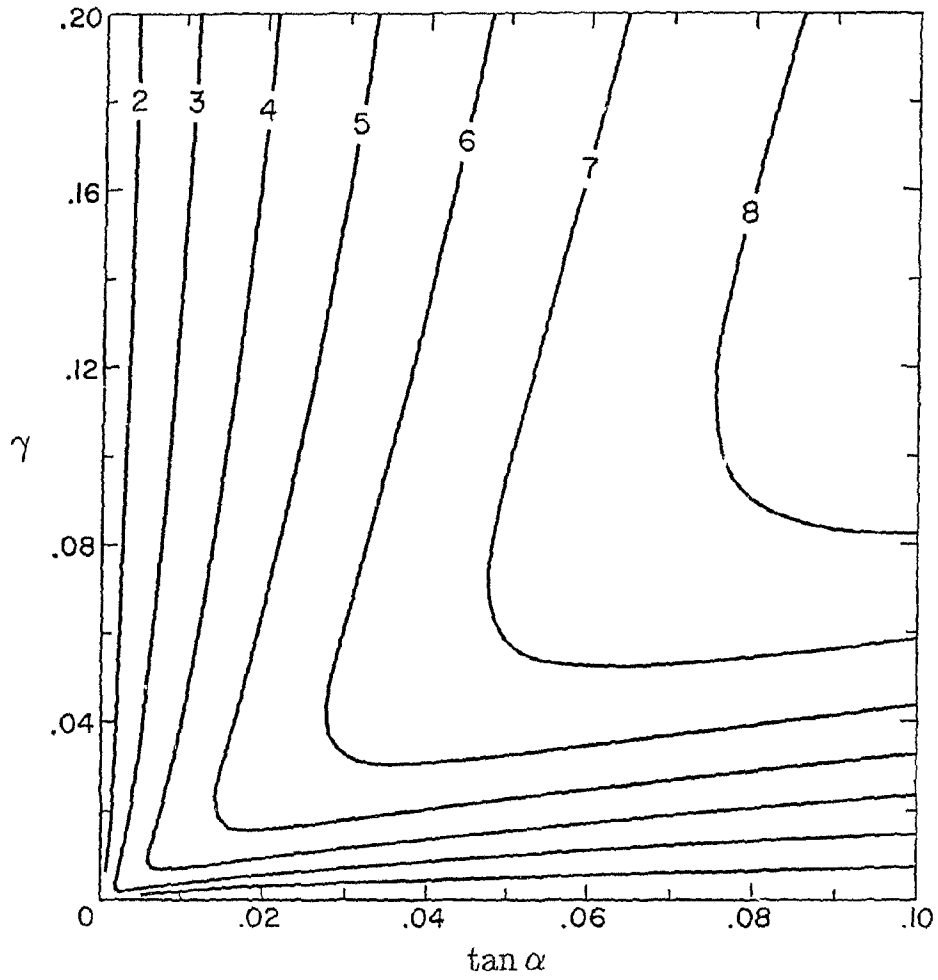


Figure 3.3: Ratio  $R$  of the sum of the incident and residual energy to the total GM79 energy, as a function of  $f/N$  and the bottom slope  $\tan \alpha$  (after Garrett and Gilbert, 1988).

### 3.3 Evaluation of the total residual energy

Let us assume that the incident energy spectrum is vertically symmetric and horizontally isotropic, as in the GM79 model spectrum of Munk (1981). Half the waves of this spectrum are going to be incident on a sloping boundary, and the incident energy density in  $(\omega, j, \phi_i)$  space is thus of the form

$$E_i(\omega, j, \phi_i) = \frac{b^2 N_o N}{4\pi} E(\omega, j) \quad (3.8)$$

where  $b = 1300m$ ,  $N_o = 5.2 \times 10^{-3} s^{-1}$  (3cph), and

$$E(\omega, j) = B(\omega) H(j) E, \quad (3.9)$$

$$B(\omega) = \frac{2f}{\pi \omega (\omega^2 - f^2)^{1/2}} \quad (3.10)$$

$$H(j) = \frac{(j^2 + j_*^2)^{-1}}{\sum_{j=1}^{\infty} (j^2 + j_*^2)^{-1}}, \quad j_* = 3, \quad (3.11)$$

and  $E = 6.3 \times 10^{-5}$  is a dimensionless constant which sets the overall energy level in the GM79 model spectrum. The total incident energy per unit mass is obtained by summing over all vertical modes and integrating over all frequencies and azimuths:

$$E_i = \frac{b^2 N_o N}{4\pi} \sum_{j=1}^{\infty} \int_f^N \int_{-\pi}^{\pi} E(\omega, j) d\phi_i d\omega$$

$$E_i = \frac{b^2 N_o N E}{2} \left( 1 - \frac{2}{\pi} \sin^{-1} \left( \frac{f}{N} \right) \right) \approx \frac{b^2 N_o N E}{2} \quad (3.12)$$

The energy of a single reflected wave component is given by (2.37),

$$E_r(\omega, j_r, \phi_r) = \left( \frac{m_r}{m_i} \right)^2 E_i(\omega, j, \phi_i),$$

$$E_r(\omega, j_r, \phi_r) = \left( \frac{m_r}{m_i} \right)^2 \frac{b^2 N_o N}{4\pi} E(\omega, j),$$

using (3.8). Defining the residual energy spectrum as the reflected energy spectrum truncated at  $j_r = j_p$ , the total residual energy per unit mass is then given by

$$E_r = \frac{b^2 N_o N}{4\pi} \sum_{j=1}^{\infty} (I_1 + I_2 + I_3), \text{ where} \quad (3.13)$$

$$I_1 = \int_f^{\omega_{j1}} \int_{-\pi}^{\pi} \left(\frac{m_r}{m_i}\right)^2 E(\omega, j) d\phi_i d\omega \quad (3.14)$$

$$\begin{aligned} I_2 &= \int_{\omega_{j1}}^{\omega_{j2}} \left\{ \int_{-\pi}^{-\phi_c} + \int_{\phi_c}^{\pi} \left(\frac{m_r}{m_i}\right)^2 E(\omega, j) d\phi_i \right\} d\omega \\ &= 2 \int_{\omega_{j1}}^{\omega_{j2}} \int_{\phi_c}^{\pi} \left(\frac{m_r}{m_i}\right)^2 E(\omega, j) d\phi_i d\omega \end{aligned} \quad (3.15)$$

$$I_3 = \int_{\omega_{j2}}^N \int_{-\pi}^{\pi} \left(\frac{m_r}{m_i}\right)^2 E(\omega, j) d\phi_i d\omega. \quad (3.16)$$

The limits of integration  $\omega_{j1}$  and  $\omega_{j2}$  are defined in such a way that, for  $f \leq \omega \leq \omega_{j1}$  and  $\omega_{j2} \leq \omega \leq N$ , we have  $j_r/j < j_p/j$  for  $0 \leq \phi_i \leq 2\pi$  (see figure 3.4). Hence in (3.14) and (3.16), all incident azimuths contribute to the residual energy spectrum. On the other hand, for  $\omega_{j1} < \omega < \omega_{j2}$ , waves with  $-\phi_c(\omega, j) < \phi_i < \phi_c(\omega, j)$  are reflected with  $j_r/j > j_p/j$ , and so do not contribute to the residual energy spectrum (3.15). An expression for the cutoff azimuthal angle  $\phi_c(\omega, j)$  is derived below (3.33).

As we expect the peak in reflected energy density at  $\omega = \omega_c$  to dominate the contributions to  $I_1$ ,  $I_2$  and  $I_3$ , we shall use an asymptotic form of (2.58) valid near the critical frequency, i.e. valid for  $x = 1 + \delta$ , where  $\delta \ll 1$ . Such an expression is given by equation (4.7) of GG88, who further assumed that  $N^2 \gg \omega_c^2$ , obtaining

$$\frac{m_r}{m_i} = -\epsilon^{-1} \left(1 - \frac{f^2}{\omega_c^2}\right) (1 + \cos \phi_i), \quad (3.17)$$

where  $\epsilon$  is defined such that

$$\omega = \omega_c(1 + \epsilon), \quad d\omega = \omega_c d\epsilon. \quad (3.18)$$

If we now let

$$A = (1 - f^2/\omega_c^2), \quad (3.19)$$

this can be rewritten as

$$\frac{m_r}{m_i} = -\epsilon^{-1} A(1 + \cos \phi_i). \quad (3.20)$$

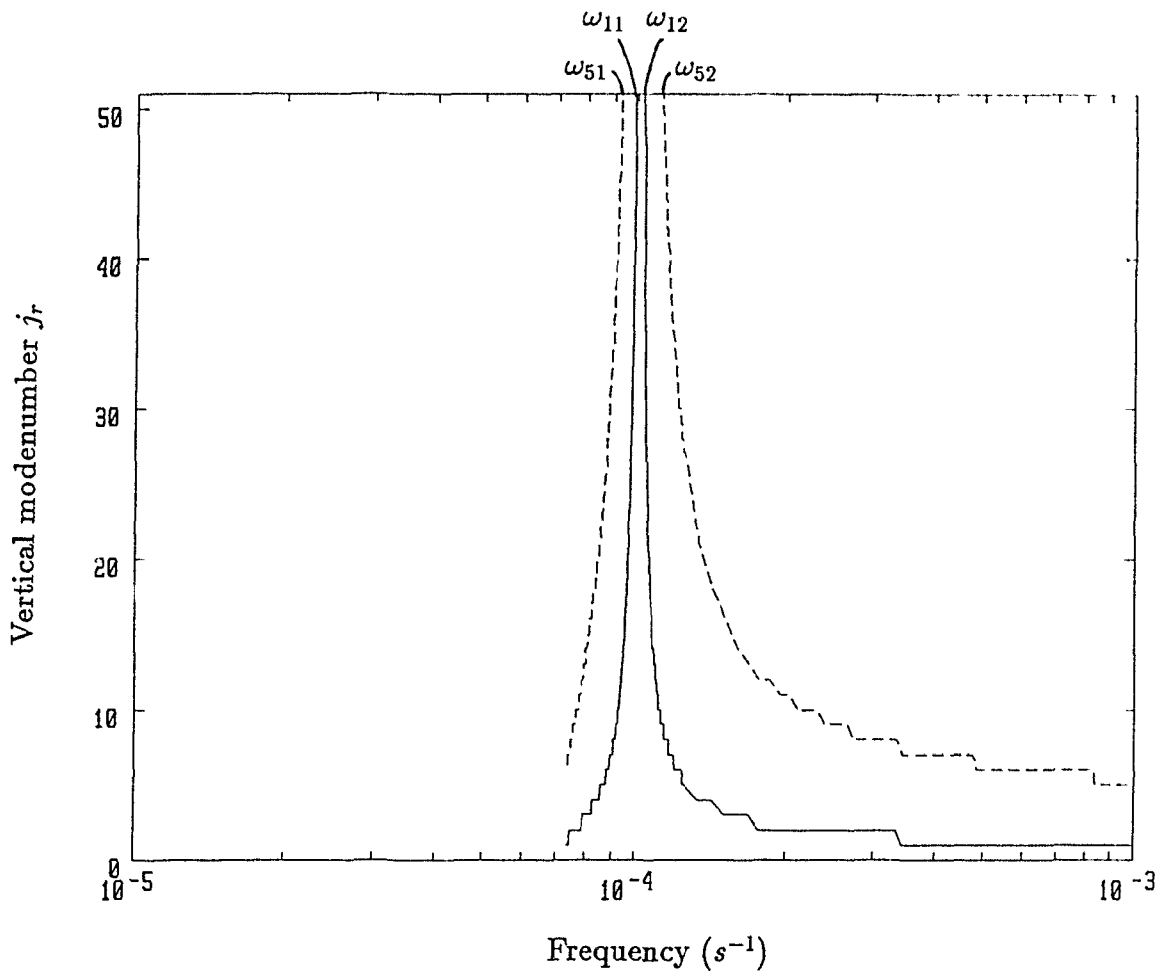


Figure 3.4: Diagram showing the maximum reflected modenumber  $j_r$  for the incident modenumbers  $j = 1$  (—) and  $j = 5$  (- - -), using (2.58) with  $\phi_i = 0$ . For  $f \leq \omega \leq \omega_{j1}$  and  $\omega_{j2} \leq \omega \leq N$ , we always have  $|j_r/j|_{max} < j_p/j$ . The range of frequencies  $\omega_{j1} < \omega < \omega_{j2}$  for which  $|j_r/j|_{max} > j_p/j$  increases with  $j$ . This figure was drawn for the particular case where  $f = 7.3 \times 10^{-5} s^{-1}$ ,  $N = 10^{-3} s^{-1}$  and  $\tan \alpha = 0.07$ , so that  $j_p = 51$  according to (3.5).

For any frequency (i.e. for any value of  $\epsilon$ ), the maximum wavenumber amplification is achieved when  $\phi_i = 0$ . Thus,

$$\left| \frac{m_r}{m_i} \right|_{\max} = 2|\epsilon^{-1}|A \quad (3.21)$$

In particular, at  $\omega = \omega_{j1} = \omega_{j2}$ , we have

$$\left| \frac{m_r}{m_i} \right|_{\max} = \left| \frac{m_p}{m_i} \right| = \frac{j_p}{j}, \quad (3.22)$$

and if we define  $\epsilon_j$  by letting

$$|\omega_{j1} - \omega_c| = |\omega_{j2} - \omega_c| = \epsilon_j \omega_c, \quad \text{where } \epsilon_j > 0, \quad (3.23)$$

it follows that

$$j_p/j = 2\epsilon_j^{-1}A,$$

$$\epsilon_j = \frac{2Aj}{j_p}. \quad (3.24)$$

### 3.3.1 Evaluation of $I_1$ and $I_3$ .

Using (3.18)–(3.20), we can rewrite (3.14) as

$$\begin{aligned} I_1 &\approx \int_{\omega_c(1-\epsilon_f)}^{\omega_c(1-\epsilon_j)} \int_{-\pi}^{\pi} \epsilon^{-2} A^2 (1 + \cos \phi_i)^2 E(\omega, j) d\phi_i d\omega \\ I_1 &\approx \omega_c \int_{-\epsilon_f}^{-\epsilon_j} \int_{-\pi}^{\pi} \epsilon^{-2} A^2 (1 + \cos \phi_i)^2 E(\omega, j) d\phi_i d\epsilon. \end{aligned} \quad (3.25)$$

If we now assume that most of the residual energy density is concentrated near the critical frequency  $\omega_c$ , i.e. assume that contributions to  $I_1$  fall off quickly away from  $\omega_c$ , then we do not need to take into account the  $\omega$ -dependence of  $E(\omega, j)$  in the GM79 model spectrum (3.10), and simply let

$$E(\omega, j) \approx E(\omega_c, j) = \text{constant}. \quad (3.26)$$

It follows that

$$I_1 \approx A^2 \omega_c E(\omega_c, j) \int_{-\epsilon_f}^{-\epsilon_j} \epsilon^{-2} d\epsilon \int_{-\pi}^{\pi} (1 + \cos \phi_i)^2 d\phi_i, \quad (3.27)$$

where

$$\int_{-\pi}^{\pi} (1 + 2 \cos \phi_i + \cos^2 \phi_i) d\phi_i = \left( \phi_i + 2 \sin \phi_i + \frac{\phi_i}{2} + \frac{\sin 2\phi_i}{4} \right) \Big|_{-\pi}^{\pi} = 3\pi,$$

so that

$$\begin{aligned} I_1 &\approx 3\pi A^2 \omega_c E(\omega_c, j) \int_{-\epsilon_f}^{-\epsilon_j} \epsilon^{-2} d\epsilon \\ I_1 &\approx 3\pi A^2 \omega_c E(\omega_c, j) \cdot \left( \frac{-1}{\epsilon} \right) \Big|_{-\epsilon_f}^{-\epsilon_j} \\ I_1 &\approx 3\pi A^2 \omega_c E(\omega_c, j) \left( \frac{1}{\epsilon_j} - \frac{1}{\epsilon_f} \right), \end{aligned} \quad (3.28)$$

$$I_1 \approx \frac{3\pi A^2 \omega_c E(\omega_c, j)}{\epsilon_j} \quad \text{for } 1/\epsilon_j \gg 1/\epsilon_f. \quad (3.29)$$

Using (3.24), this becomes

$$I_1 \approx \frac{3\pi}{2} A \omega_c j_p j^{-1} E(\omega_c, j). \quad (3.30)$$

Proceeding as we did for  $I_1$  in (3.25), we can rewrite  $I_3$  as

$$I_3 \approx \omega_c \int_{\epsilon_j}^{\epsilon_N} \int_{-\pi}^{\pi} \epsilon^{-2} A^2 (1 + \cos \phi_i)^2 E(\omega, j) d\phi_i d\epsilon,$$

where  $\epsilon_N = (N - \omega_c)/\omega_c$ , and if we let  $E(\omega, j) = E(\omega_c, j) = \text{constant}$  as in (3.26), this yields a result similar to (3.28):

$$I_3 \approx 3\pi A^2 \omega_c E(\omega_c, j) \left( \frac{1}{\epsilon_j} - \frac{1}{\epsilon_N} \right).$$

Using (3.24) and assuming that  $1/\epsilon_j \gg 1/\epsilon_N$ , which is usually a good approximation, this becomes

$$I_3 = I_1 \approx \frac{3\pi}{2} A \omega_c j_p j^{-1} E(\omega_c, j),$$

so that

$$I_1 + I_3 \approx 3\pi A \omega_c j_p j^{-1} E(\omega_c, j). \quad (3.31)$$

### 3.3.2 Evaluation of $I_2$ .

We now proceed to the evaluation of (3.15):

$$I_2 = 2 \int_{\omega_{j1}}^{\omega_{j2}} \int_{\phi_c}^{\pi} \left( \frac{m_r}{m_i} \right)^2 E(\omega, j) d\phi_i d\omega.$$

Using (3.18)-(3.20), this becomes

$$I_2 \sim 2\omega_c \int_{-\epsilon_j}^{\epsilon_j} \int_{\phi_c}^{\pi} \epsilon^{-2} A^2 (1 + \cos \phi_i)^2 E(\omega, j) d\phi_i d\epsilon.$$

If we now let  $E(\omega, j) \sim E(\omega_c, j)$  as in (3.26), a better approximation here as the frequency range involved is narrower and centered about  $\omega_c$ , we obtain

$$I_2 \sim 4A^2 \omega_c E(\omega_c, j) \int_0^{\epsilon_j} \int_{\phi_c}^{\pi} \epsilon^{-2} (1 + \cos \phi_i)^2 d\phi_i d\epsilon. \quad (3.32)$$

As we get closer to  $\omega_c$  ( $\epsilon \rightarrow 0$ ), the range of incident azimuths  $\phi_i$  for which  $j_r > j_p$  increases. Hence in the above equation, the cutoff azimuthal angle  $\phi_c$  is a function of  $\epsilon$ . It ranges from  $\phi_c = 0$  at  $\epsilon = \epsilon_j$ , to  $\phi_c = \pi$  at  $\epsilon = 0$ , its exact dependence on  $\epsilon$  being easy to deduce from (3.20):

$$\begin{aligned} \frac{j_p}{j} &= |\epsilon^{-1}| A (1 + \cos \phi_c) \\ \cos \phi_c &= \frac{|\epsilon| j_p}{A j} - 1 \\ \phi_c &= \cos^{-1} \left( \frac{|\epsilon| j_p}{A j} - 1 \right). \end{aligned} \quad (3.33)$$

Therefore,

$$I_2 \sim 4A^2 \omega_c E(\omega_c, j) \int_0^{\epsilon_j} \int_{\cos^{-1} \left( \frac{|\epsilon| j_p}{A j} - 1 \right)}^{\pi} \epsilon^{-2} (1 + \cos \phi_i)^2 d\phi_i d\epsilon. \quad (3.34)$$

Replacing  $\epsilon_j$  by its value in (3.24), this becomes

$$I_2 \sim 4A^2 \omega_c E(\omega_c, j) \int_0^{\frac{2Aj}{j_p}} \int_{\cos^{-1} \left( \frac{|\epsilon| j_p}{A j} - 1 \right)}^{\pi} \epsilon^{-2} (1 + \cos \phi_i)^2 d\phi_i d\epsilon.$$

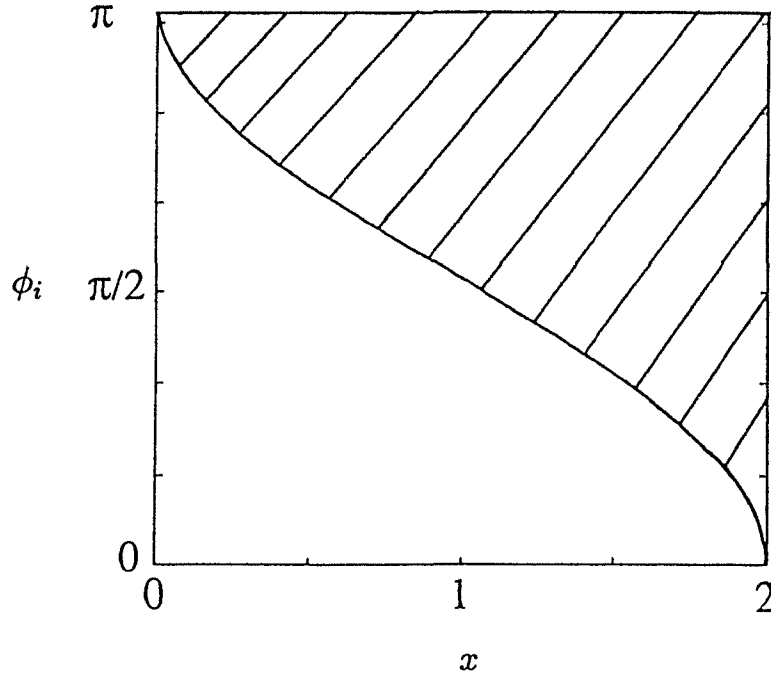


Figure 3.5: The region over which we perform the integration is hatched, and the curved line is given by  $x = 1 + \cos \phi_i$ .

This expression can be made more tractable if we use the change of variables  $x = \frac{Aj}{j_p}$ ,  $dx = \frac{j_p dc}{Aj}$ , yielding

$$I_2 \sim 4A^2 \omega_c E(\omega_c, j) \int_0^2 \int_{\cos^{-1}(x-1)}^{\pi} \left(\frac{Aj}{j_p}\right)^{-2} x^{-2} (1 + \cos \phi_i)^2 d\phi_i \cdot \left(\frac{Aj}{j_p}\right) dx$$

$$I_2 \sim 4A^2 \omega_c E(\omega_c, j) \left(\frac{Aj}{j_p}\right)^{-1} \int_0^2 \int_{\cos^{-1}(x-1)}^{\pi} x^{-2} (1 + \cos \phi_i)^2 d\phi_i dx,$$

and  $I_2$  can thus be rewritten as

$$I_2 \sim 4A \omega_c j_p j^{-1} E(\omega_c, j) \int_0^2 x^{-2} dx \int_{\cos^{-1}(x-1)}^{\pi} (1 + \cos \phi_i)^2 d\phi_i. \quad (3.35)$$

Evaluating this double integral is most easily done by changing the order of integration as follows: (see figure 3.5)

$$\int_0^2 x^{-2} dx \int_{\cos^{-1}(x-1)}^{\pi} (1 + \cos \phi_i)^2 d\phi_i = \int_0^{\pi} (1 + \cos \phi_i)^2 d\phi_i \int_{(1+\cos \phi_i)}^2 x^{-2} dx, \quad (3.36)$$

$$\int_0^2 x^{-2} dx \int_{\cos^{-1}(x-1)}^{\pi} (1 + \cos \phi_i)^2 d\phi_i = \int_0^{\pi} (1 + \cos \phi_i)^2 \left( \frac{-1}{2} + \frac{1}{(1 + \cos \phi_i)} \right) d\phi_i,$$

so that

$$I_2 \sim 4A\omega_c j_p j^{-1} E(\omega_c, j) \left[ \frac{-1}{2} \int_0^{\pi} (1 + \cos \phi_i)^2 d\phi_i + \int_0^{\pi} (1 + \cos \phi_i) d\phi_i \right] \quad (3.37)$$

$$I_2 \sim 4A\omega_c j_p j^{-1} E(\omega_c, j) \left[ -\frac{1}{2} \left( \phi_i + 2 \sin \phi_i + \frac{\phi_i}{2} + \frac{\sin 2\phi_i}{4} \right) + \phi_i + \sin \phi_i \right]_0^{\pi}$$

$$I_2 \sim 4A\omega_c j_p j^{-1} E(\omega_c, j) \left( \frac{\pi}{4} \right),$$

and we finally obtain

$$I_2 \sim \pi A\omega_c j_p j^{-1} E(\omega_c, j). \quad (3.38)$$

### 3.3.3 Total residual energy

Adding (3.38) and (3.31), we get

$$I_1 + I_2 + I_3 \approx 4\pi A\omega_c j_p j^{-1} E(\omega_c, j), \quad (3.39)$$

and substituting this back into (3.13), we get

$$E_r \approx b^2 N_o N A \omega_c j_p \sum_{j=1}^{\infty} j^{-1} E(\omega_c, j)$$

for the total residual energy per unit mass  $E_r$ . If  $E(\omega_c, j)$  is of the form proposed by Munk (1981) in (3.9)—(3.11), then

$$E_r \approx j_p b^2 N_o N E A \omega_c B(\omega_c) \underbrace{\sum_{j=1}^{\infty} j^{-1} H(j)}_{0.4}$$

$$E_r \approx 0.4 j_p b^2 N_o N E A \omega_c B(\omega_c),$$

where  $A$  is given by (3.19), and  $B(\omega_c)$  is given by (3.10), so that

$$A \omega_c B(\omega_c) = \left(1 - \frac{f^2}{\omega_c^2}\right) \omega_c \frac{2f}{\pi \omega_c} \frac{1}{(\omega_c^2 - f^2)^{1/2}},$$

$$A \omega_c B(\omega_c) = \frac{2f}{\pi \omega_c^2} (\omega_c^2 - f^2)^{1/2},$$

and it follows that the total residual energy per unit mass is given by

$$E_r \approx \frac{0.8}{\pi} j_p b^2 N_o N E \frac{f}{\omega_c^2} (\omega_c^2 - f^2)^{1/2}. \quad (3.40)$$

The ratio of the total residual energy to the total incident energy is obtained by dividing (3.40) by (3.12), yielding

$$\frac{E_r}{E_i} \approx \frac{1.6}{\pi} j_p f \omega_c^{-2} (\omega_c^2 - f^2)^{1/2}. \quad (3.41)$$

Next we seek to rewrite (3.41) as a function of only two parameters:  $\gamma = f/N$ , and the slope angle  $\alpha$ . Since  $j_p$  as given in (3.5) is already a function of  $\gamma$  and  $\alpha$ , we only need to write the rest of (3.41) in terms of these two parameters. Replacing  $\omega_c$  by (2.29), we get

$$\frac{E_r}{E_i} \approx 0.51 j_p f \frac{(N^2 \sin^2 \alpha + f^2 \cos^2 \alpha - f^2)^{1/2}}{N^2 \sin^2 \alpha + f^2 \cos^2 \alpha}$$

$$\frac{E_r}{E_i} \approx 0.51 j_p \frac{f}{N^2} \frac{[(N^2 - f^2) \sin^2 \alpha]^{1/2}}{(\sin^2 \alpha + \gamma^2 \cos^2 \alpha)}$$

which, for  $N^2 \gg f^2$ , becomes

$$\frac{E_r}{E_i} \approx 0.51 j_p \frac{f}{N^2} \frac{N \sin \alpha}{(\sin^2 \alpha + \gamma^2 \cos^2 \alpha)}$$

$$\frac{E_r}{E_i} \approx 0.51 j_p \gamma \sin \alpha (\sin^2 \alpha + \gamma^2 \cos^2 \alpha)^{-1} \quad (3.42)$$

This is the ratio of the total residual energy (reflected energy truncated at  $j_r = j_p$ ) to the total incident energy (equal to half the total GM79 energy (3.12)). For the purpose of comparison with data, it may be more relevant to compute the ratio  $R$  of the sum of the total incident and residual energy to the total GM79 energy:

$$R \approx \frac{E_i + E_r}{2E_i} = \frac{E_i + (E_r/E_i)E_i}{2E_i} \quad (3.43)$$

$$R \approx \frac{1 + (E_r/E_i)}{2} \quad (3.44)$$

and we finally obtain

$$R \approx 0.5 + 0.26j_p\gamma \sin \alpha (\sin^2 \alpha + \gamma^2 \cos^2 \alpha)^{-1}. \quad (3.45)$$

Note that the second term on the right hand side of (3.45) tends to zero as  $\alpha \rightarrow 0$ . To obtain the correct limit  $R \rightarrow 1$  as  $\alpha \rightarrow 0$ , GG88 adjusted the first term on the right hand side of (3.45) from 0.5 to 1 in (3.7). This correction was used to compensate for some of the approximations made here, e.g. (3.17), (3.26) and (3.29). Estimates of  $R$  based on (3.45), and numerical calculations of  $R$  made without any of the above approximations, were always found to be in agreement to within this correction factor of 0.5.

### 3.4 Distribution of energy within the residual spectrum

Besides allowing a verification of (3.45), the numerical calculations referred to above allow us to look at the distribution of energy within the residual spectrum. The specular reflection formula

$$E_r(\omega, j_r, \phi_r) = (m_r/m_i)^2 E_i(\omega, j, \phi_i) \quad (3.46)$$

was used for a spectrum of incident waves with the GM79 energy density, each of them giving rise to a reflected wave according to (2.58) and (2.71). The energy density of

the reflected waves was added and stored in a three-dimensional array containing a discrete number of frequency bins, modenumber bins, and azimuthal bins. Special attention was paid to what happens in the neighbourhood of the critical frequency by using a very fine grid near  $a = \tan \alpha \tan \theta_i = 1$  (in contrast with Eriksen's (1985) frequency grid which did not have an increased resolution near  $\omega_c$ ).

Figure 3.6 shows a projection of the energy contained in this three-dimensional array  $E_r(\omega, j_r, \phi_r)$  onto the frequency axis:

$$E_r(\omega) = \sum_{j_r=1}^{j_r=j_p} \int_{-\pi}^{\pi} E_r(\omega, j_r, \phi_r) d\phi_r. \quad (3.47)$$

There is a wide range of frequencies for which the residual energy density is substantially larger than the GM79 energy density. The narrow spectral valley right at  $\omega_c$  is due to truncation of the reflected spectrum at  $j_r = j_p$ . Otherwise there would have been an infinite peak there. The residual energy density equals the GM79 incident energy density at  $f$  and  $N$ , where from (2.58),  $|m_r/m_i| = 1$ .

Figure 3.7 shows a projection of  $E_r(\omega, j_r, \phi_r)$  onto the modenumber axis:

$$E_r(j_r) = \int_f^N \int_{-\pi}^{\pi} E_r(\omega, j_r, \phi_r) d\phi_r d\omega. \quad (3.48)$$

We see that the residual energy spectrum is white in modenumber space, in sharp contrast with the  $j^{-2}$  slope of the incident GM79 model spectrum (3.11) for  $j \gg j_* = 3$ . One way of interpreting this result would be to say that (2.37) exactly compensates for the  $j^{-2}$  slope of the incident spectrum (3.11) to yield a reflected energy spectrum that is white. If this interpretation is correct, we would expect the mean squared reflected shear spectrum to have a  $j^2$  slope, by virtue of (2.40) and (3.11). This is indeed the case, as can be seen on figure 3.8.

Finally, figure 3.9 shows a projection of  $E_r(\omega, j_r, \phi_r)$  onto the azimuthal axis:

$$E_r(\phi_r) = \sum_{j_r=1}^{j_r=j_p} \int_f^N E_r(\omega, j_r, \phi_r) d\omega. \quad (3.49)$$

The residual energy density is concentrated at  $\phi_r = 0^\circ$  (onslope direction) and  $\phi_r = 180^\circ$  (offslope direction). The spectral peak at  $\phi_r = 0^\circ$  is due to slightly supercritical waves ( $\omega \gtrsim \omega_c$ ) which get reflected toward shallower water, whereas the spectral peak

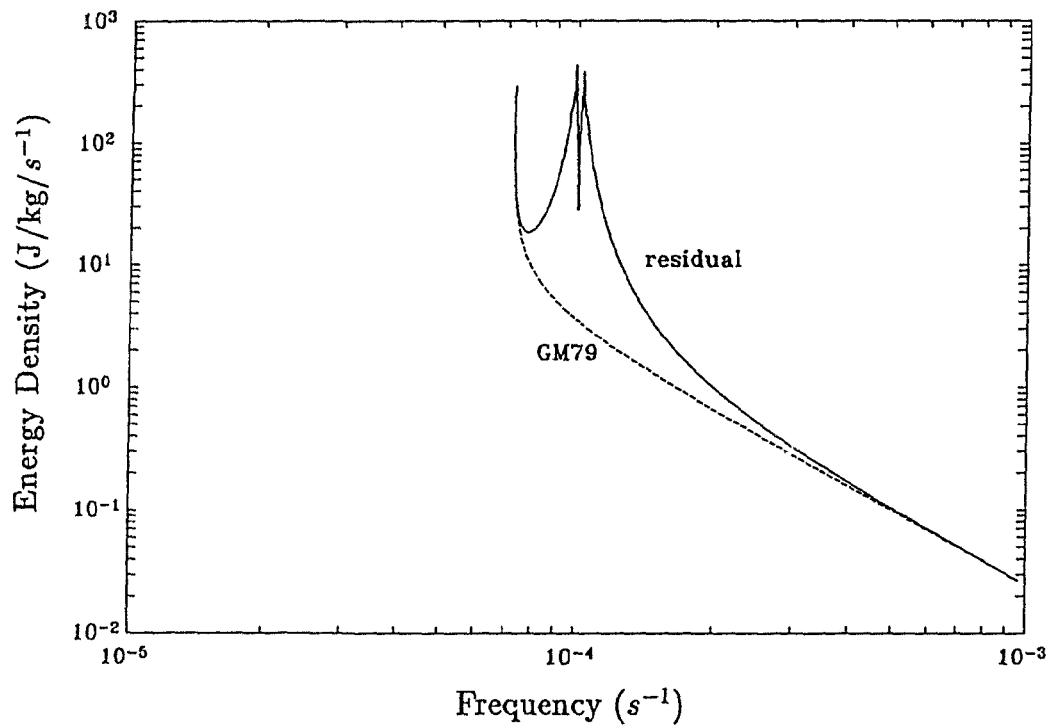


Figure 3.6: Distribution of residual energy density as a function of frequency  $\omega$  for the case where  $f = 7.3 \times 10^{-5} \text{ s}^{-1}$ ,  $N = 10^{-3} \text{ s}^{-1}$  and  $\tan \alpha = 0.07$ , so that  $\omega_c \sim 10^{-4} \text{ s}^{-1}$ . The dashed line shows the canonical GM79 energy level for the purpose of comparison.

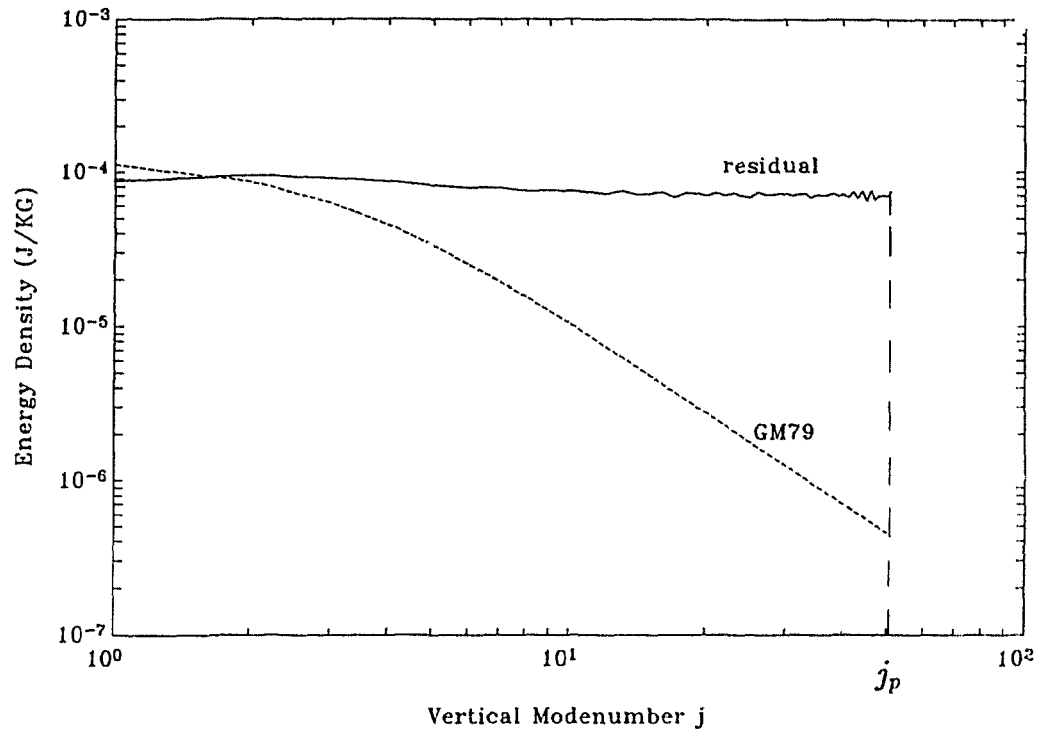


Figure 3.7: Distribution of residual energy density as a function of the reflected modenumber  $j_r$  for the case where  $f = 7.3 \times 10^{-5} s^{-1}$ ,  $N = 10^{-3} s^{-1}$  and  $\tan \alpha = 0.07$ . Its white  $j^0$  slope (—) is contrasted with the red  $j^{-2}$  slope of the GM79 model spectrum (- - -).

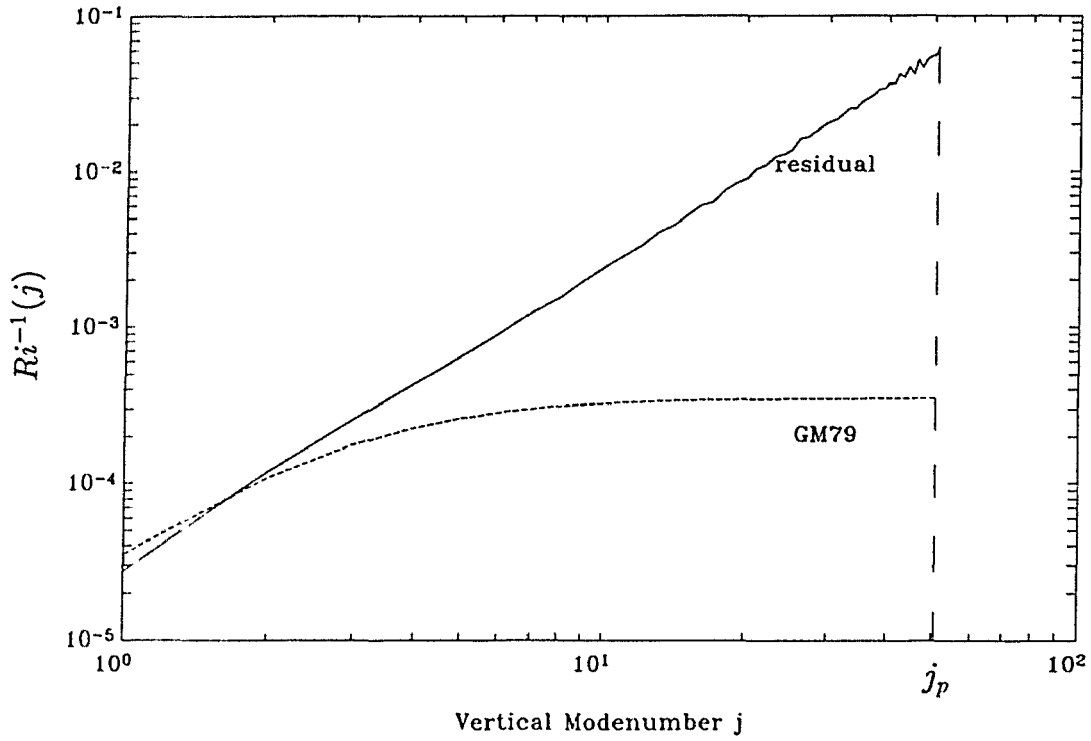


Figure 3.8: Contribution to the inverse Richardson function  $Ri^{-1} = \langle (\partial u / \partial z)^2 / N^2 \rangle$  (Munk, 1981) as a function of the reflected modenumbers  $j_r$  for  $f = 7.3 \times 10^{-5} s^{-1}$ ,  $N = 10^{-3} s^{-1}$  and  $\tan \alpha = 0.07$ . Its  $j^2$  slope (—) is contrasted with the  $j^0$  slope of the GM79 model spectrum (- - -). Note that by definition,  $j_p$  is such that  $\sum_{j=1}^{j_p} Ri^{-1}(j) = 1$ .

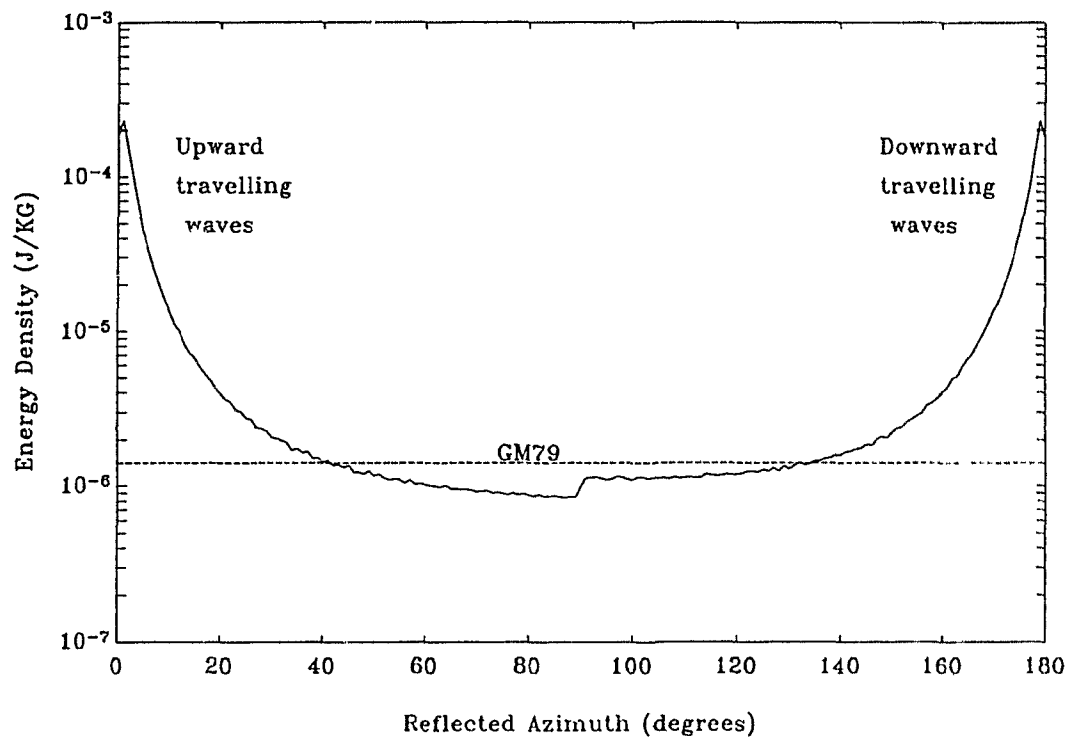


Figure 3.9: Distribution of residual energy density as a function of the reflected azimuth  $\phi_r$  for the case where  $f = 7.3 \times 10^{-5} s^{-1}$ ,  $N = 10^{-3} s^{-1}$  and  $\tan \alpha = 0.07$ . The isotropic GM79 energy level (- -) is shown for the purpose of comparison.

at  $\phi_r = 180^\circ$  is due to slightly subcritical waves ( $\omega \lesssim \omega_c$ ) which get reflected toward deeper water (see figure 2.5). The residual energy density for  $\phi_r = [-180^\circ, 0^\circ]$  is a mirror image of figure 3.9, and so is not plotted.

Figures 3.6, 3.7, 3.8 and 3.9 clearly demonstrate the extent to which the residual energy spectrum differs from the level and shape of the canonical GM79 energy spectrum. Projections of  $E_r(\omega, j_r, \phi_r)$  onto the  $(\omega, j_r)$ ,  $(j_r, \phi_r)$  and  $(\omega, \phi_r)$  planes were also plotted, but are not reproduced here as they yield little useful additional information.

### 3.5 Dissipated energy flux due to bottom drag associated with the residual currents

An estimate of the rate of energy dissipation due to the bottom stress  $\tau$  associated with the residual currents could be obtained from

$$F_{dr} = \langle \tau \cdot \mathbf{u} \rangle, \quad \tau \equiv \rho u_*^2 \hat{\mathbf{u}}, \quad (3.50)$$

where  $\rho$  is the density of the water,  $u_*$  is a friction velocity, and  $\hat{\mathbf{u}}$  is a unit vector pointing in the same direction as  $\mathbf{u}$ . Hence

$$F_{dr} = \langle \rho u_*^2 |\mathbf{u}| \rangle, \quad (3.51)$$

and taking  $u_* \approx |\mathbf{u}|/30$  as in Armi (1978), this is consistent with

$$F_{dr} = \rho C_d \langle |\mathbf{u}|^3 \rangle, \quad (3.52)$$

where  $C_d \approx 10^{-3}$ . To evaluate this, we need to know the value of  $\langle |\mathbf{u}|^3 \rangle$  that is associated with the residual internal wavefield. To that effect, we note that for the GM79 model spectrum, the mean square horizontal current associated with the whole internal wavefield is given by (Munk, 1981, equation 9.24)

$$\langle |\mathbf{u}|^2 \rangle = \frac{3}{2} b^2 N_o N E \quad (3.53)$$

$$\langle |\mathbf{u}|^2 \rangle = 4.4 \times 10^{-3} \left( \frac{N}{N_o} \right) m^2 s^{-2}, \quad (3.54)$$

where  $N_o = 5.2 \times 10^{-3} s^{-1}$ . Approximating  $\langle |\mathbf{u}|^3 \rangle$  by  $\langle |\mathbf{u}|^2 \rangle^{3/2}$ , and substituting (3.54) into (3.52), we get

$$F_{dr} \approx \rho C_d \left[ 4.4 \times 10^{-3} \left( \frac{N}{N_o} \right) \right]^{3/2} W m^{-2} \quad (3.55)$$

for the dissipated energy flux due to bottom drag associated with the GM79 horizontal currents. For reasonably modest bottom slopes ( $dh/dx < 0.10$  say), the residual currents are mostly horizontal, so that for a residual spectrum with  $R$  times the GM79 energy, the rate of energy dissipation  $F_{dr}$  should be

$$F_{dr} \approx \rho C_d \left[ 4.4 \times 10^{-3} R \left( \frac{N}{N_o} \right) \right]^{3/2} W m^{-2}, \quad (3.56)$$

where  $R$  is given by (3.7). Figure 3.10 shows contours of  $F_{dr}$  for  $C_d = 10^{-3}$  and  $N \approx 10^{-3} s^{-1}$  (0.6 cph), the value of  $N$  used in (1.2). The shape of the contours is dictated by that of the  $R$  contours shown on figure 3.3.

### 3.6 Discussion

The rate of energy dissipation due to the bottom drag associated with the residual currents ( $F_{dr}$ ) varies between about 0.1 and 0.6  $mW \cdot m^{-2}$  on figure 3.10. Those values are of the same order of magnitude as those obtained for the rate of energy dissipation ( $F_{ds}$ ) due to shear instability of the reflected waves (figure 3.2), but  $F_{ds}$  and  $F_{dr}$  are distributed differently in  $(f/N, \tan \alpha)$  space:  $F_{ds} > F_{dr}$  for low values of  $f/N$  and large bottom slopes, whereas  $F_{dr} > F_{ds}$  for large values of  $f/N$  and small bottom slopes.

The mixing efficiency  $\Gamma$  should be less for  $F_{dr}$  than for  $F_{ds}$  however, as  $F_{dr}$  results from bottom friction and presumably mixes fluid that is already mixed (Garrett, 1990). Ivey and Imberger (1990) argue that  $\Gamma$  could be as high as 0.2 for internal wave breaking above sloping bottoms ( $F_{ds}$ ), but it seems unlikely that  $\Gamma$  could be nearly as high as 0.1 for  $F_{dr}$ .

Therefore as they stand, the estimates of  $F_{ds}$  and  $F_{dr}$  given here appear too low to satisfy (1.2),  $\Gamma F_d \approx 0.3 mW \cdot m^{-2}$ , required by the boundary mixing hypothesis.

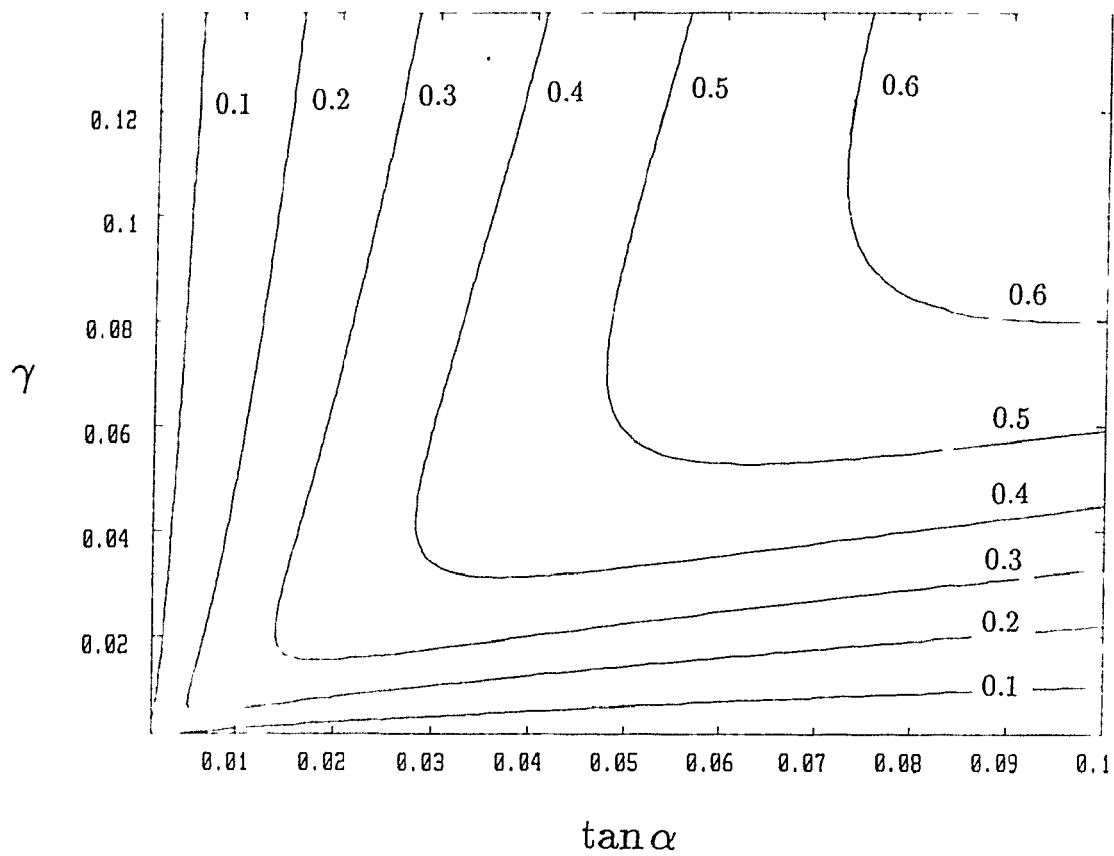


Figure 3.10: Energy dissipation rate  $F_{dr}$  due to bottom drag associated with the residual currents (in  $mW \cdot m^{-2}$ ), as a function of  $\gamma = f/N$  and the bottom slope  $\tan \alpha$ , using (3.56) with  $C_d = 10^{-3}$  and  $N = 10^{-3} s^{-1}$ .

They are of the right order of magnitude however, and so we cannot completely rule out the possibility that internal wave reflection off sloping bottoms may be a major agent of diapycnal mixing in the abyssal ocean.

A more definitive answer awaits more theoretical work as well as more observational work. Among other things, the theoretical work should address the issue of how the GG residual spectrum relaxes back to a more typical shape. In the next chapter, it is argued that rapid spectral changes with height above sloping bottoms could be partly due to geometric effects, but energy redistribution via non-linear processes undoubtedly plays a role too.

Non-linear processes would presumably transfer energy away from  $\omega_c$  to adjacent frequency bands (figure 3.6). One assumes that they would also transfer energy in vertical wavenumber space to restore the more typical  $j^{-2}$  slope, but we do not know *a priori* whether the dominant energy transfer would take place from low  $j$ 's to high  $j$ 's or vice-versa, as figure 3.7 shows that the energy density at low  $j$ 's is slightly depleted with respect to the GM79 energy level. Finally, non-linear processes would also have to redistribute energy in azimuthal space (figure 3.9), but nothing is known about how an anisotropic internal wave spectrum might relax back to horizontal isotropy (Müller et al., 1986).

# Chapter 4

## The effects of a non-uniform slope

### 4.1 Introduction

Internal wave measurements made in the first 100m or so above sloping bottoms often depart noticeably from the canonical Garrett–Munk model spectrum (Wunsch, 1976; Wunsch and Webb, 1979). However, the extent of this departure is highly variable, especially in the neighbourhood of the critical frequency  $\omega_c$ . There are locations where energy enhancement near  $\omega_c$  is quite pronounced (Eriksen, 1982), and others where it is absent (Thorpe, 1988).

In this chapter, I examine the possibility that the shape of the underlying seafloor may be responsible for some of the variability in energy content seen at the critical frequency. For waves of a given frequency incident on a bottom of non-uniform slope, the wave ray slope matches the local bottom slope only in a few specific locations, so that we may ask whether large enhancements of vertical shear and energy density near the critical frequency can still be expected in those locations, as in the uniform slope case.

Baines (1971a, 1971b) has done much of the pioneering work on the scattering of internal waves off irregular topography. He pointed out the importance of using the proper form of the radiation condition, which requires the scattered waves to carry energy away from the boundary. For the “flat-bump” case where the bottom slope  $dh/dx$  is everywhere less than the characteristic slope  $s$ , Baines (1971a) showed that

the back-scattered wave usually does not vanish, so that the simple application of ray theory (e.g. Longuet-Higgins, 1969) is incorrect.

## 4.2 Sinusoidal topography

Strictly speaking, the reflection laws of chapter 2 are only valid for infinite sloping planes. It is therefore not obvious that they can be used to provide a good description of the interaction of internal waves with a bottom of non-uniform slope, and if so, under what conditions.

A logical first step in the study of internal wave scattering by irregular topography is to investigate the problem of a single wave component incident on sinusoidal topography of infinitesimal amplitude. The solution of this problem could then be used to determine the scattered wavefield over arbitrarily complicated topography, subject to linearisation of the boundary condition.

To simplify matters, Baines (1971a) assumed that both the wave motion and the bottom topography are independent of the alongslope  $y$ -coordinate. This two-dimensional assumption, together with the incompressibility condition  $\nabla \cdot \mathbf{u} = 0$ , enabled him to describe the wave motion in terms of a streamfunction, and thus facilitated analytical treatment of the problem. He let a monochromatic wave of frequency  $\omega$ , characteristic slope  $s = \tan \mu$  (2.16), and wavenumber ( $sK_1, K_1$ ) in  $(x, z)$  space be incident on a sinusoidal bottom

$$h(x) = d \cos lx \quad (4.1)$$

where  $d$  is the amplitude of the sinusoidal perturbation, and  $l$  is the topographic wavenumber. Making the "flat-bump" assumption

$$\left| \frac{dh}{dx} \right|_{\max} = ld < s \quad \text{for } -\infty < x < \infty \quad (4.2)$$

and assuming that  $K_1 d \ll 1$  and  $ld \ll 1$ , Baines found that, in addition to the specularly reflected wave whose wavenumber is  $(sK_1, -K_1)$ , two scattered waves were generated with wavenumbers

$$\mathbf{K}' = (sK_1 \pm l, -|K_1 \pm l/s|) \quad (4.3)$$

The sum (+) wave is always forward-scattered, whereas the difference (-) wave can be either forward-scattered when  $l < sK_1$ , or back-scattered when  $l > sK_1$ . Denoting by  $F_i$  the energy flux associated with the incident wave, and by  $F_{\pm}$  the energy flux associated with the sum and difference waves, Baines showed that

$$\frac{F_{\pm}}{F_i} = \left| K_1 \pm \frac{l}{s} \right| K_1 d^2 \quad (4.4)$$

to first order accuracy in  $K_1 d$  and  $ld$ .

Rubenstein (1988) expanded the work of Baines (1971a) by applying (4.4) to a more general bathymetric profile, using the empirical power spectrum of topographic variations introduced by Bell (1975b), and assuming the downward propagating half of the GM79 model spectrum (Munk, 1981) was incident on that bottom. He found that the principal interactions involve the scattering of low-frequency, low-wavenumber incident waves into higher wavenumbers.

Because of its higher wavenumbers, the scattered wavefield has elevated shear levels compared to the incident wavefield; Rubenstein found that the inverse Richardson number ( $Ri^{-1}$ ) for the scattered wavefield, summed from mode  $j = 1$  to  $j = 260$ , is increased by a factor of about 3.6 with respect to the incident wavefield. This is important, as it shows that we can expect enhanced internal wave breaking above a bumpy bottom even when the mean slope on a larger scale is effectively zero. The mechanism leading to shear enhancement here is thus conceptually different from that envisaged in chapter 2, where the bottom was smooth but had a non-zero mean slope.

The conclusions of Rubenstein (1988) may be qualitatively true, but they are quantitatively very uncertain, as there are serious problems associated with the use of (4.4), the cornerstone of his paper. Perhaps the most serious problem is that (4.4) was obtained under the assumption that the bottom slope is everywhere less than the characteristic slope (4.2). Shadowing effects are thus strictly forbidden, and the critical case where  $dh/dx = s$  locally, which is so important for the intensification of

the vertical shear ((2.40) and (2.58)), cannot be dealt with explicitly.

Another problem with (4.4) is that it is only accurate to first-order in  $K_1 d$  and  $ld$ . Mied and Dugan (1976) numerically performed a higher-order perturbation expansion involving a finite set of  $2n_{\max} + 1$  discrete, scattered horizontal wavenumbers

$$K_x' = sK_1 \pm nl \quad n = 0, 1, 2, 3, \dots, n_{\max}. \quad (4.5)$$

Their higher-order solution for the scattered wavefield agrees remarkably well with the first-order solution of Baines (1971a) for  $ld \leq s/6$ , i.e. the contributions from  $n \geq 2$  are then unimportant. However, when the bottom slope  $ld$  becomes steeper than about  $s/2$ , they find that the series solution (4.5) fails to converge. This is unfortunate, in that it does not take us nearly as close to the critical case as is desirable; in the wave breaking model of GG88, it was typically found that 80% of the total shear comes from waves with ray slopes within  $\pm 20\%$  of the critical wave ray slope.

Mied and Dugan (1976) also pointed out that (4.4) only conserves the energy flux of the incident wave to  $O(K_1^2 d^2/s^2)$ , so that for a given bathymetric profile for which  $K_1 d$  is fixed, Baines' solution will do much worse at conserving the energy flux of the incident wave at near-inertial frequencies than at higher frequencies. This, as well as violations of the flat-bump assumption (4.2), severely limits the ability of (4.4) to describe the interaction of near-inertial waves with the ocean bottom, which is what Rubenstein (1988) was primarily concerned with.

### 4.3 Local topographic effects

Given this inability to deal explicitly with the critical case using a Fourier representation of the topography, one can at least try to determine some properties of the scattered wavefield for particular local topographic shapes.

Baines (1971b) developed a two-dimensional theory for the scattering of internal waves in which the critical case can be dealt with explicitly, provided  $dh/dx = s$  at a single location in the bathymetric profile. Using the same radiation condition as in Baines (1971a), he was able to reduce the problem of determining the scattered

wavefield to a pair of coupled integral equations with two unknown functions. He cast the problem in terms of the characteristic coordinates

$$\xi = z + sx, \quad \eta = z - sx \quad (4.6)$$

where  $z$  is the vertical (upwards) coordinate,  $x$  is the cross-isobath (onshore) coordinate, and  $s$  is the characteristic (or wave ray) slope. The origin of both the characteristic and Cartesian coordinate systems is chosen to coincide with the single location in the bathymetry profile where  $dh/dx = s$ . Now for smoothly-varying topography, the bottom can often be regarded as either locally convex ( $d^2h/dx^2 < 0$ ) or concave ( $d^2h/dx^2 > 0$ ). It should therefore be useful to look at properties of the scattered wavefield for both of these cases.

### 4.3.1 Locally convex topography

For locally convex topography with radius of curvature  $R$  at the origin, Baines (1971b) showed that, for  $|\xi/R| \ll 1$ , the equation for the bottom can be approximated by

$$\eta = -c_1\xi^2, \quad c_1 = \frac{(1+s^2)^{3/2}}{8s^2R} \quad (4.7)$$

in terms of the characteristic coordinates (figure 4.1). This equation is symmetric in  $\xi$ , an asymmetric term proportional to  $\xi^3/R^2$  having been neglected. Baines let a plane wave with stream function

$$\psi_i = \epsilon \exp\{i(K_1\xi - \omega t)\}, \quad (4.8)$$

of infinitesimal amplitude  $\epsilon$ , total wavenumber  $K_1(1+s^2)^{1/2}$ , and frequency  $\omega$ , be incident on idealised topography specified exactly by (4.7). He obtained an analytical solution for the scattered wavefield, and expressed it as a superposition of a back-reflected (or back-scattered) wave  $\psi_R$ , a wave transmitted to the right  $\psi_{Tr}$ , and a wave transmitted to the left  $\psi_{Tl}$  (see fig 4.1). His solution may be conveniently summarised as follows:

$$\psi_R(\xi, t) = 0 \quad (-\infty < \xi < \infty) \quad (4.9)$$

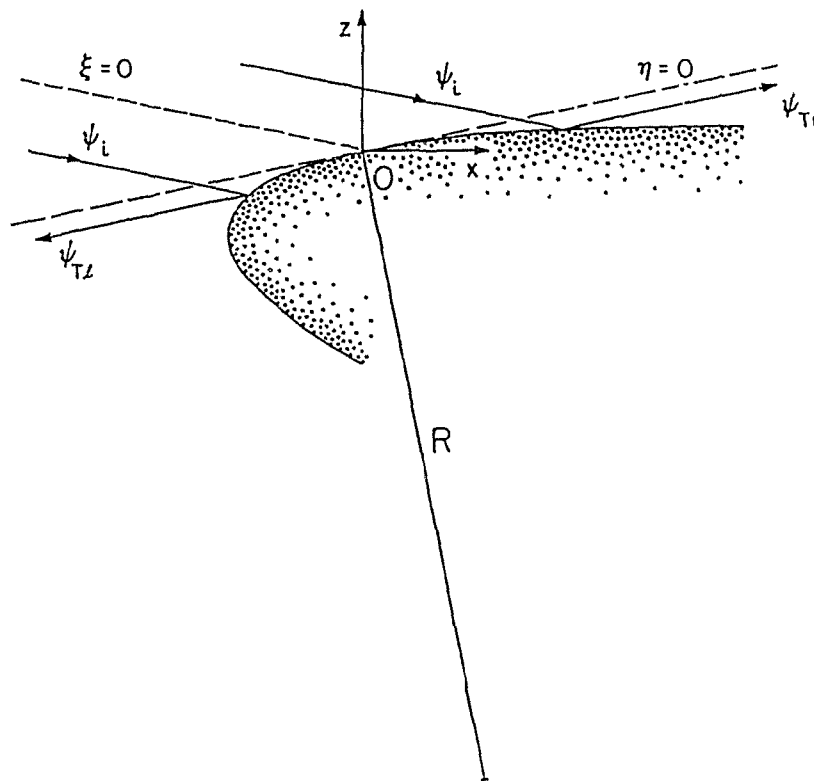


Figure 4.1: A plane wave with stream function  $\psi_i$  is incident on topography specified by (4.7) and gives rise to a wave transmitted to the left,  $\psi_{Tl}$ , and a wave transmitted to the right,  $\psi_{Tr}$ . The back-reflected wave  $\psi_R$  vanishes for this particular bottom shape. The arrows point in the direction of energy propagation, and the wave ray slope is  $s = 0.2$ . The origin coincides with the single location in the bathymetry profile where the bottom slope matches the wave ray slope, and  $R$  denotes the radius of curvature of the topography there. The characteristic coordinates are  $\xi = z + sx$ ,  $\eta = z - sx$ .

$$\psi_{Tr}(\eta, t) = \psi_{T\ell}(\eta, t) = -\epsilon \exp\{-K_1(\eta/c_1)^{1/2}\} \exp(-i\omega t) \quad (0 < \eta < \infty) \quad (4.10)$$

$$\psi_{Tr}(\eta, t) = -\epsilon \exp\{i[K_1(|\eta|/c_1)^{1/2} - \omega t]\} \quad (-\infty < \eta < 0) \quad (4.11)$$

$$\psi_{T\ell}(\eta, t) = -\epsilon \exp\{-i[K_1(|\eta|/c_1)^{1/2} + \omega t]\} \quad (-\infty < \eta < 0) \quad (4.12)$$

It is worth analysing this solution in some detail. The vanishing of the back-scattered wave (4.9) is a property of the particular bottom shape specified by (4.7): symmetric in  $\xi$  and parabolic in the characteristic coordinates, with slope at infinity asymptotic to that of the  $\xi$ -characteristics (see figure 4.1). The back-scattered wave does not necessarily vanish for other bottom shapes.

For the region above the grazing characteristic ( $\eta > 0$ ), where purely specular reflection would produce no motion, (4.10) describes an evanescent field of oscillatory motions with velocity amplitude

$$\left| \frac{\partial \psi_T}{\partial \eta} \right| = \frac{\epsilon K_1}{2(c_1 \eta)^{1/2}} \exp\{-K_1(\eta/c_1)^{1/2}\} \quad (0 < \eta < \infty) \quad (4.13)$$

where  $\epsilon K_1$  is the velocity amplitude of the incident wave. The time-averaged kinetic energy density is thus given by

$$\frac{1}{4} \left| \frac{\partial \psi_T}{\partial \eta} \right|^2 = \frac{\epsilon^2 K_1^2}{16(c_1 \eta)} \exp\{-2K_1(\eta/c_1)^{1/2}\} \quad (0 < \eta < \infty). \quad (4.14)$$

The  $e$ -folding scale associated with the exponential factor in (4.14) is given by  $\eta = c_1/4K_1^2 = (1 + s^2)^{3/2}/(32s^2 K_1^2 R) \approx (32s^2 K_1^2 R)^{-1}$ . It is therefore very sensitive to our choice of  $s, K_1$  and  $R$ . For example, it equals  $1250m$  for  $K_1 = 10^{-3}m^{-1}$ ,  $s = 0.9b$ ,  $R = 10^4m$ , but merely equals  $12.5m$  for  $K_1 = 10^{-2}m^{-1}$  with  $s$  and  $R$  unchanged, indicating a much faster rate of decay of the scattered wavefield for large incident wavenumbers (small incident wavelengths). Note that the distance from the  $\eta = 0$  characteristic is given by  $|\eta|/(1 + s^2)^{1/2}$ , which approximately equals  $|\eta|$  for small wave ray slopes, and that the kinetic energy density in (4.14) decays as  $\eta^{-1}$  for  $0 < \eta \ll c_1/4K_1^2$ .

In the region below the grazing characteristic ( $\eta < 0$ ), i.e. for  $\eta$ -characteristics which intersect the bottom, (4.11) and (4.12) describe a field of propagating internal waves with velocity amplitude

$$\left| \frac{\partial \psi_T}{\partial \eta} \right| = \frac{\epsilon K_1}{2(c_1 |\eta|)^{1/2}} \quad (-\infty < \eta < 0) \quad (4.15)$$

and time-averaged kinetic energy density

$$\frac{1}{4} \left| \frac{\partial \psi_T}{\partial \eta} \right|^2 = \frac{\epsilon^2 K_1^2}{16c_1 |\eta|} = \frac{\epsilon^2 K_1^2 s^2 R}{2(1+s^2)^{3/2} |\eta|} \quad (-\infty < \eta < 0). \quad (4.16)$$

As Baines (1971b) pointed out, perhaps the most significant feature of the field of motion (4.9)–(4.12) is that the kinetic energy density near  $\eta = 0$  is proportional to  $\epsilon^2 K_1^2 R/|\eta|$ , as can be seen from (4.14) and (4.16). There is a singularity at  $\eta = 0$ , and the strength of this singularity increases with the local radius of curvature  $R$  ( $R = \infty$  for a bottom of uniform slope). Now with  $\psi_R = 0$ , the condition that the total stream function  $\psi$  must vanish on the boundary reduces to

$$\psi_i + \psi_{Tl} = 0 \quad \text{on } \xi = -(|\eta|/c_1)^{1/2} \quad (4.17)$$

$$\psi_i + \psi_{Tr} = 0 \quad \text{on } \xi = (|\eta|/c_1)^{1/2} \quad (4.18)$$

A similar boundary condition involving only incident and reflected wave components can be used to derive the specular laws of reflection of chapter 2. Hence we expect the latter to be valid for  $\eta < 0$ , i.e. for the region of the fluid where  $\eta$ -characteristics intersect the bottom. To verify this, we first need to find a relationship between the bottom slope  $dh/dx$  and the characteristic coordinate  $\xi$  for the idealised topography shown on figure 4.1. Substituting  $\xi = h(x) + sx$  and  $\eta = h(x) - sx$  into (4.7), and differentiating with respect to  $x$ , we obtain

$$\frac{dh}{dx} = \frac{s(1 - 2c_1 \xi)}{(1 + 2c_1 \xi)}. \quad (4.19)$$

The bottom is thus vertical at  $\xi = -1/(2c_1)$ , and horizontal at  $\xi = 1/(2c_1)$ . We also verify that  $dh/dx = s$  at  $\xi = 0$ , and  $dh/dx \rightarrow -s$  as  $\xi \rightarrow \pm\infty$ , i.e. the bottom slope is critical at  $\xi = 0$ , and is parallel to the  $\xi$ -characteristics at  $\xi \rightarrow \pm\infty$ , as stated earlier. The next step consists of defining the phase function

$$\Phi(\eta, t) = K_1 \left( \frac{|\eta|}{c_1} \right)^{1/2} - \omega t \quad (4.20)$$

for the wavefield  $\psi_{Tr}(\eta, t)$  given in (4.11). Subject to the *WKB* approximation (Gill 1982, p. 300), a local wavenumber  $K'(\eta)$  may then be defined by

$$K'(\eta) = \frac{\partial}{\partial \eta} \Phi(\eta, t) = \frac{K_1 \operatorname{sgn}(\eta)}{2c_1^{1/2} |\eta|^{1/2}}, \quad (4.21)$$

yielding the wavenumber amplification

$$\frac{K'}{K_1} = \frac{-1}{2c_1^{1/2} |\eta|^{1/2}}. \quad (4.22)$$

A similar amplification in velocity amplitude was implicit in (4.15). Now by virtue of (4.18), we can replace  $|\eta|^{1/2}$  by  $c_1^{1/2} \xi$ , so that

$$\frac{K'}{K_1} = \frac{-1}{2c_1 \xi} \quad (4.23)$$

Rearranging terms in (4.19), we get

$$\xi = \frac{-(dh/dx - s)}{2c_1(dh/dx + s)} \quad (4.24)$$

and substituting this into (4.23), we obtain

$$\frac{K'}{K_1} = \frac{(dh/dx + s)}{(dh/dx - s)} \quad (4.25)$$

To show that (4.25) is equivalent to (2.28), we let  $dh/dx = \tan \alpha$  and  $s = \tan \mu$ , yielding (2.60) and hence

$$\frac{K'(\eta)}{K_1(\xi)} = \frac{\sin(\alpha + \mu)}{\sin(\alpha - \mu)}. \quad (4.26)$$

By virtue of (4.6), the vertical wavenumber amplification is also given by (4.26), whereas the horizontal wavenumber amplification is given by the negative of that. Equation (4.26) is thus consistent with specular reflection theory (2.28), as could be expected from the simple form of the boundary condition (4.18). This is an important result. It suggests that when the back-scattered wave either vanishes or is small

enough to be neglected compared to the incident and reflected waves, then internal wave reflection off a bottom of non-uniform slope does not differ significantly from reflection off a uniform slope, the rules for which are well known. The implications of this for ocean mixing are that, for a given frequency, large enhancements of vertical shear (2.40) and energy density (2.37) can still be expected above locally convex topography in the neighbourhood of points where  $dh/dx = s$ .

### 4.3.2 Locally concave topography

Using the same formalism as in Baines (1971b), Baines (1974, appendix 1) examined the problem of internal wave scattering off locally concave topography. For  $|\xi/R| \ll 1$ , the equation for the bottom can be approximated by (see figure 4.2)

$$\eta = c_1 \xi^2, \quad \text{where } c_1 = \frac{(1+s^2)^{3/2}}{8s^2 R}. \quad (4.27)$$

Substituting  $\xi = h(x) + sx$  and  $\eta = h(x) - sx$  into (4.27), and differentiating with respect to  $x$ , we can obtain a formula for the bottom slope  $dh/dx$  as a function of the characteristic coordinate  $\xi$  (cf. (4.19))

$$\frac{dh}{dx} = \frac{s(1+2c_1\xi)}{(1-2c_1\xi)}. \quad (4.28)$$

The topographic shape described by (4.27) is thus horizontal at  $\xi = -1/(2c_1)$ , and vertical at  $\xi = 1/(2c_1)$ . We still have  $dh/dx = s$  at  $\xi = 0$ , and  $dh/dx \rightarrow -s$  at  $\xi \rightarrow \pm\infty$ , as for figure 4.1. For an incident plane wave with stream function

$$\psi_i(\xi, t) = \epsilon \exp\{i(K_1\xi - \omega t)\}, \quad (-\infty < \xi < \infty) \quad (4.29)$$

as in (4.8), Baines' solution for the scattered wavefield may be expressed as the superposition of a back-reflected wave  $\psi_R$  and a  $\eta$ -dependent field of motion  $\psi_T$ , where

$$\psi_R(\xi, t) = \epsilon \exp\{-i(K_1\xi + \omega t)\} \quad (-\infty < \xi < \infty) \quad (4.30)$$

and

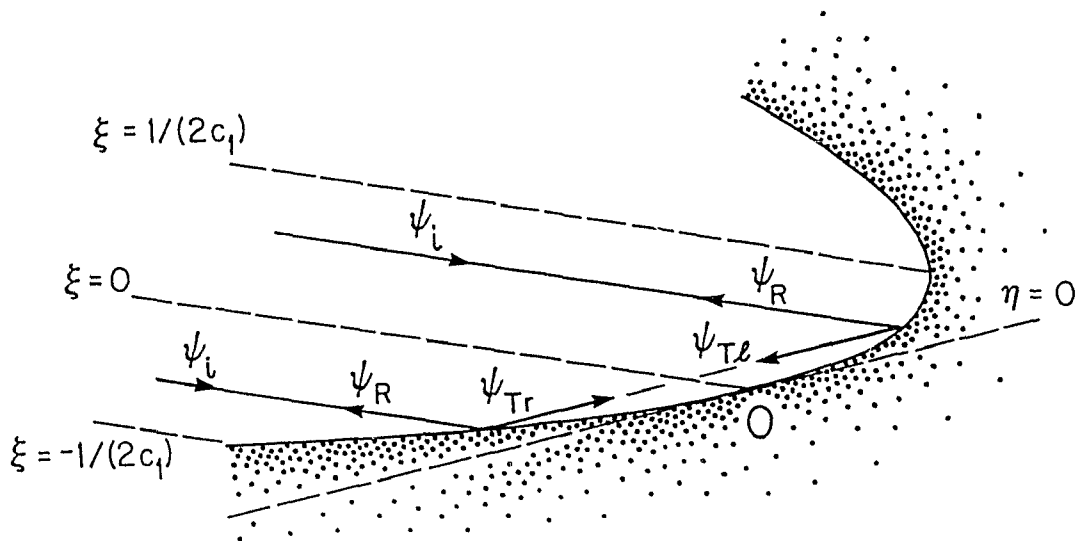


Figure 4.2: Same as figure 4.1, but for topography specified by (4.27). The back-reflected wave  $\psi_R$  has the same magnitude as the incident wave  $\psi_i$ , and we have a pure standing wave pattern. The bottom is vertical at  $\xi = 1/(2c_1)$ , and horizontal at  $\xi = -1/(2c_1)$ .

$$\psi_T(\eta, t) = -2\epsilon \cos \left\{ K_1 \left( \frac{\eta}{c_1} \right)^{1/2} \right\} \exp(-i\omega t). \quad (0 < \eta < \infty) \quad (4.31)$$

Perhaps the most striking feature of this solution is that the back-reflected wave  $\psi_R$  has exactly the same amplitude as the incident wave  $\psi_i$ , and since it travels in the opposite direction, a standing wave pattern results:

$$\psi_i(\xi, t) + \psi_R(\xi, t) = 2\epsilon \cos(K_1 \xi) \exp(-i\omega t). \quad (4.32)$$

The total stream function  $\psi = \psi_i + \psi_R + \psi_T$  is thus equal to zero at  $\xi = \pm(\eta/c_1)^{1/2}$ , as required by the no-normal flow boundary condition. Note that (4.31) also represents a standing wave pattern, with velocity amplitude

$$\left| \frac{\partial \psi_T}{\partial \eta} \right| = \frac{\epsilon K_1}{(c_1 \eta)^{1/2}} \sin \left\{ K_1 \left( \frac{\eta}{c_1} \right)^{1/2} \right\} \quad (4.33)$$

$$= \frac{\epsilon K_1}{(c_1 \eta)^{1/2}} \left\{ K_1 \left( \frac{\eta}{c_1} \right)^{1/2} - \frac{K_1^3}{3!} \left( \frac{\eta}{c_1} \right)^{3/2} + \dots \right\} \quad (4.34)$$

which, for  $K_1(\eta/c_1)^{1/2} \ll 1$ , reduces to (after correcting equation (A13) of Baines (1974) for a missing factor  $K_1^2$ )

$$\left| \frac{\partial \psi_T}{\partial \eta} \right| \approx \frac{\epsilon K_1^2}{c_1} = \epsilon K_1 \cdot \frac{8s^2(K_1 R)}{(1+s^2)^{3/2}} \quad (4.35)$$

where  $\epsilon K_1$  is the velocity amplitude of the incident wave. Interestingly enough, this velocity field is independent of the  $\eta$ -coordinate, and no singularity arises unless the radius of curvature  $R$  becomes infinite (the uniform slope case). It follows from (4.35) that, for  $0 < \eta \ll c_1/K_1^2$ , the time-averaged kinetic energy density above locally concave topography is given by

$$\frac{1}{4} \left| \frac{\partial \psi_T}{\partial \eta} \right|^2 \approx \frac{\epsilon^2 K_1^4}{4c_1^2}. \quad (4.36)$$

This can be compared with the time-averaged kinetic energy density above locally convex topography (4.14) which, for  $0 < \eta \ll c_1/4K_1^2$ , is approximately equal to  $\epsilon^2 K_1^2/16c_1\eta$  (same as (4.16)). Assuming that  $R$  and  $dh/dx$  (and therefore  $c_1$ ) are

the same at two mooring sites, the first one being locally concave and the second one convex, we find that very close to the bottom, i.e. for  $0 < \eta \ll c_1/4K_1^2 \approx (32s^2K_1^2R)^{-1}$ ,

$$\frac{(K.E.)_{\text{concave}}}{(K.E.)_{\text{convex}}} \approx \frac{(\epsilon^2 K_1^4 / 4c_1^2)}{(\epsilon^2 K_1^2 / 16c_1 \eta)} = \frac{4K_1^2 \eta}{c_1} \ll 1. \quad (4.37)$$

This suggests that close to the bottom, internal wave measurements made above locally concave topography are less likely to show energy enhancement at the critical frequency than those made above locally convex topography. To understand why locally concave sites should not tend to show energy enhancement near  $\omega_c$ , we first rewrite (4.31) as

$$\psi_T(\eta, t) = \psi_{Tr}(\eta, t) + \psi_{Tl}(\eta, t) \quad (4.38)$$

where

$$\psi_{Tr}(\eta, t) = -\epsilon \exp \left\{ -i \left[ K_1 \left( \frac{\eta}{c_1} \right)^{1/2} + \omega t \right] \right\} \quad (0 < \eta < \infty) \quad (4.39)$$

$$\psi_{Tl}(\eta, t) = -\epsilon \exp \left\{ i \left[ K_1 \left( \frac{\eta}{c_1} \right)^{1/2} - \omega t \right] \right\} \quad (0 < \eta < \infty) \quad (4.40)$$

$$(4.41)$$

The above expressions for  $\psi_{Tr}(\eta, t)$  and  $\psi_{Tl}(\eta, t)$  are of the same form as (4.11) and (4.12), which were themselves shown to be consistent with Phillips' law of reflection for a bottom of uniform slope. This suggests we can interpret Baines' (1974) solution for the scattered wavefield (4.30)–(4.31) in terms of a series of specular reflections off the concave bottom. The first stage of these reflections occurs when the incident wave  $\psi_i(\xi, t)$  impinges on  $\xi = -(\eta/c_1)^{1/2}$  to generate  $\psi_{Tr}(\eta, t)$ , and on  $\xi = (\eta/c_1)^{1/2}$  to generate  $\psi_{Tl}(\eta, t)$ . The second stage of reflections occurs when  $\psi_{Tr}(\eta, t)$  impinges on  $\xi = (\eta/c_1)^{1/2}$ , and  $\psi_{Tl}(\eta, t)$  impinges on  $\xi = -(\eta/c_1)^{1/2}$  to generate  $\psi_R(\xi, t)$ . The situation is drawn schematically on figure 4.2.

Now if we let  $K'(\eta)$  denote the local (WKB) value of the reflected wavenumber after the first reflection, we could proceed as we did for convex topography and show that the wavenumber amplification  $K'/K_1$  is again given by (4.25). This result is not

surprising in itself. What is interesting though is that, for the second reflection, the wavenumber amplification  $K''/K'$  is equal to  $-(K'/K_1)^{-1}$  for topography specified exactly by (4.27), due to the assumed symmetry of the reflecting surface with respect to  $\xi$ . This yields  $K'' = -K_1$ , and provides us with a simple explanation for the form of the back-reflected wave  $\psi_R(\xi, t)$  given in (4.30).

The absence of a singularity in the velocity field near  $\eta = 0$  is due to the fact that the wave reflected at  $\xi = 0^+$  has a phase shift of  $\pi$  with respect to the wave reflected at  $\xi = 0^-$ , so that they interfere destructively. More generally, the wave  $\psi_{Tl}$  reflected at  $\xi = (\eta/c_1)^{1/2}$  has a phase shift of  $\pi + 2K_1(\eta/c_1)^{1/2}$  with respect to the wave  $\psi_{Tr}$  reflected at  $\xi = -(\eta/c_1)^{1/2}$ . We would expect them to interfere constructively when

$$\pi + 2K_1 \left( \frac{\eta}{c_1} \right)^{1/2} = 2n\pi \quad n = 1, 2, 3, \dots \quad (4.42)$$

$$\text{i.e. when} \quad K_1 \left( \frac{\eta}{c_1} \right)^{1/2} = (2n - 1) \frac{\pi}{2} \quad n = 1, 2, 3, \dots \quad (4.43)$$

When this condition is satisfied, we find that the velocity amplitude (4.33) for the total  $\eta$ -field of motion becomes twice that associated with  $\psi_{Tl}$  or  $\psi_{Tr}$  alone (see 4.15), as is indeed expected for constructive interference. This lends further support to the assertion that Baines' solution for the scattered wavefield (4.30)–(4.31) may be interpreted in terms of specular reflection theory.

I now summarize the key results of this section. For locally convex topography specified exactly by (4.7), the back-scattered wave is identically zero (4.9). There is a singularity in energy density at  $\eta = 0$ , and the strength of this singularity is proportional to the local radius of curvature  $R$  of the topography. For  $\eta$ -characteristics which come directly in contact with the bottom (i.e. for  $\eta < 0$ ), Baines' (1971b) solution for the scattered wavefield (4.11)–(4.12) is consistent in a *WKB* sense with the reflection law of Phillips (1977). For  $\eta > 0$ , there exists an evanescent field of oscillatory motions (4.10) whose origin cannot be explained by purely specular reflection, but there is no energy flux associated with it.

For locally concave topography specified exactly by (4.27), the back-reflected wave has the same amplitude as the incident wave, and the resulting field of motion is that of a standing wave. It is possible to interpret this solution in terms of a

series of specular reflections off the concave bottom. Close to the origin (where  $dh/dx \approx s$ ),  $\psi_{Tl}$  and  $\psi_{Tr}$  interfere destructively, and no singularity occurs. Locally concave topography is thus less likely to show energy enhancement near  $\omega_c$  than locally convex topography.

## 4.4 Generalisation of the concavity criterion to the case where $N = N(z)$

For the sake of simplicity, Baines (1971b, 1974 appendix 1) assumed  $N = \text{constant}$  in his theory. In this section, I examine how vertical variations of the buoyancy frequency  $N$  may affect the effective concavity of a given bathymetric profile.

### 4.4.1 A simple criterion: $\partial\omega_c/\partial z > 0$

Let us consider a bathymetric profile (figure 4.3) such that the bottom slope at the origin O equals the wave ray slope for a given frequency  $\omega = \omega_{cO}$ . By analogy with figure 4.2, we shall classify as effectively concave any site for which wave rays at that particular frequency are reflected toward shallower water at A, and toward deeper water at B. In such a case, the critical frequency is less than  $\omega_{cO}$  at A, but is greater than  $\omega_{cO}$  at B ( $\omega_{cA} < \omega_{cO} < \omega_{cB}$ ). Taking  $z$  as positive upwards, concavity thus implies  $\partial\omega_c/\partial z > 0$ . To find out when this simple concavity criterion is satisfied, we note that the square of the critical frequency  $\omega_c$  is given by

$$\omega_c^2 = N^2 \sin^2 \alpha + f^2 \cos^2 \alpha \quad (4.44)$$

where  $N$  is the buoyancy frequency,  $f$  is the inertial frequency, and  $\tan \alpha$  is the local bottom slope. Differentiating both sides with respect to  $z$ , and noting that  $\partial f/\partial z = 0$ , we obtain

$$\omega_c \frac{\partial \omega_c}{\partial z} = N \frac{\partial N}{\partial z} \sin^2 \alpha + N^2 \sin \alpha \cos \alpha \frac{\partial \alpha}{\partial z} - f^2 \cos \alpha \sin \alpha \frac{\partial \alpha}{\partial z}, \quad (4.45)$$

$$= N \frac{\partial N}{\partial z} \sin^2 \alpha + (N^2 - f^2) \sin \alpha \cos \alpha \frac{\partial \alpha}{\partial z}, \quad (4.46)$$

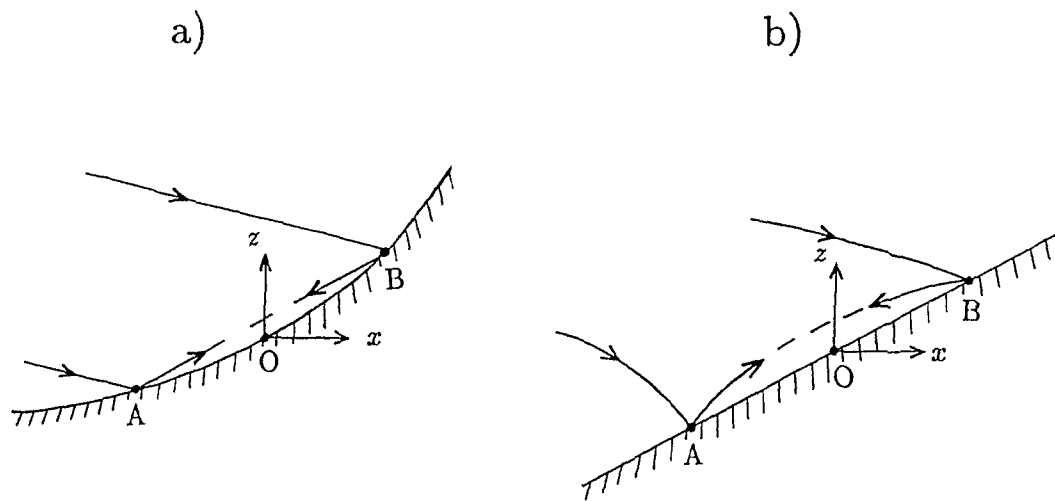


Figure 4.3: Two examples of locally concave topography: a)  $N$  is constant and the bottom slope decreases with depth, b) the bottom slope is constant and  $N$  decreases with depth. Wave rays are drawn for the frequency which is critical at the origin  $O$ .

so that

$$\frac{\partial \omega_c}{\partial z} = \left( \frac{\sin^2 \alpha}{\omega_c} \right) \left[ N \frac{\partial N}{\partial z} + \frac{(N^2 - f^2)}{\tan \alpha} \frac{\partial \alpha}{\partial z} \right]. \quad (4.47)$$

Thus  $\partial \omega_c / \partial z > 0$  requires

$$N \frac{\partial N}{\partial z} + \frac{(N^2 - f^2)}{\tan \alpha} \frac{\partial \alpha}{\partial z} > 0, \quad (4.48)$$

which for  $\partial N / \partial z = 0$  is satisfied when  $\partial \alpha / \partial z > 0$ , and for  $\partial \alpha / \partial z = 0$  is satisfied when  $\partial N / \partial z > 0$ , corresponding to the two special cases drawn on figure 4.3. For the common oceanic situation where  $N^2 \gg f^2$ , (4.48) simply becomes

$$\frac{\partial N}{\partial z} + \frac{N}{\tan \alpha} \frac{\partial \alpha}{\partial z} > 0. \quad (4.49)$$

This can be further simplified to

$$\frac{\partial}{\partial z}(\alpha N) > 0 \quad \text{for } \tan \alpha \ll 1. \quad (4.50)$$

#### 4.4.2 WKB-stretching: $\partial^2 h' / \partial x^2 > 0$

The slope of internal wave rays is given by

$$\tan \mu = \left( \frac{\omega^2 - f^2}{N^2 - \omega^2} \right)^{1/2}, \quad (4.51)$$

so that wave rays become straight lines in an ocean where  $N$  varies with depth if we use the transformation

$$\delta h' = \left( \frac{N^2 - \omega^2}{N_o^2 - \omega^2} \right)^{1/2} \delta h, \quad (4.52)$$

where  $N_o$  is some arbitrary constant. Thus

$$\lim_{\delta x \rightarrow 0} \frac{\delta h'}{\delta x} = \frac{\partial h'}{\partial x} = \left( \frac{N^2 - \omega^2}{N_o^2 - \omega^2} \right)^{1/2} \frac{\partial h}{\partial x} \quad (4.53)$$

$$= \left( \frac{N^2 - \omega^2}{N_o^2 - \omega^2} \right)^{1/2} \tan \alpha. \quad (4.54)$$

Since the slope of internal wave rays does not change with depth in this WKB-stretched frame of reference, we would have a situation conceptually equivalent to the constant  $N$ , constant bottom slope of Phillips (1977, p.227) when  $\partial^2 h' / \partial x^2 = 0$ . Thus for concavity, we simply require that  $\partial^2 h' / \partial x^2 > 0$ , i.e.

$$\frac{\partial}{\partial x} \left( \frac{\partial h'}{\partial x} \right) = \frac{\partial}{\partial x} \left[ (N^2 - \omega^2)^{1/2} \tan \alpha \right] > 0. \quad (4.55)$$

Evaluating this derivative along the boundary  $z = h(x)$ , where  $\delta z = \tan \alpha \delta x$ , this becomes

$$\tan \alpha \frac{\partial}{\partial z} \left[ (N^2 - \omega^2)^{1/2} \tan \alpha \right] > 0, \quad (4.56)$$

or simply

$$\frac{\partial}{\partial z} \left[ (N^2 - \omega^2)^{1/2} \tan \alpha \right] > 0, \quad (4.57)$$

$$(N^2 - \omega^2)^{-1/2} N \frac{\partial N}{\partial z} \tan \alpha + (N^2 - \omega^2)^{1/2} \frac{\partial}{\partial z} (\tan \alpha) \frac{\partial \alpha}{\partial z} > 0. \quad (4.58)$$

Multiplying this by  $(N^2 - \omega^2)^{1/2} / \tan \alpha$ , we get

$$N \frac{\partial N}{\partial z} + \frac{(N^2 - \omega^2)}{\tan \alpha} \frac{1}{\cos^2 \alpha} \frac{\partial \alpha}{\partial z} > 0. \quad (4.59)$$

The effective boundary concavity is thus frequency dependent. For the particular case where  $\omega = \omega_c$ , we have

$$\cos^2 \alpha = \cos^2 \mu = \frac{N^2 - \omega^2}{N^2 - f^2}, \quad (4.60)$$

and (4.59) reduces to (4.48), as it should.

### 4.4.3 Application to a model ocean.

Throughout most of the ocean,  $N$  generally decreases with depth ( $\partial N / \partial z > 0$ ), and (4.48) tells us that a bottom of constant slope is then effectively concave. Let us quantify this statement by evaluating (4.48) for the particularly simple profile of  $N(z)$  proposed by Garrett and Munk (1972) for the Pacific Ocean:

$$N(z) = 0 \quad \text{for } -200m < z < 0 \quad (4.61)$$

$$= N_o \exp\left(\frac{z+200}{1300}\right) \quad \text{for } z \leq -200m \quad (4.62)$$

where  $N_o=3$  cph. Replacing (4.62) into (4.48), we get

$$NN_o \frac{\partial}{\partial z} \left[ \exp\left(\frac{z+200}{1300}\right) \right] + \frac{(N^2 - f^2)}{\tan \alpha} \frac{\partial \alpha}{\partial z} > 0, \quad (4.63)$$

$$\frac{N^2}{1300} + \frac{(N^2 - f^2)}{\tan \alpha} \frac{\partial \alpha}{\partial z} > 0, \quad (4.64)$$

which for  $N^2 \gg f^2$  reduces to

$$\frac{1300}{\tan \alpha} \frac{\partial \alpha}{\partial z} > -1. \quad (4.65)$$

Thus when  $\partial\alpha/\partial z > -\tan\alpha/1300m$ , the topography can be considered locally concave. Conversely, the topography will be considered convex when  $\partial\alpha/\partial z < -\tan\alpha/1300m$ . Taking  $\tan\alpha = 0.10$  for example, the topography would be effectively convex only when  $\partial\alpha/\partial z < -7.7 \times 10^{-5}m^{-1}$ , which requires the slope to decrease by 0.01 for  $\delta z \sim 130m$ . For  $\tan\alpha = 0.01$ , convexity would only require the bottom slope to decrease by 0.001 for  $\delta z \sim 130m$ .

#### 4.4.4 Application to the case of the Bermuda slope.

Wunsch (1972a) recomputed the power spectrum from the thermistor data of Haurwitz, Stommel and Munk (1959), and found evidence of energy enhancement near  $\omega_c$  at  $\sim 500m$  depth near Bermuda. At that depth,  $\partial N/\partial z < 0$  in the North Atlantic mid-ocean gyre, but since  $\partial\alpha/\partial z > 0$ , we may ask whether the local increase of  $N$  with depth can make up for this and render the WKB-stretched topography convex. Rough estimates for the various parameters of (4.48), using the information available in HSM (1959) and Wunsch (1972a,b), are

$$\frac{\partial N}{\partial z} \approx \frac{2.5cph - 1.7cph}{-730m + 500m} \approx -3.5 \times 10^{-3}cph \ m^{-1}$$

$$N \approx 1.7cph, \quad f = 4.46 \times 10^{-2}cph, \quad \tan \alpha \approx 0.25,$$

$$\frac{\partial \alpha}{\partial z} \approx \frac{0.10 - 0.25}{-900m + 500m} \approx 3.75 \times 10^{-4}m^{-1},$$

and we get

$$N \frac{\partial N}{\partial z} + \frac{(N^2 - f^2)}{\tan \alpha} \frac{\partial \alpha}{\partial z} \approx -1.6 \times 10^{-3}cph \ m^{-1},$$

which suggests effectively convex topography, according to (4.48). Therefore the observed energy enhancement near  $\omega_c$  may not be inconsistent with the concave versus convex hypothesis at that Bermuda site.

#### 4.4.5 Other observational support

Thorpe (1987a) made detailed near-bottom measurements of currents and temperature on the continental slope southwest of Ireland, in a range of depths where  $\partial N/\partial z > 0$  and  $\partial \alpha/\partial z > 0$  so that the bottom is definitely concave (4.48), and found no statistically significant energy enhancement near  $\omega_c \approx f$  (see his figure 11).

Lai and Sanford (1986, p.664) remark that some 50km north of site D on the New England continental slope, current meter data from mooring 458 consistently show low energy densities at  $\omega_c \approx f$  compared to other moorings, possibly due to the more pronounced concavity of the bottom at that site.

Kunze and Sanford (1986) found enhanced energy densities at near-inertial frequencies near the top of Caryn seamount, in a depth range where the bottom slope is either constant or convex. They found less near-inertial energy at the concave sides of the seamount.

## 4.5 Energy back-scatter off rounded and sharp corners

The topographic shapes considered in section 4.3 are highly idealised, being perfectly symmetric with respect to  $\xi$ , and with bottom slope at infinity asymptotic to that of the  $\xi$ -characteristics. Baines (1971b) briefly examined the effect of relaxing those assumptions about the shape of the topography by studying the problem of a wave incident on topography specified by (see figure 4.4)

$$\eta = -c_1\xi^2 \quad (\xi_L < \xi < \xi_R) \quad (4.66)$$

$$\eta = -c_1\xi_R(2\xi - \xi_R) \quad (\xi > \xi_R) \quad (4.67)$$

$$\eta = -c_1\xi_L(2\xi - \xi_L) \quad (\xi < \xi_L) \quad (4.68)$$

where  $c_1 = (1+s^2)^{3/2}/8s^2R$  as before, and we have  $\xi_L < 0$ ,  $|\xi_L| < \xi_R$ . Such topography is locally convex near the origin, but becomes plane on either side of it, with bottom slope a continuous function of  $\xi$ . Baines investigated the nature of the solution for the scattered wavefield near the origin and at large distances from it. He pointed out that the singularities (e.g. (4.15)) associated with the reflected waves are still present, so that we may still expect large energy and shear enhancement near  $\omega_c$  for the topographic shape shown on figure 4.4. He also found that the back-scattered wave does not vanish near  $\xi = 0$ , and the velocity associated with it is finite and continuous there. However, while Baines pointed this out, he did not provide any estimate of the resulting back-scattered energy flux.

Sandstrom (1972) also investigated the problem of a wave incident on a bottom where two asymptotically plane sections come together in a rounded corner. His method of solution uses specular reflection theory as a first approximation for the scattered wavefield, and then gets rid of the wave components which violate the radiation condition through a series of iterations. Among other things, he found that the amplitude of the back-scattered wave is maximum for a sharp corner. Hence one could obtain an upper bound for the back-scattered energy flux from a rounded corner (e.g. figure 4.4) by letting  $R$  go to zero.

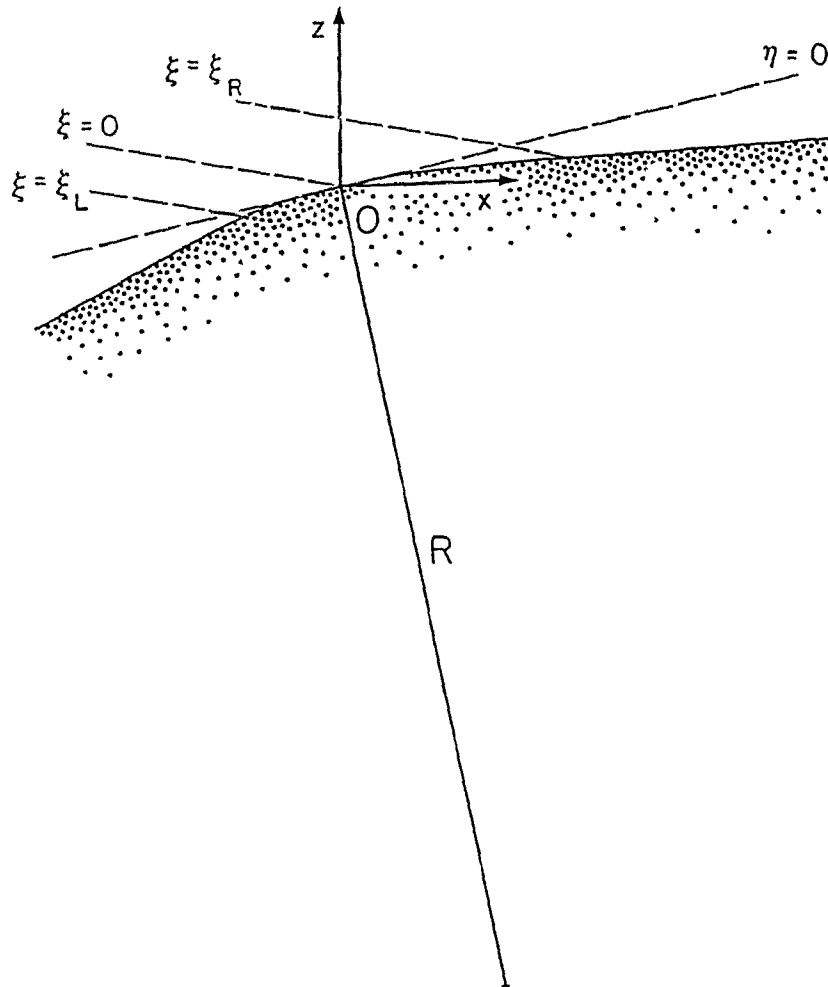


Figure 4.4: Topographic shape described by (4.66)–(4.68). The bottom slope for  $\xi > \xi_R$  ( $\xi < \xi_L$ ) is given by (4.19) evaluated at  $\xi = \xi_R$  ( $\xi = \xi_L$ ).

Gilbert and Garrett (1989, section 4) extended Hurley's (1970) theory to evaluate the total energy flux that is back-scattered from a sharp convex corner. They found it amounts to 1.5% of the energy flux incident over a single wavelength. On that basis alone, one may argue that the back-scattered energy flux is small enough to be neglected, especially as it represents an upper bound for the total energy flux that might be back-scattered from a rounded convex corner. But GG89 point out that if the back-scattered energy flux occurred mostly in the critical region where  $dh/dx \approx s$ , it would affect GG88's estimates of the dissipated energy flux by lowering them.

As a rough criterion, the results of Sandstrom (1972) suggest that internal wave reflection off an isolated, rounded corner, can be adequately described by specular reflection theory when  $R$  is comparable to or larger than the incident wavelength ( $KR \gtrsim 1$ ). We do not know whether this criterion would remain valid for more realistic topographic shapes, but if it did, the implications for ocean mixing would be important. For the typical oceanic internal wavefield (Munk, 1981), we would expect all incident waves to be specularly reflected when  $R$  is only on the order of a few  $km$ 's or more. An interesting question then is to ask how the reflected wavefield might vary with height above the bottom over a convex portion of the topography.

## 4.6 Kinematic effects of finite topography

Referring to figure 4.5, let us suppose the anchor weight of a mooring line is at  $A$ , where the bottom slope is  $\tan \alpha$ , and the local radius of curvature of the topography is equal to  $R$ . For the sake of simplicity, we assume  $R = \text{constant}$ , and allow a single azimuthal angle of incidence ( $\phi_i = 0$  for onshore propagation of energy, following Eriksen (1982)). Rays from all internal wave frequencies ( $f < \omega < N$ ) are allowed to be incident on the bottom however.

Suppose the mooring line has a sensor (e.g. current meter) at  $C$ , some height  $h$  above the bottom. Not all reflected rays will intersect the sensor, but one that does is drawn on figure 4.5. It is inclined at an angle  $\mu$  with respect to the horizontal which is determined by its frequency, and impinges on the bottom at  $B$ , where the local bottom slope is  $\tan \beta$ . Choosing the origin of a Cartesian coordinate system at the

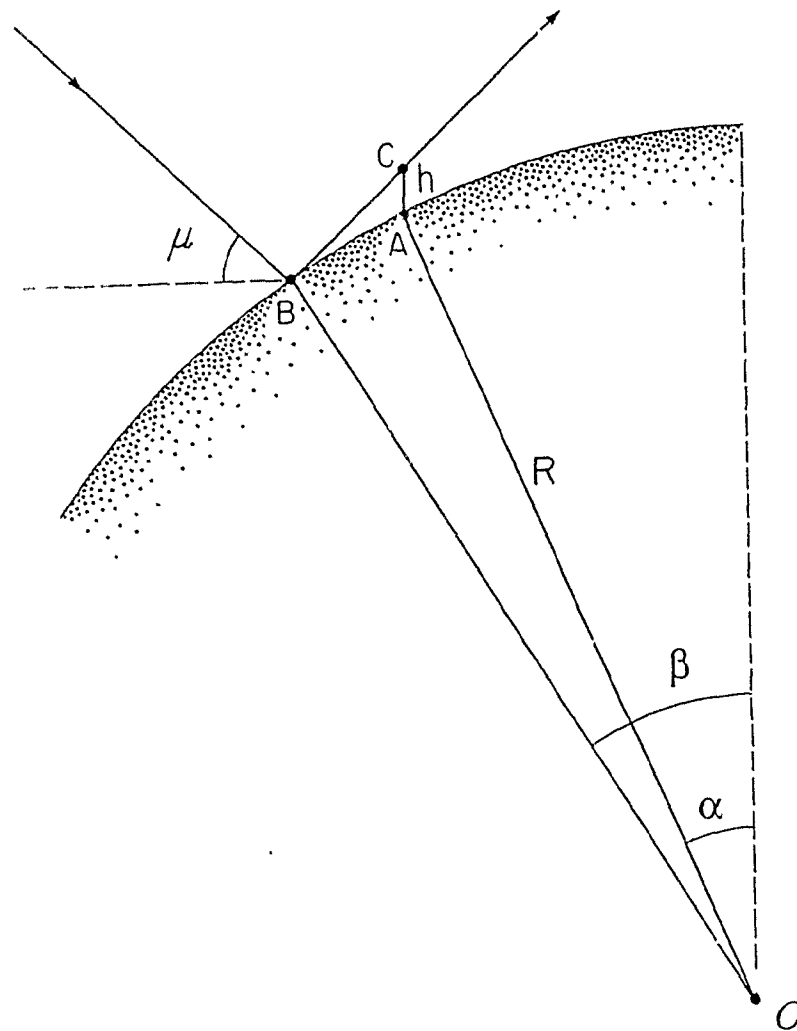


Figure 4.5: A mooring is deployed over locally convex topography. Its anchor weight lies at A, where the bottom slope is  $\tan \alpha$  and the radius of curvature is equal to  $R$ . A wave ray inclined at an angle  $\mu$  with respect to the horizontal impinges on the bottom at B, where the local slope is  $\tan \beta$ . The reflected wave ray intersects our mooring line at C, some height  $h$  above the bottom.

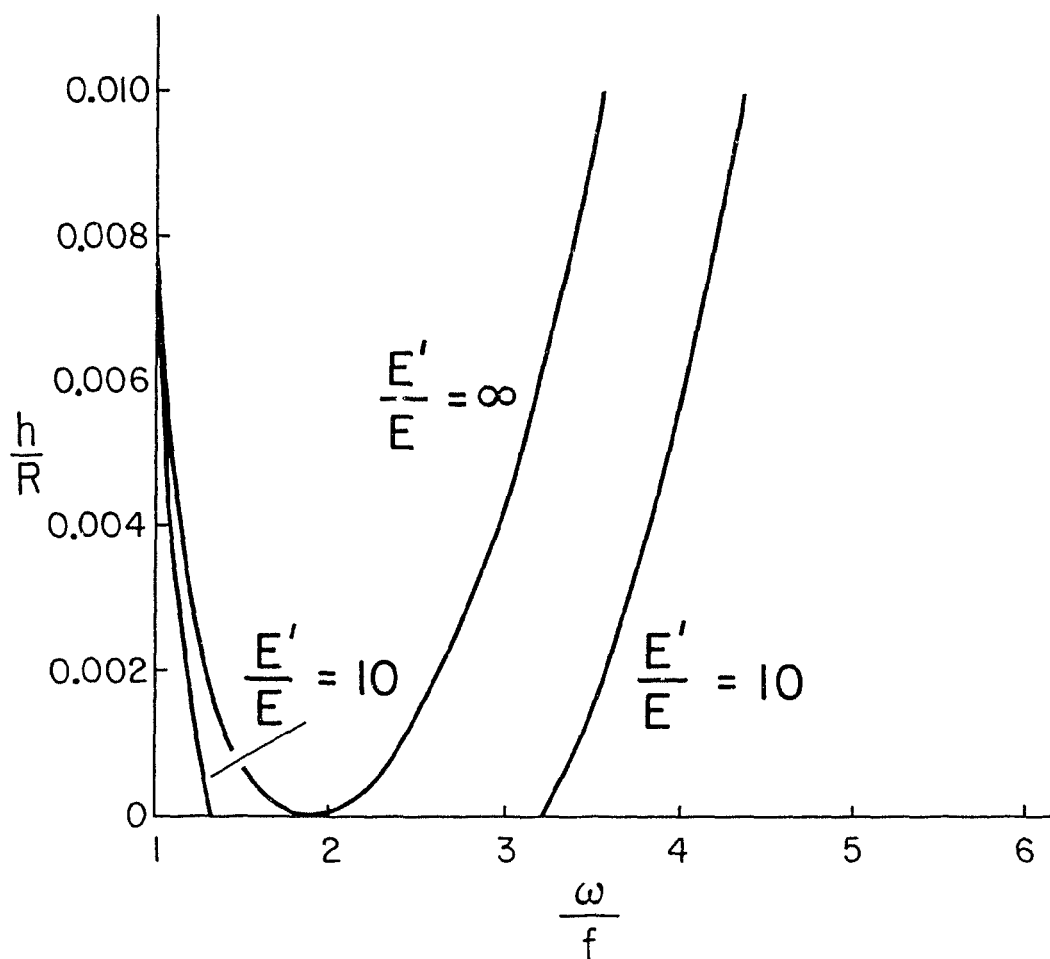


Figure 4.6: Variation of the reflected energy spectrum with height above the bottom for the idealised topography shown on figure 4.5, taking  $N/f = 13.1$  and  $\tan \alpha = 0.125$ . The energy density amplification  $E'/E$  is given by the square of the wavenumber amplification (2.37).

center of the circle of radius  $R$ , the coordinates of the points A, B, C are then given by

$$A = (-R \sin \alpha, R \cos \alpha),$$

$$B = (-R \sin \beta, R \cos \beta),$$

$$C = (-R \sin \alpha, R \cos \alpha + h).$$

We thus have

$$\frac{z_C - z_B}{x_C - x_B} = \tan \mu, \quad (4.69)$$

$$\frac{R \cos \alpha + h - R \cos \beta}{-R \sin \alpha + R \sin \beta} = \tan \mu, \quad (4.70)$$

$$\frac{\cos \alpha - \cos \beta + \frac{h}{R}}{\sin \beta - \sin \alpha} = \frac{\sin \mu}{\cos \mu}, \quad (4.71)$$

$$\cos \alpha \cos \mu - \cos \beta \cos \mu + \frac{h}{R} \cos \mu = \sin \beta \sin \mu - \sin \alpha \sin \mu, \quad (4.72)$$

$$\cos \alpha \cos \mu + \sin \alpha \sin \mu + \frac{h}{R} \cos \mu = \cos \beta \cos \mu + \sin \beta \sin \mu, \quad (4.73)$$

$$\cos(\alpha - \mu) + \frac{h}{R} \cos \mu = \cos(\beta - \mu), \quad (4.74)$$

and we finally obtain

$$\beta = \cos^{-1} \left\{ \cos(\alpha - \mu) + \frac{h}{R} \cos \mu \right\} + \mu. \quad (4.75)$$

For any specific instrument on a mooring line, the parameters  $\tan \alpha$  and  $h/R$  are constant, so that (4.75) essentially gives us  $\beta$  as a function of  $\mu$ . Critical reflection occurs when  $\beta = \mu = \mu_c$ , in which case (4.75) reduces to

$$\cos(\alpha - \mu_c) + \frac{h}{R} \cos \mu_c = 1 \quad (4.76)$$

Right on the bottom ( $h = 0$ ), this yields  $\mu_c = \alpha$ , as expected. However, at some height  $h$  above the bottom,  $\mu_c$  can take two values. The smaller one ( $\mu_c < \alpha$ ) results from critical reflection at a point shallower than  $A$ , whereas the larger one ( $\mu_c > \alpha$ ) results from critical reflection at a point deeper than  $A$ . Both values of  $\mu_c$  satisfy (4.76) and can be found by iteration for given values of  $\tan \alpha$  and  $h/R$ . The frequencies corresponding to these values of  $\mu$  are easily obtained from the dispersion relation, which we write here as

$$\frac{\omega}{f} = \left[ \frac{1 + (N/f)^2 \tan^2 \mu}{1 + \tan^2 \mu} \right]^{1/2} \quad (4.77)$$

The linear inviscid theory of Phillips (1977) predicts an infinite wavenumber amplification (4.26) for critical reflection ( $\mu = \beta$ ), and therefore an infinite energy density amplification  $E'/E$  (2.37). Figure 4.6 shows how the frequency of critically reflected waves varies with height above the bottom for the case where  $N/f = 13.1$  and  $\tan \alpha = 0.125$ . Using (4.75), we can also find two values of  $\mu$  (and hence  $\omega$ ) for which the wavenumber amplification (4.26) equals  $\sqrt{10}$ , so that the reflected energy density  $E'$  is 10 times greater than the incident energy density  $E$  (2.37). The frequency for which  $E'/E = 10$  varies with height above the bottom, and this is also shown on figure 4.6.

On linear inviscid grounds alone, figure 4.6 thus predicts a rapid evolution of the reflected energy spectrum with height above the bottom. Right on the bottom, there is a single singularity at  $\omega_c \sim 1.9f$ . But merely 50m above the bottom, taking  $R \approx 25km$  for example would yield  $h/R \approx 0.002$ , and figure 4.6 then predicts enhanced energy densities over a broad range of frequencies for  $\omega \geq 2.6f$ , and over a very narrow range of frequencies for  $\omega \approx 1.3f$ .

My main objective in presenting this model was simply to point out that current meters (or other sensors) placed at different heights above a non-uniformly sloping bottom do not feel the same topography. Therefore, in addition to non-linear and viscous effects, finite topographic effects could play a role in the rapid change with

height of internal wave spectra observed by Eriksen (1982) at a few mooring sites. To carefully determine the importance of finite topographic effects at a particular site, we would have to relax our assumption that  $R = \text{constant}$ . We would also have to consider the truly three-dimensional nature of the topography and the incident wavefield, which was ignored in this chapter. Since the Garrett–Munk internal wave spectrum is isotropic, that would imply allowing for waves to be incident at any angle with respect to the isobaths (i.e.  $\phi_i = -\pi, \pi$  instead of just  $\phi_i = 0$ ). It would also imply allowing for alongslope variations of the topography.

## 4.7 Summary

In this chapter, I have made the following points:

1. The formalism of Baines (1971a) for the scattering of internal waves off infinitesimal sinusoidal topography was used beyond its realm of applicability by Rubenstein (1988).
2. To my knowledge, the solutions of Baines (1971b, 1974) for the scattering of internal waves off idealised convex and concave topographic shapes are the only ones which deal explicitly with the critical case.
3. By defining a local wavenumber for the scattered wavefield, it is possible to show that Baines' solutions are consistent in a WKB sense with specular reflection theory.
4. Energy enhancement at the critical frequency  $\omega_c$  is less likely to be observed above concave than above convex topography.
5. A bottom of constant slope is effectively concave (convex) when the buoyancy frequency decreases (increases) with depth.
6. The work of Sandstrom (1972) suggests that for rounded corners, the back-scattered energy flux is negligible when  $KR \gtrsim 1$ .

7. Rapid spectral changes can be expected from purely geometric reasons above a non-uniformly sloping bottom, and need not result solely from non-linear and viscous processes.

## Chapter 5

# The Scotian Rise and Slope Internal Wavefield

### 5.1 Introduction

In this chapter, I analyse historical current meter data from the Scotian Rise and Slope to look for evidence of energy enhancement and/or cross-isobath alignment of motions at the critical frequency  $\omega_c$ .

The current meter data were collected for the purpose of studying low frequency (sub-inertial) motions on the Scotian Rise and Slope, not for the purpose of studying internal wave reflection off sloping bottoms. Consequently, the vertical spacing between current meters is large at most moorings; there is usually only one current meter in the first 100m above the bottom, which does not allow us to study the vertical structure of some of the small-scale processes known to occur above sloping topography (e.g. Thorpe, 1987a). Nevertheless, since all the moorings considered here did have a current meter within 100m of the bottom, it should be possible to look for evidence of near-bottom energy enhancement at  $\omega_c$  in a manner analogous to Eriksen (1982).

## 5.2 Description of the data base

### 5.2.1 Current meter data

The Bedford Institute of Oceanography deployed several moorings on the Scotian Rise and Slope during the 1970's and 1980's. Figure 5.1 shows the locations of the moorings used here. They come from two main sources, each of which is labeled with a different letter.

The most abundant source of data, labelled S, was collected in 1975–78 during the Shelf Break Experiment (Lively, 1979a,b). It was collected for the purpose of studying low-frequency motions on the Scotian Rise and Slope. Louis, Petrie and Smith (1982) used it to look at some of the properties of topographic Rossby waves on the Scotian Slope, and Smith and Petrie (1982) examined the low-frequency, cross-shelf eddy fluxes of heat and salt near the shelf break.

The second source of data, labelled R, was collected in 1980–81 during the Scotian Rise Experiment (also known as RISEX). The original aim of this experiment was to study the spatio-temporal structure of topographic Rossby waves on the Scotian Rise (Lively, 1984). The mean currents from the deepest current meter of each of the RISEX moorings were used by Hogg (1983) in his paper on the deep circulation of the western North Atlantic.

Tables 5.1 and 5.2 provide a convenient summary of the current meter data collected during those experiments. In table 5.1, the bottom depth and current meter depths are only nominal; small differences on the order of about 10–20m may have occurred from one mooring deployment to the next. Similarly, most of the deployment dates, recovery dates and lengths of deployment in table 5.2 are only approximate. The reader is referred to Lively (1979a,b, and 1984) for more detailed information about the rates of data return from the Shelf Break and Risex Experiments.

When referring to a specific mooring in the remainder of this chapter, I will often use a shorthand notation containing information about both the location and time at which that mooring was deployed. For example, if I write something about mooring S3E, it should be understood that my statement applies to mooring location S3 (table 5.1), mooring deployment period E (table 5.2).

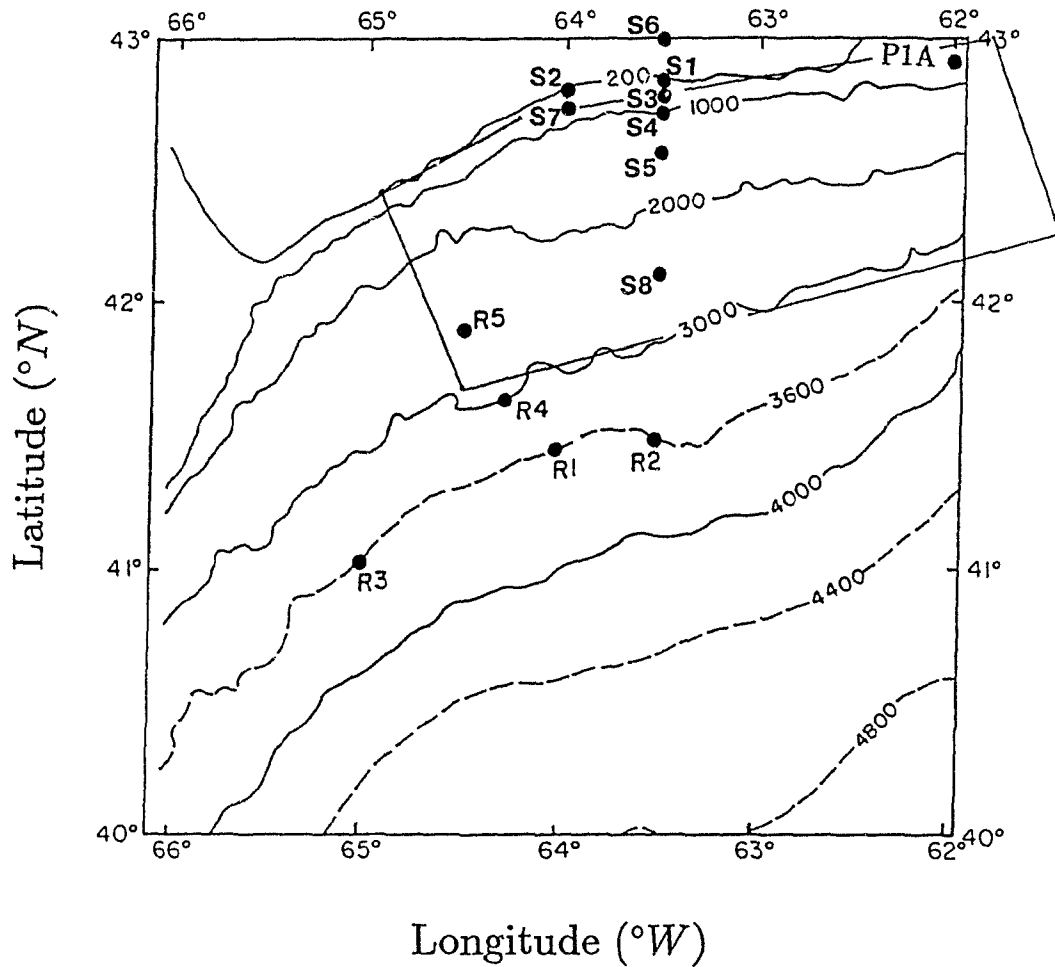


Figure 5.1: Map of the Scotian Rise and Slope showing the location of moorings used in this chapter. The letter S refers to moorings from the 1975–78 Shelf Break experiment, R refers to moorings from the 1980–81 Risex Experiment, and mooring P1A is Petrie’s (1975) mooring 1A. The hydrographic data used to plot figure 5.2 comes from subarea 33 of Drinkwater and Trites (1987), whose perimeter is shown here as a thin line.

Mooring	Latitude	Longitude	Bottom depth	Current meter depths
S1	42°48.6'N	63°30.0'W	250m	20,50,100,150,230m
S2	42°46.8'N	64°00.0'W	250m	20,50,230m
S3	42°45.0'N	63°30.0'W	710m	230,500,690m
S4	42°40.4'N	63°30.0'W	1010m	50,100,150,500,690,990m
S5	42°30.5'N	63°30.0'W	1550m	50,150,1530m
S6	43°00.5'N	63°30.0'W	170m	20,50,100,150m
S7	42°41.7'N	64°00.0'W	710m	230,690m
S8	42°01.0'N	63°30.0'W	2550m	70,1500,2530m
R1	41°20.0'N	63°58.0'W	3600m	200,500,1000,2900,3500m
R2	41°27.0'N	63°30.0'W	3600m	3500m
R3	41°00.0'N	65°00.8'W	3600m	3500m
R4	41°38.6'N	64°17.7'W	3000m	200,1000,2900m
R5	41°53.2'N	64°31.7'W	2500m	200,500,1000,2400m

Table 5.1: Mooring locations on the Scotian Rise and Slope. The letter S stands for the Shelf Break experiment, and R stands for the Risex experiment.

Mooring deployment period	Deployment date dd/mm/yy	Recovery date dd/mm/yy	Length of deployment (days)	Comments
A	13/12/75	06/04/76	115	Mooring S1 only
B	06/04/76	05/07/76	90	S1 and S4 only
C	05/07/76	17/10/76	104	
D	17/10/76	16/12/76	60	
E	16/12/76	02/04/77	107	
F	02/04/77	09/07/77	98	
G	09/07/77	04/01/78	179	Data from S1, S2,S4,S6 only
H	04/11/80	03/03/81	119	Poor data return, except for R5.
I	03/03/81	06/05/81	64	Poor data return
J	06/05/81	24/10/81	171	Good data return, except for R5.

Table 5.2: Mooring deployment periods on the Scotian Rise and Slope. Periods A to G are from the Shelf Break Experiment, and periods H to J are from the Risex Experiment.

### 5.2.2 Hydrographic data

Drinkwater and Trites (1987) collected historical Knudsen bottle data and CTD data from the Scotian Shelf and Slope region, and calculated monthly averages and standard deviations of temperature and salinity at discrete depths for 35 subareas. Figure 5.2 shows yearly-averaged profiles of temperature, salinity, and buoyancy frequency for subarea 33 of their report, which coincides with the area of interest here.

The monthly-averaged data of Drinkwater and Trites (1987, figure 5j) show that seasonality is mostly confined to the top 100m. However, even at larger depths, there are large standard deviations of temperature and salinity (but not necessarily density), part of the variability being attributable to the presence or absence of Gulf Stream eddies on the Scotian Slope. Figure 5.2 represents the best available spatio-temporal average of hydrographic properties on the Scotian Slope, and is plotted here for that reason, given the multitude of mooring locations and deployment periods considered in this chapter.

At greater depths, an average buoyancy frequency profile computed from 13 CTD casts on the Scotian Rise (Bob Lively, pers. comm.), shows that between 1000m and 3500m depth,  $\bar{N} \approx 0.6cph \pm 15\%$ .

### 5.2.3 Bathymetric data

Figure 5.3 shows bathymetric profiles at  $63^{\circ}30'W$  and  $64^{\circ}W$ , where all the Shelf Break Experiment current meter data was collected. The bathymetric data used to draw those profiles dates back to a 1962 survey by CHS Kapuskasing. The survey lines were oriented North-South, ended at about 2000m depth, and the horizontal spacing between consecutive lines was two nautical miles ( $3.7km$ ). Successive depth readings on a given survey line were taken approximately one kilometer apart.

Comparing this bathymetric data with a more recent echo sounder survey made near  $63^{\circ}30'W$ , during Batfish station 34 of Sandstrom and Elliott (1989), suggests the profiles are accurate near the shelf break. However, they become somewhat less reliable at depths larger than about 700m, where the 1962 depth readings were generally rounded to the nearest multiple of 10 fathoms.

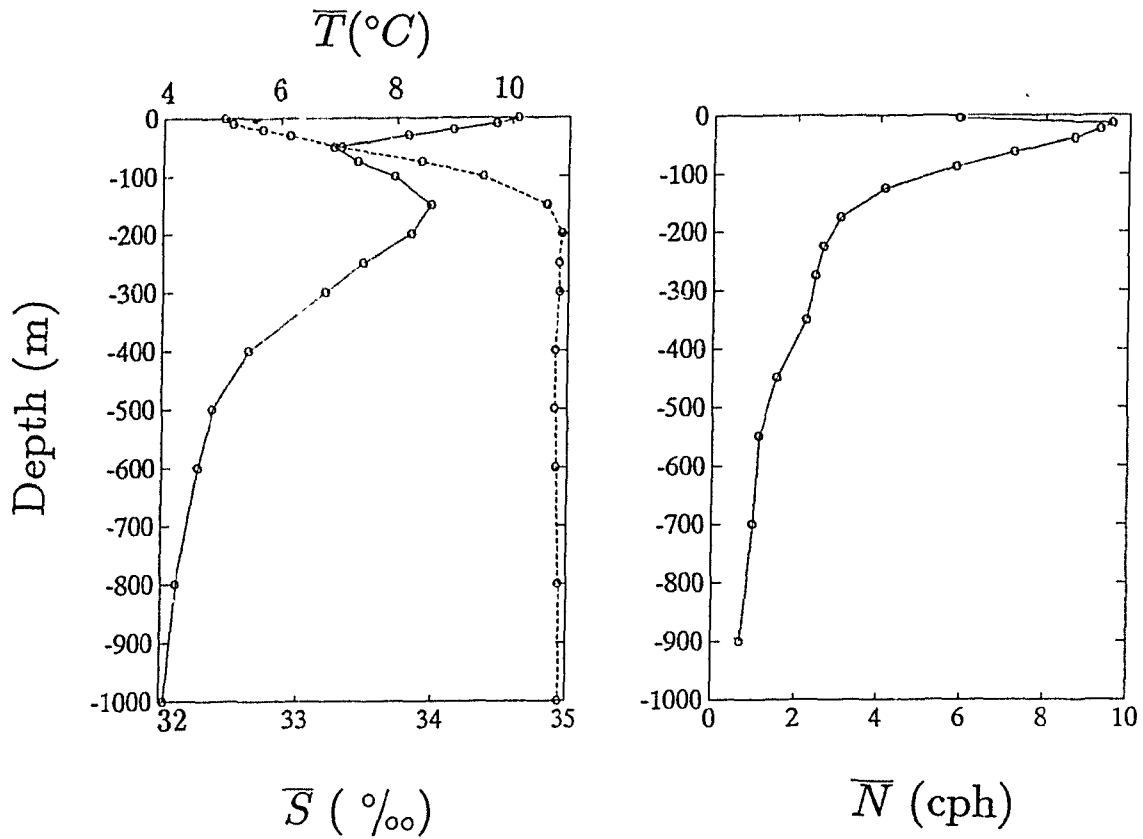


Figure 5.2: Yearly-averaged profiles of temperature (—) and salinity (- - -) on the Scotian Slope (left), and buoyancy frequency (right), based on data from subarea 33 of Drinkwater and Trites (1987) (shown on figure 5.1). The discrete depths at which  $\bar{T}$ ,  $\bar{S}$  and  $\bar{N}$  were evaluated are indicated by small circles.

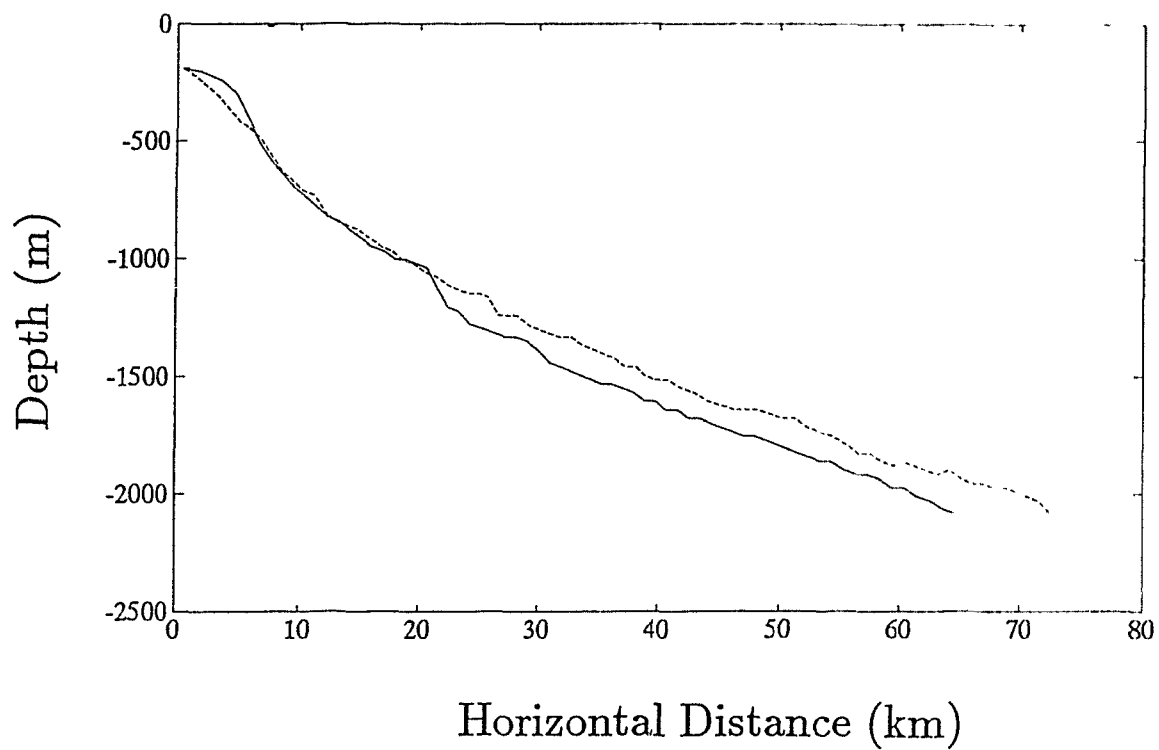


Figure 5.3: Bathymetric profiles at  $63^{\circ}30'W$  (—) and  $64^{\circ}W$  (- - -) on the Scotian Slope. Horizontal distance is measured from the 100 fathom contour at both longitudes.

## 5.3 Testing the critical reflection hypothesis

### 5.3.1 Estimation of $\omega_c$

To determine whether there is energy enhancement at the critical frequency, we must first estimate  $\omega_c$  itself, given by (2.29):

$$\omega_c^2 = N^2 \sin^2 \alpha + f^2 \cos^2 \alpha. \quad (5.1)$$

To that effect, Eriksen (1982) remarked that  $N$  and  $\tan \alpha$  are usually not easy to estimate to an accuracy better than roughly a factor of two. The possible implications of this are illustrated in figure 5.4, where my best guess for  $\omega_c$  at  $63^\circ 30' W$ , based on the data used to plot figures 5.2 and 5.3, is shown together with lower and upper bounds that allow for a  $\pm 33\%$  uncertainty in both  $N$  and  $\tan \alpha$ . My best guesses for  $\bar{N}$ ,  $\tan \alpha$ , and hence  $\omega_c$  at each of the moorings are given in table 5.3.

On the Scotian Rise and Slope, we may know the time-averaged buoyancy frequency  $\bar{N}(z)$  to within better than  $\pm 33\%$ , and we may also know the large-scale bottom slope (defined on a scale of a few km's) to within better than  $\pm 33\%$ . However, because  $N$  is time-dependent, and because the value of the bottom slope depends on the spatial scale over which we measure it, the uncertainties depicted on figure 5.4, although large, may not be unrealistic.

For the range of slopes encountered on the Scotian Slope,  $\cos \alpha \sim 1$ , so that  $\omega_c^2 \sim N^2 \sin^2 \alpha + f^2$ . Allowing for a  $\pm 33\%$  uncertainty in both  $N$  and  $\tan \alpha$  as in figure 5.4,  $\omega_c$  should then be found in a range of frequencies such that

$$\left(\frac{2}{3}\right)^4 N^2 \sin^2 \alpha + f^2 < \omega_c^2 < \left(\frac{4}{3}\right)^4 N^2 \sin^2 \alpha + f^2. \quad (5.2)$$

Figure 5.4 shows that the value of  $\omega_c$  is most sensitive to the values of  $N$  and  $\sin \alpha$  at depths less than about 1200m. However at greater depths, where  $N \sin \alpha \ll f$ , (5.2) yields  $\omega_c \approx f$  regardless of a possible  $\pm 33\%$  uncertainty in  $N$  and  $\sin \alpha$ .

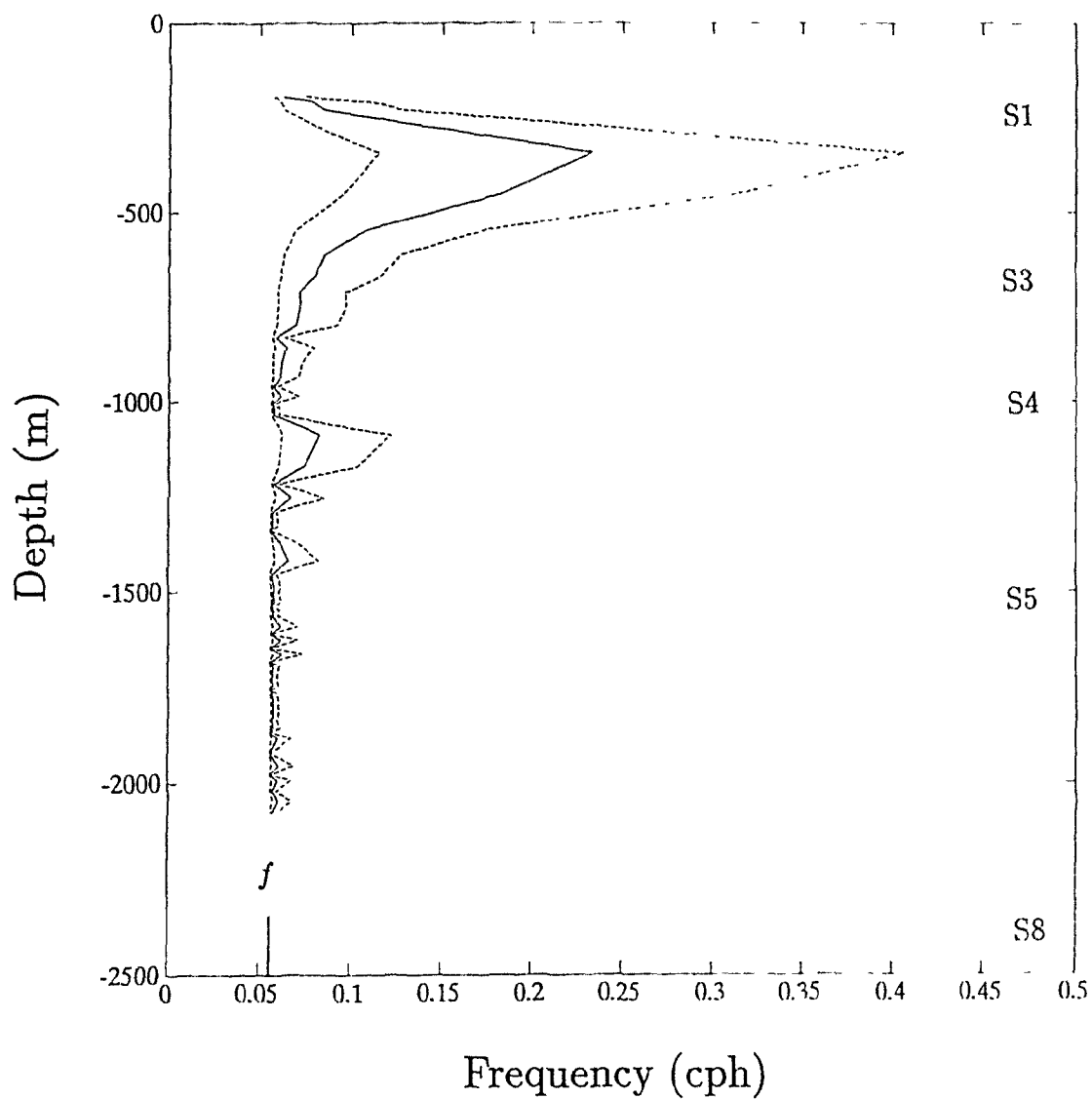


Figure 5.4: Critical frequency  $\omega_c$  at  $63^{\circ}30'W$ , allowing for a  $\pm 33\%$  uncertainty in both  $N$  and  $\tan \alpha$ . For this particular, arbitrary choice of the percentage of uncertainty, the upper bounds for  $N$  and  $\tan \alpha$  are twice as large as the lower bounds. The inertial frequency is  $f \sim 0.056 \text{ cph}$  over most of the Scotian Slope.

Mooring	Depth	Buoyancy frequency $\bar{N}(z)$	Bottom slope $\tan \alpha$	$\bar{N} \sin \alpha$	Critical frequency $\bar{\omega}_c =$ $(\bar{N}^2 \sin^2 \alpha + f^2 \cos^2 \alpha)^{1/2}$
S1	250m	2.6 cph	0.025	(0.065 cph)	$0.086cph = 1.52f$
S2	250m	2.6 cph	0.046	(0.120 cph)	$0.132cph = 2.33f$
S3	710m	1.0 cph	0.050	(0.050 cph)	$0.076cph = 1.34f$
S4	1010m	0.7 cph	0.030	0.021 cph	$0.0604cph = 1.07f$
S5	1550m	0.6 cph	0.020	0.012 cph	$0.0576cph = 1.02f$
S6	170m	3.0 cph	0.005	0.015 cph	$0.0587cph = 1.03f$
S7	710m	1.0 cph	0.050	(0.050 cph)	$0.076cph = 1.34f$
S8	2550m	0.6 cph	0.020	0.012 cph	$0.0571cph = 1.02f$
R1	3600m	0.6 cph	0.010	0.006 cph	$0.0553cph = 1.005f$
R2	3600m	0.6 cph	0.010	0.006 cph	$0.0555cph = 1.005f$
R3	3600m	0.6 cph	0.010	0.006 cph	$0.0550cph = 1.005f$
R4	3000m	0.6 cph	0.012	0.007 cph	$0.0559cph = 1.01f$
R5	2500m	0.6 cph	0.020	0.012 cph	$0.0569cph = 1.02f$

Table 5.3: Cutoff frequency  $\bar{N} \sin \alpha$  for internal edge waves, and critical frequency  $\bar{\omega}_c$  at various mooring sites on the Scotian Rise and Slope. The values of  $\bar{N} \sin \alpha$  such that  $\bar{N} \sin \alpha \gtrsim f$  are indicated in parentheses. See the text for a discussion of the uncertainties.

### 5.3.2 A list of criteria

In chapter 2 it was shown that the reflection of internal waves off a bottom of constant slope, in a constant- $N$  ocean, should lead to energy enhancement at the critical frequency  $\omega_c$  (2.37). However in chapter 4, it was argued that such energy enhancement was less likely to be observed above concave topography than above convex topography (4.37). For the data set at hand here, we can test those predictions about the presence or absence of energy enhancement at  $\omega_c$  by looking for

- 1a) a spectral peak above the background energy level at  $\omega_c$
- 1b) near-bottom energy enhancement at  $\omega_c$  for instruments at different heights above the bottom, but on the same mooring
- 1c) near-boundary energy enhancement at  $\omega_c$  for instruments at the same depth, but on different moorings
- 1d) a spectral level at  $\omega_c$  larger than that given by the GM79 model spectrum.

A second major prediction of internal wave reflection theory is that current ellipses should tend to orient themselves nearly perpendicular to the isobaths upon reflection (2.71). Hence we should also look for

- 2) a pronounced anisotropy at  $\omega_c$ , the major axis of current ellipses being oriented in the cross-isobath direction.

Criterion 1a was successfully used by Sandstrom (1966) and Eriksen (1982) at mooring sites where the critical frequency was well separated from the energetic tidal and inertial frequencies. Such a separation is necessary if we wish to unambiguously interpret a spectral peak above the 'background' energy level at  $\omega_c$  as the signature of internal wave reflection. Unfortunately,  $\omega_c$  is close to  $f$  or  $M_2$  at all the mooring sites considered here (except for S2, see table 5.3), so that criterion 1a is not going to be very useful.

Criterion 1b was also used successfully by Eriksen (1982) at a few moorings. It can be used at most of the moorings considered here, as the majority of them have two or

more current meters in the vertical. However, we should bear in mind this criterion fails to take into account the slantwise propagation of internal wave energy, as pointed out in section 4.6, and so may not be completely unambiguous. For example, current meters at different heights above the bottom on a given mooring may not measure the same near-inertial wave packets, due to the nearly horizontal energy propagation of these waves.

Criterion 1c was used by Thorpe (1987a, figure 11) at a site where the critical frequency was close to the inertial frequency ( $\omega_c \approx f$ ), a situation where this criterion should be most useful. It can be used in a few cases for the data set under consideration here. However, for mooring sites where  $\omega_c \approx M_2$ , I will not use criterion 1c when the fractional change of depth between two moorings is important, due to sizeable variations in the expected amplitude of the barotropic tide.

Although criterion 1d does not on its own constitute evidence of critical internal wave reflection, it could be used to support successful tests based on other criteria, especially when  $\omega_c > M_2$ , where there is some degree of universality in the spectral levels (Wunsch, 1976). However, Fu (1981) has shown that such universality does not exist near  $f$  in the deep ocean, so that criterion 1d is not useful at those moorings where  $\omega_c \sim f$ . It is not useful at those moorings where  $\omega_c \sim M_2$  either, since internal tides were excluded from the internal wave model of Garrett and Munk (1972). Application of criterion 1d will thus be limited to mooring S2 for the present data set.

Criterion 2 was successfully used by Eriksen (1982) for mooring sites on Muir Seamount and the New England continental slope, but it failed at mooring 636 of the Western Boundary Sill Experiment. At the deeper moorings where  $\omega_c \sim f$ , we do not *a priori* expect the quasi-circular near-inertial motions to have a well-defined orientation. Hence we expect criterion 2 should be most useful here in water shallower than about 1000m, where  $\omega_c$  becomes appreciably greater than  $f$  (table 5.3).

## 5.4 Results

Hundreds of autospectra were computed from the data set described in tables 5.1 and 5.2. In this section, my description of the results will be kept as succinct and factual as possible, postponing further discussion until the next section. The reader is referred to Appendix A for a description of the techniques of data analysis used.

In order to compare the kinetic energy spectra from instruments at different depths, I normalised them with respect to a common value of  $\overline{N}$ , taking into account the prediction that we should have

$$\text{Kinetic energy} \propto \overline{N} \tag{5.3}$$

according to WKB theory (Gill 1982, p.300). Briscoe (1975) has shown that normalising the kinetic energy spectra in this manner brings them within close agreement in the internal wave continuum ( $\omega > M_2$ ). It also reduces variability at the inertial frequency  $f$ , but not to the same extent as it does for  $\omega > M_2$ . Note that right at  $M_2$ , such WKB-scaling may reduce the variability in spectral levels when the baroclinic tide dominates the barotropic tide, but it increases the variability otherwise.

The values of  $\overline{N}(z)$  used for the WKB-normalisation are the climatological, yearly-averaged values shown on figure 5.2. While this may be justified for  $z \leq -150\text{m}$ , where the monthly-averaged data of Drinkwater and Trites (1987, figure 5j) show little seasonal variations, I did not attempt such WKB-scaling within the top 100m of the water column, thus precluding the use of criterion 1b at moorings S1, S2, and S6.

### 5.4.1 The Risex Experiment

The critical frequency is very close to the inertial frequency at all the Risex moorings (see table 5.3). Therefore, in order to look for evidence of critical internal wave reflection at those moorings, we rule out the use of criteria 1a, 1d and 2 (see section 5.3.2). That leaves us with criteria 1b and 1c, and so we shall look for near-boundary energy enhancement at  $\omega_c \sim f$  in the vertical and horizontal directions, however weak those criteria may be. Criterion 1b can be used at moorings R1J, R4J and

R5H, where we have several current meters in the vertical, and criterion 1c can be used to compare the 2900m spectra from moorings R1J and R4J.

For mooring R1J, figure 5.5 shows no clear evidence of near-bottom energy enhancement at  $\omega_c \sim f$ . The near-inertial peak at 3500m is about the same as at 200m, and is not significantly greater than at 1000m. It is significantly greater than the 2900m inertial peak however. Note that at moorings R2J and R3J, where we have a single current meter at 3500m depth, the spectra are very similar in both shape and level to the 3500m spectrum from mooring R1J.

For mooring R4J, the situation is somewhat different, in that figure 5.6 does show hints of near-boundary energy enhancement at  $\omega_c \sim f$ . The horizontal energy enhancement with respect to the 2900m spectrum at mooring R1J is significant at the 95% level, but the vertical energy enhancement is not.

At mooring R5H, the situation is different still (see figure 5.7). This time, the largest energy densities are observed at mid-depth instead of near the surface or bottom, but those differences are not significant. The overall conclusion we are thus led to draw so far from the Risex data set is that there is no clear evidence of near-bottom energy enhancement at  $\omega_c \sim f$  on the Scotian Rise.

#### 5.4.2 The Shelf Break Experiment

Since mooring S8 was approximately at the same depth as mooring R5, we should expect similar results at both moorings. Comparing the 2530m kinetic energy spectrum from mooring S8E with the 2400m spectrum from mooring R5H (figure 5.7), both of which are representative of winter conditions, I found that the two spectra were indeed very similar in shape and level. At mooring S8, criterion 1b could only be used for period F, when it was found that the near-inertial peak was stronger at 2530m than at 1500m, but not significantly so.

At mooring S5, there are signs of near-boundary energy enhancement at  $\omega_c \approx f$  for periods C, D, and F, when good data were obtained. The spectra from period F are shown on figure 5.8, where we see that the near-boundary energy enhancement is significant in the vertical, but not in the horizontal. For period C, the near-boundary

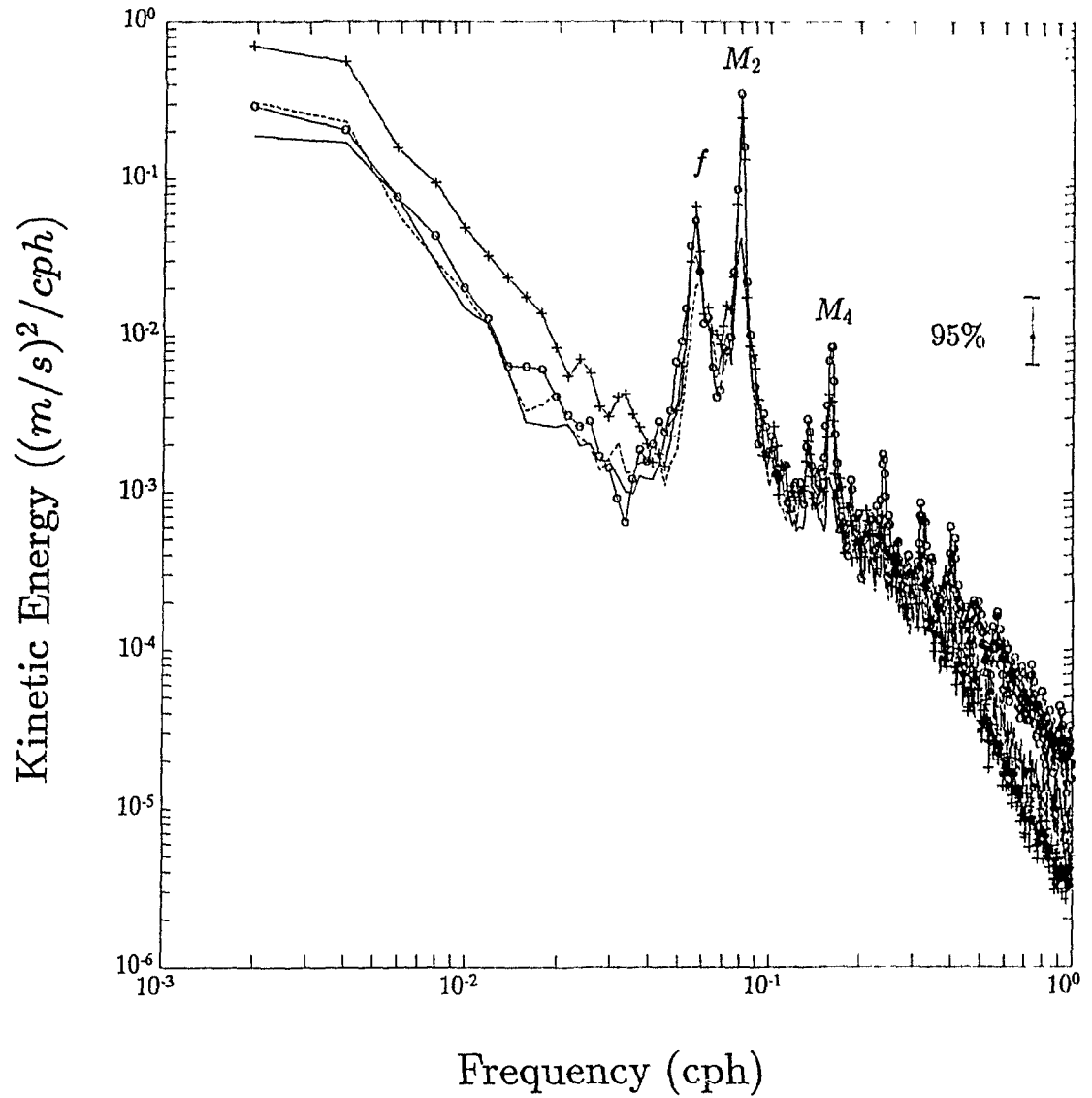


Figure 5.5: Kinetic energy spectra for mooring R1J (depth = 3600m): 200m (  $\circ$  ), 1000m (—), 2900m (- - -) and 3500m ( + ), with  $\nu = 28$ . The spectra are WKB-normalised with respect to  $N = 1\text{cph}$ .

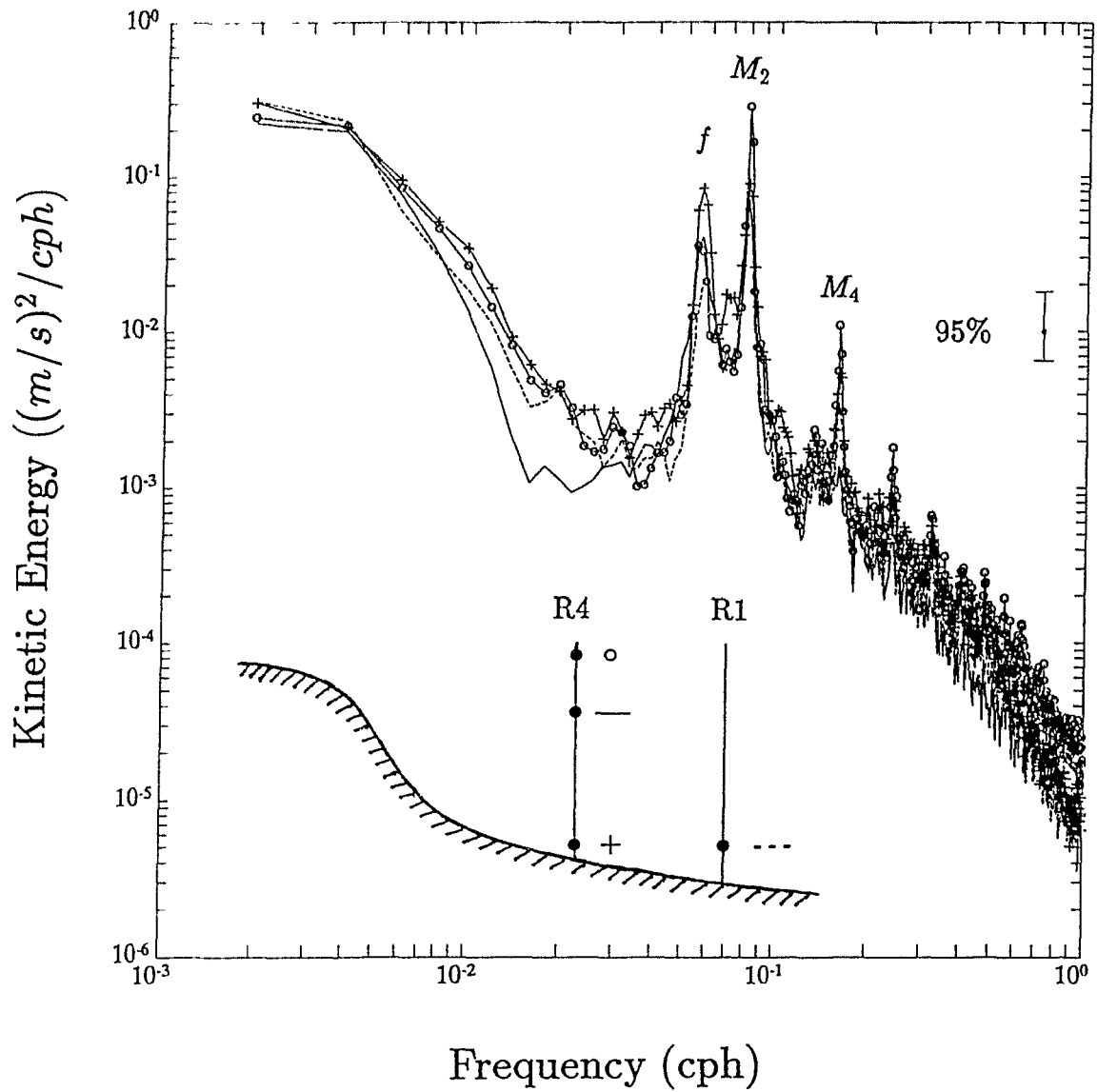


Figure 5.6: Kinetic energy spectra from 200m ( o ), 1000m (—) and 2900m ( + ) at mooring R4J (depth = 3000m), and from 2900m ( - - - ) at mooring R1J (depth = 3600m), with  $\nu = 28$ . The spectra are WKB-normalised with respect to  $N = 1cph$ .

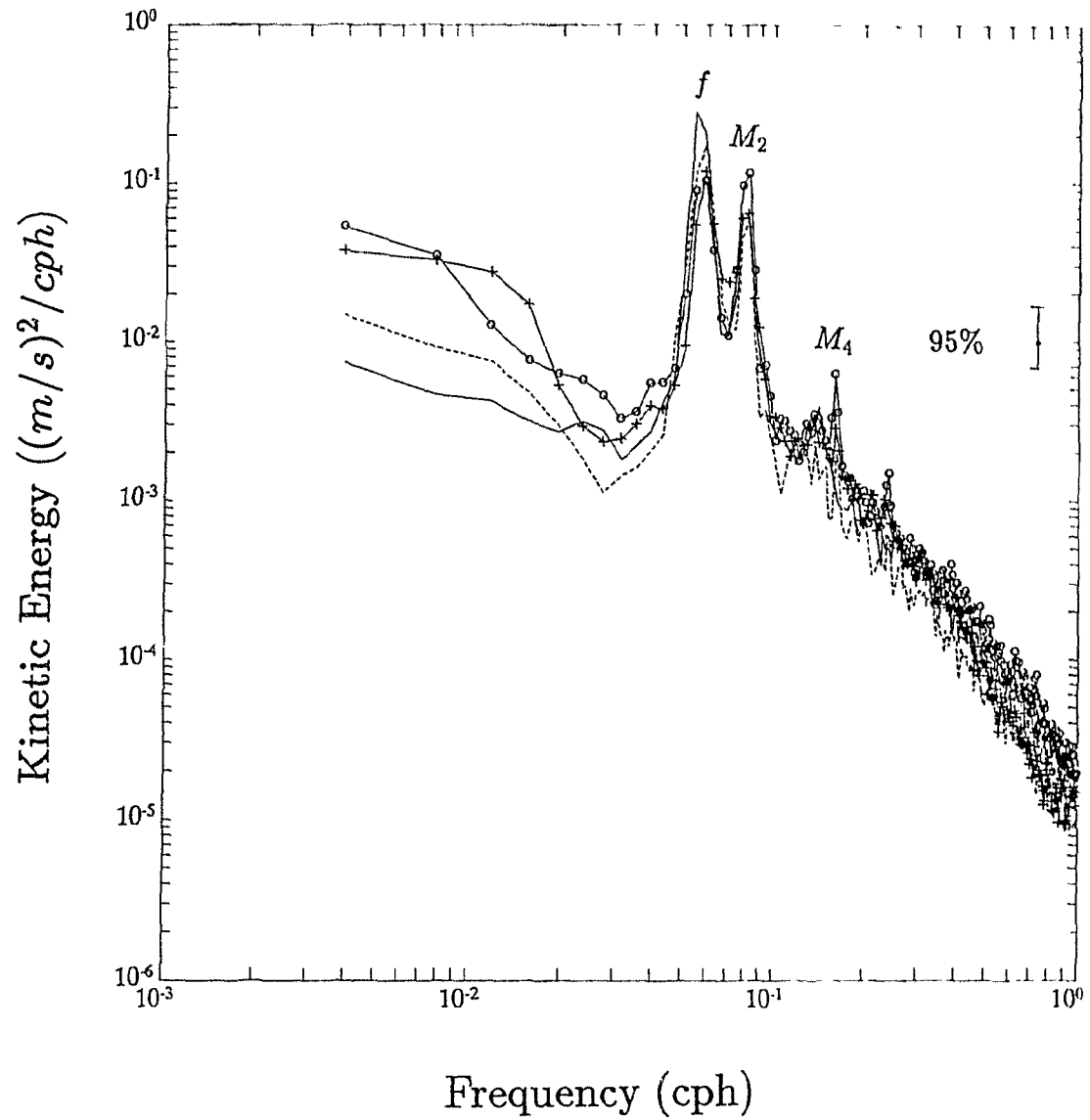


Figure 5.7: Kinetic energy spectra for mooring R5H (depth  $\approx 2500\text{m}$ ): 200m (  $\circ$  ), 500m (—), 1000m (- - -) and 2400m ( + ), with  $\nu = 40$ . The spectra are WKB-normalised with respect to  $N = 1\text{cph}$ .

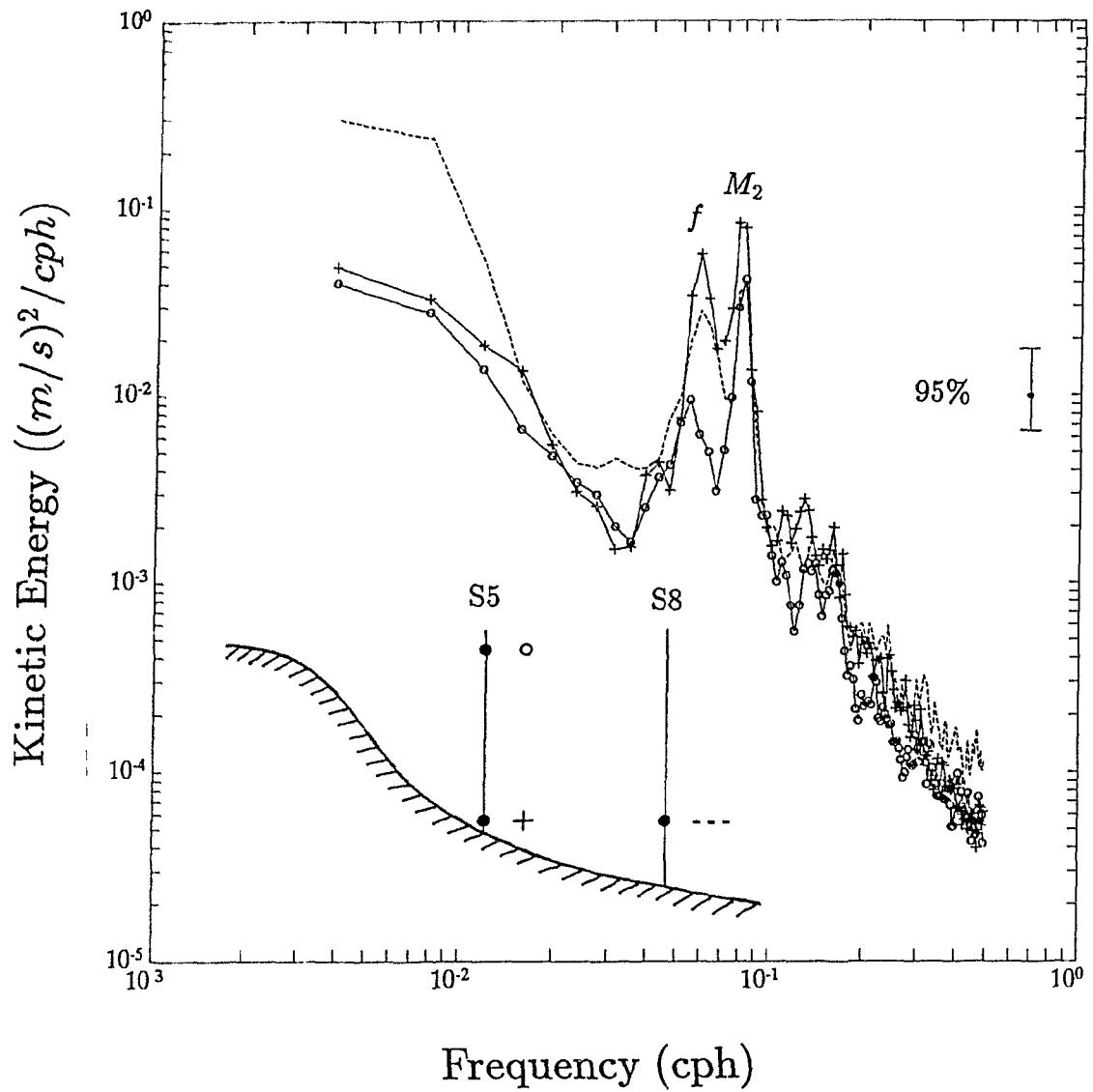


Figure 5.8: Kinetic energy spectra from 150m (o) and 1530m (+) at mooring S5F (depth = 1550m), and from 1500m (- - -) at mooring S8F (depth = 2550m), with  $\nu = 32$ . The spectra are WKB-normalised with respect to  $N = 1cph$ .

energy enhancement is significant in both the vertical and the horizontal, whereas for period D, it is not significant in either direction.

It is not entirely clear whether it is more relevant to use criterion 1b or 1c in order to look for energy enhancement at the critical frequency, but on figure 5.6, we see that near-boundary energy enhancement at  $\omega_c \approx f$  is more pronounced in the horizontal than in the vertical, whereas on figure 5.8, the reverse is true. At the very least, this suggests that there is no systematic bias between the use of either one of these two criteria.

At mooring S4, I also found signs of near-boundary energy enhancement at  $\omega_c \approx f$  for periods C, E and F, when good data were obtained. Figure 5.9 shows the spectra from period E, where we see that the near-inertial peak is significantly higher near the bottom than at other depths. Interestingly enough, the inertial peak is also broader near the bottom. The near-bottom energy enhancement at  $\omega_c \approx f$  is also significant for period C, but not for period F.

Note that figure 5.3 suggests the presence of a bump on an otherwise rather smooth profile at about 1000m depth at  $63^{\circ}30'W$ , raising the possibility that mooring S4 sat on a bump. A close look at the echo sounder data from Batfish station 34 of Sandstrom and Elliot (1989) confirms the presence of that bump. It is about 2.5 km wide and extends from about 980m to 1100m depth. The bottom slope ranges from 0 to 0.10 on that bump, possibly explaining the breadth of the near-inertial peak on figure 5.9 ( $\omega_c \approx 1.07f$  according to table 5.3).

Continuing our progression toward the shelf break, we find that at moorings S3 and S7, there is usually some evidence of near-bottom energy enhancement throughout most of the internal waveband. A good example of this is shown on figure 5.10 for mooring S3E. A comparison with the 690m spectrum from mooring S4E (figure 5.9) shows a similar near-boundary energy enhancement in the horizontal direction. For mooring S3F, near-bottom energy enhancement was only observed for  $\omega > M_2$ , with the largest enhancement at  $M_4$ .

Figure 5.11 shows that 20m above the bottom at mooring S3E, current ellipses are oriented normal to isobaths over a very broad range of frequencies, so that criterion 2 is apparently satisfied. By contrast, figure 5.12 shows that 480m above the bottom,

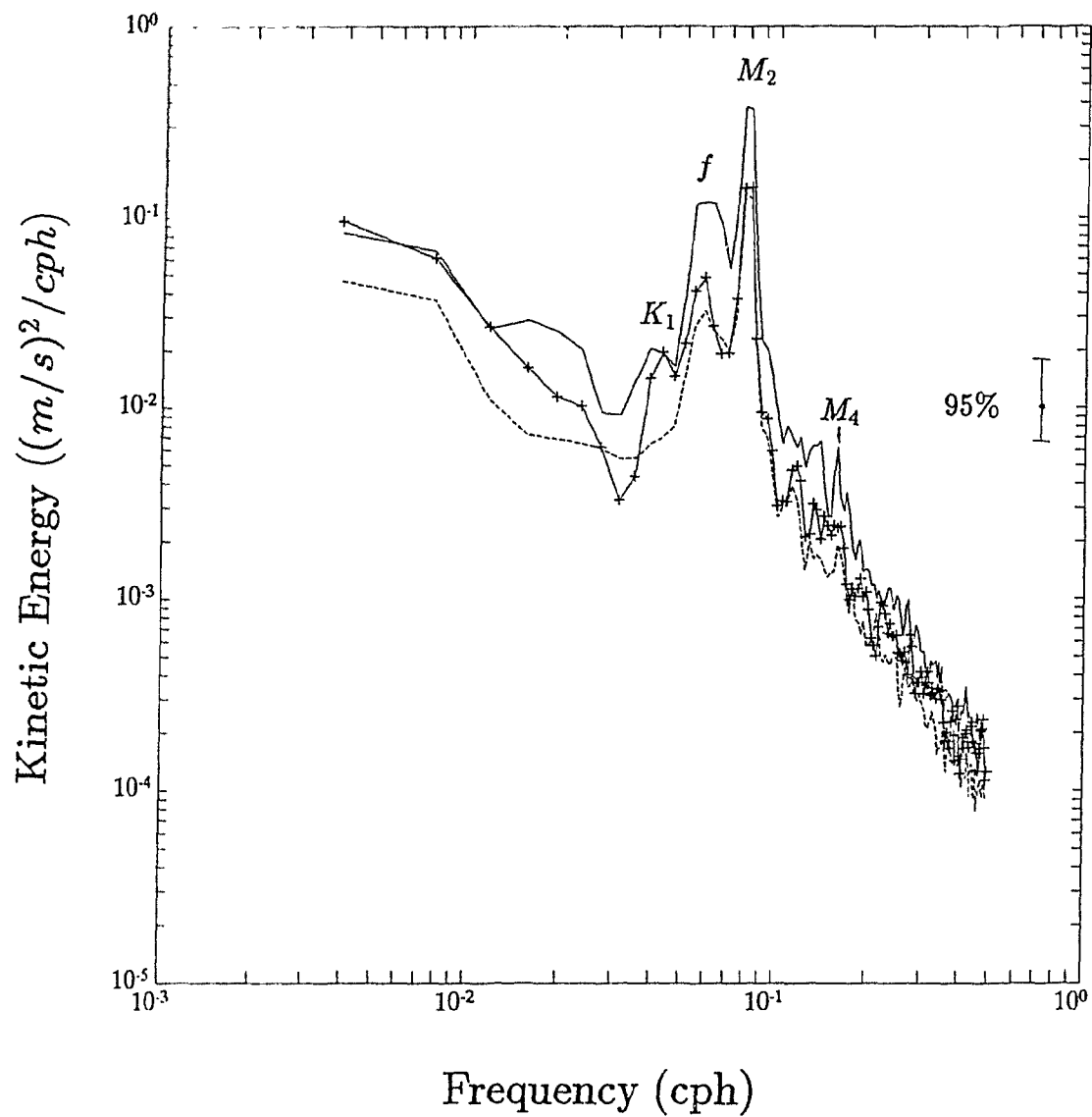


Figure 5.9: Kinetic energy spectra at 150m (+), 690m (- -) and 990m (—) for mooring S4E (depth = 1010m), with  $\nu = 35$ . The spectra were normalised with respect to  $N = 1cph$ .

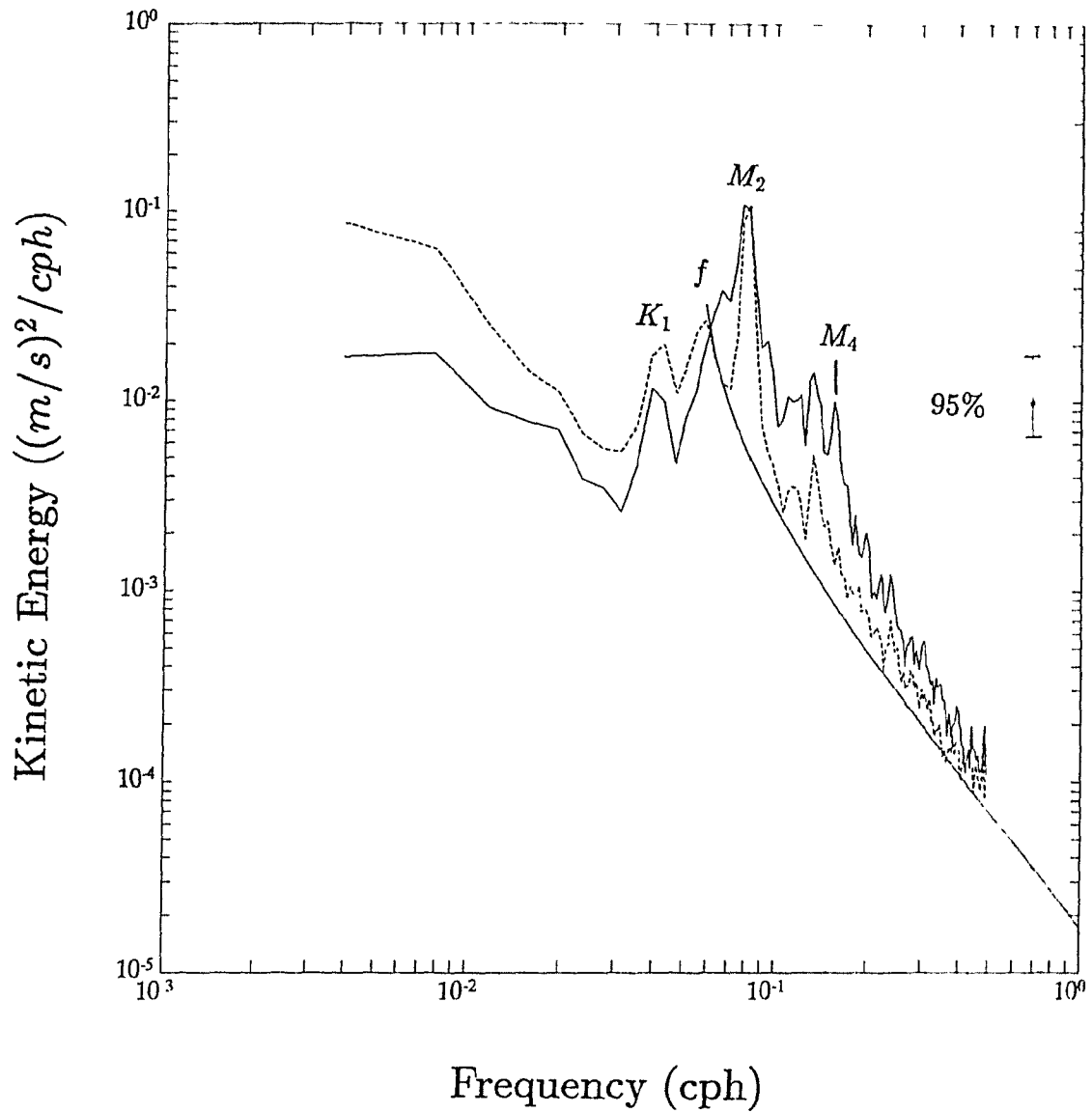


Figure 5.10: Kinetic energy spectra from 230m (- - -) and 690m (—) at mooring S3E (depth =710m), with  $\nu = 36$ . The spectra are WKB-normalised with respect to  $N = 1\text{cph}$ , and are compared with the GM79 model spectrum.

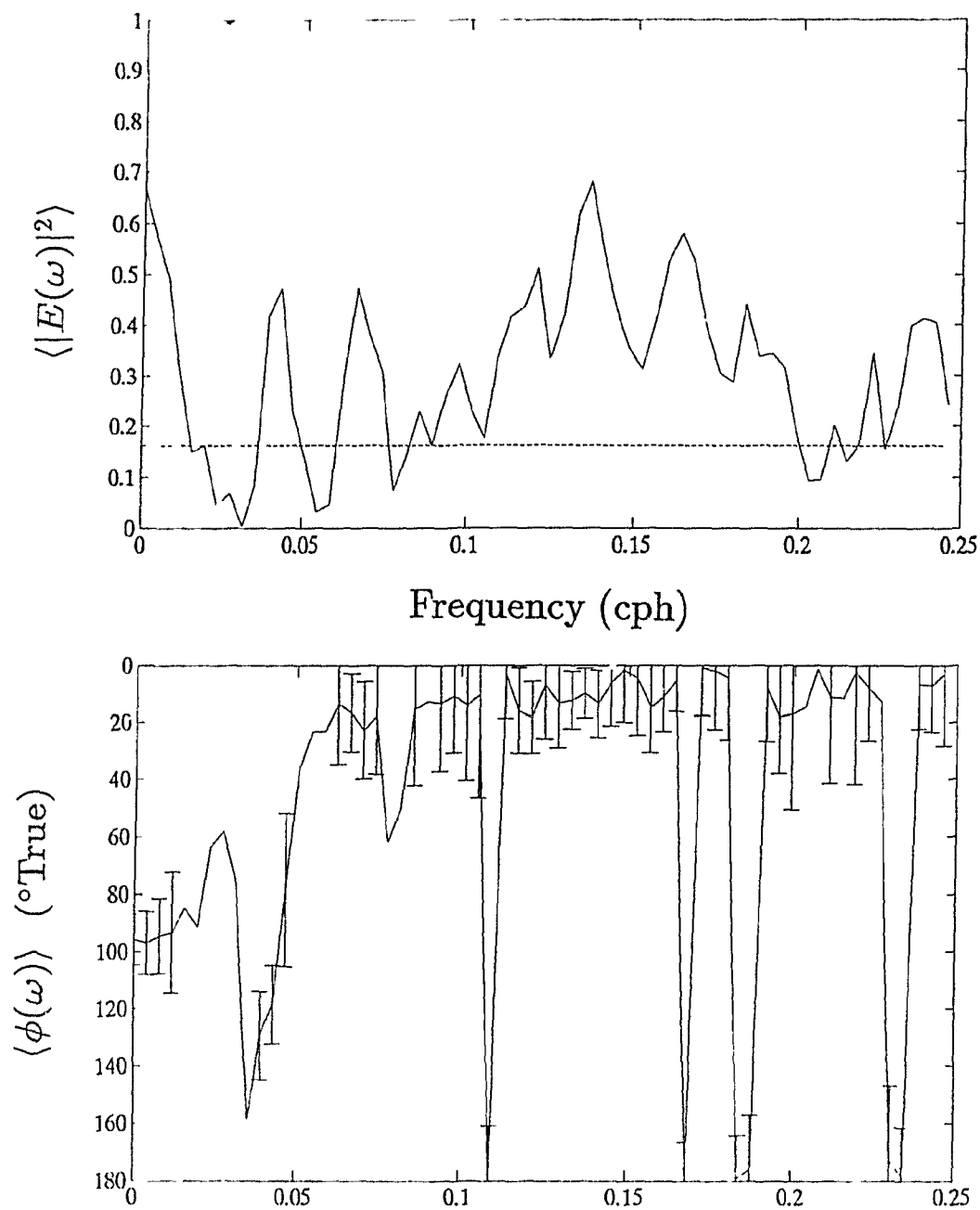


Figure 5.11: Current ellipse orientation and stability 20m above the bottom at mooring S3E. The dashed line on the upper plot represents the 95% significance level for zero true coherence between clockwise and anticlockwise velocities. The 95% confidence intervals for ellipse orientation are shown on the lower plot ( $\nu = 36$ ).

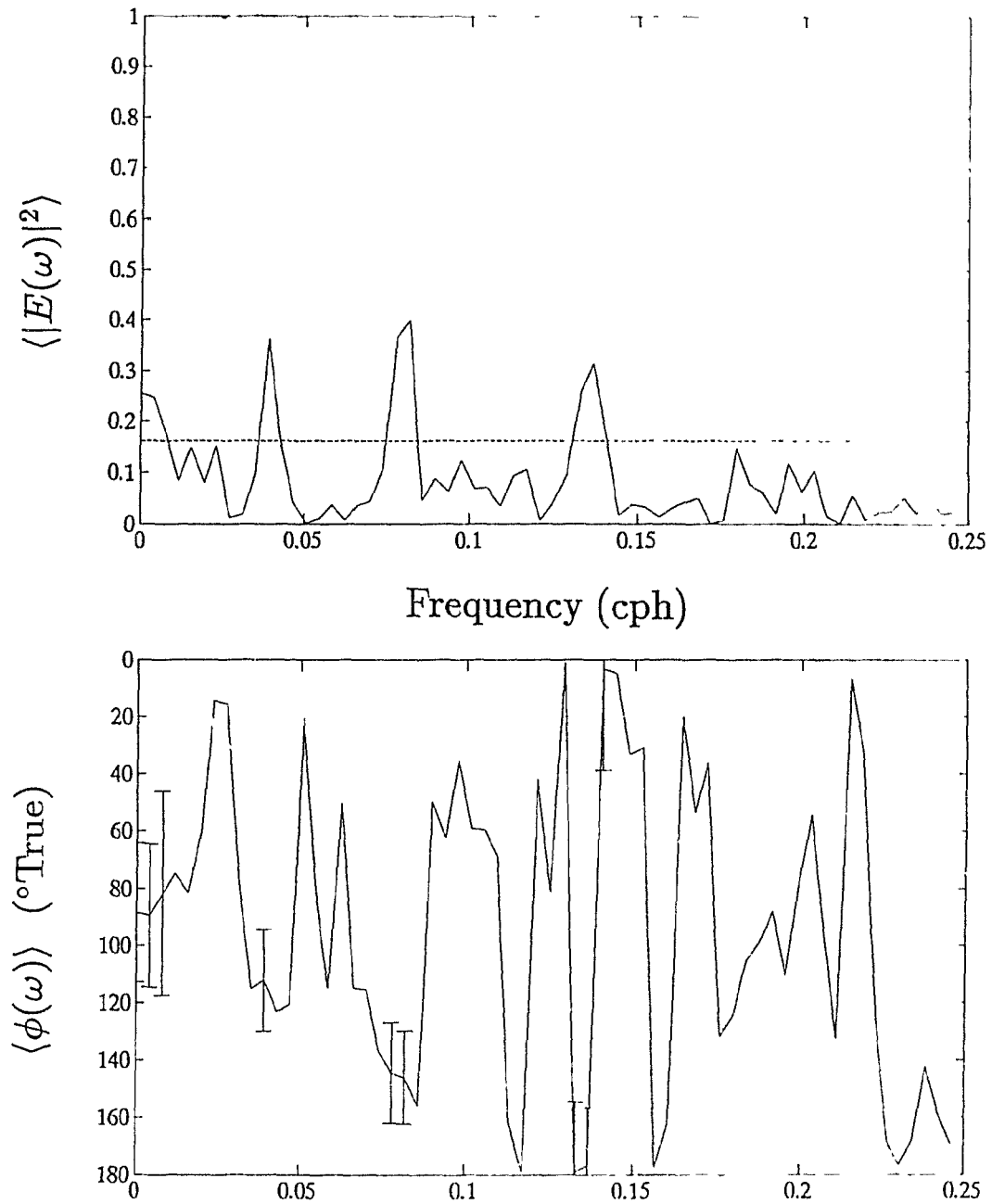


Figure 5.12: Current ellipse orientation and stability 480m above the bottom at mooring S3E. The dashed line on the upper plot represents the 95% significance level for zero true coherence between clockwise and anticlockwise velocities. The 95% confidence intervals for ellipse orientation are shown on the lower plot ( $\nu = 36$ ).

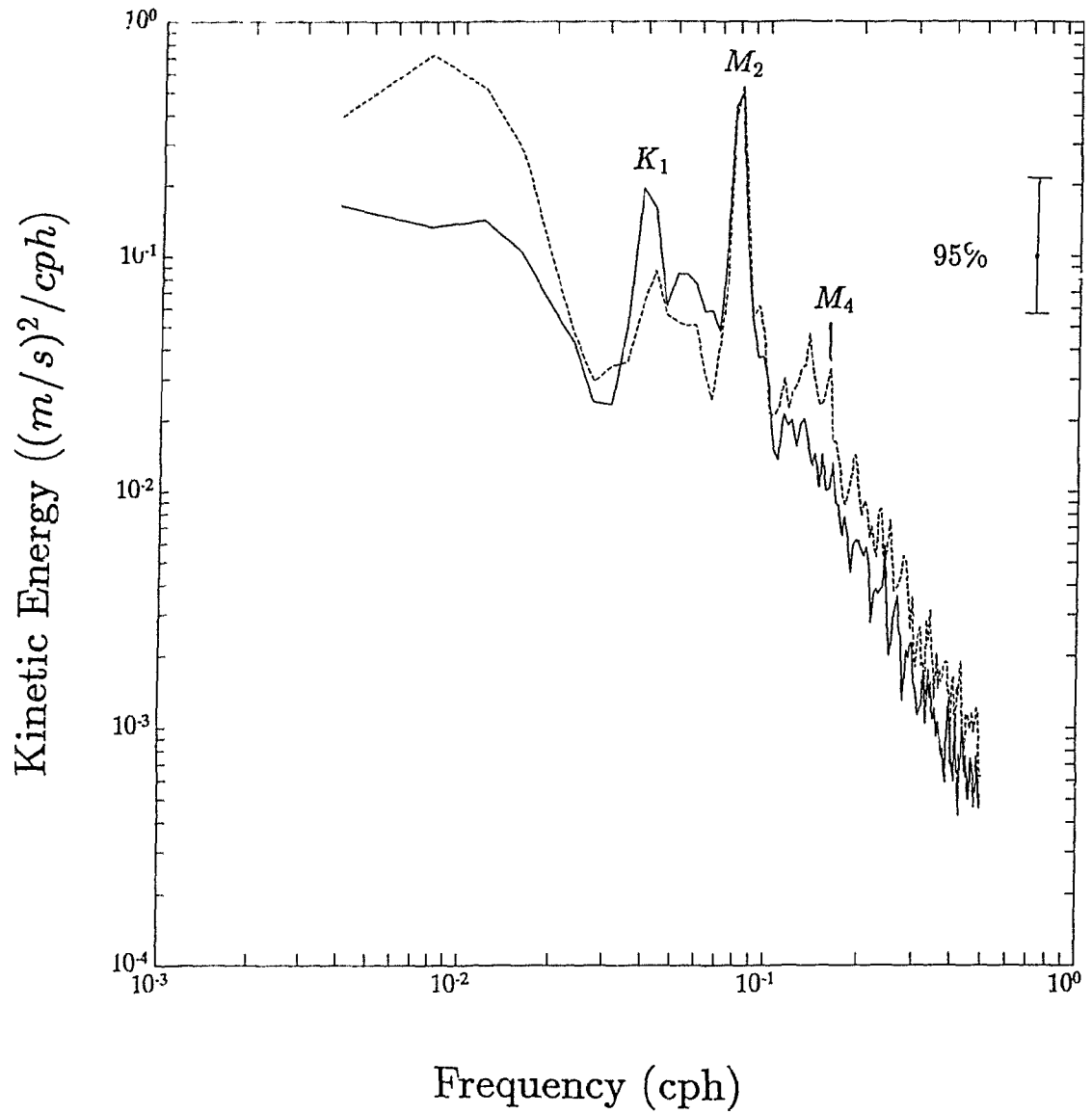


Figure 5.13: Kinetic energy spectra 20m above the bottom at moorings S1D (—) and S2D (- -), where the local depth is  $\approx 250m$  ( $\nu = 18$ ).

stable current ellipse orientations are only found at the tidal frequencies.

Comparisons were made between data from the deepest current meters at moorings S3 and S7 for periods D, E and F. Although I found some differences between them, none of the data from mooring S7 is shown here, for economy of space. In almost all cases, I found evidence for a cross-isobath alignment of motions over a broad range of frequencies in the internal waveband (as in figure 5.11).

Figure 5.13 compares kinetic energy spectra 20m above the bottom at moorings S1D and S2D. There is more energy at S2 in the neighbourhood of  $M_4$ , possibly due to the fact that  $M_4$  is near-critical at that site (see table 5.3). The difference is not significant at the 95% level, but  $M_4$  is also slightly stronger at S2 than at S1 for periods E and G, the other two periods for which we have simultaneous data from this pair of instruments. Similarly, Huthnance and Baines (1982) observed a strong  $M_4$  near the bottom at a mooring where  $\omega_c \approx M_4$  on the Northwest African Shelf.

A summary of the results is given in table 5.4, where each mooring site is classified as either concave or convex, depending on whether  $\partial\omega_c/\partial z > 0$  (concave) or  $\partial\omega_c/\partial z < 0$  (convex). Overall the Scotian Slope is mostly concave (see figure 5.4).

## 5.5 Discussion

### 5.5.1 Energy enhancement (or lack thereof) at mooring sites where $\omega_c \sim f$ .

According to table 5.3, the critical frequency is close to the inertial frequency at moorings R1, R2, R3, R4, R5, S4, S5, S6 and S8, i.e. at 9 of the 13 mooring sites considered in this chapter. The results obtained at those moorings are quite variable (table 5.4); they vary from one mooring site to the next during a given mooring period, and they also vary from one mooring period to the next at a given mooring site.

Deviations of the time-averaged buoyancy frequency  $\bar{N}(z)$  from the climatological mean (figure 5.2) could explain some of the variability in the results, as criterion 1b involved WKB-scaling with respect to  $\bar{N}$  (5.3). I attempted to minimize this source

Mooring	Concave or Convex	Successful tests (95% significant)	Unsuccessful tests (not significant)	Comments	
S1(.086)	convex		D(2),E(2),G(2)	Large bump at $\approx 1000m$	
S2(.132)	concave	D(1d,2),E(1d,2), G(1d,2)	D(1a),E(1a), G(1a)		
S3(.076)	concave	E(2),F(2)	D(1b,2),E(1b,1c), F(1b,1c)		
S4(.060)	?	C(1b),E(1b)	F(1b)		
S5(.058)	?	C(1b,1c),F(1b)	D(1b,1c),F(1c)		
S6(.059)	?		F(1c)		
S7(.076)	concave	C(1b,2),E(2), F(1b,2)	D(1b,2),E(1b)		
S8(.057)	?		F(1b)		sig. at 80% level
R1(.055)	?		J(1b)		K.E.(3500m) > K.E.(2900m)
R2(.056)	?				K.E.( $\omega = f$ ) $\sim$ R1 (3500m)
R3(.055)	?			K.E.( $\omega = f$ ) $\sim$ R1 (3500m)	
R4(.056)	?	J(1c)	J(1b)		
R5(.057)	?		H(1b)		

Table 5.4: Results of tests aimed at determining whether critical internal wave reflection was observed at moorings from the Shelf Break and Risex Experiments. In column 1 the critical frequency (in cph) at each of the mooring sites is written in parentheses. In columns 3 and 4 the capital letters refer to the mooring periods listed in table 5.2, and the numbers in parentheses refer to the criteria given in section 5.3.2.

of error, by limiting the use of criterion 1b to records longer than two months and at least 150m deep, but deviations of  $\bar{N}$  from the climatological mean could still affect the significance of the tests performed with that particular criterion.

Another way of explaining the variability of the results would be to invoke the intermittent nature of inertial wave generation (e.g. Smith, 1989); complex demodulation at the inertial frequency for the Risex data shows the usual burstlike character of the near-inertial motions. Given that, together with the slantwise propagation of near-inertial wave packets, it seems possible that current meters near the surface would have more near-inertial energy at times, current meters near the bottom would have more near-inertial energy at other times, as would current meters at intermediate depths, and there is some evidence for all of those situations occurring in the data.

### 5.5.2 Internal wave reflection versus internal tide generation at mooring sites where $\omega_c \approx M_2$ .

20m above the bottom at moorings S3 and S7, current ellipses are oriented normal to isobaths over a wide range of internal wave frequencies (both above and below  $M_2$ ), as can be seen on figure 5.11 for example. There is also some evidence of near-bottom energy enhancement over much of the internal waveband (e.g. figure 5.10). Yet figure 5.4 shows that  $\partial\omega_c/\partial z > 0$  at 700m depth, so that the topography is locally concave.

This modest near-bottom energy enhancement near  $\omega_c$  at a concave site could be due to departures from  $\xi$ -symmetry in the bathymetry profile (see figure 4.2). Such asymmetries would lead to slightly different wavenumber amplifications upon reflection on either side of the concave corner, since (4.23) would no longer be valid, and this would prevent exact cancellation of the reflected waves.

The other reason why  $\psi_{Tr}$  and  $\psi_{Tl}$  cancelled each other at  $\omega_c$  on figure 4.2 was that the incident wave  $\psi_i$  had the same amplitude on both sides of the origin (which coincides with the critical point on that figure). Since  $\omega_c \approx M_2$  at moorings S3 and S7, one cannot rule out the possibility that the energy enhancement and cross-isobath alignment of motions seen at those moorings could be due to internal tide generation,

followed by a non-linear energy cascade to other internal wave frequencies. The body force  $\mathbf{F}$  responsible for the generation of the internal tide is such that

$$|\mathbf{F}| \propto \frac{N^2(z) z (dh/dx)}{k^2}, \quad (5.4)$$

as  $Q_x$  and  $\omega_T$  are constants in (2.86). Figure 5.14 shows contours of constant amplitude of  $\mathbf{F}$  at  $63^\circ 30' W$ . The tangential (or critical) concave corner for the internal tide is close to mooring S3, at a depth of about 600–700m (figure 5.4), and we see that  $|\mathbf{F}|$  is stronger on the shallow side of it than on the deep side. In fact  $|\mathbf{F}|$  varies rapidly with depth in the neighbourhood of the tangential concave corner, so that exact cancellation of waves generated on either side of it does not seem possible. In that sense the process of internal tide generation differs markedly from the process of internal wave reflection.

### 5.5.3 Energy density at the first overtide ( $M_4$ ).

The energy density at  $M_4$  is detectable above the background energy level nearly everywhere on the Scotian Rise and Slope, as can be seen on most of the spectra shown here. For the purpose of comparison with other published data from the Scotian Slope, figure 5.15 shows the kinetic energy spectra from Petrie's (1975) mooring 1A, deployed for 35 days starting March 1, 1973, at  $62^\circ W$ , in 540m deep water (see figure 5.1).

The most striking feature of that plot is that  $M_4$  is much stronger at 490m depth than at 290m. In fact at 490m, the  $M_4$  peak is comparable in size with the  $M_2$  peak, most of the energy at  $M_4$  ( $\sim 90\%$ ) being in the North velocity component. The ratio  $P_{vv}/P_{uu}$  of North to East kinetic energy is roughly equal to  $(\omega/f)^2$  over a broad range of frequencies ( $M_2 \leq \omega \leq M_4$ ) at that current meter, consistent with a unidirectional field of internal waves travelling in the North-South direction; the orientation of the current ellipse at  $M_4$  itself is  $0^\circ T \pm 5^\circ T$  (A.17).

In view of the recent theoretical work of Thorpe (1987b), it now appears possible to offer an explanation for the unusual size of the  $M_4$  peak seen at Petrie's mooring 1A. Thorpe showed that when a train of finite amplitude internal waves reflects off

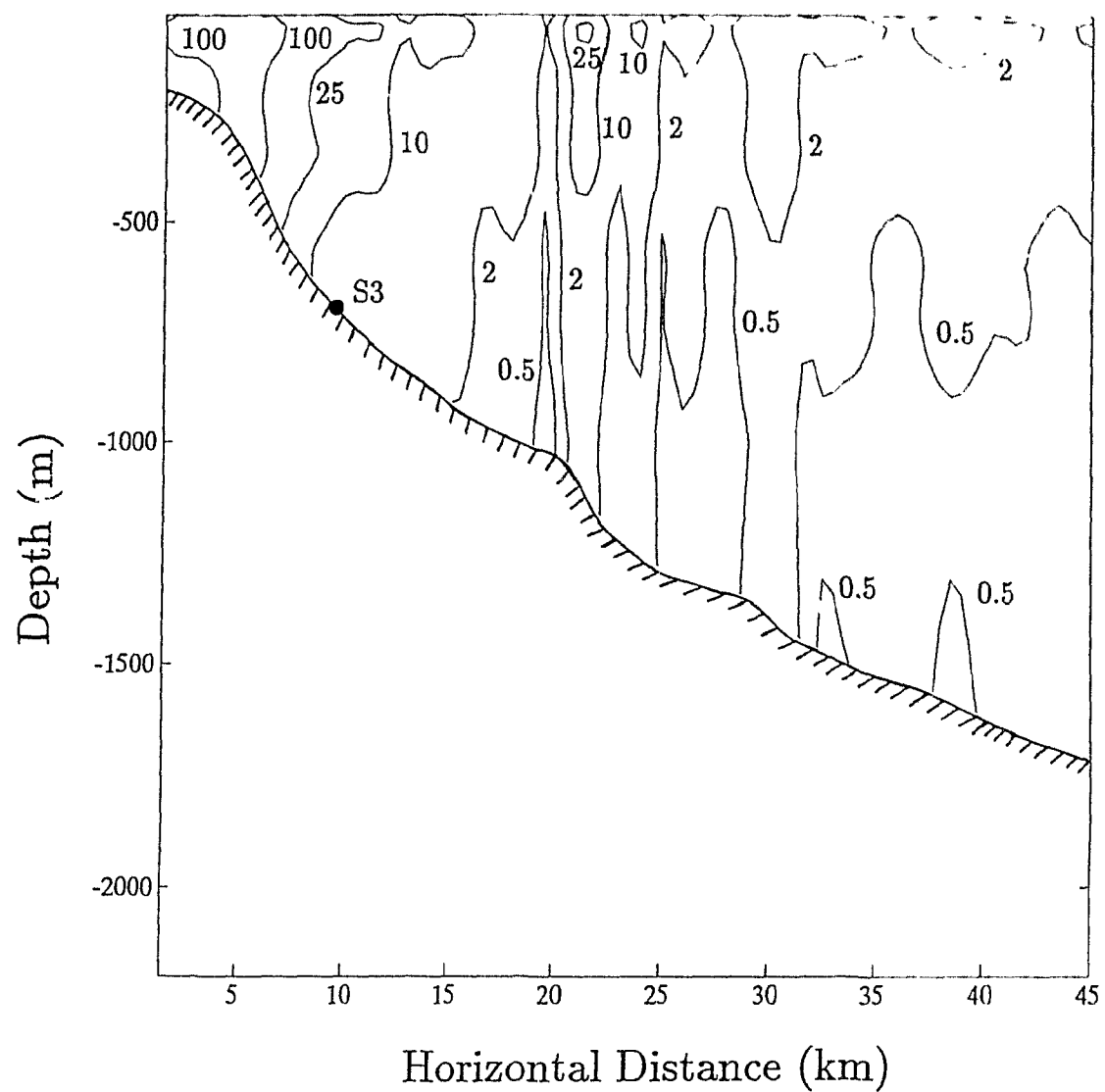


Figure 5.14: Contours of equal amplitude of the body force responsible for the generation of the internal tide at  $63^{\circ}30'W$ , using (5.4). Horizontal distance is measured from the 100 fathom depth contour.

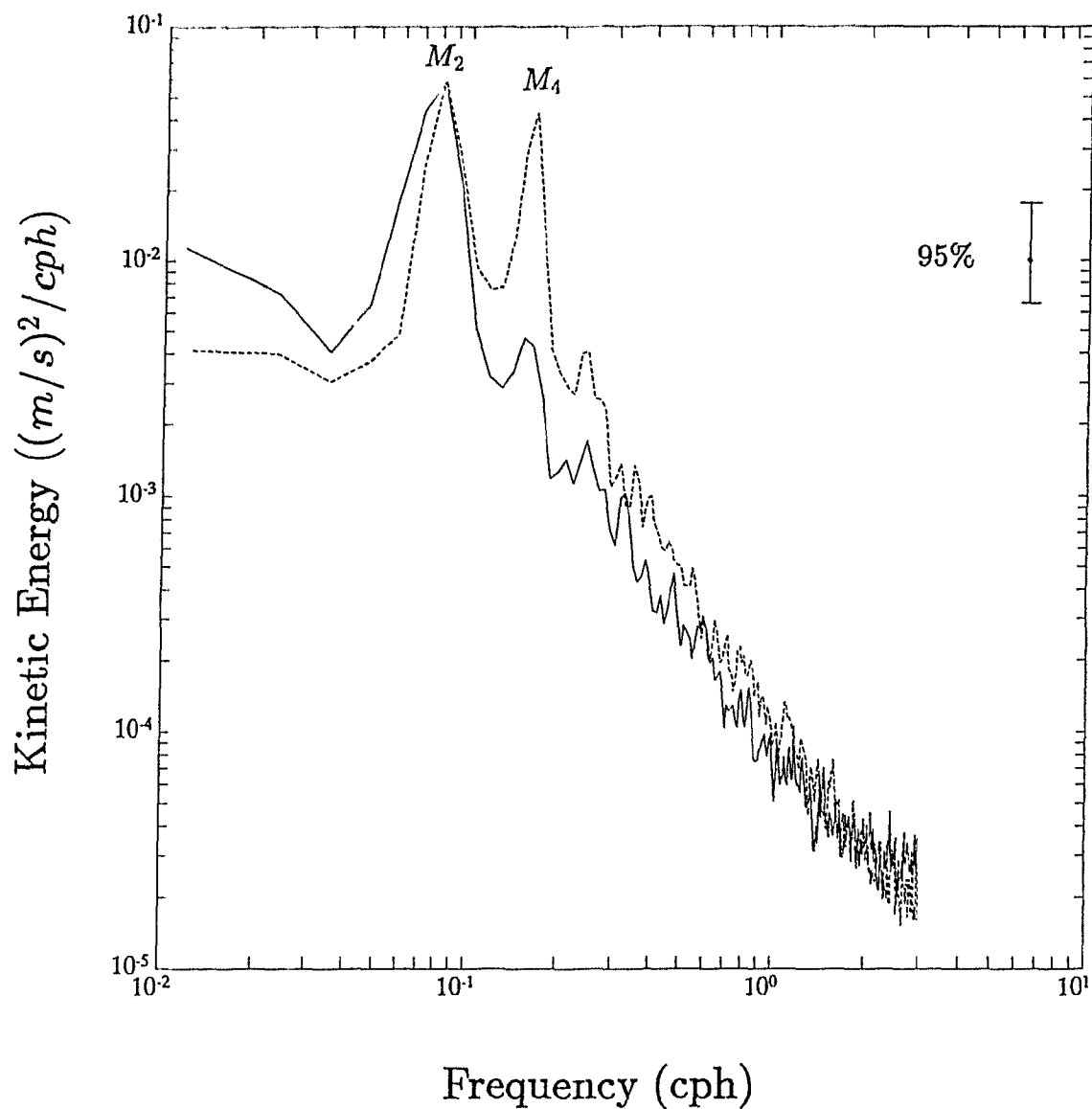


Figure 5.15: Kinetic energy spectra at 290m (—) and 490m (- - -) for Petrie's (1975) mooring 1A (depth = 540m), with  $\nu = 34$ . The spectra were WKB-normalised with respect to the value of  $\bar{N}$  at 490m (1.4 cph).

a bottom of constant slope, resonance between the incident and reflected waves is possible at second order only for  $\alpha < 8.4^\circ$  and  $\mu < 30^\circ$ , a condition that can be met everywhere on the Scotian Slope at  $63^\circ 30'W$  (figure 5.3).

Taking  $\bar{N} \approx 1.4cph$  (figure 5.2) and  $\tan \alpha \approx 0.045$  (figure 7 of Petrie (1975)) as reasonable values of the buoyancy frequency and bottom slope at that mooring, Thorpe's theory (see his figure 2) predicts a singularity at a wave ray slope of  $\approx 0.10$ , corresponding to  $\omega \approx 0.15cph$  (2.16). This is close to  $M_4$ , and so it seems possible that the reflection (not generation) of the internal tide at that location may have caused the unusually large  $M_4$  peak.

None of the spectra I computed show as dramatic near-bottom energy enhancement at  $M_4$  as figure 5.15. However, figure 5.17 does show one instance where  $P_{vv}/P_{uu} \approx (\omega/f)^2$  at  $M_4$  for mooring S3F, as for Petrie's mooring 1A. Taking  $\bar{N} \approx 1.0cph$  and  $\tan \alpha \approx 0.05$  as reasonable values of the buoyancy frequency and bottom slope at mooring S3 (table 5.3), figure 2 of Thorpe (1987b) predicts a second order singularity for  $\tan \mu \approx 0.12$ , corresponding to  $\omega \approx 0.13cph$  (2.16).

Taking another look at figure 5.10 with that prediction in mind, we find that the largest near-bottom energy enhancement at mooring S3E is in fact roughly centered at that frequency. We thus have an alternative explanation for the broadband near-bottom energy enhancement observed at mooring S3E, and it has the distinct advantage of not being affected by the destructive interference near a concave corner discussed in chapter 4 (figure 4.2).

In that context, it is worth mentioning that for the GM79 model internal wave spectrum (in which tides are excluded), the maximum vertical energy flux occurs at  $\omega = \sqrt{2}f$ . This nearly coincides with the  $M_2$  frequency on the Scotian Rise and Slope, as  $M_2 = \sqrt{2}f$  at  $43^\circ$  latitude. Consequently, apart from any consideration for the internal tide generation or reflection problem, we would expect a substantial downward flux of internal wave energy to be incident on the Scotian Slope near  $\omega \approx M_2$ . Non-linear reflection of these waves could lead to the broadband near-bottom energy enhancement shown on figure 5.10 for example.

### 5.5.4 Evidence for bottom-trapped buoyancy oscillations with $\omega > f$ ?

Thompson and Luyten (1976) have provided evidence for the existence of bottom-trapped buoyancy oscillations (Rhines, 1970) at frequencies lower than the inertial frequency. In the context of this thesis however, what is interesting about Rhines' internal edge waves is that, as the bottom slope becomes steeper and  $N$  increases,  $N \sin \alpha$  eventually becomes greater than  $f$ , and bottom-trapped motions become possible in the frequency band normally reserved to freely-propagating internal waves ( $f < \omega < N$ ).

The possibility of trapped waves (or nearly-trapped waves) with  $\omega > f$  above sloping topography has not received much attention in the literature, but Huthnance (1989) points out that "continuity of mode forms near  $\omega = f$  (Huthnance, 1978) suggests that trapped waves approaching  $\omega = f$  from lower frequencies should continue as nearly-trapped waves for  $\omega$  exceeding  $f$ . The bottom trapped waves of Rhines (1970) in realistic contexts are obvious candidates."

Figure 5.16 compares the frequency cutoff  $\bar{N} \sin \alpha$  for Rhines' internal edge waves with the critical frequency (5.1) at  $63^\circ 30' W$ , based on the values of  $\bar{N}$  and  $\sin \alpha$  shown on figures 5.2 and 5.3. At depths larger than 700m,  $\bar{N} \sin \alpha < f$ , but at shallower depths,  $\bar{N} \sin \alpha$  gets well into the internal wave band, and becomes virtually undistinguishable from  $\omega_c$  between 300m and 600m depth.

According to table 5.3, the frequency cutoff for internal edge waves should be about 0.050cph at mooring S3 (700m depth), close to the inertial frequency  $f$ . For the three periods when the deepest current meter at mooring S3 worked properly (D, E and F), I found that  $P_{vv} > P_{uu}$  at  $\omega = f$ , possibly indicating the presence of Rhines' waves in the data, since inertial motions are circular and should have  $P_{uu} = P_{vv}$ . This is shown for period F on figure 5.17, where we see that  $P_{vv} = 2.2P_{uu}$  at the inertial frequency. Using (A.17), I found that the ellipse orientation at  $f$  for the same mooring period was  $13^\circ T \pm 14^\circ T$ , roughly perpendicular to the isobaths and consistent with (2.97), which predicts  $\phi \approx 0^\circ T$ .

To further emphasize the point that motions with properties (2.95) similar to

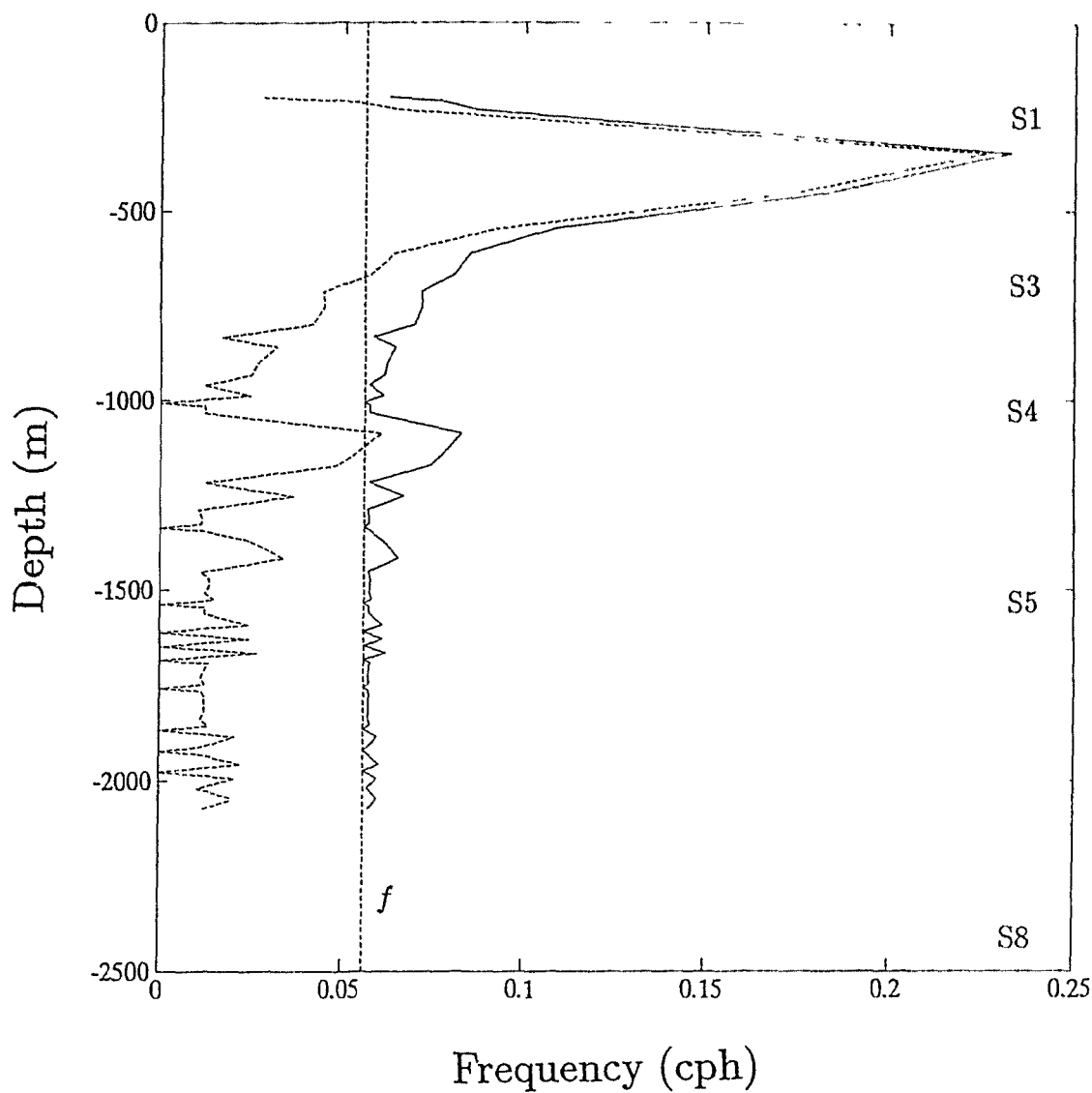


Figure 5.16: Frequency cutoff  $\bar{N} \sin \alpha$  for Rhines' internal edge waves (dashed line) versus  $\bar{\omega}_c = (\bar{N}^2 \sin^2 \alpha + f^2 \cos^2 \alpha)^{1/2}$  (solid line) at  $63^\circ 30' W$ . The vertical dashed line is drawn at the inertial frequency ( $\omega = f$ ).

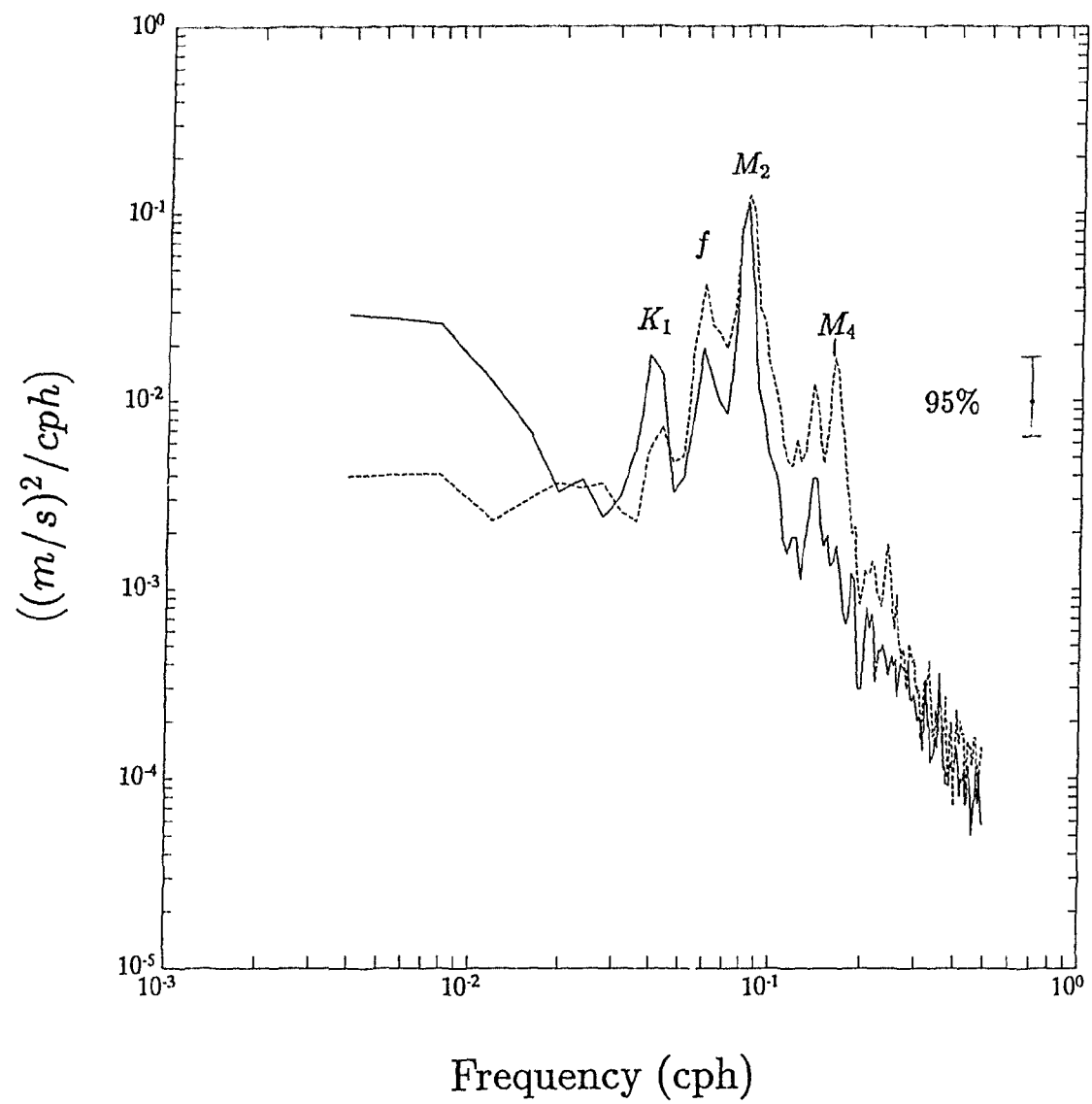


Figure 5.17: East (—) and North (- - -) velocity spectra 20m above the bottom at mooring S3F ( $\nu = 32$ ).

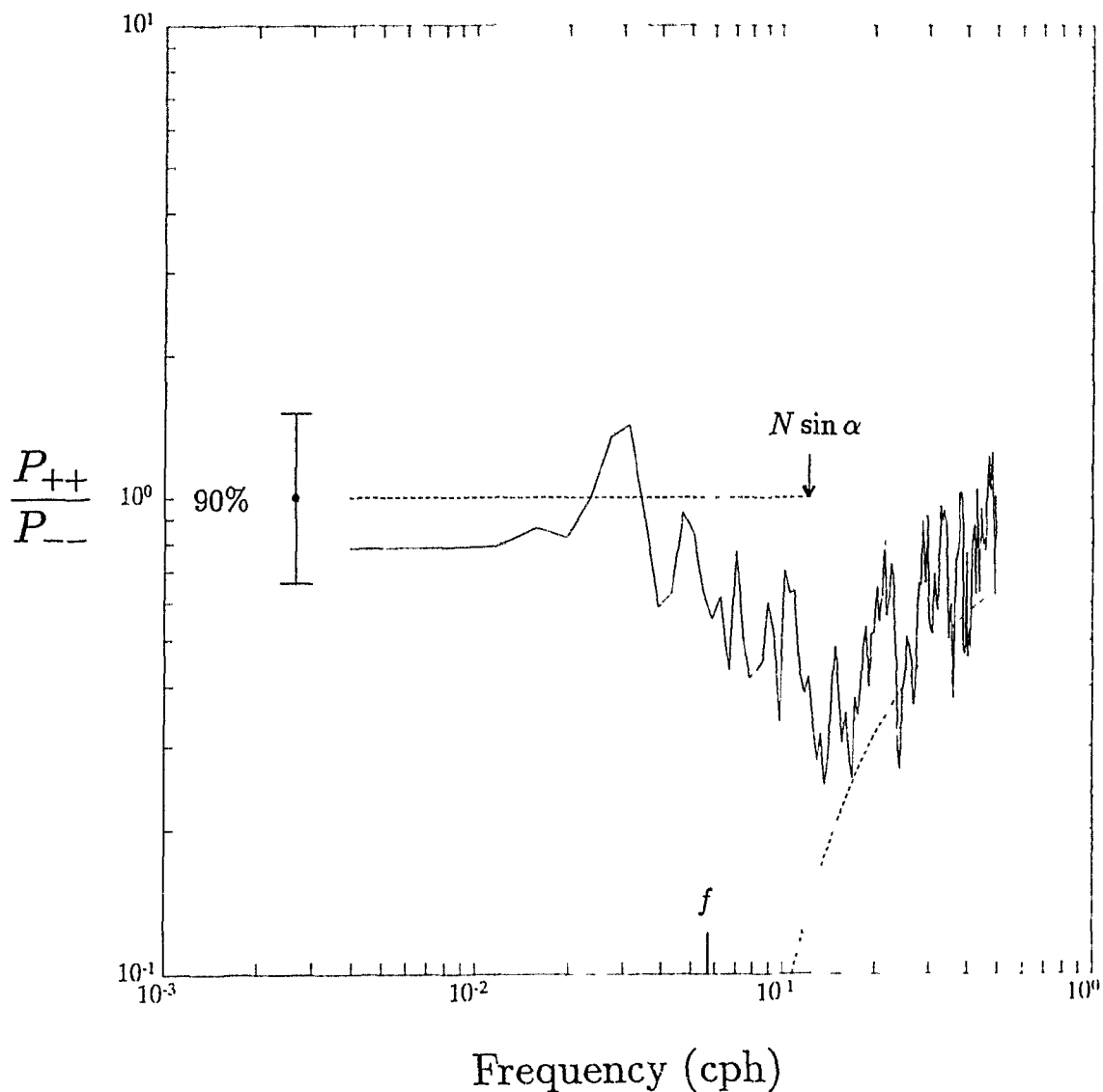


Figure 5.18: Ratio  $P_{++}/P_{--}$  of anticlockwise to clockwise kinetic energy 20m above the bottom at mooring S2G ( $\nu = 61$ ). The curved dashed line represents the theoretical ratio (2.18) for linear internal waves, whereas the horizontal dashed line represents the theoretical ratio  $P_{++}/P_{--} = 1$  for Rhines' internal edge waves. The 90% confidence intervals assume a Fisher's F distribution for the ratio of two independent chi-squared distributions (Jenkins and Watts, 1968, p.85).

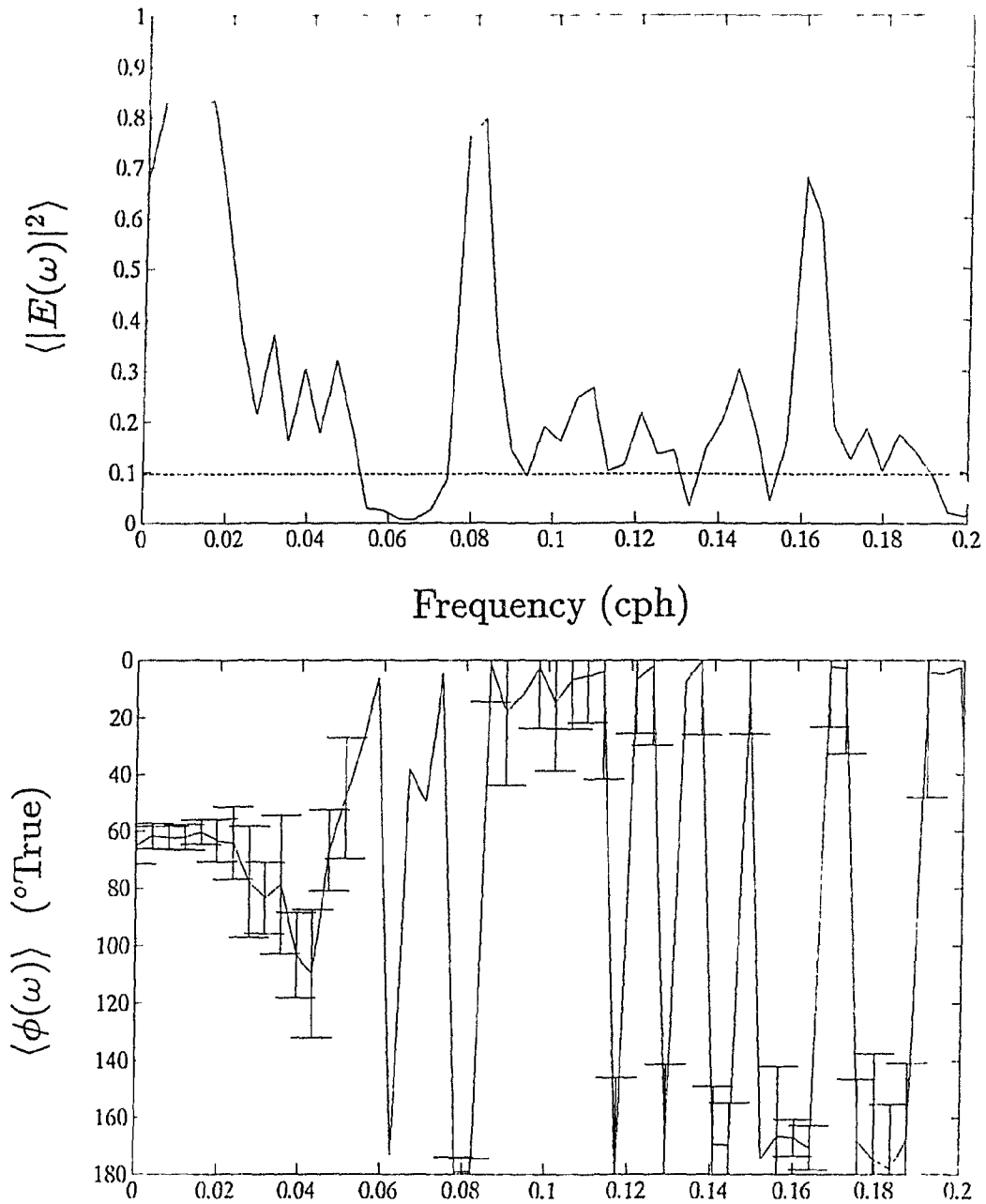


Figure 5.19: Current ellipse orientation and stability 20m above the bottom at mooring S2G. The dashed line on the upper plot represents the 95% significance level for zero true coherence between clockwise and anticlockwise velocities. The 95% confidence intervals for ellipse orientation are shown on the lower plot ( $\nu = 61$ ).

Rhines' bottom-trapped waves could play a role within the internal waveband at mooring sites where  $\bar{N} \sin \alpha \gtrsim f$ , figure 5.18 presents another type of information. It shows that the ratio  $P_{++}/P_{--}$  of anticlockwise to clockwise kinetic energy at mooring S2G starts to deviate systematically from the prediction of linear internal wave theory (2.18) at about 0.14cph, close to the value of  $\bar{N} \sin \alpha$  given for mooring S2 in table 5.3. However, changes of current ellipse orientation with frequency that seem consistent with (2.97) only occur at frequencies below the diurnal tide, where  $P_{++}/P_{--}$  is closer to 1 (see figure 5.19).

Huthnance and Baines (1982) showed that the  $M_2$  tide itself was consistent at times with Rhines' bottom-trapped waves at one of their moorings. They called for a more detailed investigation of the phenomenon, pointing out the fact that we do not know much about the possible radiational energy losses of these waves when  $N \sin \alpha > f$  over only a finite portion of the bathymetry profile, as is the case here (figure 5.16).

## Chapter 6

# A closer look at the 3–4 day motions from the Western Boundary Sill Experiment.

Eriksen's (1982) most convincing evidence of energy enhancement near  $\omega_c$  came from mooring 636 of the Western Boundary Sill Experiment, originally deployed to measure the flow of Antarctic Bottom Water into the Northwest Atlantic Basin (Whitehead and Worthington, 1982). In this chapter, I try to determine whether the energetic motions with 3–4 day periods observed at that mooring can indeed be attributed to internal wave reflection off a sloping bottom.

### 6.1 The low-frequency currents

The main objective of the Western Boundary Sill Experiment (WBSE) was to measure the average flow rate of Antarctic Bottom Water (AABW) into the Northwest Atlantic Ocean. To this end, the buoy group of the Woods Hole Oceanographic Institution deployed two moorings at about  $4^\circ\text{N}$ , between the Ceara Rise and the mid-Atlantic ridge, from December 9, 1977, to December 5, 1978. Mooring 636 was deployed at  $4^\circ 2.5'\text{N}$ ,  $39^\circ 40.6'\text{W}$ , and mooring 637 was deployed at  $4^\circ 1.3'\text{N}$ ,  $39^\circ 19.0'\text{W}$ . Both moorings had current meters at 10m, 50m, 100m and 200m above the bottom. The

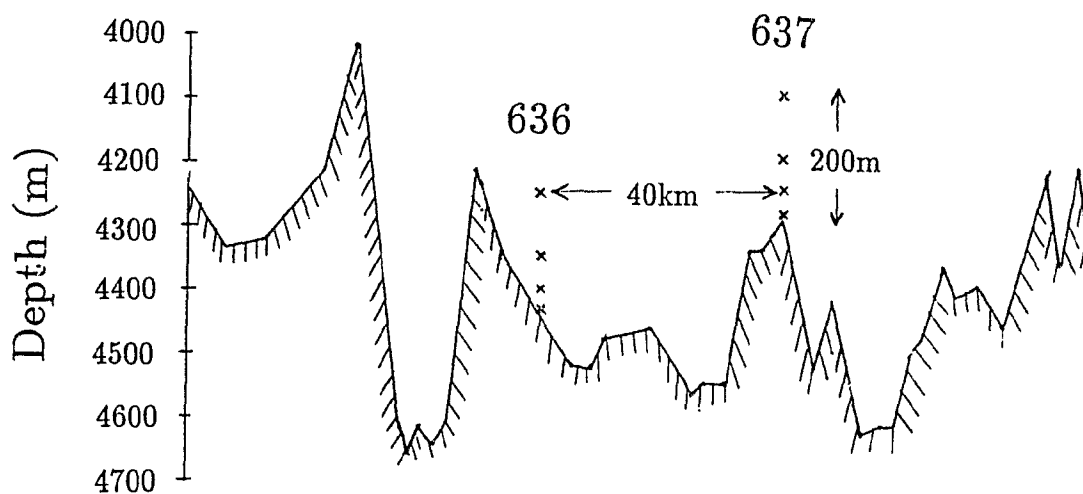


Figure 6.1: Topography in the vicinity of moorings 636 and 637 of the Western Boundary Sill Experiment, based upon the East-West transect at  $4^{\circ}N$  shown on figure 4 of Whitehead and Worthington (1982).

local depth was 4456m at mooring 636, and 4304m at mooring 637 (see figure 6.1).

In this chapter, I concern myself mostly with data from mooring 636, where Erikssen (1982) found the clearest evidence of near-bottom energy enhancement at what he estimated to be the critical frequency  $\omega_c$ . Average hydrographic properties at that mooring are summarised in tables 6.1 and 6.2. Salinity was not directly measured by the current meters, but is readily obtained from temperature, using a linear  $T-S$  relation derived from CTD stations near the moorings.

Whitehead and Worthington (1982) (hereafter WW82) analysed the low-frequency current and temperature signals at moorings 636 and 637. Figure 8 of their paper shows stick diagrams of the low-passed velocity, as well as curves of the low-passed current speed, direction, and potential temperature. Surges of AABW into the Northwest Atlantic with a roughly 60-day period are clearly seen on that figure. Those

Instrument	Depth (m)	Height above bottom (m)	$\bar{\theta}$ ( $^{\circ}\text{C}$ )	$\bar{S}$ ( $\text{‰}$ )
6361	4256	200	1.568	34.853
6362	4356	100	1.276	34.818
6363	4406	50	1.146	34.803
6364	4446	10	1.055	34.792

Table 6.1: Average potential temperature  $\bar{\theta}$  and salinity  $\bar{S}$  at mooring 636.

Instruments	Height above bottom	$\partial\bar{\theta}/\partial z$ ( $\times 10^{-3} \text{ }^{\circ}\text{Cm}^{-1}$ )	$\partial\bar{S}/\partial z$ ( $\times 10^{-4} \text{ ‰m}^{-1}$ )	$\bar{N}$ ( <i>cph</i> )
6361-6362	150m	2.92	3.5	0.94
6362-6363	75m	2.61	3.0	0.90
6363-6364	30m	2.27	2.8	0.82

Table 6.2: Average temperature gradient, salinity gradient, and buoyancy frequency at mooring 636.

surges are shown here on figure 6.2, where I plotted the East and North components of the low-passed velocity for the four current meters at mooring 636.

The low-pass filter used to draw figure 6.2 is a triangular window whose transfer function has its first zero at a period of 7.1 days (local inertial period); it effectively removes all internal wave motions. By contrast, WW82's low-passed currents were subjected to a Gaussian filter with a 1-day half width. That filter passed 95% of the energy at periods longer than five days, which explains why the energetic 3-4 day temperature and velocity oscillations can still be seen on WW82's figure 8.

Note on figure 6.2 that the zonal velocity component is consistently eastward 10m above the bottom ( $\bar{u} = 2.0\text{cm s}^{-1}$ ), whereas it fluctuates a few times from eastward to westward at other heights above the bottom. A strong mean eastward flow is also present 10m above the bottom at mooring 637 ( $\bar{u} = 2.8\text{cm s}^{-1}$  according to table 1 of WW82). The mechanism responsible for the confinement of this mean eastward flow near the bottom is not known (WW82), part of the difficulty residing in the fact that we do not know the orientation of isobaths at moorings 636 and 637.

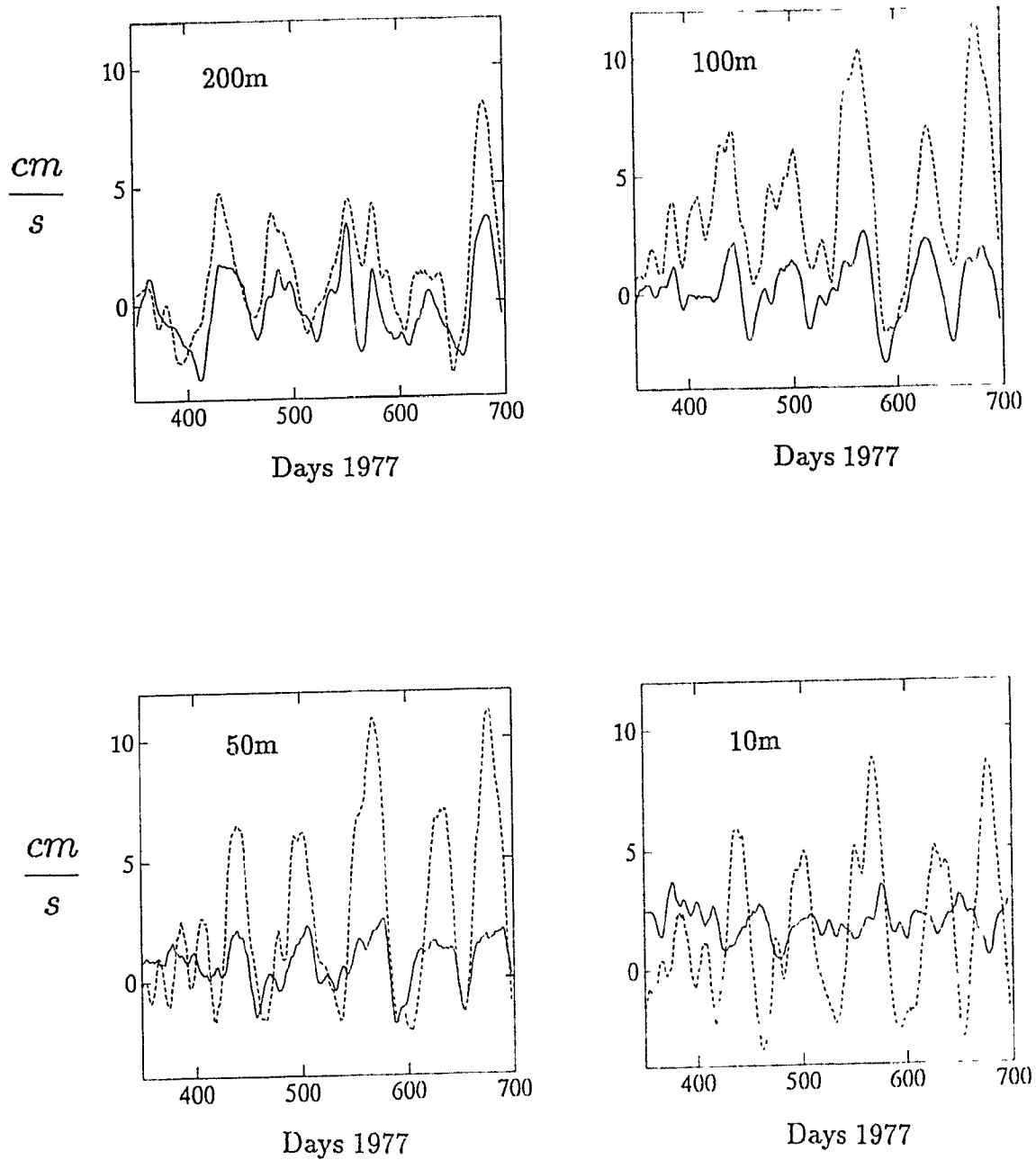


Figure 6.2: Low-passed East (—) and North (- - -) velocity components 10m, 50m, 100m and 200m above the bottom at mooring 636. The plots start on day 350, 1977, and end on day 332, 1978 (day 697 here).

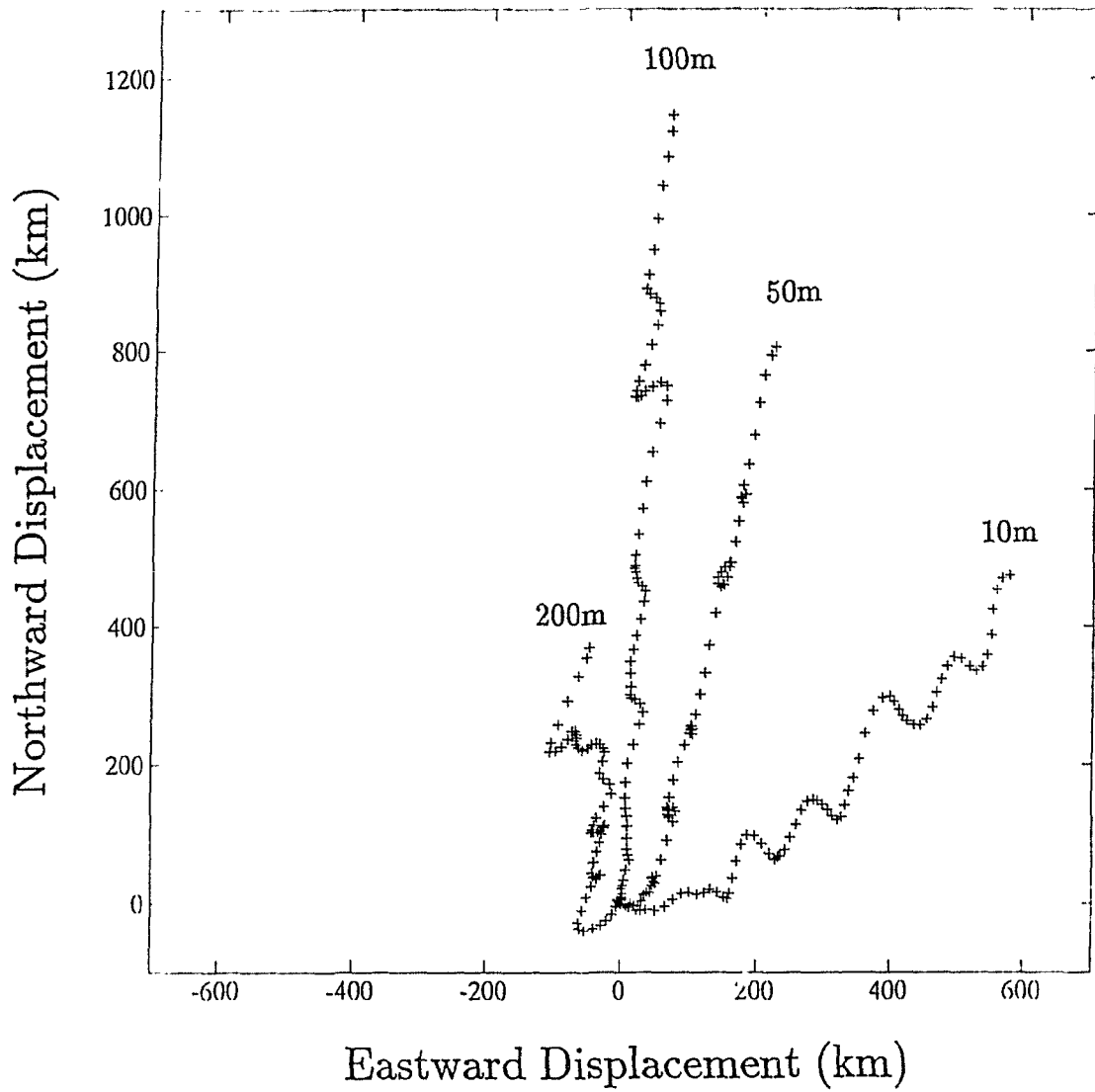


Figure 6.3: Progressive vector diagrams 10m, 50m, 100m and 200m above the bottom at mooring 636. The plots start on day 350, 1977, and end on day 332, 1978. Tick marks are drawn every 5 days.

Figure 6.1 may tell us that the bottom shallows towards the west at mooring 636, but it does not tell us the orientation and magnitude of  $\nabla h$  there. The most detailed bathymetric map available for the area, produced by Moody et al. (1979), and shown on figure 2 of WW82, does not help us solve that problem either due to its lack of resolution.

Progressive vector diagrams for the four current meter records at mooring 636 are drawn on figure 6.3 (cf WW82's figure 7a). A surprising feature of this graph is that currents turn clockwise as we approach the bottom instead of anticlockwise; the sense of rotation of the low-frequency currents is thus opposite to what one would expect in an Ekman layer above flat or sloping topography (see the data from mooring 349 of Wunsch and Hendry (1972) for an example from the continental slope).

Also note that the flow 10m above the bottom appears to be bimodal: during periods of strong northward flow, it is reasonably well aligned with the flow at other depths, but as soon as that northward flow weakens, it veers towards the Southeast and becomes misaligned with the flow at other depths.

## 6.2 Power spectral analysis at mooring 636

### 6.2.1 Kinetic energy spectra

Kinetic energy spectra were computed for the four current meters at mooring 636, and are shown on figure 6.4. The spectra agree quite well with those shown on figure 7 of Eriksen (1982), except that Eriksen did not plot the 50m spectrum due to its similarity to the 10m spectrum. Also note that Eriksen plotted twice the kinetic energy in  $(cm/s)^2/cph$ , whereas I plot the kinetic energy itself in  $(m/s)^2/cph$ .

The near-bottom energy enhancement ranges roughly from 0.005 cph to 0.05 cph (periods between 20 and 200 hours), with a peak in energy density centered at 0.0117 cph (85.5 hour or 3.56 day period) for all four instruments. The inertial frequency at that location is 0.00587 cph (170.3 hour period), so that the energy peak occurs well within the internal waveband at  $\omega \approx 2f$ .

Following Eriksen (1982) in taking  $N \approx 0.8cph$ , and assuming that the bottom

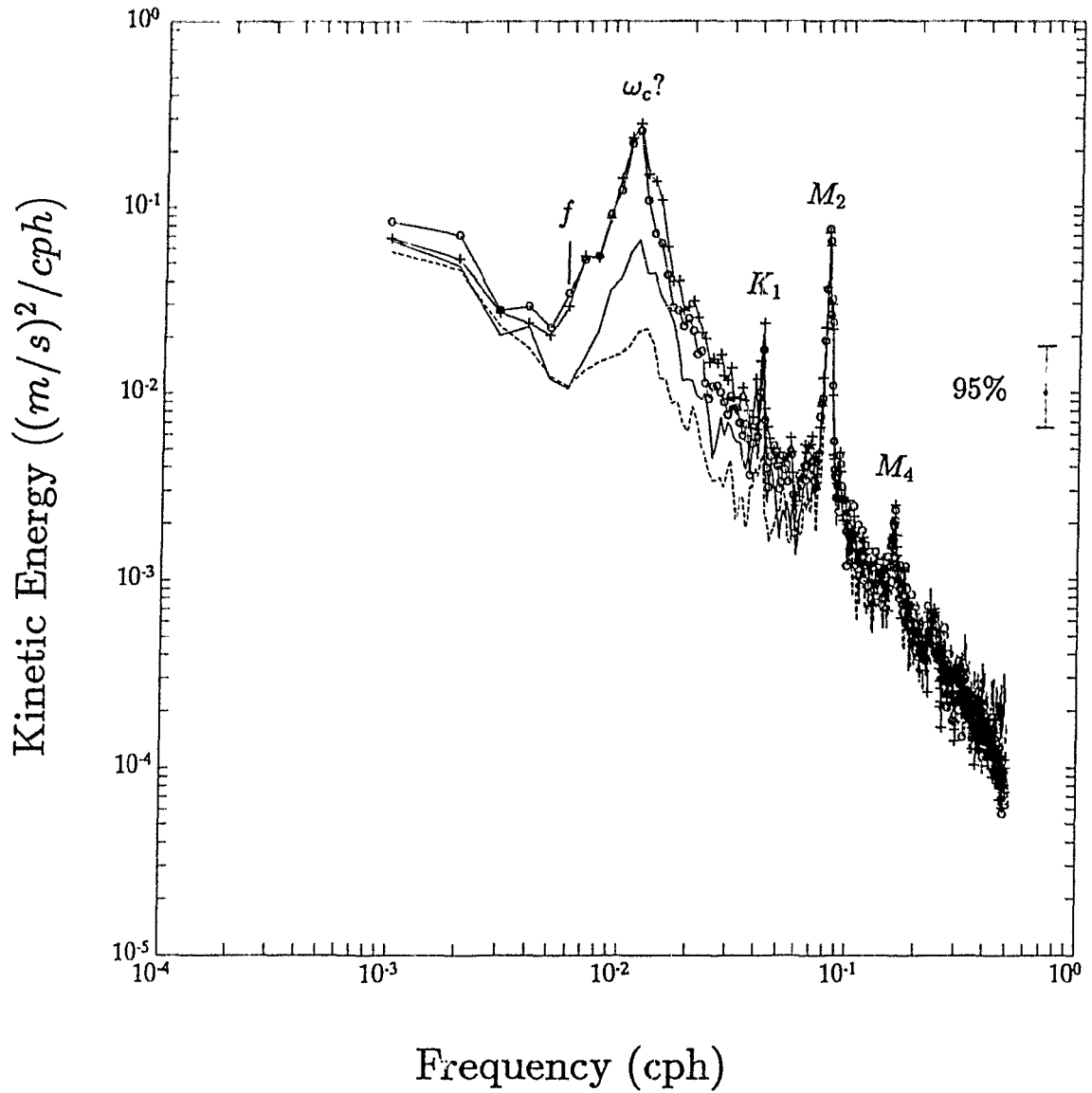


Figure 6.4: Kinetic energy spectra at 10m ( + ), 50m ( o ), 100m ( — ) and 200m ( - - ) above the bottom at mooring 636 ( $\nu = 30$ ). The inertial frequency is  $f = 5.87 \times 10^{-3} \text{ cph}$ .

slope at mooring 636 is 0.015, as estimated from the East-West transect shown on figure 6.1, we obtain  $\omega_c = (N^2 \sin^2 \alpha + f^2 \cos^2 \alpha)^{1/2} \approx 0.0133 \text{cph}$ . This estimate of the critical frequency compares well with the energy enhancement shown on figure 6.4.

However, I should point out that while Eriksen's estimate of  $N$  is consistent with the values given here in table 6.2, his estimate of the bottom slope probably is a lower bound. For any orientation of the isobaths other than North-South, the bottom slope would be larger. Hence it can be argued that Eriksen's estimate of the critical frequency  $\omega_c$  probably is a lower bound too.

### 6.2.2 Temperature spectra

The temperature autospectra at 10m, 50m, 100m and 200m above the bottom were also computed. Figure 6.5 shows these spectra without any normalisation with respect to the vertical temperature gradients. They all show a peak at 0.0117 cph, but unlike the kinetic energy spectra, this time the 10m record does not have the largest peak. Table 6.2 suggests this is probably due to the fact that the temperature gradient 10m above the bottom is smaller than at other heights above the bottom, given the tendency for  $\partial\bar{\theta}/\partial z$  to decrease as we approach the bottom.

### 6.2.3 Rotary spectra and the ratio $P_{++}/P_{--}$

Using the clockwise ( $u_-$ ) and anticlockwise ( $u_+$ ) rotary velocity components

$$u_- = (u - iv)/\sqrt{2} \quad (6.1)$$

$$u_+ = (u + iv)/\sqrt{2}, \quad (6.2)$$

I computed the clockwise and anticlockwise autospectra  $P_{--}$  and  $P_{++}$  at each current meter (see Appendix A). For linear, freely-propagating internal waves, the ratio of anticlockwise to clockwise kinetic energy is given by (2.18)

$$\frac{P_{++}}{P_{--}} = \left( \frac{\omega - f}{\omega + f} \right)^2, \quad (6.3)$$

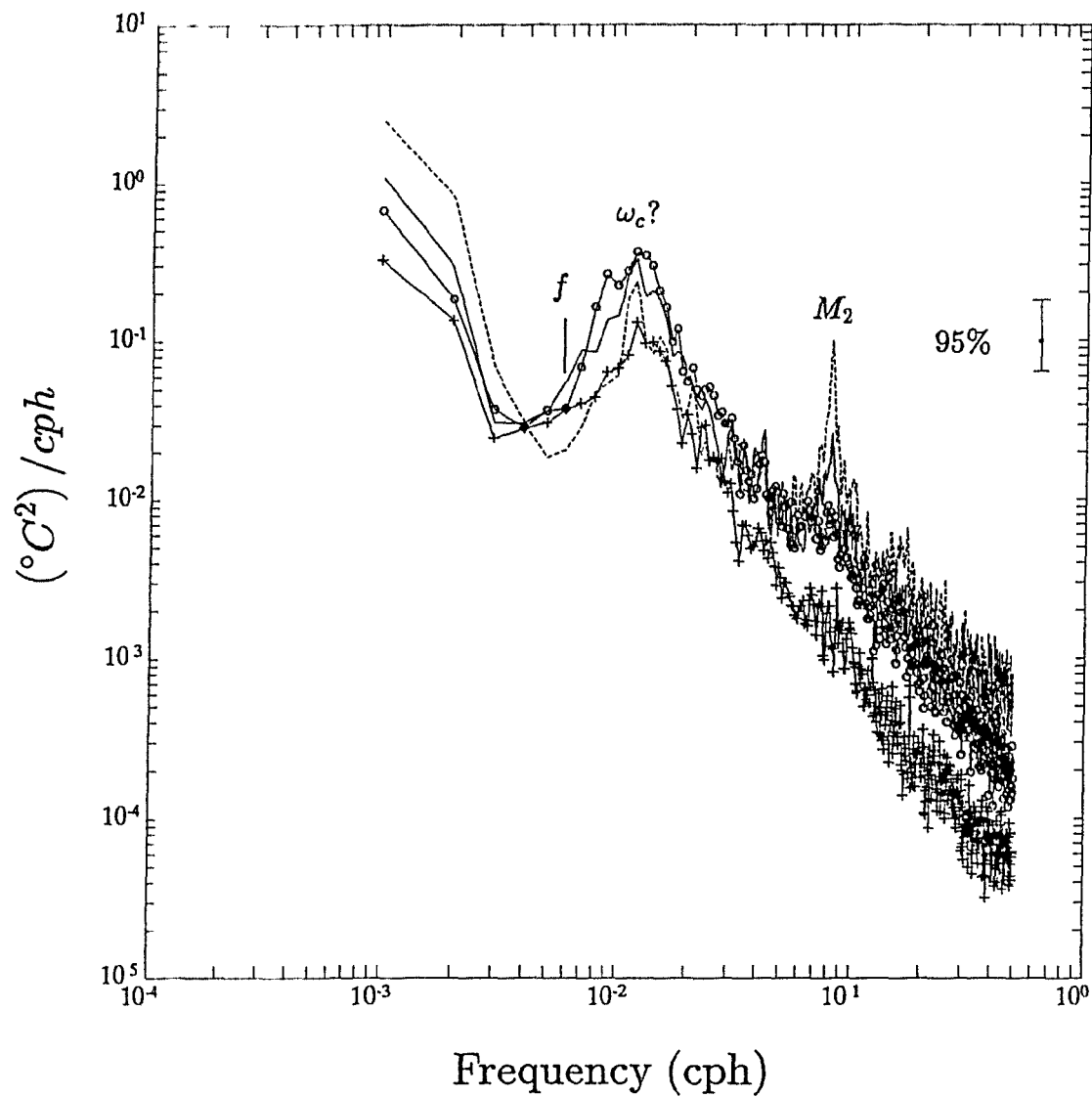


Figure 6.5: Temperature spectra 10m (+), 50m (o), 100m (—) and 200m (- - -) above the bottom at mooring 636 ( $\nu = 30$ ).

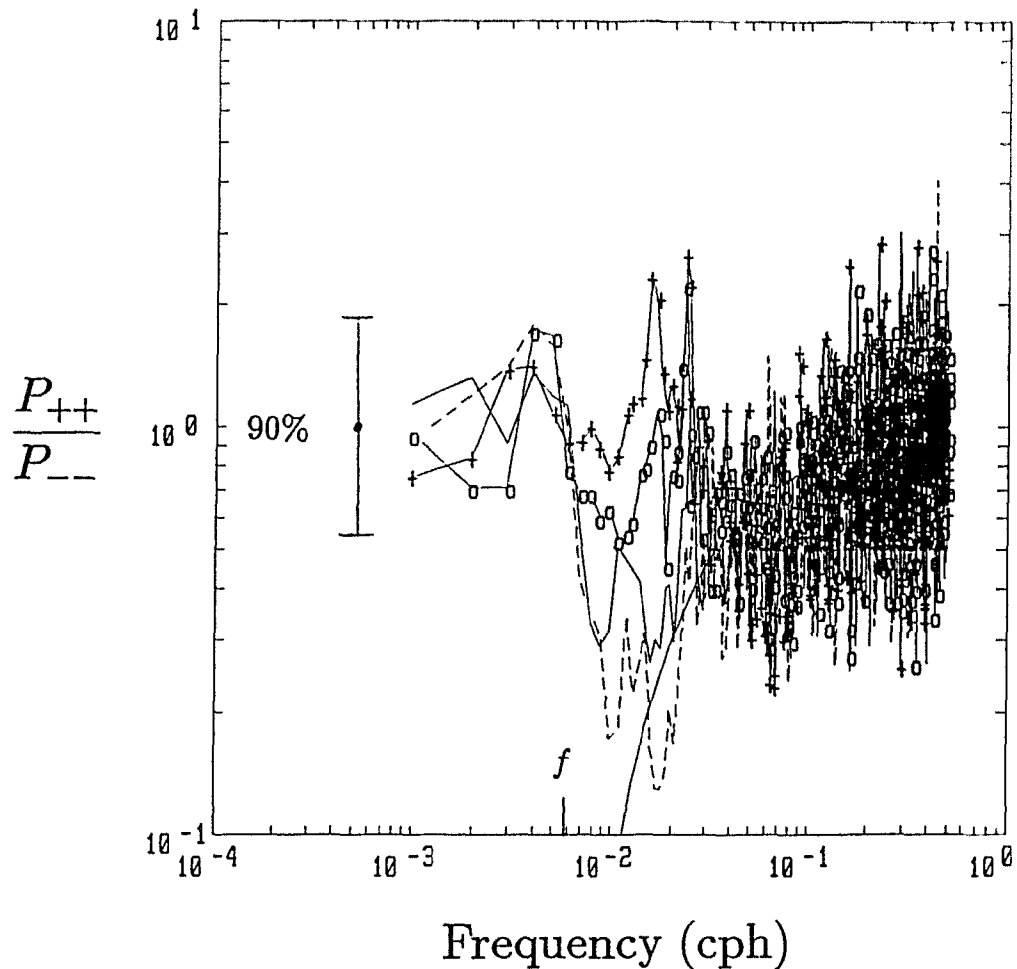


Figure 6.6: Ratio  $P_{++}/P_{--}$  at 10m (+), 50m (o), 100m (—) and 200m (- - -) above the bottom at mooring 636 ( $\nu = 30$ ). The theoretical ratio (6.3) for linear, freely propagating internal waves, is also shown for the purpose of comparison. The 90% confidence intervals assume a Fisher's F distribution for the ratio of two independent chi-squared distributions (Jenkins and Watt, 1968, p.85).

independently of the directional properties of the wavefield. On figure 6.6, I plotted  $P_{++}/P_{--}$  as a function of frequency at 10m, 50m, 100m and 200m above the bottom. Interestingly enough, I find large deviations from the predictions of linear internal wave theory (6.3) in the range of frequencies for which near-bottom kinetic energy enhancement is observed. More interesting still, I find that in the neighbourhood of the energy peak ( $\omega \approx 0.0117cph$ ), the largest departure from internal wave theory occurs at 10m above the bottom, followed by the departures at 50m, 100m and 200m in that order. There thus seems to be a one to one correspondance between kinetic energy enhancement and the degree of departure from (6.3) near  $\omega = 0.0117cph$ ; the records with the most kinetic energy at  $\omega = 0.0117cph$  are the least internal wave like.

To explain this, a physically appealing hypothesis would be that the energetic 3-4 day motions at WBSE mooring 636 are in fact Rhines' (1970) internal edge waves, described in chapter 2. Water parcel motions should then be rectilinear, implying the ratio (2.95)

$$\frac{P_{++}}{P_{--}} = 1. \quad (6.4)$$

Looking at figure 6.6, we find that at 10m and 50m above the bottom,  $P_{++}/P_{--}$  is closer to 1 than to the internal wave line for  $\omega \leq 0.025cph$ , in rough agreement with (6.4). To further test the hypothesis that the 3-4 day motions could be a manifestation of Rhines' trapped waves, we next try to find out whether the orientation of these motions changes with frequency according to (2.97):

$$\phi = \cos^{-1} \left( \frac{\omega}{N \sin \alpha} \right). \quad (6.5)$$

### 6.3 Ellipse orientation and stability at mooring 636

It was pointed out by Eriksen (1982, p.533) that the orientation of current ellipses at mooring 636 (shown on figure 9 of his paper) is not consistent with internal wave

reflection theory: "... the critical period ellipses seem to turn with depth much more than they do with frequency. Furthermore, orientation is nearly parallel to the low frequency flow at each level rather than perpendicular to the isobaths inferred from the bathymetry shown on Figure 6 and the mean currents. Both of these characteristics conflict with the linear model for internal wave reflection considered so far. In addition the current ellipses are more narrow than would be expected from linear internal waves at  $\omega \sim 2f$ , even if waves were unidirectional." He suggested that the lack of agreement between observed current ellipse orientations and what linear internal wave reflection theory predicts " is a manifestation of complex nonlinear interaction of the wave field with the strong mean and low frequency currents."

Using the method outlined in appendix A, I computed both ellipse orientation and stability as a function of frequency at 10m, 50m, 100m and 200m above the bottom, shown on figures 6.7, 6.8, 6.9 and 6.10 respectively. Those plots essentially agree with Eriksen's figure 9, but with the added advantage that they tell us something about the stability of the orientations. We find as he did that current ellipses do not turn much with frequency, and that the energetic 3-4 day motions are parallel to the orientation of the low-frequency flow oscillations at each height above the bottom.

We also find that at 10m, 50m and 100m above the bottom, ellipse stability falls below the 95% significance level for zero true stability at about the same frequency ( $\omega \approx 0.0225cph$ ) as the ratio  $F_{++}/P_{--}$  returns to the linear internal wave line on figure 6.6. If those motions were a manifestation of Rhines' internal edge waves (possible for  $\tan \alpha \approx 0.03$ ), equation (6.5) predicts that ellipse orientation should then vary by as much as  $60^\circ$  from  $\omega = 0.0225cph$  to  $\omega = 0.01cph$ . Figures 6.7, 6.8 and 6.9 show that this is clearly not the case, casting doubts on the Rhines wave hypothesis.

In summary then, Eriksen's interpretation of the 3-4 day motions at mooring 636 as bottom-reflected internal waves fails to explain why the current ellipses near  $\omega_c$  are not perpendicular to the inferred North-South orientation of the isobaths, whereas an interpretation of those motions in terms of Rhines' internal edge waves fails to explain the lack of turning of the current ellipses with frequency.

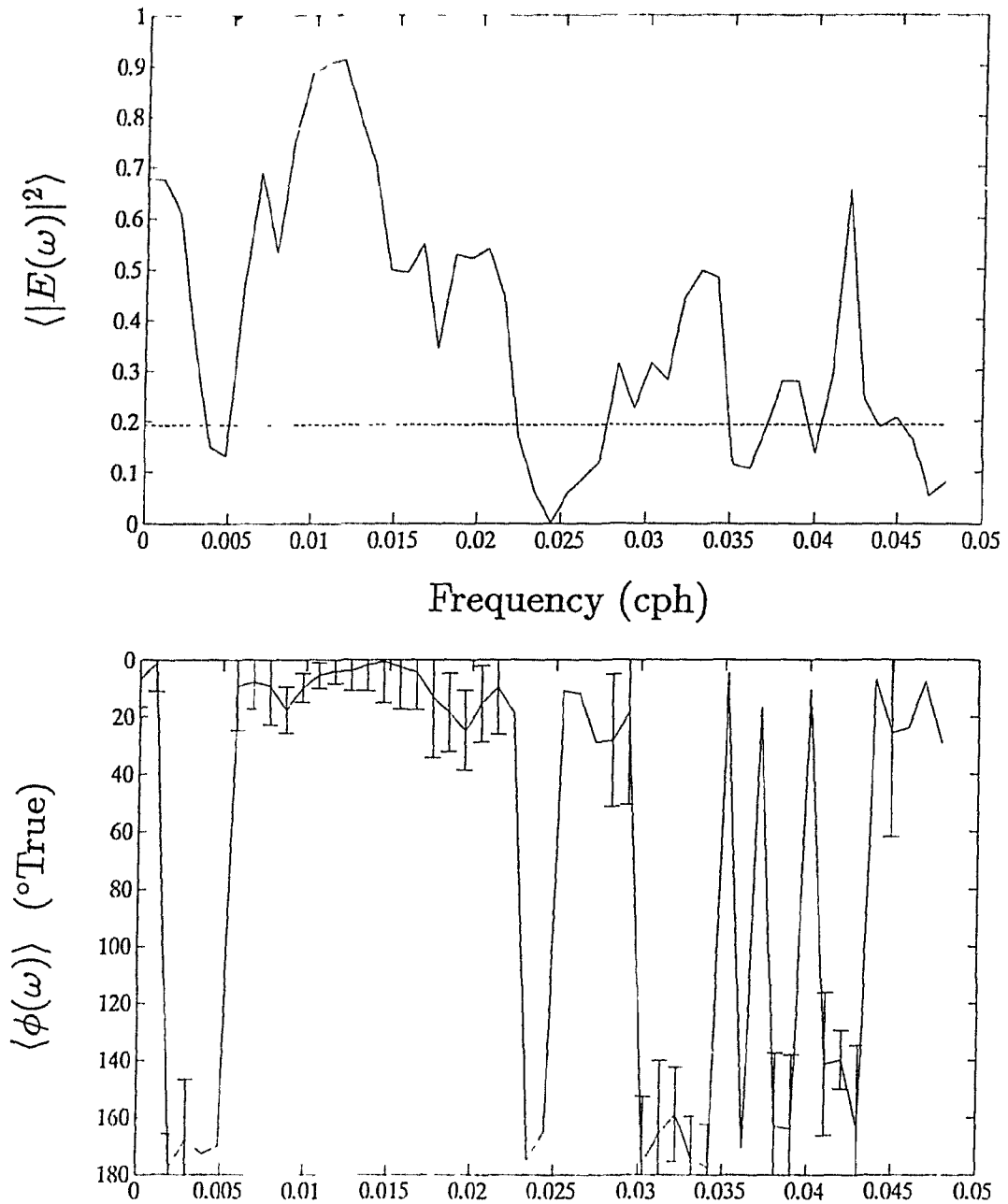


Figure 6.7: Current ellipse orientation and stability 10m above the bottom at mooring 636. The dashed line on the upper plot represents the 95% significance level for zero true coherence between clockwise and anticlockwise velocities. The 95% confidence intervals for ellipse orientation are shown on the lower plot ( $\nu = 30$ ).

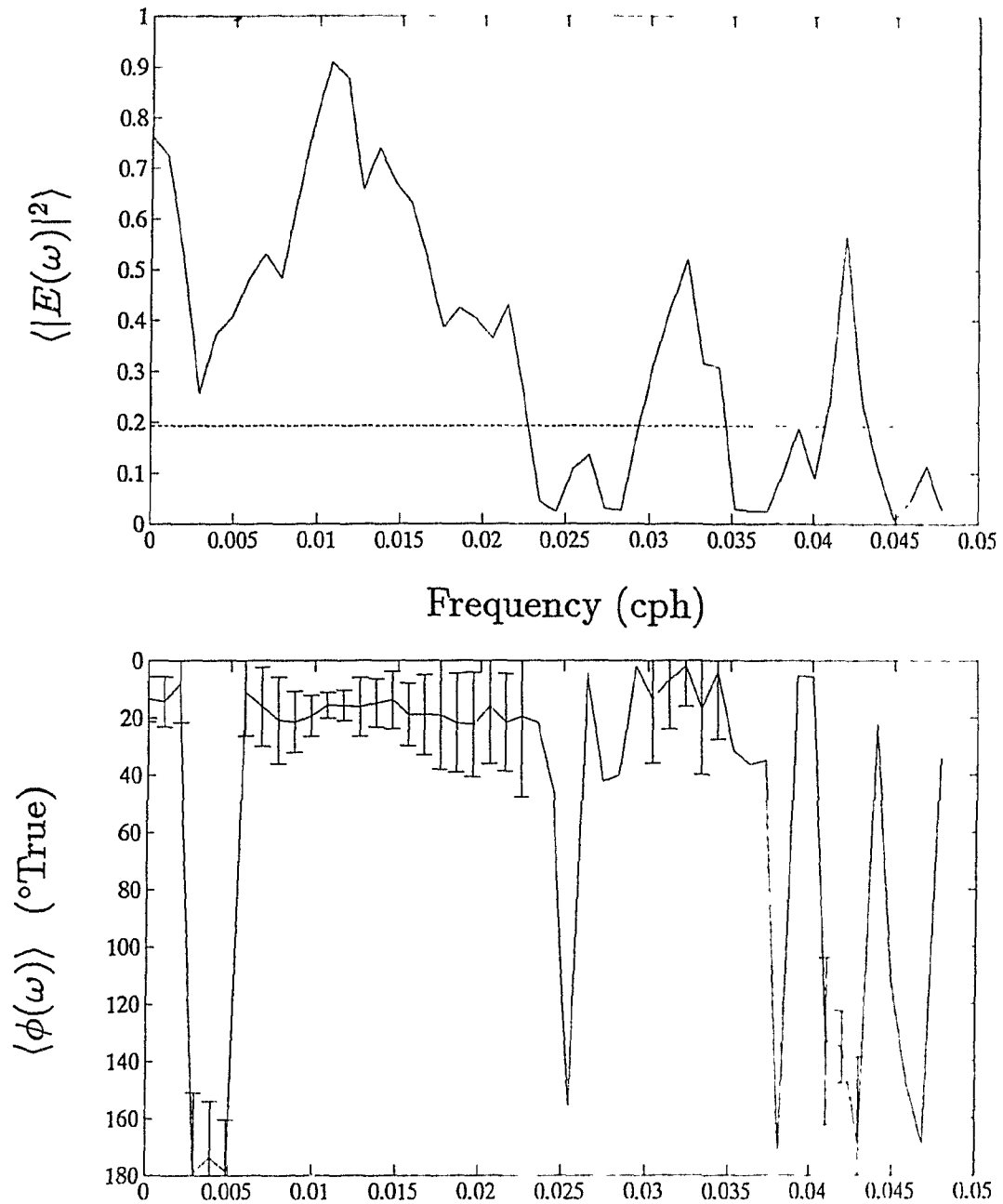


Figure 6.8: Current ellipse orientation and stability 50m above the bottom at mooring 636. The dashed line on the upper plot represents the 95% significance level for zero true coherence between clockwise and anticlockwise velocities. The 95% confidence intervals for ellipse orientation are shown on the lower plot ( $\nu = 30$ ).

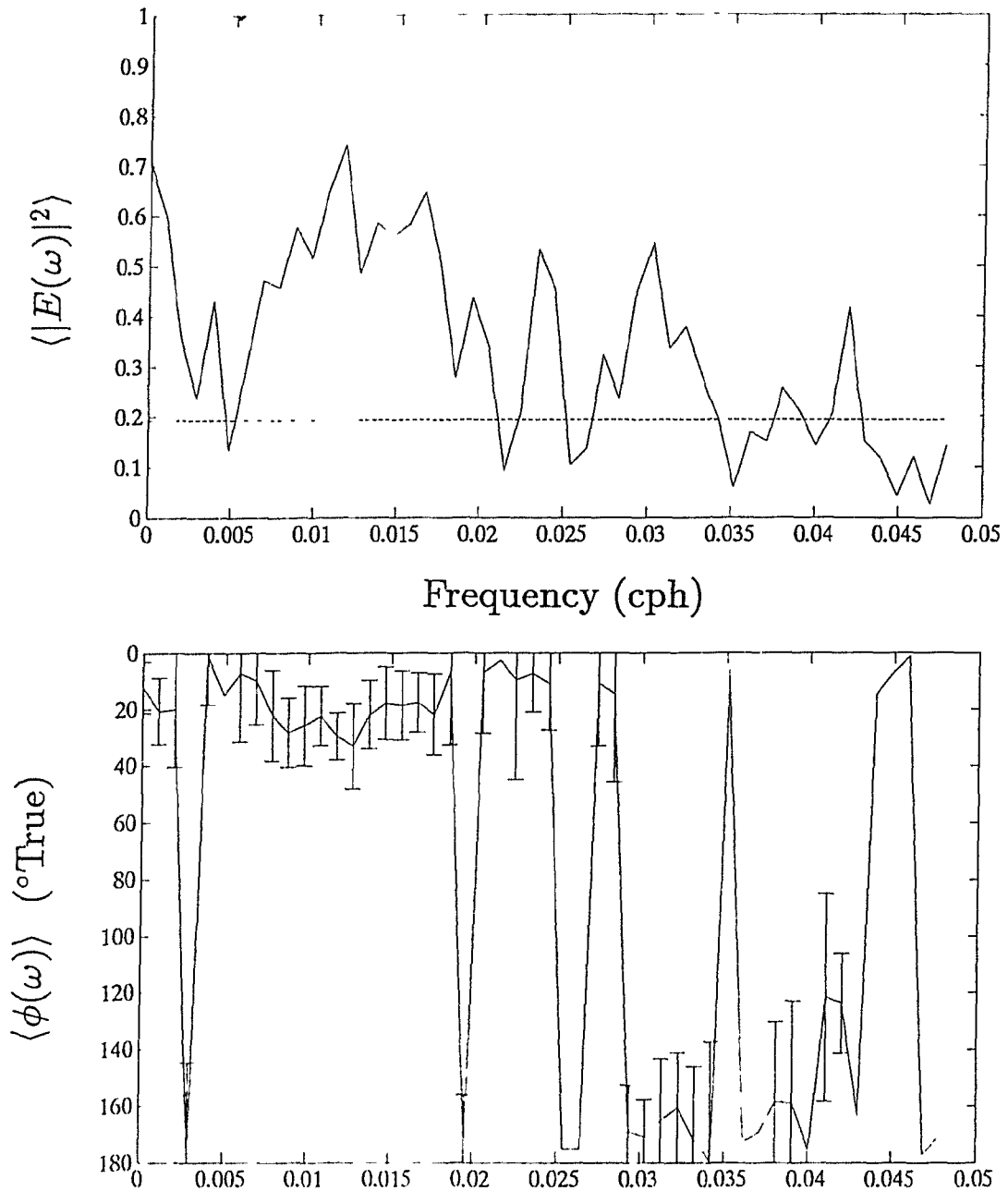


Figure 6.9: Current ellipse orientation and stability 100m above the bottom at mooring 636. The dashed line on the upper plot represents the 95% significance level for zero true coherence between clockwise and anticlockwise velocities. The 95% confidence intervals for ellipse orientation are shown on the lower plot ( $\nu = 30$ ).

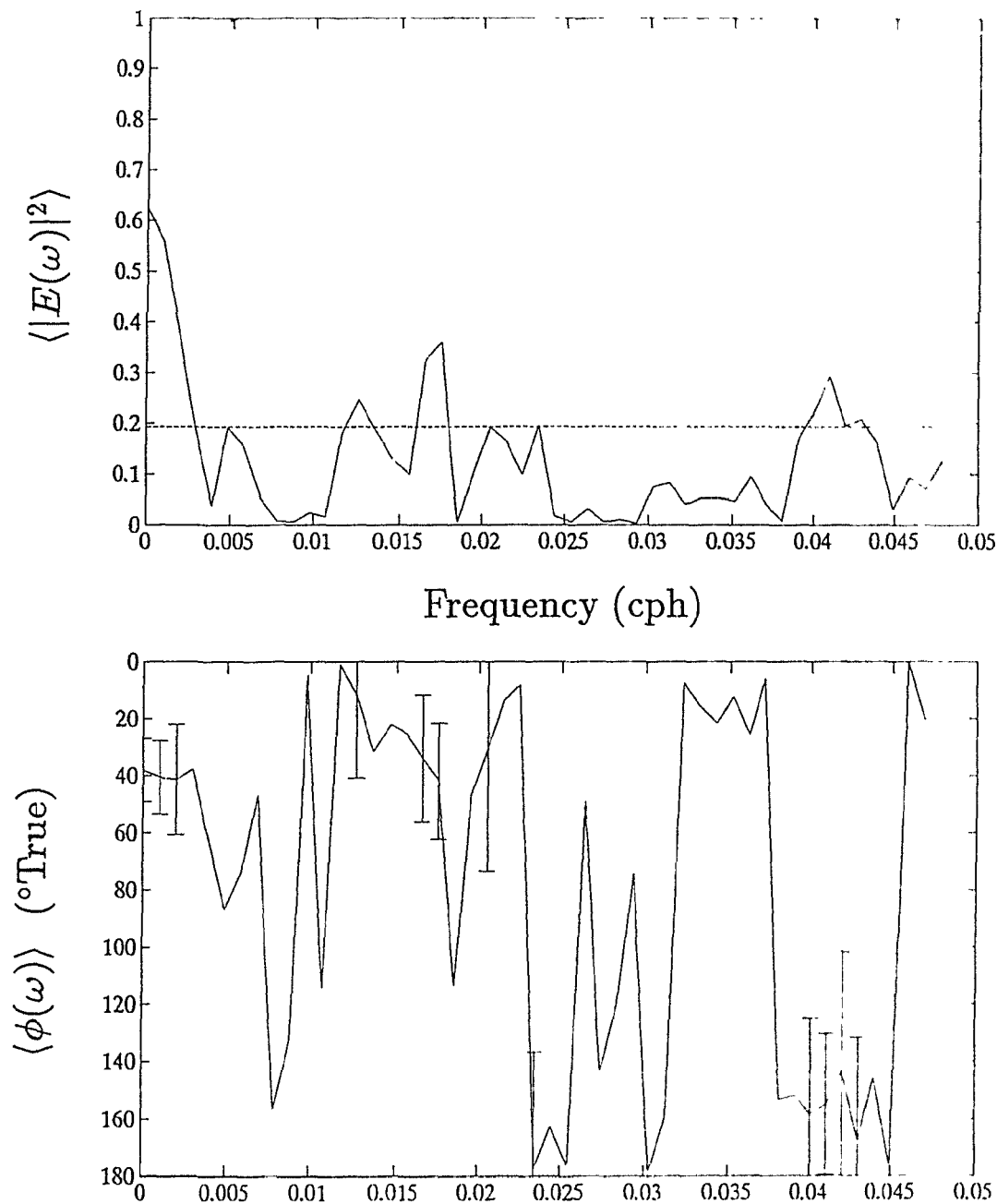


Figure 6.10: Current ellipse orientation and stability 200m above the bottom at mooring 636. The dashed line on the upper plot represents the 95% significance level for zero true coherence between clockwise and anticlockwise velocities. The 95% confidence intervals for ellipse orientation are shown on the lower plot ( $\nu = 30$ ).

## 6.4 Power spectral analysis at mooring 637

Mooring 637 was deployed 40 *km* to the east of mooring 636, near the top of an abyssal hill, at a depth of 4304m (see figure 6.1). Figures 6.11, 6.12 and 6.13 show the kinetic energy spectra, temperature spectra and ratio  $P_{++}/P_{--}$  50m, 100m and 200m above the bottom at mooring 637. Data from the current meter 10m above the bottom were judged to be of lesser quality by NODC (National Oceanographic Data Center), and so were not sent to me. Comparing those figures with the corresponding ones from mooring 636, we notice major differences, but also some similarities.

A first obvious difference in the kinetic energy spectra is that an inertial peak ( $f = 5.87 \times 10^{-3}cph$ ) is present at mooring 637, whereas it could not be discerned at mooring 636 (figure 6.4). It is possible that the inertial peak at mooring 636 was simply overshadowed by the broadband energy enhancement centered at  $\omega = 0.0117cph \sim 2f$ .

A second difference is that while mooring 637 shows some near-bottom kinetic energy enhancement at  $\omega = 0.0117cph$ , the energy levels are not nearly as elevated as at mooring 636; comparing the 50m records from each mooring, we find that the spectral level at mooring 637 is about 5 times lower than at mooring 636. The range of frequencies over which we observe near-bottom kinetic energy enhancement is also narrower at mooring 637.

Now turning our attention to figure 6.12, we find that the 50m and 100m records both show increased temperature variance at  $\omega = 0.0117cph$ . The peak at 100m is narrow, whereas the peak at 50m is broad, extending from  $0.0117cph$  to  $0.0156cph$ . 200m above the bottom, a peak at  $\omega = 0.0117cph$  is also present, but its relative size compared to neighbouring peaks is much smaller.

Finally, looking at figure 6.13, we find that the ratio  $P_{++}/P_{--}$  is close to the internal wave line for  $\omega \geq 0.0117cph$  at all heights above the bottom, in sharp contrast with figure 6.6. Yet we should note that there is some similarity between  $P_{++}/P_{--}$  200m above the bottom at mooring 636, and  $P_{++}/P_{--}$  50m above the bottom at mooring 637, both of which were approximately at the same depth.

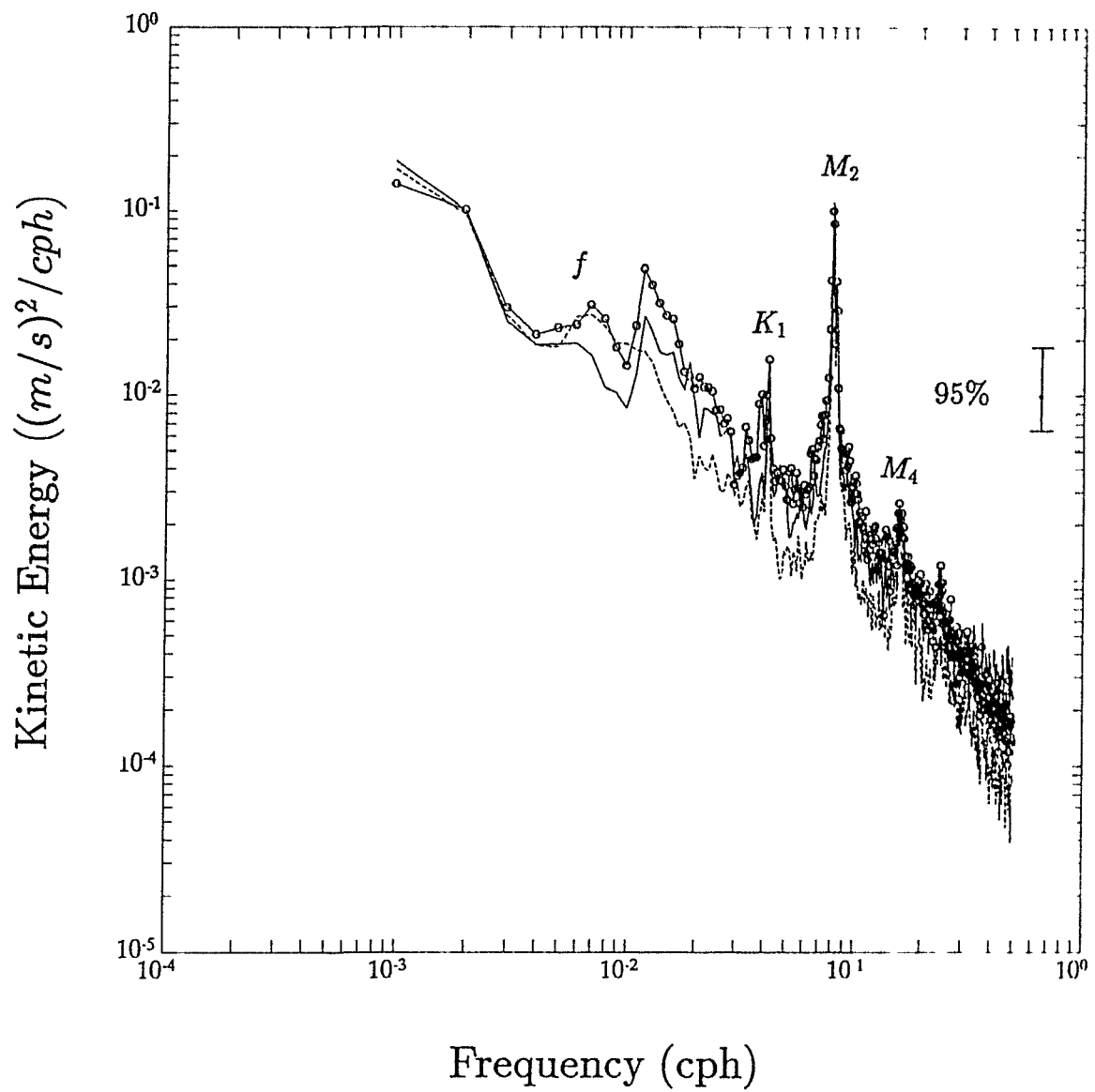


Figure 6.11: Kinetic energy spectra 50m ( o ), 100m (—) and 200m ( - - - ) above the bottom at mooring 637 ( $\nu = 30$ ).

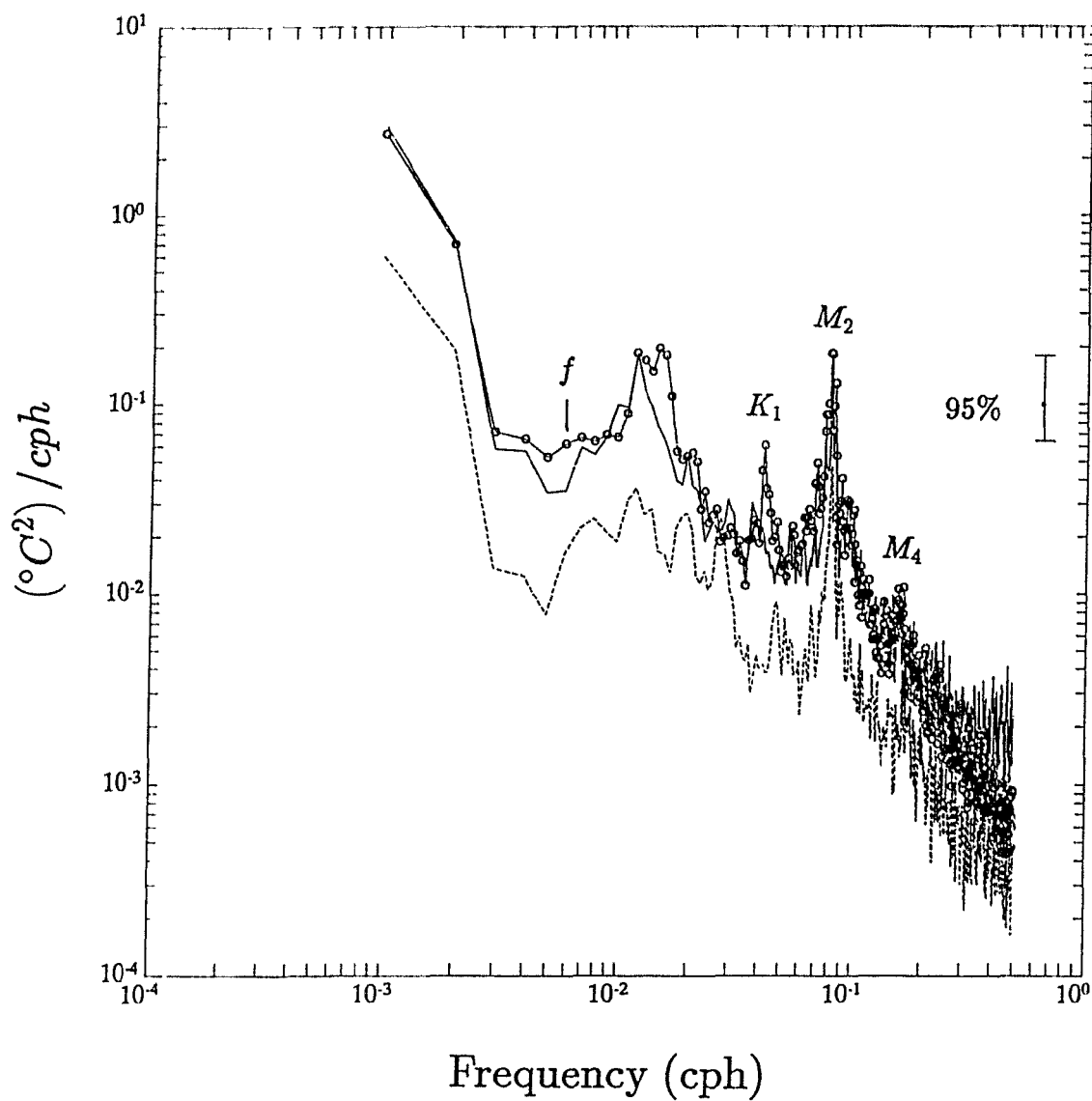


Figure 6.12: Temperature spectra 50m ( o ), 100m (—) and 200m (- - -) above the bottom at mooring 637 ( $\nu = 30$ ).

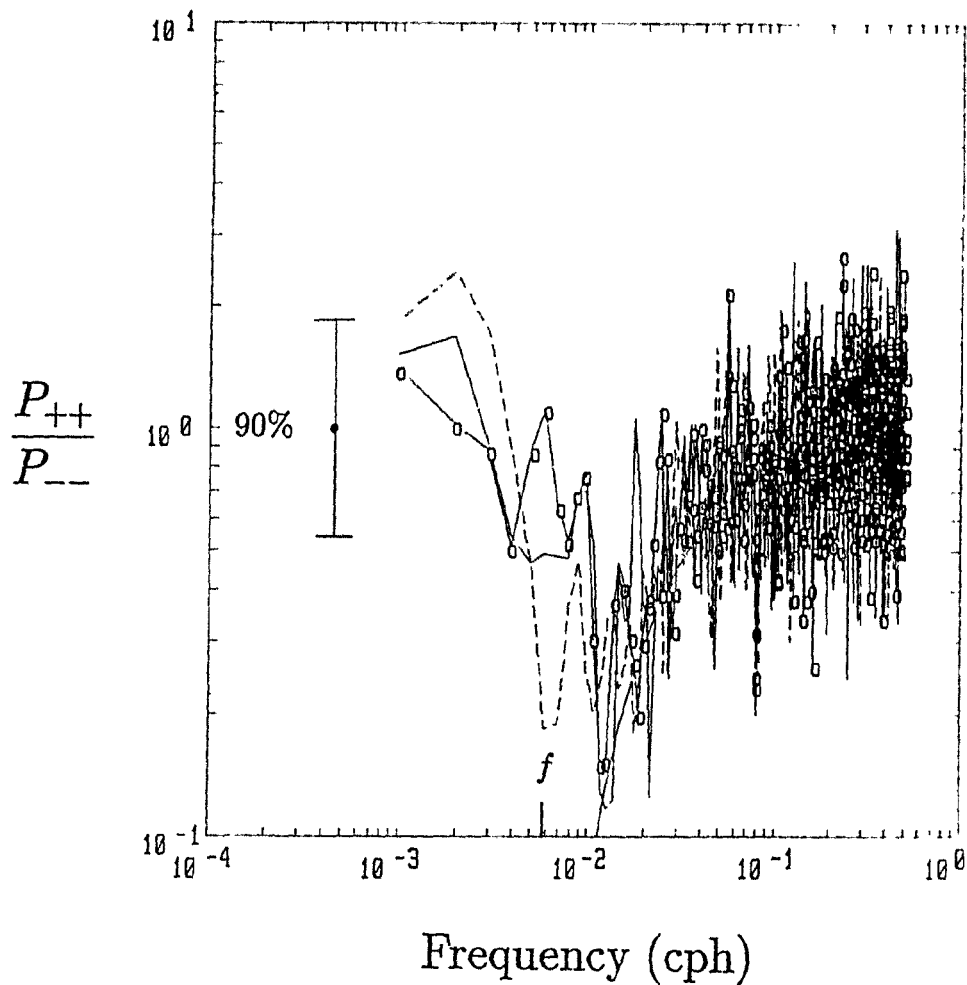


Figure 6.13: Ratio  $P_{++}/P_{--}$  at 50m ( $\circ$ ), 100m ( $-$ ) and 200m ( $- -$ ) above the bottom at mooring 637 ( $\nu = 30$ ). The theoretical ratio (6.3) for linear, freely-propagating internal waves, is shown for the purpose of comparison. The 90% confidence intervals assume a Fisher's F distribution for the ratio of two independent chi-squared distributions.

## 6.5 Cross-spectral analysis

### 6.5.1 In the horizontal: mooring 636 versus mooring 637

Since moorings 636 and 637 both display near-bottom energy enhancement at  $\omega = 0.0117\text{cph}$ , it seems worthwhile to find out whether motions at the two moorings are correlated at that frequency.

Figure 6.14 shows cross-spectra between the current meter 200m above the bottom at mooring 636, and the current meter 50m above the bottom at mooring 637 (4256m and 4254m deep respectively), for the clockwise velocity and temperature signals. The cross-spectrum for anticlockwise velocity is not shown due to a lack of coherence, and also because  $P_{++}/P_{--} \ll 1$  at  $\omega \approx 0.0117\text{cph}$  for those two current meters.

For the clockwise velocity signals, there is a strong coherence peak at the semidiurnal tide (not shown on figure 6.14), a few weak peaks near the diurnal tide, and another peak spreading across four adjacent frequency bins from 0.0117cph to 0.0146cph. The latter coherence peak coincides perfectly with the range of frequencies with the most kinetic energy within the internal waveband 50m above the bottom at mooring 637 (figure 6.11). The clockwise velocity signals are not significantly out of phase in that frequency band (0.0117cph–0.0146cph).

For the temperature signals, the strongest correlation peak occurs at low frequencies, due to the strong two-month flow oscillations (figure 6.2), but significant correlation peaks are also found at the diurnal frequency, and at 0.0137–0.0146cph, where the temperature signals are not significantly out of phase. Note that 50m above the bottom at mooring 637, the maximum temperature variance within the internal waveband occurred at 0.0146cph (figure 6.12).

### 6.5.2 In the vertical: mooring 636

I also computed cross-spectra between like components of the motion at various heights above the bottom at mooring 636. This was done for clockwise velocity, anticlockwise velocity, East velocity, North velocity, and temperature, between all possible pairs of current meters (200m–100m, 200m–50m, 200m–10m, 100m–50m,

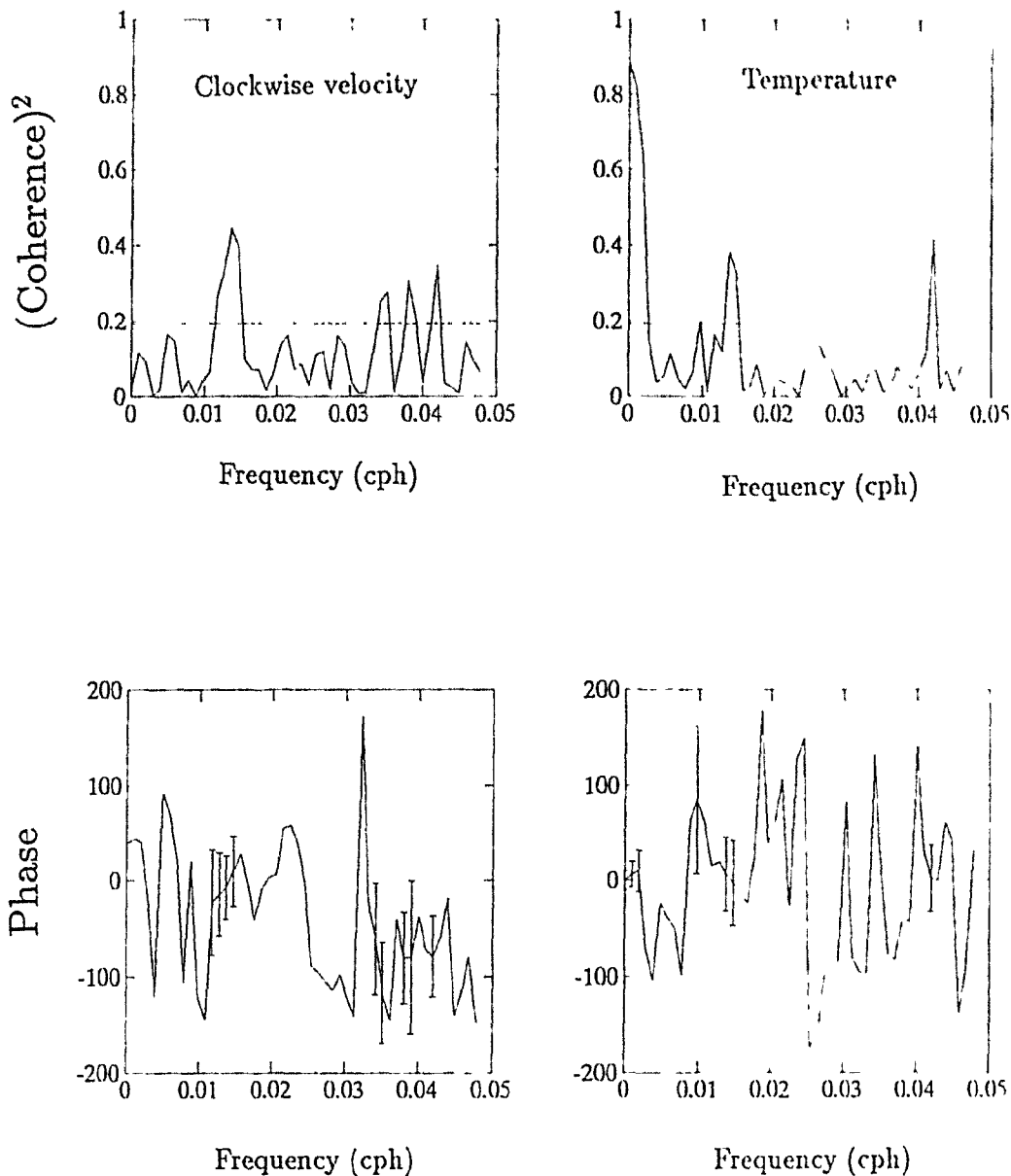


Figure 6.14: Cross-spectra between the current meter 200m above the bottom at mooring 636, and the current meter 50m above the bottom at mooring 637, both of which were at the same depth. The cross-spectrum for clockwise velocity is shown on the left, and that for temperature is shown on the right. A positive phase means that the signal at mooring 637 leads the signal at mooring 636. The dashed line represents the 95% significance level for zero true coherence on the upper plots, and the 95% confidence intervals for phase are shown on the lower plots ( $\nu = 30$ ).

100m–10m and 50m–10m).

Figure 6.15 shows some of the results obtained for the temperature signals. The results obtained for the velocity signals, especially for the North velocity component which dominates the records, are similar and so are not described.

We can see on figure 6.15 that for the 50m–10m pair of current meters, the temperature signals are highly correlated between 0.004cph and 0.025cph, where they are not significantly out of phase. For the 100m–10m pair of instruments, the signals are correlated between 0.006cph and 0.022cph, where they are not significantly out of phase for the most part. However, there is a suggestion that the temperature record at 100m may lead that at 10m by  $\approx 20^\circ$  (the phase difference is significantly different from zero for 5 out of 17 frequency bins between 0.006cph and 0.022cph, suggesting more than pure randomness). For the other pairs of current meters, the temperature signals are also correlated over a broad range of frequencies centered at  $\omega \approx 0.012cph$ , and the phase lead or lag is generally not significantly different from zero.

## 6.6 Complex demodulation at $\omega = 0.0117cph$ .

One of the goals of this chapter was to investigate whether the energy enhancement near  $\omega = 0.0117cph$  at mooring 636 could be due to something other than internal wave reflection off a sloping bottom. With that in mind, I now examine the possibility that the energetic motions with 3–4 day periods might be generated by lower frequency motions, such as the pulses of AABW into the Northwest Atlantic with roughly 60–day periods (figure 6.2).

After multiplying the original time series by  $\exp(-i\omega t)$ , where  $\omega = 0.0117cph$ , I low-passed the resulting time series with the same filter as in section 6.1, i.e. with a triangular window whose transfer function has its first zero at a period of 7.1 days (the pass band is  $0.0117 \pm 0.0059cph$ ).

The East and North components of the demodulated currents are plotted on figure 6.16, where we see that the north velocity component at 10m and 50m is dominated by two large bursts of energy, near days 380 and 620. Comparing figure 6.16 with figure 6.2, we see that those bursts are not related in any obvious way to fluctuations

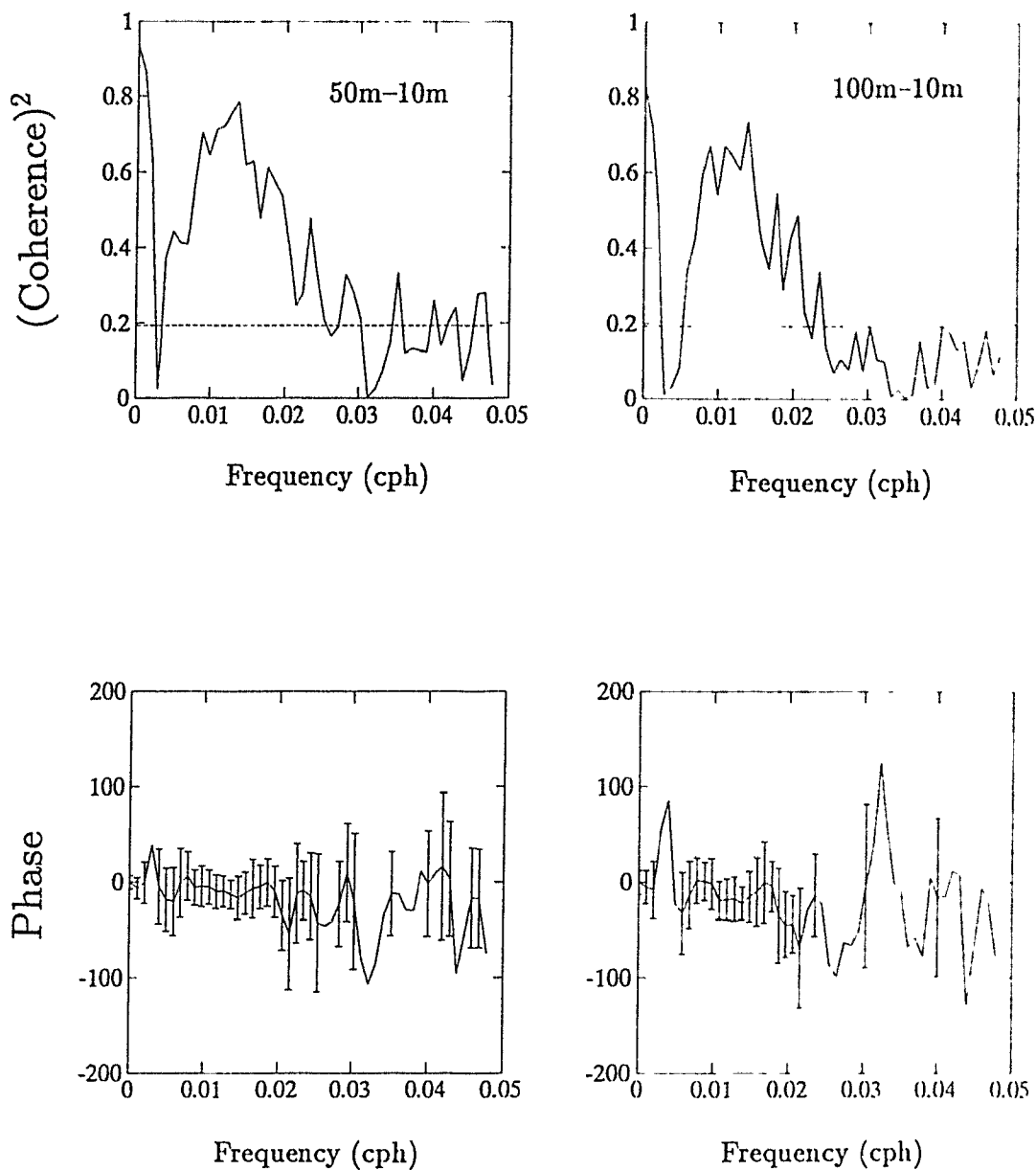


Figure 6.15: Temperature cross-spectra, for the 50m-10m pair of current meters (left), and the 100m-10m pair of current meters (right), at mooring 636. On the upper plots, the dashed line represents the 95% significance level for zero true coherence. The 95% confidence intervals for phase are shown on the lower plots ( $\nu = 30$ ). A positive phase means that the 10m signal leads the signal at 50m or 100m.

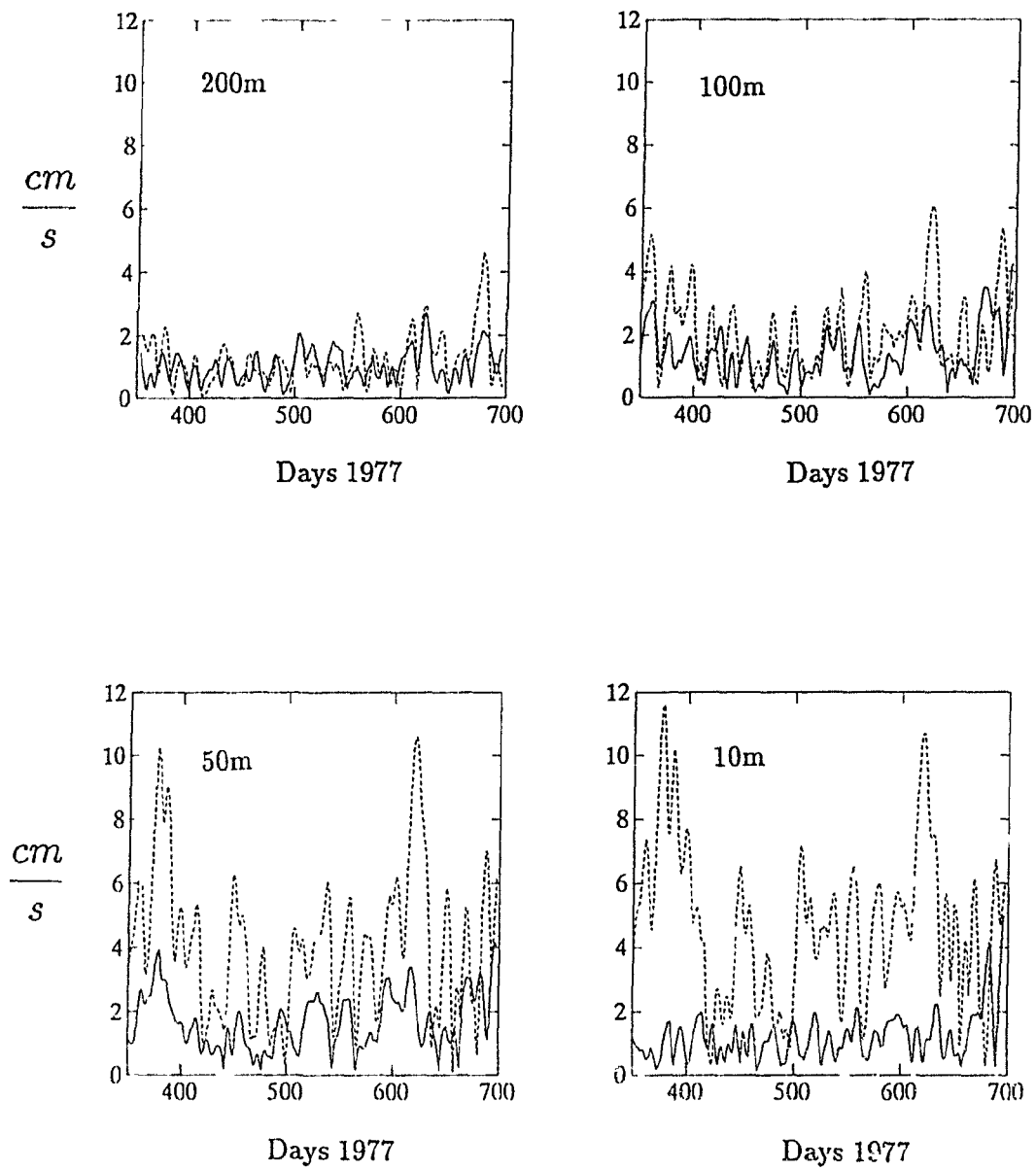


Figure 6.16: East (—) and North (- - -) components of the velocity complex demodulated at  $\omega = 0.0117cph$  10m, 50m, 100m and 200m above the bottom at mooring 636. The plots start on day 350, 1977, and end on day 332, 1978 (day 697 here).

of the low-frequency flow.

To be more quantitative about this, I computed cross-spectra between the complex demodulated currents shown on figure 6.16, and the low-frequency currents shown on figure 6.2. For the energetic north velocity component, no significant correlations were obtained at 10m above the bottom. A few marginally significant correlation peaks were obtained at other heights above the bottom, but they all occurred at different frequencies, suggesting they may be purely random. Hence there seems to be no clear relationship between the low-frequency currents and the currents demodulated at  $\omega = 0.0117cph$ . The same conclusion holds for the temperature signals as well.

## 6.7 Discussion

Eriksen (1982) pointed out that while the energetic motions with  $\omega \approx 0.012cph$  at mooring 636 could be due to critical internal wave reflection, they violate one of the basic criteria listed in section 5.3.2, namely that the major axis of the current ellipses should be oriented normal to the isobaths. This is not a trivial discrepancy, as the mechanism leading to energy enhancement near the critical frequency involves a 'squeezing' of the reflected wavebeam (relative to the width of the incident wavebeam) in the vertical plane normal to the isobaths (figure 2.2). It is hard to envisage how internal wave reflection could lead to enhanced motions in a vertical plane roughly parallel to the isobaths, as seems to be the case here.

Another puzzling feature of the motions with  $\omega \approx 0.012cph$  at mooring 636 is that they do not satisfy the consistency relation (2.18) for freely-propagating internal waves (figure 6.6). At 10m and 50m above the bottom, those motions are essentially rectilinear, apparently more consistent with the prediction of Rhines (1970) for internal edge waves (2.95). Agreement with Rhines' theory is only partial however, since the orientation of those quasi-rectilinear motions does not vary with frequency according to (2.97), as can be seen on figures 6.7, 6.8 and 6.9.

### 6.7.1 Horizontal and vertical cross-spectra

Results obtained from the horizontal and vertical cross-spectra do not seem to support the critical internal wave reflection hypothesis either. Figure 6.14 shows that for  $\omega \approx 0.012cph$ , the motions at mooring 636 are coherent with those at mooring 637, some 40 km away. Significant coherences within the internal waveband over horizontal distances of the order of a few tens of kilometers are rare but not unheard of in the deep ocean. For example, Fu (1981) obtained significant coherences over horizontal separations up to 70 km at mid-latitudes for the inertial frequency.

For the mid-latitude internal wave model proposed by Garrett and Munk (1972), the horizontal distance at which the coherence drops to 0.5 is given by

$$\Delta X_{0.5} = \frac{58m \cdot 3cph}{(\omega^2 - f^2)^{1/2}}, \quad (6.6)$$

where  $\omega$  and  $f$  are expressed in *cph*. For  $\omega = 1.17 \times 10^{-2}cph$  and  $f = 5.87 \times 10^{-3}cph$ , this yields  $\Delta X_{0.5} = 17km$ , so that the coherence should be less than 0.5 (or the squared coherence should be less than 0.25) at a separation of 40 km. Rearranging terms in the above formula, we could alternatively evaluate  $\omega_{0.5}$  for  $\Delta X = 40km$ , obtaining  $\omega_{0.5} = 7.3 \times 10^{-3}cph = 1.24f$ .

A direct comparison of this prediction with figure 6.14 is not warranted, as the latter does not show a 'monotonic' decrease of coherence with frequency in the internal waveband, but we find that the squared coherence on figure 6.14 is larger than 0.25 at  $\omega \approx 0.012cph$ .

Such a high coherence over a distance of 40km is rather surprising, because Wunsch and Webb (1979) and Eriksen (1980) showed that at low latitudes, currents are generally coherent over smaller spatial scales than at mid-latitudes, not the opposite. The observed coherence becomes doubly puzzling when we consider the fact that based on the critical internal wave reflection hypothesis, the observed field of motions, if dominated by the reflected wavefield, should be unusually rich in motions with small horizontal and vertical scales (figures 2.2 and 2.4).

The horizontal and vertical scales of motion should be reduced by the same factor upon reflection, because conservation of frequency implies that  $\tan \theta_r = \tan \theta_i$ , which

in turn implies that  $m_r/m_i = \kappa_r/\kappa_i$ , where  $m$  and  $\kappa$  are the vertical and horizontal components of the wavenumber vector respectively.

Just as figure 6.14 suggests large horizontal scales of motion, figure 6.15 suggests that the dominant vertical scales of motion at mooring 636 are large too. For all pairs of instruments in the vertical, the phase leads or lags are generally not significantly different from zero in the frequency band of interest ( $\omega \approx 0.012cph$ ). This is true for all the signals analysed: clockwise velocity, anticlockwise velocity, East velocity, North velocity and temperature.

### 6.7.2 Harmonic generation of the peak at $\omega \approx 2f$ ?

The largest spectral enhancement at mooring 636 occurs at about twice the inertial frequency ( $\omega \approx 2f \pm 0.17f$  for the spectral resolution used in figure 6.4). Is this purely coincidental? Could spectral enhancement at  $\omega \approx 2f$  result from non-linear effects involving the inertial frequency  $f$ ?

For the case of the  $M_2$  tide, non-linear effects generally give rise to an  $M_4$  peak which is smaller than the 'parent'  $M_2$  peak (figure 5.15 is really an exceptional case). Therefore, if the example of the tide is at all relevant, it becomes hard to explain how a large energy peak at  $\omega \sim 2f$  might result from non-linear effects at mooring 636, given the absence of an inertial peak at that location.

### 6.7.3 Alternative explanation for $P_{++}/P_{--} \approx 1$ near the bottom at mooring 636.

Could the 3-4 day motions be internal waves, and yet not satisfy (2.18)? Looking at figure 6.1, we see that the seamount or ridge on which mooring 636 lies is not isolated; it effectively lies within a 'valley' whose width is only of the order of a few tens of kms.

Now Gill (1982, p.248) suggests that for internal waves, rotation effects become important only when the horizontal scale of motion exceeds the vertical scale by a factor of  $N/f$ . For the case at hand, it seems reasonable to assume that the horizontal scale of motion  $L$  cannot exceed the width of the valley, and so I let  $L \lesssim 32\text{km}, 35\text{km}$ ,

40km and 90km at 10m, 50m, 100m and 200m above the bottom respectively.

For the vertical scale of motion  $H$ , I pick  $H \gtrsim 1500m$ . This choice is consistent with estimates of the dominant vertical scale of motion, based on the phase lags shown on figure 6.15 for the 100m–10m pair of current meters. For those values of  $L$  and  $H$ , I get  $L/H \lesssim 21, 23, 27$  and  $60$  at 10m, 50m, 100m and 200m above the bottom respectively, compared with  $N/f \approx 150$  using the values of  $N$  found in table 6.2.

Those values of  $L/H$  are only approximate, but they qualitatively support the claim that internal wave current ellipses could be very flat, with  $P_{++}/P_{--} \approx 1$  near the bottom at mooring 636. As for the preferred orientation of the ellipses, nearly due North and aligned with the low-frequency flow oscillations, it could also be due to the narrowness of the valley, a few tens of *kms* wide compared to a few hundreds of *kms* for the internal Rossby radius of deformation  $NH/f$  at that latitude; the major axis of the current ellipses could then be parallel to the longitudinal axis of the valley (e.g. Artale and Gasparini, 1990). Due to its poor resolution, the most detailed bathymetric map for the area (Moody et al., 1979) does not allow us to determine the orientation of that hypothetical valley, but figures 6.7 and 6.8 would suggest a roughly North–South orientation.

# Chapter 7

## Conclusions and Discussion

In the first part of this chapter, I give a summary of the material presented in previous chapters, reemphasizing only the most crucial points. This is followed by a discussion based on the principal conclusions of the thesis.

### 7.1 Summary of the thesis

In chapter 1, I put the problem of internal wave reflection off sloping bottoms into its oceanographic context, mentioning the claim by Eriksen (1985) that it could be the dominant cause of diapycnal mixing in the deep ocean. Following Garrett and Gilbert (1988), I also discussed the energetic requirements of an effective diapycnal mixing for the ocean that would arise solely from vigorous mixing at ocean boundaries, followed by advection and stirring into a quiescent ocean interior.

In chapter 2, I reviewed some of the basic concepts of linear internal wave theory, and derived the laws of specular internal wave reflection off sloping topography. Those laws predict that upon reflection, the wavenumber of the incident waves should be amplified over a wide range of frequencies and incident azimuthal angles (figure 2.4). At the critical frequency  $\omega_c$ , for which the slope of internal wave rays matches the bottom slope, there is a singularity in the wavenumber amplification. According to linear, inviscid, specular reflection theory, this should lead to large enhancements in energy density and vertical shear near  $\omega_c$ .

In chapter 3, the consequences for ocean mixing of such increases in vertical shear and energy density were examined, based on the model of Garrett and Gilbert (1988). Their estimates of the rate of energy dissipation  $F_{ds}$ , due to shear instability of the reflected waves, are generally less than  $1mW \cdot m^{-2}$  for realistic values of the bottom slope  $\tan \alpha$  and the ratio  $f/N$  of the inertial to the buoyancy frequency (figure 3.2). This is more than one order of magnitude lower than Eriksen's (1985) estimates of the redistributed energy flux ( $10\text{--}30 mW m^{-2}$ ), and does not seem large enough to sustain a vertical eddy diffusivity of  $10^{-4}m^2s^{-1}$  in the ocean interior.

In the rest of chapter 3, I dealt with the energy spectrum that is left after elimination of the waves that are assumed to undergo shear instability, and break upon reflection. I referred to this spectrum as the residual energy spectrum, and derived a simple analytical formula for its total energy content, using the same approximations as Garrett and Gilbert (1988) in their derivation of the reflected shear spectrum.

As a complement to the work of Garrett and Gilbert (1988), I calculated the rate of energy dissipation  $F_{dr}$  that could be associated with bottom drag caused by the residual currents. I found that  $F_{dr}$  is always less than  $0.7mW \cdot m^{-2}$  for  $N = 10^{-3}s^{-1}$  (figure 3.10). As we would expect the mixing efficiency  $\Gamma$  to be much smaller than 0.25 for energy dissipation within the benthic boundary layer, those estimates of  $F_{dr}$  probably cannot sustain an effective vertical diffusivity of  $10^{-4}m^2s^{-1}$  in the ocean interior either (1.2). Finally, the distribution of the residual energy in frequency, wavenumber and azimuthal space was shown to be quite different from that of the canonical GM79 spectrum (figures 3.6, 3.7 and 3.9). Further energy dissipation may result from the relaxation of the residual spectrum back to a more typical form, but this was not quantified.

In chapter 4, I drew attention to how little is known about the interaction of internal waves with irregular topography. Idealised topographic shapes were considered in an attempt to understand some aspects of the scattering problem, neglecting topographic variations in the alongslope direction in all cases. Among other things, I pointed out that the approach taken by Rubenstein (1988) to investigate the scattering of near-inertial waves off irregular topography, using a Fourier representation of abyssal hill topography together with Baines' (1971a) linear solution for sinusoidal

topography, is inappropriate. I also pointed out that the solutions of Baines (1971b, 1974) lead to the conclusion that the kinetic energy density at the critical frequency should be less above concave than above convex topography. And last but not least, I pointed out, using specular reflection theory as a first approximation, that rapid variations of the internal wavefield can be expected above a non-uniformly sloping bottom (figures 4.5 and 4.6). The energy redistribution inferred by Eriksen (1982, 1985), from observations made at different heights above the bottom at a few mooring sites, could therefore be largely due to geometric effects.

In chapter 5, I used historical current meter data from the Scotian Rise and Slope in order to look for evidence of critical internal wave reflection. To that end, a set of criteria was proposed and discussed in section 5.3.2, and then applied to the data. I found some evidence of energy enhancement at  $\omega_c \approx f$  in a few cases (see table 5.4). At moorings S3 and S7 (see figure 5.1), where  $\omega_c \approx M_2$ , I found that current ellipses tended to be oriented normal to the isobaths throughout most of the internal waveband (e.g. figure 5.11). I suggested that those observations could be due to internal wave reflection, but could also be attributed to internal tide generation or reflection, followed by a non-linear energy cascade to higher frequencies. The latter possibility was examined in light of the theory of Thorpe (1987b).

In chapter 6, I reexamined data from mooring 636 of the Western Boundary Sill Experiment to verify whether the energetic 3–4 day motions seen at that mooring are due to critical internal wave reflection, as postulated by Eriksen (1982). I found as he did that the motions are parallel to the inferred orientation of the isobaths, not normal to them, thus violating one of the predictions of specular internal wave reflection theory (figure 2.5).

Moreover, I found that the 3–4 day motions are coherent over a horizontal scale of at least 40km. Such a large coherence scale appears to be inconsistent with the transfer of energy to smaller scales that should occur due to internal wave reflection. The 3–4 day motions are also coherent over at least 200m in the vertical at mooring 636, and the measured phase leads or lags are generally not significantly different from zero, implying large vertical scales of motion.

I also found that the ratio of anticlockwise to clockwise kinetic energy  $P_{++}/P_{--}$  for

the 3–4 day motions 10m and 50m above the bottom at mooring 636 does not satisfy (2.18), predicted for linear internal wave theory, but is more consistent with (2.95) instead, predicted for Rhines' (1970) internal edge waves (see figure 6.6). However, agreement with the theory of Rhines is rather limited, as the current ellipses do not turn with frequency according to (2.97) (see figures 6.7, 6.8 and 6.9).

Since mooring 636 lies within a 'valley' whose width is small compared to the internal Rossby radius of deformation, it seems possible that the preferred orientation of the motions in the North-South direction at 10m, 50m and 100m above the bottom is in fact parallel to the longitudinal axis of that valley.

### Principal Conclusions

1. The process of internal wave reflection off sloping topography probably leads to rates of energy dissipation near the boundary that are much smaller than claimed by Eriksen (1985). As they stand, the estimates of  $F_{ds}$  and  $F_{dr}$  given in chapter 3 do not seem large enough to sustain an effective vertical eddy diffusivity of  $10^{-4}m^2s^{-1}$  in the ocean interior, but are within the right order of magnitude. Further energy dissipation might result from the relaxation of the residual spectrum back to a more typical form.
2. Locally concave topography should tend to inhibit energy enhancement at the critical frequency  $\omega_c$ , due to destructive interference of the reflected waves near the critical point.
3. Rapid variations of internal wave spectra with height above the bottom can be expected for purely geometric reasons above non-uniformly sloping topography, and need not result solely from non-linear and viscous processes.
4. Current meter data from the Scotian Rise and Slope show signs of critical internal wave reflection at a few mooring sites. However, due to the fact that  $\omega_c \approx f$  or  $M_2$  at the majority of the moorings, it is difficult to offer a completely unambiguous interpretation of the data in favor of the critical reflection hypothesis.

5. The pronounced near-bottom enhancement of 3–4 day motions observed by Eriksen (1982) at WBSE mooring 636 does not seem to be consistent with internal wave reflection theory. It is not consistent with Rhines' internal edge waves either. The narrow width of the 'valley' within which mooring 636 was deployed seems to affect the nature of the observed motions, whether trapped or propagating.

## 7.2 Discussion and suggestions for future work

Although the estimates of the rates of energy dissipation  $F_{ds}$  and  $F_{dr}$  given in chapter 3 are apparently too low to satisfy  $\Gamma F_d \approx 0.3mW m^{-2}$ , required by the boundary mixing hypothesis, they are within the right order of magnitude. In fact it is possible that when the rate of energy dissipation due to internal wave reflection off sloping bottoms is added to the rates of energy dissipation due to other mechanisms, such as the generation of the internal tide by the surface tide (e.g. Munk, 1966, Bell, 1975a), or the bottom drag associated with the mean currents (Armi, 1978), the total energy dissipation rate  $F_d$  from all of those processes may be large enough that  $\Gamma F_d \approx 0.3mW m^{-2}$  would be satisfied.

More theoretical and observational work is thus necessary before a definitive statement about the importance of internal wave reflection off sloping bottoms as a boundary mixing mechanism can be made. Some of the necessary studies are discussed below.

### Theoretical studies

Figures 3.6, 3.7 and 3.9 show that the distribution of energy in the residual spectrum of Garrett and Gilbert (1988) is very different from that of the canonical GM79 model spectrum. Can the existing theories of non-linear interactions among internal waves help resolve the issue of how the residual spectrum might relax back to a more typical shape, and what would be the additional energy dissipation rate associated with that relaxation?

The residual spectrum has much more energy than the GM79 model spectrum over a wide range of frequencies centered about  $\omega_c$  (figure 3.6). The relaxation of a small spike on an otherwise smooth spectrum was studied by McComas (1977), under the assumption of weakly non-linear interactions, but in light of the criticism of Holloway (1980), it seems very unlikely that weakly non-linear theory could adequately describe the relaxation of the residual spectrum back to a more typical shape.

The eikonal approach of Henyey et al. (1986) may seem more promising at first, as it does not assume the interactions are weak, but it involves an assumption of scale separation between the small amplitude 'test waves' and the dominant scales of motion. This assumption breaks down here, as figure 3.7 shows that the residual energy spectrum is white in modenumber space.

It is also worth mentioning that while the weakly non-linear theory has had some success explaining the observed vertical symmetry of the internal wavefield at frequencies well above the inertial frequency (Müller et al., 1986), no attempt has yet been made to explain how an anisotropic internal wavefield, such as the one shown on figure 3.9, may relax to horizontal isotropy. Hence for all of the above reasons, it seems fair to say that in their present state, the existing theories of non-linear energy transfer among internal waves would not allow us to deal properly with the problem of the relaxation of the residual spectrum.

In chapter 4, it was argued that energy enhancement at the critical frequency  $\omega_c$  is less likely to be observed above concave than above convex topography. This is a useful prediction, in that it represents a first attempt at determining which type of conditions may or may not favor energy enhancement (and dissipation) due to the critical reflection of internal waves. Could other factors affect the likelihood of observing energy enhancement at the critical frequency?

I would like to suggest that when  $N \sin \alpha \ll f$  at a given mooring site, so that  $\omega_c \sim f$  (2.29), the orientation of the isobaths could be one such factor. The linear reflection laws of Eriksen (1982), derived in chapter 2 and valid on an  $f$ -plane, predict that maximum wavenumber amplification upon reflection should occur for onslope incident energy propagation (i.e.  $\phi_i = 0$ , see figure 2.4).

However, on a  $\beta$ -plane, near-inertial motions are very unlikely to have  $\phi_i = 0$  when

the onslope direction is poleward, due to the turning latitude effect (Kroll, 1975). This may help explain the overall absence of large energy enhancement at  $\omega_c \sim f$  on the Scotian Rise, where isobaths are oriented roughly East-West, so that near-inertial motions are more likely to have  $\phi_i \approx \pm\pi/2$ . A more quantitative investigation of this phenomenon could probably be carried out using the wave functions of Munk and Phillips (1968).

Further theoretical work on the interaction of internal waves with irregular topography is needed. Alongslope variations of the bathymetry were neglected in chapter 4 for waves incident on a non-uniformly sloping bottom, and were also neglected in the analytical and numerical models of internal tide generation described in chapter 2. This assumption made the problem two-dimensional in both cases, allowing the use of a streamfunction which greatly simplified the mathematics. However, empirical evidence suggests that the neglect of alongslope variations of the bathymetry may not be justified in many situations, at least for the internal tide generation problem.

For instance, using remote sensing techniques, New (1988) found that near the shelf break in the Bay of Biscay area, the main internal wave packets generated by the tide seem to be radiating from topographic ridges between canyons. Sandstrom et al.(1989) also report large internal tides, as well as packets of large amplitude, high frequency internal waves, near a prominent submarine canyon at the edge of the Scotian Shelf. Moreover, Huthnance and Baines (1982) found that the baroclinic tidal currents off Northwest Africa are much stronger than the estimate for internal tides generated by the onshore component of the barotropic tidal current alone. They suggest that the strong baroclinic currents could be caused by the longshore component of the barotropic current interacting with 'unknown' longshore topographic irregularities in the shelf and slope.

For the internal tide generation problem, the inclusion of three-dimensional effects will likely require the introduction of more sophisticated numerical models. However, for the internal wave reflection/scattering problem, specular reflection theory could probably be used as a first approximation to investigate how internal wave spectra vary with height above a non-uniformly sloping bottom, proceeding in a manner analogous to section 4.6, where the radius of curvature of the topography was assumed

much larger than the incident wavelength.

The idealised problem of a horizontally isotropic internal wavefield, incident on a half-sphere which lies on an otherwise flat bottom, could provide us with useful insight about the manner in which the internal wavefield varies with height above a large, isolated seamount, for example. It is necessary that we account for such geometric effects before inferences about the role of non-linear and viscous effects in the rapid spectral changes that occur above sloping bottoms can be made.

When the radius of curvature of the topography is comparable to the incident wavelength, specular reflection theory is still fairly accurate, but as the radius of curvature becomes smaller than the incident wavelength, correction terms to specular reflection theory become increasingly important (Sandstrom, 1972). For internal wave reflection/scattering off rough topography, a question which then arises is: what is the effective bottom slope that is felt by a given incident wavetrain? A rough measure of the steepness of random abyssal hills can be obtained from the empirical topographic spectrum of Bell (1975b, p. 884), which suggests an r.m.s. bottom slope of 0.03, 0.07, and 0.16 when integrated up to topographic wavenumbers  $0.1 \text{ cycle km}^{-1}$ ,  $0.5 \text{ cycle km}^{-1}$  and  $2.5 \text{ cycle km}^{-1}$  respectively. The effective bottom slope felt by a spectrum of incident internal waves should then be a function of the incident wavenumber, with the short waves presumably 'seeing' a steeper bottom than the long waves. Currently available theories of internal wave scattering off irregular topography do not allow us to quantify that statement however.

To better explain some of the observations made at moorings 636 and 637 of the Western Boundary Sill Experiment, an extension of the existing theories of trench waves and/or channel waves would also seem worthwhile. Brink (1983) has shown that for baroclinic trench waves, the alongslope velocity is a maximum at the deepest part of the trench, and then decays with height above that trough, qualitatively consistent with the observations. Figure 1b of Brink (1983) shows that the decay is rapid when the width of the trench is a few times smaller than the internal Rossby radius of deformation, as is the case at mooring 636.

Interpreting the data at moorings 636 and 637 in terms of the theory of Brink (1983) is not justified however, because trench waves require a large depth contrast

between the flat shelf region and the flat-bottom deep ocean; the valley shown on figure 6.1 is only 200m–300m deep in a total fluid depth of about 4500m. Furthermore, whereas Rhines' (1970) bottom-trapped waves may exist above  $f$ , it is far from clear whether some of the results for baroclinic trench waves, derived for  $\omega \ll f$ , would remain valid in the internal waveband.

A careful investigation of the manner in which the consistency relations for internal waves may change as we approach a sloping bottom should also be done. To illustrate the need for this, let us consider the inviscid problem of a wave which reflects off a vertical wall with an oblique azimuthal angle of incidence. The onslope velocity component of the incident and reflected waves must cancel each other at the wall in order to satisfy the boundary condition of no normal flow, but the alongslope velocity component of the incident and reflected waves are phase-locked at the wall and add up constructively. Consequently, in the immediate vicinity of a vertical wall, motions should be rectilinear, and we should have  $P_{++}/P_{--} = 1$  instead of  $P_{++}/P_{--} = [(\omega - f)/(\omega + f)]^2$ . We need to verify whether this result would still hold above sloping topography, as it may explain the variation of  $P_{++}/P_{--}$  with height above the bottom that was observed at mooring 636 for example (figure 6.6).

## Observational studies

More observational studies are also needed if we wish to determine the importance of internal wave reflection off sloping bottoms as an agent of diapycnal mixing in the deep ocean. In fact the final verdict will have to come from the observations.

As a first step, a very inexpensive way of studying internal wave reflection off sloping bottoms would be to analyse the existing data bases of currents and temperature collected above sloping topography, and look for evidence of energy enhancement at the critical frequency  $\omega_c$ , as was done in chapter 5. The analysis of data from a variety of locations may reveal whether factors such as boundary concavity, or the orientation of the isobaths, tend to favor or inhibit energy enhancement at the critical frequency. We should also gain a better knowledge of the climatology of the internal wavefield above sloping bottoms from that exercise.

New experiments aimed specifically at studying the problem of internal wave reflection off sloping bottoms should involve a dense sampling of the water column in the first 100m or so above the bottom. Armi and D'Asaro (1980) have investigated the structure of the boundary layer over flat topography, on the Hatteras abyssal plain, with current meters at 15m, 25m, 35m, 45m, 55m, 65m and 85m above the bottom at one of their moorings, but such detailed current measurements have not been performed above sloping topography yet.

Locations where  $\omega_c \approx f$  or  $M_2$  may yield results that are harder to interpret in terms of the critical internal wave reflection hypothesis. However, they should not be avoided, as inertial and tidal motions are usually the most energetic signals within the internal waveband, and hence are the most likely to lead to large values of the rate of energy dissipation. Some of the ambiguity in the results obtained from moorings where  $\omega_c \approx f$  could easily be removed by taking into account the slantwise propagation of inertial wave packets. The comparison of spectral peaks at  $\omega_c$  in an oblique direction would then replace criteria 1b and 1c of section 5.3.2.

A better evaluation of the role of boundary mixing in the deep ocean, whether caused by internal wave reflection and/or other mechanisms, will also require measurements of the rates of dissipation of kinetic energy and temperature variance in the boundary layer. At present, direct estimates of mixing with microstructure measurements are not easy to make in the abyssal ocean due to the weakness of the temperature and velocity gradients, but Thorpe (1987a) was able to obtain indirect estimates of mixing, using the empirical relationship of Dillon (1982) between the scale of overturns and the Ozmidov scale.

Efforts to monitor the exchange of water properties between the ocean interior and the fluid within the boundary layer should also be made if we wish to elucidate the role of boundary mixing in the ocean. Naturally occurring or deliberately injected tracers might be useful in that respect.

# Appendix A

## Data analysis techniques

### A.1 Estimation of the auto and cross-spectra, and number of equivalent degrees of freedom.

The Welch method of auto and cross-spectral estimation was always used in this thesis. For the computation of the autospectra, a time series  $x(t)$  of length  $T$  is first subdivided into several shorter sections of length  $M$ , each of which is Fast Fourier Transformed, and an average autospectrum

$$\langle \Gamma(\omega) \rangle = \langle X(\omega)X^*(\omega) \rangle \quad (\text{A.1})$$

is then calculated from the individual autospectra, where  $*$  denotes a complex conjugate, and the angled brackets denote the averaging process. Similarly, two time series  $x_1(t)$  and  $x_2(t)$  can be subdivided into several shorter sections of length  $M$ , each of which is Fast Fourier Transformed, and an average cross-spectrum

$$\langle K_{12}(\omega) \rangle \exp(i\langle \phi_{12}(\omega) \rangle) = \frac{\langle X_1^*(\omega)X_2(\omega) \rangle}{\langle X_1(\omega)X_1^*(\omega) \rangle^{1/2} \langle X_2(\omega)X_2^*(\omega) \rangle^{1/2}} \quad (\text{A.2})$$

is then calculated from the individual cross-spectra, where  $\langle K_{12}(\omega) \rangle$  is the estimated coherence spectrum, and  $\langle \phi_{12}(\omega) \rangle$  is the estimated phase spectrum. The Hanning window, given by

$$w(t) = 0.5 - 0.5 \cos(2\pi t/M), \quad 0 < t < M \quad (\text{A.3})$$

was used in all cases, and successive windows were routinely overlapped by 50% to increase the number of equivalent degrees of freedom. The properties of the Hanning window were studied in detail by Nuttall (1971), who calls it the 'cosine data window'. Table 6 of his paper indicates that for 50% fractional overlap between successive data pieces, we obtain 92% of the maximum number of equivalent degrees of freedom. Combining this information with the formula appearing at the bottom of table 4B of his paper, together with equation (33) and table 1 of his paper, we get the approximate formula

$$\nu \approx 3.82 \left( \frac{T}{M} \right) - 2.24 \quad (\text{A.4})$$

for the number of equivalent degrees of freedom obtained with 50% fractional overlap of successive windows. Table 4B of Nuttall (1971) suggests this formula may slightly underestimate the number of degrees of freedom, but never by more than about 0.25 for  $\nu < 100$ , which covers most practical cases.

## A.2 Estimation of the 95% confidence intervals and significance levels.

I have used figure 3.10 of Jenkins and Watts (1968) in order to obtain lower and upper bounds for the autospectral estimates such that

$$\text{Pr} \left\{ \text{Lower bound} \leq \frac{\Gamma(\omega)}{\langle \Gamma(\omega) \rangle} \leq \text{Upper bound} \right\} = 0.95, \quad (\text{A.5})$$

where  $\Gamma(\omega)$  is the true autospectrum of the parent time series, and  $\langle \Gamma(\omega) \rangle$  is the estimated autospectrum. The ratio  $\Gamma(\omega)/\langle \Gamma(\omega) \rangle$  should lie within those bounds 19 times out of 20, but could lie outside of them by pure luck 1 time out of 20.

The 95% significance level for zero true coherence between two time series  $x_1(t)$  and  $x_2(t)$  is given to a very good approximation by (Thompson, 1979)

$$\langle K_{12}^2 \rangle_{0.95} = 1 - 0.05^{2/(\nu-2)}, \quad (\text{A.6})$$

i.e. for zero true coherence, the estimated squared coherence  $\langle K_{12}^2(\omega) \rangle$  should be less than  $(K_{12}^2)_{0.95}$  19 times out of 20. For the phase spectrum, the 95% confidence intervals are given by (Jenkins and Watts, 1968, p. 435)

$$\phi_{12}(\omega) = \langle \phi_{12}(\omega) \rangle \pm \sin^{-1} \left[ \sqrt{\frac{2}{\nu-2} f_{2,\nu-2}(0.95) \frac{1 - \langle K_{12}^2(\omega) \rangle}{\langle K_{12}^2(\omega) \rangle}} \right] \quad (\text{A.7})$$

where  $\phi_{12}(\omega)$  is the true phase spectrum,  $\langle \phi_{12}(\omega) \rangle$  is the estimated phase spectrum,  $\langle K_{12}^2(\omega) \rangle$  is the estimated squared coherence spectrum, and  $f_{2,\nu-2}(0.95)$  is related to Fisher's F distribution (see figure 3.12 of Jenkins and Watts (1968)).

It turns out that the expression within square brackets in (A.7) is equal to one when  $\langle K_{12}^2(\omega) \rangle = (K_{12}^2)_{0.95}$ . Hence a simple formula for  $f_{2,\nu-2}(0.95)$  can be obtained from the value of  $(K_{12}^2)_{0.95}$  given in (A.6):

$$f_{2,\nu-2}(0.95) = \frac{\nu-2}{2} \frac{(K_{12}^2)_{0.95}}{1 - (K_{12}^2)_{0.95}}. \quad (\text{A.8})$$

Note that (A.7) is such that it gives no confidence intervals for the phase when  $\langle K_{12}^2(\omega) \rangle < (K_{12}^2)_{0.95}$ .

### A.3 Clockwise and anticlockwise velocity spectra

Instead of using the cartesian East and North velocity components  $u$  and  $v$ , it is sometimes useful to work with the clockwise and anticlockwise velocity components  $u_-$  and  $u_+$ , defined here as in Müller et al. (1978):

$$u_- = (u - iv)/\sqrt{2} \quad (\text{A.9})$$

$$u_+ = (u + iv)/\sqrt{2}. \quad (\text{A.10})$$

The clockwise and anticlockwise autospectra  $P_{--}$  and  $P_{++}$  are respectively given by

$$P_{--} = 0.5(P_{uu} + P_{vv} - 2Q_{uv}), \quad (\text{A.11})$$

$$P_{++} = 0.5(P_{uu} + P_{vv} + 2Q_{uv}), \quad (\text{A.12})$$

where  $Q_{uv}$  is the quadrature spectrum between  $u$  and  $v$ , and is such that  $Q_{uv} > 0$  when  $u$  leads  $v$ . From the above equations, it follows that

$$P_{--} + P_{++} = P_{uu} + P_{vv}, \quad (\text{A.13})$$

so that the total kinetic energy is given by

$$K.E. = \frac{1}{2} (P_{--} + P_{++}). \quad (\text{A.14})$$

## A.4 Current ellipse orientation and stability

Following Gonella (1972, p.837), I now introduce the concepts of ellipse orientation and stability by defining  $\langle E(\omega) \rangle$  as

$$\langle E(\omega) \rangle = \langle |E(\omega)| \exp(i2\langle \phi(\omega) \rangle) \rangle = \frac{\langle U_+(\omega)U_-(\omega) \rangle}{\langle U_-(\omega)U_-^*(\omega) \rangle^{1/2} \langle U_+(\omega)U_+^*(\omega) \rangle^{1/2}}, \quad (\text{A.15})$$

where  $U_-(\omega)$  and  $U_+(\omega)$  are the Fourier transforms of the clockwise and anticlockwise velocities, the angled brackets denote spectral averaging over adjacent data pieces,  $\langle \phi(\omega) \rangle$  is the estimated orientation spectrum, and  $\langle |E(\omega)| \rangle$  is what Gonella (1972) calls the coefficient of ellipse stability; it gives us a statistical measure of the stability of the estimated orientation  $\langle \phi(\omega) \rangle$ .

It is clear from the form of (A.15) that  $\langle |E(\omega)| \rangle$  is simply the estimated coherence spectrum between the clockwise and anticlockwise velocities, and  $2\langle \phi(\omega) \rangle$  is the estimated phase spectrum. Hence we can assign to those quantities the same confidence intervals we would assign any other type of coherence or phase spectrum. The 95% significance level for zero true ellipse stability is thus (cf A.6)

$$\langle |E(\omega)|^2 \rangle_{0.95} = 1 - 0.05^{2/(\nu-2)}, \quad (\text{A.16})$$

and the 95% confidence intervals for current ellipse orientation are (cf A.7)

$$\phi(\omega) = \langle \phi(\omega) \rangle \pm \frac{1}{2} \sin^{-1} \left[ \sqrt{\frac{2}{\nu-2} f_{2,\nu-2}(0.95) \frac{1 - \langle |E(\omega)|^2 \rangle}{\langle |E(\omega)|^2 \rangle}} \right], \quad (\text{A.17})$$

where  $\phi(\omega)$  is the true orientation spectrum, and  $\langle \phi(\omega) \rangle$  is the estimated orientation spectrum. The ellipse orientation can take any value within a total range of angles equal to  $180^\circ$  (e.g.  $0^\circ\text{T}$ – $180^\circ\text{T}$ ). Other directions are simply redundant ( $300^\circ\text{T} = 120^\circ\text{T}$  for example). Note that when  $\langle |E(\omega)|^2 \rangle < \langle |E(\omega)|^2 \rangle_{0.95}$ , (A.17) gives no confidence intervals for the ellipse orientation.

In terms of spectral quantities computed in a Cartesian frame of reference, the ellipse stability could alternatively be computed as

$$\langle |E(\omega)|^2 \rangle = \left\langle \frac{(P_{uu} + P_{vv})^2 - 4(P_{uv}^2 - P_{uu}P_{vv})}{(P_{uu} + P_{vv})^2 - 4Q_{uv}^2} \right\rangle, \quad (\text{A.18})$$

where  $P_{uv}$  is the co-spectrum between  $u$  and  $v$ , and the ellipse orientation  $\langle \phi(\omega) \rangle$  could be computed as

$$\langle \phi(\omega) \rangle = 0.5 \tan^{-1} \left( \left\langle \frac{2P_{uv}}{P_{uu} - P_{vv}} \right\rangle \right). \quad (\text{A.19})$$

Those equations yield the same results as (A.15), but are awkward to use, and are certainly not as transparent as (A.15) in terms of their meaning.

# Appendix B

## Permission to use published work

Part of chapter 3 is based on the paper of Garrett and Gilbert (1988). Permission to use this material for the purpose of inclusion in my thesis has been obtained from Elsevier Science Publishers B.V., Physical Sciences & Engineering Division, P.O. Box 330, 1000 AH Amsterdam, The Netherlands.

A more substantial part of chapter 4 is based on the paper of Gilbert and Garrett (1989). Permission to use this material for the purpose of inclusion in my thesis has been obtained from the American Meteorological Society, 45 Beacon Street, Boston, Massachusetts 02108, U.S.A.

## REFERENCES

- Armi, L. 1978. Some evidence for boundary mixing in the deep ocean. *J. Geophys. Res.*, **83**: 1971-1979.
- Armi, L. 1979. Effects of variations in eddy diffusivity on property distributions in the oceans. *J. Mar. Res.*, **37**: 515-530.
- Armi, L. and R.C. Millard 1976. The bottom boundary layer of the deep ocean. *J. Geophys. Res.*, **81**: 4983-4990.
- Armi, L. and E. D'Asaro 1980. Flow structures of the benthic ocean. *J. Geophys. Res.*, **85**: 469-484.
- Artale, V. and G.P. Gasparini 1990. Simultaneous temperature and velocity measurements of the internal wave field in the Corsican channel (Eastern Ligurian Sea). *J. Geophys. Res.*, **95**: 1635-1645.
- Baines, P.G. 1971a. The reflexion of internal/inertial waves from bumpy surfaces. *J. Fluid Mech.*, **46**: 273-291.
- Baines, P.G. 1971b. The reflexion of internal/inertial waves from bumpy surfaces. Part 2. Split reflexion and diffraction. *J. Fluid Mech.*, **49**: 113-131.
- Baines, P.G. 1973. The generation of internal tides by flat-bump topography. *Deep-Sea Res.*, **20**: 179-205.
- Baines, P.G. 1974. The generation of internal tides over steep continental slopes. *Phil. Trans. Roy. Soc. London, Ser. A*, **277**: 27-58.
- Baines, P.G. 1982. On internal tide generation models. *Deep-Sea Res.*, **29**: 307-338.
- Bell, T.H. 1975a. Topographically generated internal waves in the deep ocean. *J. Geophys. Res.*, **80**: 320-327.
- Bell, T.H. 1975b. Statistical features of sea-floor topography. *Deep-Sea Res.*, **22**: 883-892.

- Bird, A.A., G.L. Weatherly and M. Wimbush 1982. A study of the boundary layer over the eastward scarp of the Bermuda Rise. *J.Geophys.Res.*, **87**: 7941-7954.
- Brink, K.H. 1983. Some effects of stratification on long trench waves. *J.Phys.Oceanogr.*, **13**: 496-500.
- Briscoe, M.G. 1975. Preliminary results from the trimoored Internal Wave Experiment (IWEX). *J.Geophys.Res.*, **80**: 3872-3884.
- Bryan, F. 1987. Parameter sensitivity of primitive equation ocean general circulation models. *J.Phys.Oceanogr.*, **17**: 970-985.
- Cacchione, D. and C. Wunsch 1974. Experimental study of internal waves over a slope. *J. Fluid Mech.*, **66**: 223-239.
- Cox, C.S. and Sandstrom, H. 1962. Coupling of internal and surface waves in water of variable depth. *J.Oceanogr Soc.Japan*, **20th Ann. Vol.**: 499-513.
- Dillon, T.M. 1982. Vertical overturns: a comparison of Thorpe and Ozmidov length scales. *J.Geophys.Res.*, **87**: 9601-9613.
- Drinkwater, K.F. and R.W. Trites, 1987. Monthly means of temperature and salinity in the Scotian Shelf region., *Canadian technical report of fisheries and aquatic sciences No.1539*, iv + 101p.
- Eriksen, C.C. 1980. Evidence for a continuous spectrum of equatorial waves in the Indian Ocean. *J. Geophys. Res.*, **85**: 3285-3303.
- Eriksen, C.C. 1982. Observations of internal wave reflection off sloping bottoms. *J. Geophys. Res.*, **87**: 525-538.
- Eriksen, C.C. 1985. Implications of ocean bottom reflection for internal wave spectra and mixing. *J. Phys. Oceanogr.*, **15**: 1145-1156.
- Fofonoff, N.P. 1969. Spectral characteristics of internal waves in the ocean. *Deep-Sea Res.*, **16**: 58-71.

- Fu, L.L. 1981. Observations and models of inertial waves in the deep ocean. *Rev. Geophys. Space Phys*, **19**: 141–170.
- Garrett, C.J.R. 1979. Comment on 'Some evidence for boundary mixing in the deep ocean' by Laurence Armi. *J. Geophys. Res.*, **84**: 5095.
- Garrett, C.J.R. 1990. The role of secondary circulation in boundary mixing. *J. Geophys. Res.*, **95**: 3181–3188.
- Garrett, C.J.R. 1991. Marginal mixing theories. *Atmosphere–Ocean* (in press).
- Garrett, C.J.R. and W.H. Munk 1972. Space-time scales of internal waves. *Geophys. Fluid Dyn.*, **2**: 225–264.
- Garrett, C.J.R. and W.H. Munk 1975. Space-time scales of internal waves: A progress report. *J. Geophys. Res.*, **80**: 291–297.
- Garrett, C.J.R. and D. Gilbert, 1988. Estimates of vertical mixing by internal waves reflected off a sloping bottom. In *Small-scale turbulence and mixing in the ocean.*, J.C.J. Nihoul and B.M. Jamart (editors), Elsevier, Amsterdam, pp. 405–423.
- Gilbert, D. and C.J.R. Garrett 1989. Implications for ocean mixing of internal wave scattering off irregular topography. *J. Phys. Oceanogr.*, **19**: 1716–1729.
- Gill, A.E., 1982. *Atmosphere–Ocean Dynamics*. Academic Press, New York, 662 pp.
- Gonella, J. 1972. A rotary-component method for analysing meteorological and oceanographic vector time series. *Deep Sea Res.*, **19**: 833–846.
- Gregg, M.C. 1987. Diapycnal mixing in the thermocline: a review. *J. Geophys. Res.*, **92**: 5249–5286.
- Gregg, M.C. 1989. Scaling turbulent dissipation in the main thermocline. *J. Geophys. Res.*, **94**: 9686–9698.

- Haurwitz, B., H. Stommel and W.H. Munk, 1959. *On the thermal unrest in the ocean. In The atmosphere and sea in motion, Rossby Memorial Volume*, B. Bolin (editor), Rockefeller Univ. Press, pp. 74-94
- Heney, F.S., J. Wright and S.M. Flatté 1986. Energy and action flow through the internal wave field: an eikonal approach. *J. Geophys. Res.*, **91**: 8487-8495.
- Hogg, N.G. 1983. A note on the deep circulation of the western North Atlantic: its nature and causes. *Deep-Sea Res.*, **30**: 945-961.
- Hogg, N.G., P. Biscaye, W. Gardner and W.J. Schmitz 1982. On the transport and modification of Antarctic bottom water in the Vema Channel. *J. Mar. Res.*, **40**: 231-263.
- Holloway, G. 1980. Oceanic internal waves are not weak waves. *J. Phys. Oceanogr.*, **10**: 906-914.
- Hurley, D.G. 1970. Internal waves in a wedge-shaped region. *J. Fluid Mech.*, **43**: 97-120.
- Huthnance, J.M. 1978. On coastal trapped waves: analysis and numerical calculation by inverse iteration. *J. Phys. Oceanogr.*, **8**: 74-92.
- Huthnance, J.M. 1989. Internal tides and waves near the continental shelf edge. *Geophys. Astrophys. Fluid Dynamics*, **48**: 81-106.
- Huthnance, J.M. and P.G. Baines 1982. Tidal currents in the Northwest African upwelling region. *Deep-Sea Res.*, **29**: 285-306.
- Ivey, G.N. and R.I. Nokes 1989. Vertical mixing due to the breaking of critical internal waves on sloping boundaries. *J. Fluid Mech.*, **204**: 479-500.
- Ivey, G.N. and J. Imberber, 1990. The nature of turbulence in a stratified fluid. Part 1: the efficiency of mixing. *Submitted to J. Phys. Oceanogr.*

- Jenkins, G.M. and D.G. Watts, 1968. *Spectral analysis and its applications.*, Holden-Day, Oakland, California, 525 pp.
- Kunze, E. and T.B. Sanford 1986. Near-inertial wave interactions with mean flow and bottom topography near Caryn seamount. *J. Phys. Oceanogr.*, **16**: 109-120.
- Lai, D.Y. and T.B. Sanford 1986. Observations of hurricane-generated, near-inertial slope modes. *J. Phys. Oceanogr.*, **16**: 657-666.
- LeBlond, P.H. and L.A. Mysak, 1978. *Waves in the Ocean.* Elsevier, 602 pp.
- Lighthill, M.J., 1978. *Waves in fluids.* Cambridge University Press, 504 pp.
- Lively, R.R. 1979a. Current meter and meteorological observations on the Scotian Shelf: December 1975 to January 1978. Volume 1: December 1975 to December 1976. Bedford Institute of Oceanography data series report BI-D-79-1, 280pp.
- Lively, R.R. 1979b. Current meter and meteorological observations on the Scotian Shelf: December 1975 to January 1978. Volume 2: December 1976 to January 1978. Bedford Institute of Oceanography data series report BI-D-79-1, 368pp.
- Lively, R.R. 1984. Current meter observations on the Scotian Rise for November 1980 to October 1981. *Canadian technical report of hydrography and ocean sciences no. 50*, 156 pp.
- Longuet-Higgins, M.S. 1969. On the reflection of wave characteristics from rough surfaces. *J. Fluid Mech.*, **37**: 231-250.
- Louis, J.P., B.D. Petrie and P.C. Smith 1982. Observations of topographic Rossby waves on the continental margin off Nova Scotia. *J. Phys. Oceanogr.*, **12**: 47-55.
- McComas, C.H. 1977. Equilibrium mechanisms within the oceanic internal wavefield. *J. Phys. Oceanogr.*, **7**: 836-845.

- Mied, R.P. and J.P. Dugan 1976. Internal wave reflexion from a sinusoidally corrugated surface. *J. Fluid Mech.*, **76**: 259-272.
- Moody, R., D.E. Hayes and S. Connary 1979. Bathymetry of the continental margin of Brazil, *Map number 892*, Am. Assoc. Petrol. Geol., Tulsa, Oklahoma.
- Müller, P., D.J. Olbers and J. Willebrand 1978. The Iwex spectrum *J. Geophys. Res.*, **83**: 479-500.
- Müller, P., G. Holloway, F.S. Henyey and N. Pomphrey 1986. Nonlinear interactions among internal gravity waves. *Rev. of Geoph.*, **24**: 493-536.
- Munk, W.H. 1966. Abyssal recipes. *Deep-Sea Res.*, **13**: 207-230.
- Munk, W.H., 1981. Internal waves and small-scale processes. In *Evolution of physical oceanography scientific surveys in honor of Henry Stommel*, B.A. Warren and C. Wunsch (editors), M.I.T. Press, Cambridge, Massachusetts, pp. 264-291.
- Munk, W.H. and N. Phillips 1968. Coherence and band structure of inertial motion in the sea. *Rev. Geophys. Space Phys.*, **6**: 447-472.
- New, A.L. 1988. Internal tidal mixing in the Bay of Biscay. *Deep-Sea Res.*, **35**: 691-709.
- Nuttall, A.H., 1971. Spectral estimation by means of overlapped fast Fourier transform processing of windowed data. *NUSC Rep. 4169*, Nav. Underwater Syst. Center, New London, Conn., viii + 40 pp.
- Oakey, N.S. 1982. Determination of the rate of dissipation of turbulent energy from simultaneous temperature and velocity shear microstructure measurements. *J. Phys. Oceanogr.*, **12**: 256-271.
- Olbers, D.J. 1983. Models of the oceanic internal wavefield. *Rev. Geoph. Space Phys.*, **21**: 1567-1606.

- Petrie, B. 1975. M2 surface and internal tides on the Scotian shelf and slope. *J. Mar. Res.*, **33**: 303-323.
- Phillips, O.M. 1963. Energy transfer in rotating fluids by reflection of inertial waves. *Phys. Fluids*, **6**: 513-520.
- Phillips, O.M., 1966. *The Dynamics of the Upper Ocean*. Cambridge University Press, New York, 261pp.
- Phillips, O.M., 1977. *The Dynamics of the Upper Ocean. 2nd ed.*, Cambridge University Press, New York, 336 pp.
- Phillips, O.M., J.H. Shyu, and H. Salmun 1986. An experiment on boundary mixing: mean circulation and transport rates. *J. Fluid. Mech.*, **173**: 473-499.
- Rhines, P.B. 1970. Edge-, Bottom-, and Rossby waves in a rotating stratified fluid. *Geophys. Fluid Dyn.*, **1**: 273-302.
- Rubenstein, D. 1988. Scattering of inertial waves by rough bathymetry. *J. Phys. Oceanogr.*, **18**: 5-18.
- Sandstrom, H., 1966. The importance of topography in generation and propagation of internal waves. *Ph.D. thesis*, University of California at San Diego, 105 pp.
- Sandstrom, H. 1969. Effect of topography on propagation of waves in stratified fluids. *Deep-Sea Res.*, **16**: 405-410.
- Sandstrom, H., 1972. The effect of boundary curvature on reflection of internal waves. *Mémoires Société Royale de Liège*, 6ème série, tome IV, pp. 183-190.
- Sandstrom, H. 1976. On topographic generation and coupling of internal waves. *Geoph. Fluid Dyn.*, **7**: 231-270.
- Sandstrom, H., J.A. Elliott and N.A. Cochrane 1989. Observing groups of solitary internal waves and turbulence with BATFISH and echo-sounder. *J. Phys. Oceanogr.*, **19**: 987-997.

- Sandstrom, H. and J.A. Elliot 1989. Atlas of physical oceanographic data for current surge studies on the Scotian Shelf: 1983. *Canadian technical report of hydrography and ocean sciences No. 114*, 379 pp.
- Saunders, P.M., 1987. Flow through Discovery Gap. *J. Phys. Oceanogr.*, **17**: 631-643.
- Smith, P.C. 1989. Inertial oscillations near the coast of Nova Scotia during CASP. *Atmosphere-Ocean*, **27**: 181-209.
- Smith, P.C. and B.D. Petrie 1982. Low-frequency circulation at the edge of the Scotian Shelf. *J. Phys. Oceanogr.*, **12**: 28-46.
- Thompson, R.O.R.Y. 1979. Coherence significance levels. *J. Atm. Sc.*, **36**: 2020-2021.
- Thompson, R.O.R.Y. and J.R. Luyten 1976. Evidence for bottom-trapped topographic Rossby waves from single moorings. *Deep-Sea Res.*, **23**: 629-635.
- Thorpe, S.A. 1987a. Current and temperature variability on the continental slope. *Phil. Trans. R. Soc. London, Series A*, **323**: 471-517.
- Thorpe, S.A. 1987b. On the reflection of a train of finite amplitude internal gravity waves from a uniform slope. *J. Fluid Mech.*, **178**: 279-302.
- Thorpe, S.A., 1988. Benthic boundary layers on slopes. In *Small-scale turbulence and mixing in the ocean*. J.C.J. Nihoul and B.M. Jamart (editors), Elsevier, Amsterdam, pp. 425-433.
- Thorpe, S.A. and Haines, A.P. 1987. A note on observations of wave reflection on a 20° slope. Appendix to S.A. Thorpe, *J. Fluid Mech.*, **178**: 279-302.
- Thorpe, S.A., P. Hall and M. White 1990. The variability of mixing at the continental slope. *Phil. Trans. R. Soc. Lond. A*, **331**: 183-194.
- Whitehead, J.A. 1989. Surges of Antarctic Bottom Water into the North Atlantic. *J. Phys. Oceanogr.*, **19**: 853-861.

- Whitehead, J.A. and L.V. Worthington 1982. The flux and mixing rates of Antarctic Bottom Water within the North Atlantic. *J. Geophys. Res.*, **87**: 7903-7924.
- Wunsch, C. 1968. On the propagation of internal waves up a slope. *Deep-Sea Res.*, **15**: 251-258.
- Wunsch, C. 1969. Progressive internal waves on slopes. *J. Fluid Mech.*, **35**: 131-144.
- Wunsch, C. 1972a. The spectrum from two years to two minutes of temperature fluctuations in the main thermocline at Bermuda. *Deep-Sea Res.*, **19**: 577-593..
- Wunsch, C. 1972b. Temperature microstructure on the Bermuda slope with application to the mean flow. *Tellus*, **XXIV**: 350-367.
- Wunsch, C. 1976. Geographical variability of the internal wavefield: A search for sources and sinks. *J. Phys. Oceanogr.*, **6**: 471-485.
- Wunsch, C. and R. Hendry 1972. Array measurements of the bottom boundary layer and the internal wave field on the continental slope. *Geophys. Fluid Dyn.*, **4**: 101-145.
- Wunsch, C. and S. Webb 1979. The climatology of deep ocean internal waves. *J. Phys. Oceanogr.*, **9**: 235-243.